ADSORPTION, CO-ADSORPTION AND CATALYTIC REACTIONS ON Rh(111) AND Ru(001) SURFACES

Thesis by

Patricia Ann Thiel

In Partial Fulfillment of the Requirements
for the Degree of
Doctor of Philosophy

California Institute of Technology
Pasadena, California

1981

(Submitted December 1, 1980)

Table of Contents

Table of Contents (continued)

VII. Appendices

Acknowledgments

It has been a pleasure and a privilege to do my graduate work as a member of Professor Henry Weinberg's research group at Caltech for many reasons. First, I have had the opportunity to work with an exceptionally competent, cooperative, supportive and even-tempered group of people: Brad Anton, Bill Bowser, Chi-Ming Chan, Howard Evans, Tom Felter, Lynn Forester, Fritz Hoffmann, Dale Ibbotson, Ellen Williams, Steve Wittrig and Jenna Zinck. Second, I had the opportunity to work with Dr. John Yates, whose enormous enthusiasm for science is inspiring. Third, I had the benefit of interacting with very skillful and pleasant staff members. I am particularly indebted to Pat Bullard, George Griffith, Pat Lee, Kathy Lewis, Chick Nakawatase, Ray Reed, Tony Stark, Elmer Szombathy and John Yehle for both their professionalism and their friendships. Finally, and most important, I was able to learn from Henry Weinberg, who taught and showed me a great deal about scientific insight and integrity.

I thank my friends in the department for having made the past four years of my life memorable (and bearable) in many nonscientific respects.

I have received financial support in the form of Graduate Fellowships from the National Science Foundation and International Business Machines, Incorporated. I am also indebted to the American Vacuum Society for a Scholarship.

Abstract

The adsorption of oxygen, hydrogen, carbon monoxide, nitric oxide and water on Rh(111) and Ru(001) surfaces has been studied using the techniques of high-resolution electron energy loss spectroscopy, low-energy electron diffraction, Auger electron spectroscopy, ultraviolet photoelectron spectroscopy and thermal desorption mass spectrometry. In many cases co-adsorption experiments have provided insight into the nature of interaction between different adsorbates, with potential implications for heterogeneous catalytic reaction mechanisms.

The interaction of oxygen with Rh(111) consists of adsorption, irreversible thermally induced ordering and disordering phenomena, dissolution into the subsurface region and desorption. The thermodynamic parameters which describe these phenomena have been investigated. The forms of the kinetic rate expressions for the catalytic reaction of adsorbed oxygen with hydrogen are different for ordered and disordered arrays of oxygen adatoms. In agreement with co-adsorption studies of hydrogen and oxygen, and supported by studies of hydrogen chemisorption on clean Rh(111), this implies that the rate of adsorption of hydrogen is sensitive to the structure of the adsorbed oxygen lattice.

Two forms of molecularly adsorbed NO are readily distinguished on a Ru(001) surface by the frequencies of the nitrogen-oxygen stretching vibrations, which can then be used to observe the influence of co-adsorbates. Oxygen, nitrogen and hydrogen adatoms compete selectively for the adsites which are occupied by multiply-coordinated NO, whereas CO competes for adsites occupied by the singly-coordinated molecular NO. Carbon monoxide can even induce conversion of adsorbed molecular NO from sites of single coordination to sites of multiple coordination with the metal substrate.

Water interacts with the Ru(001) surface to form chemisorption bonds, but it also forms intermolecular hydrogen bonds which are of comparable strength. This leads to formation of layered, hydrogen bonded aggregates at all coverages. The properties of the first two layers are distinct from those of the subsequent ice multilayers, and a specific structural model for the hydrogen bonded lattices is proposed. A thermally induced ordering effect is observed which is analogous to the vitreous-to-cubic phase transformation of bulk ice.

1.

Introduction

The study of the structure and properties of molecules adsorbed on metal surfaces from the gas phase is a very active area of current research. The purpose of this research is to elucidate the physics and chemistry of the gas-metal interaction and to gain thereby a working understanding of the fundamental processes which are involved in such important phenomena as heterogeneous catalysis, surface corrosion, lubrication, adhesion, alloy segregation and electrochemistry. By using single crystals of metals and state-of-the-art vacuum technology, the surface scientist may choose to study model systems in which the conditions of surface cleanliness, surface structure, surface composition and exposure of the surface to the gas phase are well-controlled variables. These are the types of experiments described in this thesis. The conditions of such experiments are usually less complicated than the conditions which prevail in the processes which the experiments serve to model, such as heterogeneous catalysis, although recent experiments have been designed specifically to bridge the gap between these model systems and more "realistic" systems (e.g., 1, 2).

In the course of studying the chemistry of an atom or molecule adsorbed on a metal surface, valuable insight can be gained from a knowledge of metallic complexes and compounds. Perhaps the most obvious example of this is the interpretation of the vibrational spectra of adsorbed carbon monoxide in terms of the number of metal atoms to which the CO molecule is coordinated. Based directly upon the infrared spectra of metal carbonyls (3), surface scientists use the rule of thumb that a C-O stretching frequency above 1950 cm^{-1} indicates coordination to a single metal atom, a frequency between 1950 and 1850 cm^{-1} is indicative of bonding to two metal atoms, and lower frequencies are characteristic of higher coordination. This is a consequence of increased back-donation of metallic electron density into the $2\pi^*$ antibonding orbital of CO as the coordination of the CO to the surface or to the cluster increases (4). The development of the sensitive vibrational spectroscopy known as high resolution electron energy loss spectroscopy (EELS), and its application as a surface technique in particular, has fostered increasing reliance on the validity of comparisons between the vibrational properties of well characterized ligands in metallic compounds and adsorbates on metallic surfaces, in order to make identification of the adsorbates possible. This and other types of comparisons rest upon the basic assumption that the electronic structure of a metal atom or a small metal cluster is sufficiently similar to that of the extended metal surface, that the interaction with the ligand/adsorbate is also similar. This in turn implies that the chemisorption bond can be considered as a localized interaction involving only a few metal atoms. While this is certainly not true universally, it appears to be true in specific cases, some of which have been investigated in the course of preparing the present thesis. Several recent reviews (5 - 7) provide quite thorough discussions of various aspects of the metal cluster-metal surface analogy, both in terms of dynamic properties such as catalytic activity and ligand fluxionality/adsorbate mobility, and in terms of static properties such as the structure and bond energies of the ligand/adsorbate.

Two very recent measurements serve to illustrate the two approaches to the metal cluster-metal surface analogy nicely. In one experiment, the valence bandwidths of metal clusters deposited on amorphous carbon substrates were measured with X-ray photoelectron spectroscopy (8). It appears that the valence bandwidth converges to that of the bulk metal, for the transition metals Rh, Pd, Ir and Pt, only when the average cluster size is in excess of approximately 400 metal atoms (approximately 15 Å in diameter, assuming hemispherical clusters) (8). To the extent that a catalytic reaction or chemisorption bond requires interaction with the extended metal surface, then, one must use experimental or theoretical metal clusters containing hundreds of metal atoms to model bulk properties. On the other hand, another very recent investigation indicates that the chemisorption bond formed by one particular adsorbate may be considered a localized interaction involving isolated surface complexes. The research group of G. Ertl has studied the interaction of PF_3 with surfaces of Fe, Ru, Pd, Ir and Pt (9). They have compared the photoelectron spectra obtained in these surface studies with the photoelectron spectra of corresponding metal-PF_3 complexes, making use of the fact that there are many ligand valence orbitals uninvolved in bonding to the metal which can be used as energy references. Only the $8a_1$ orbital undergoes an energy shift due to bonding. This shift is quite sensitive to the metal substrate, and in every case this energy shift is very similar to that observed for the corresponding complex involving PF_3 and a single metal atom. This implies that the interaction of PF_3 with the surface is well modelled as an isolated surface complex (9).

A metal-ligand complex which is familiar to inorganic chemists, but whose analog has been regarded with some skepticism by surface chemists, is the metal-dioxygen complex. This type of complex forms by electron donation from the metal to the partially filled antibonding π_g orbital of the oxygen ligand (10, 11, 12). Depending upon the extent of electron transfer, this results in a "superoxo" or "peroxo" ligand, with formal O-O bond orders of 1.5 and 1.0, respectively. "Molecular oxygen" adsorbed on a metal surface has not been a popular concept because of the difficulty of proving its existence. Oxygen dissociates readily on the Group VIII transition metal surfaces (13), and evidence for associative adsorption has been indirect, until recently. The advent of EELS has provided direct, convincing spectroscopic proof that the oxygen-oxygen bond remains intact following adsorption on some metal surfaces below room temperature. The most notable cases to date are Pt(14), Ag(15) and possibly Ni(16). On these surfaces, the oxygen-oxygen stretch of adsorbed dioxygen occurs at 870, 630 and 907 cm^{-1}, respectively. The vibrational frequency observed for oxygen on Ag(110), 630 cm^{-1} (15), is slightly below the range of frequencies associated with singly- or doubly-coordinated peroxo complexes, 790 to 932 cm^{-1} (11), whereas the frequencies of dioxygen adsorbed on Pt(111) (14) and (possibly) on Ni(100) (16) are in the appropriate range. The frequencies of the metallic superoxo complexes occur between 1075 and 1195 cm^{-1} (11). Backx has proposed that back-donation from the filled π_u bonding orbital of adsorbed dioxygen to the metal may account for the lowering of the O-O frequency on Ag(110) relative to the metallic complexes (15). Even though the adsorbed dioxygen is thought to lie parallel to the metal surface (14, 15, 17), the oxygen-oxygen vibration may be dipole allowed due to charge fluctuation perpendicular to the metal surface as the oxygen atoms move parallel to the surface (15). It is interesting to note that just such a charge fluctuation has been postulated to occur for CO adsorbed on Cu(100) to account for the observed rate of damping of the vibrationally excited molecule, i.e. to explain the infrared linewidth of the carbon-oxygen stretch (18). Alternatively, the O-O vibration may be mechanically coupled to the metal-O vibration and be dipole-allowed by this mechanism (14).

The kinetics of the adsorption of oxygen on Rh(111) at 335 K, discussed in Chapter 3, is one of the indirect pieces of evidence which supports the existence of adsorbed dioxygen and which predates the EELS experiments. The rate of adsorption of oxygen on Rh(111) clearly follows (first-order) Langmuir adsorption kinetics, but only one adsorption site is involved per molecule. If dissociation of the oxygen molecule were a necessary prerequisite for adsorption, the (second-order) kinetics would reflect the necessity for two adjacent adsorption sites for each adsorption event. Apparently, at 335 K, the lifetime of the adsorbed dioxygen is sufficiently long to govern the adsorption kinetics but far too short to be observed spectroscopically (19). At 170 K, the rate of adsorption indicates that a mobile precursor is involved, as discussed in Chapter 1. This mobile precursor may well be molecular oxygen also.

Other evidence for nondissociative adsorption of oxygen has been obtained from O_2^{18}-O_2^{16} isotopic mixing experiments on Pt(100) (20) and Ag(110) (15,21) samples, where absence of $O^{16}O^{18}$ in a desorption feature indicates that the O-O bond has remained intact, as well as from X-ray and ultraviolet photoemission experiments on Pt(111) (14) and polycrystalline Ag (22) surfaces. Molecular oxygen may exist also under some conditions on the (110) surface of Ir, based upon Auger electron spectroscopy and irreversible thermal changes in the work function (17). Thus, adsorption of dioxygen occurs on a variety of crystallographic planes of a variety of metals (Ni, Rh, Ir, Pt, Ag), which indicates that it is a general phenomenon. Identification of these species in terms of "superoxo" or "peroxo" like compounds has been available only from the

EELS data, however. This identification is quite important in terms of discussing the reactive intermediates which may be formed in catalytic reactions such as epoxidation of ethylene over Ag catalyst (19).

It is also interesting to compare the interaction of molecular water with a metal surface to its interaction with metal atoms in aquometallic clusters and complexes. As discussed in Chapter 9, the adsorption of H_2O on the hexagonal surface of ruthernium has been studied, and the vibrational, geometric, electronic and thermodynamic properties of the adsorbate have been investigated in detail. One of the most intriguing aspects of the study was the observation of the intramolecular deformation mode at a frequency of 1510 to 1640 cm^{-1} in the EEL spectra. The frequency increased monotonically with increasing coverage of H_2O, as shown in Fig. 5 of Ch. 9. The frequency at 1640 cm^{-1} was observed for multilayers of ice on the Ru(001) surface and compares well with the infrared frequency of the absorption feature assigned to the scissoring mode of water in crystalline ices, 1650 cm^{-1} (23). The large shift in frequency with coverage is attributed to a smooth progression, from a state at low coverage in which a large fraction of the total adsorbed water is bound directly to the Ru surface (chemisorbed H_2O) to a state at higher coverage in which most of the water molecules are bound in an ice-like multilayer. The fact that the scissoring frequency, ν_s, is so low for the chemisorbed H_2O can be explained in terms of bonding via electron donation from the water to the metal substrate. As discussed in detail by Hauge, et. al. (24), a rationalization for the lowering of ν_s is available from an examination of the photoelectron spectrum of H_2O.

Removal of an electron from either the $1b_1$ or $3a_1$ orbitals of gaseous water causes a widening of the H-O-H bond angle and a corresponding decrease in ν_s(25). The decrease in ν_s can be accounted for therefore by partial electron donation from the molecular $3a_1$ and/or $1b_1$ orbitals to the metal substrate upon adsorption. Values of ν_s between 1498 and 1535 cm^{-1} have been reported for metal-sulfate (selenate) aquo complexes (26), where the metal atoms are Ni, Mg, Co, Zn, Fe, Mn and Cu. There was no apparent correlation between ν_s and the frequency of the O-H stretch, ν_{OH}, which led Oswald (26) to conclude that ν_{OH} is more sensitive to intermolecular hydrogen bonding than to the metal-ligand interaction. This is in complete agreement with our results also, which show that ν_{OH} of H_2O on Ru(001) maintains a constant value (within the limits of uncertainty) at all coverages, 3370 ± 50 cm^{-1}, because hydrogen-bonded clusters of water molecules form at all coverages. Photoionization of H_2O via either the $1b_1$ or $3a_1$ orbitals causes ν_{OH} to decrease by 440 cm^{-1} or to remain constant, respectively.

Furthermore, matrix-isolation studies of water bound to the Group IIIA metal atoms have suggested that increases in the metal-H_2O bond strengths may correlate with decreases in ν_s(24). Decreases in ν_s of 10 to 21 cm^{-1} are observed in these experiments, relative to the scissoring frequency of matrix-isolated H_2O, 1593 cm^{-1}.

It is interesting to note also that a relatively large H-O-H bond angle has been reported for chemisorbed H_2O on Ru(001): $116 \pm 10^{\circ}$ (27). This value is derived from an extrapolation of directional electron-induced emission of H^+ ions from chemisorbed H_2O to field-free conditions (27).

[However, it must be kept in mind that the angular distributions of ions emitted as a result of ESD may be subject to other influences whose relative importance are as yet unknown. These influences include the interaction between the emitted electron and its image charge in the metal, as well as possible bond re-orientation as a result of electronic excitation (final state effects).] The H-O-H bond angle in isolated H_2O is 104.5^o. As noted above, a broadening of the H-O-H bond angle results from photoionization of the $3a_1$ or $1b_1$ orbitals of molecular H_2O. Thus, electron donation from chemisorbed water to the Ru substrate may account for both experimental observations: the large H-O-H bond angle, and the low values of ν_s. It is noteworthy that electron donation from H_2O to the metal has been postulated to occur even when the metal is a very strong electron donor, such as lithium. This is based on experiments with matrix isolated Li-H_2O clusters (28) and with water adsorbed on a Li substrate (29).

Metal cluster chemistry has proven valuable in elucidating metal surface chemistry also in the area of nitric oxide adsorption. The adsorption of nitric oxide on Ru(001) has been studied in detail, primarily with EELS, and co-adsorption with other adsorbates has proven particularly informative in identifying adsite symmetries. This research is the topic of Chapters 6, 7 and 8.

The EEL spectrum of NO on Ru(001) shows two loss features in the energy range where the N-O stretching mode, ν_{NO}, of molecularly adsorbed NO would be expected, i.e. between 1350 and 2000 cm^{-1}, in analogy with the infrared spectra of metal compounds containing nitrosyl ligands (3, 30, 31). The frequencies of these two features are shown in Fig. 1 of Ch. 6. In metal nitrosyl complexes, frequencies between

1750 and 2000 cm^{-1} are usually associated with a linear and terminal M-N-O (formally NO^+) configuration (3, 30, 31). (A transition metal atom is symbolized by "M".) Frequencies between 1525 and 1750 cm^{-1} are generally due to bent nitrosyls (formally NO^-) with M-N-O angles between 119^o and 177^o. Frequencies below 1525 cm^{-1} are associated with coordination of the nitrosyl ligand to multiple metal centers. For example, in the compound $Ru_3(CO)_{10}(NO)_2$, with doubly coordinated nitrosyls, ν_{NO} occurs at 1533 to 1500 cm^{-1} (32, 33). In $(C_5H_5)_3Co_3(NO)_2$, with nitrosyls coordinated to three metal atoms, ν_{NO} falls to 1405 cm^{-1} (34). It must be kept in mind that correlations between vibrational frequencies and bonding configurations in metal nitrosyl complexes are not exact due to (at least in part) the variable electronic influence of the other ligands in the complex (30, 31, 35). It should be remembered also that influences such as dipole-dipole coupling can cause coverage-dependent frequency shifts of up to 35 cm^{-1} for adsorbates on metal surfaces, as has been shown recently, for example, in the case of CO adsorbed on Pd(100) (36a) and Cu(111) (36b). However, the values of ν_{NO} in metal nitrosyl compounds provide the only reasonable reference for assigning the vibrational features observed for NO adsorbed on metal surfaces, and it is on this basis that the original bonding configurations of NO on Ru(001) were assigned (37). The co-adsorption experiments of Chapters 6 to 8 have confirmed these assignments. The loss feature which occurs at 1380 to 1525 cm^{-1} for NO adsorbed on Ru(001) is due to NO bound at a site of threefold coordination ("bridged" NO). The other vibrational frequency ranges from 1780 to 1820 cm^{-1} and is due to molecular NO bound linearly to a single metal atom.

Carbon monoxide competes preferentially for the sites of single coordination (cf. Ch. 7), whereas atomic nitrogen, oxygen and hydrogen compete with nitric oxide for the three-fold adsites. This site competition is quite clearly and unambiguously evident in the EEL spectra. Adsorption of carbon monoxide can even cause conversion of some of the terminally bound NO to multiply coordinated NO, which has been observed directly in the EEL spectra. This surface reaction has a close analogue in the reactions of two metal cluster compounds, $Os_3(CO)_{12}$ (38) and $Ru_3(CO)_{12}$ (39). These trinuclear clusters have twelve linear and terminal carbonyl ligands. They react with nitric oxide gas to form compounds of the formula $M_3(CO)_9(NO)_2$, in which three of the carbonyl ligands on one metal atom have been replaced by two terminal nitrosyl ligands. This reaction sequence is illustrated in Fig. 4 of Ch. 7. Finally, the reaction of these compounds with CO forms products of the type $M_3(CO)_{10}(NO)_2$, in which both nitrosyl ligands are now two-fold coordinated (bridged), a single terminal CO has been added, and a M-M bond has been broken. Thus, the conversion of the nitrosyl ligand by CO(g) from a state of single coordination with the metal to a state of multiple coordination occurs in both a metal surface reaction and a metal cluster reaction.

Co-adsorption of nitric oxide and hydrogen has shown that atomic hydrogen preferentially adsorbs in the three-fold hollow sites on Ru(001). This conclusion was reached also for hydrogen adsorbed on the hexagonal surface, Ni(111), based upon a multiple scattering analysis of the low-energy electron diffraction (LEED) features (40). These features, due to variations of the diffracted current with variations in the incident beam voltage, showed that hydrogen was bound in the two inequivalent types of hollow sites with equal Ni-H bond lengths of 1.84 ± 0.06 Å, or a metal-H distance along the surface normal of 1.15 ± 0.1 Å. These parameters are reasonably close to the Ni-H bond lengths in the compound $H_3Ni(C_5H_5)_4$, wherein the Ni atoms form a tetrahedron and the hydride ligands bridge the three triangular faces of the Ni_4 cluster. In this compound the Ni-H bond lengths are 1.716 to 1.678 Å, and the H atoms are positioned 0.907 Å above the Ni_3 faces, on the average (41, 42). However, M-H bond lengths in metal hydrides are not very sensitive to the degree of hydride coordination: terminal M-H bond lengths vary from 1.60 to 1.78 Å, M_2H bond lengths vary from 1.71 to 1.88 Å, and average M_3H bond lengths are 1.69 and 1.73 Å in the two systems which have been studied (42). Three-fold coordination of adsorbed hydrogen has been deduced also from EELS data for a Pt(111) surface, with Pt-H bond lengths of 1.76 Å and a surface-hydrogen separation of 0.76 Å (43).

Perhaps a more interesting aspect of the cluster hydride-surface "hydride" structural comparison is the observation that interstitial hydrogen atoms have been identified in the transition metal compounds $[HCo_6(CO)_{15}]^-$ (42), $[HNi_{12}(CO)_{21}]^{3-}$ (42), $[H_2Ni_{12}(CO)_{21}]^{2-}$ (42), and $[Rh_{13}(CO)_{24}H_3]^{2-}$ (5). While it has been well established that hydrogen diffuses into the bulk of metallic Pd, there is recent evidence that subsurface diffusion of hydrogen may be a more general phenomenon, occurring also on Ni and Pt surfaces (44). The characteristics of interstitial metal hydrides undoubtedly will provide a fertile area of comparison for inorganic and surface chemists.

In conclusion, many analogies between metal surfaces and metal clusters have been discovered during the course of the present research. The comparisons range from the basic identification of surface complexes such as adsorbed dioxygen, to the nature of bond formation in a metal-aquo moiety, to the displacement and conversion of nitrosyl ligands by reaction with carbon monoxide. The broader goal of this research has been to investigate the physical chemistry of the interaction of gases with Group VIII transition metal surfaces, with particular emphasis on interactions which are relevant to heterogeneous catalysis and electrochemistry. The experimental techniques employed in these investigations include thermal desorption mass spectrometry, low-energy electron diffraction, ultraviolet photoelectron spectroscopy, Auger electron spectroscopy, changes in the contact potential which result from adsorption, and high resolution electron energy loss spectroscopy. These techniques have provided information directly on rates of adsorption and desorption, the kinds of two-dimensional adsorbate and substrate lattices which form, the identity of reaction products, and the energies of electronic and vibrational transitions of the metal-adsorbate complex. Based on these data, models have been proposed which describe explicitly the types of adsorption sites which are occupied, the nature of adsorbate-adsorbate interactions, the chemical identity and structure of adsorbed intermediates and the thermodynamic parameters involved in adsorption and desorption reactions.

Chapters 1 and 2 present experimental investigations of adsorption of oxygen and hydrogen on the (111) surface of Rh. These chapters provide the groundwork for Chapter 3, which discusses the catalytic reaction between adsorbed oxygen and gaseous hydrogen to produce water, catalyzed by the Rh(111) surface. These findings are clarified and supported by the data of Chapter 4, which presents a study of oxygen and hydrogen co-adsorbed on Rh(111). Chapter 5 discusses the adsorption of carbon monoxide on the Rh(111) surface, which provides an interesting contrast to the interaction of CO with the Ru(001) surface.

The adsorption of nitric oxide, and its co-adsorption with CO, N, O and H on Ru(001) are the subjects of Chapters 6, 7 and 8. These investigations concern primarily the vibrational properties of the adsorbed overlayers.

Finally, chemisorption and hydrogen bonding are the topics of Chapter 9, which presents an analysis of the adsorption of H_2O on Ru(001). A detailed description of the properties and nature of hydrogen-bonded clusters on the Ru substrate is proposed. Following the conclusions are several appendices which describe research in which the author of this thesis was not the principal investigator, and one appendix (Appendix 4) which describes the mechanical design and operation of an ultraviolet radiation source for use in angle-resolved photoelectron spectroscopic studies.

References.

1. H. P. Bonzel and H. J. Krebs, Surface Sci. 91, 499 (1980); also H. J. Krebs, H. P. Bonzel and G. Gafner, Surface Sci. 88, 269 (1979).
2. T. E. Madey, D. W. Goodman and R. D. Kelley, J. Vacuum Sci. Technol. 16, 433 (1979).
3. K. Nakamoto, Infrared and Raman Spectra of Inorganic and Coordination Compounds, John Wiley and Sons, New York (1978).
4. G. Blyholder, J. Phys. Chem. 68, 2772 (1964); G. Blyholder and M. Allen, J. Am. Chem. Soc. 91, 3158 (1969); G. Blyholder, J. Vacuum Sci. Technol. 11, 865 (1974); G. Blyholder, J. Phys. Chem. 79, 756 (1975).
5. E. L. Muetterties, T. N. Rhodin, E. Band, C. F. Brucker and W. R. Pretzer, Chem. Rev. 79, 91 (1979).
6. M. Moskovits, Acc. Chem. Res. 12, 229 (1979).
7. J. M. Basset and R. Ugo, "Structure and Electronic Relations Between Molecular Clusters and Small Particles: An Essay to the Understanding of Very Small Particles," Ch. 2 of Aspects of Homogeneous Catalysis, 3 , R. Ugo, Ed., D. Reidel Publishing Co., Dordrecht, Holland (1977) p. 137.
8. R. C. Baetzold, M. G. Mason and J. F. Hamilton, J. Chem. Phys. 72, 366 (1980).
9. G. Ertl, presented at The 4th Int. Conf. on Solid Surfaces and 3rd European Conf. on Surface Sci., Cannes, France (September 1980).

10. J. S. Valentine, Chem. Rev. 73, 235 (1973).

11. L. Vaska, Acc. Chem. Res. 9, 175 (1976).

12. A. B. P. Lever and H. B. Gray, Acc. Chem. Res. 11, 348 (1978).

13. J. Küppers and G. Ertl, Surface Sci. 77, L647 (1978).

14. J. L. Gland, B. A. Sexton and G. B. Fisher, Surface Sci. 95, 587 (1980); also G. B. Fisher, B. A. Sexton and J. L. Gland, J. Vacuum Sci. Technol. 17, 144 (1980).

15. C. Backx, C. P. M. de Groot and P. Biloent, Surface Sci., to be published; also Proc. 4th Int. Conf. Solid Surfaces and 3rd European Conf. Surface Sci., Cannes, France (September 1980) 248.

16. G. Dalmai-Imelik, J. C. Bertolini and J. Rousseau, Surface Sci. 63, 67 (1977).

17. J. L. Taylor, D. E. Ibbotson and W. H. Weinberg, Surface Sci. 79, 349 (1979).

18. M. Persson and B. N. J. Persson, Proc. I.R.I.S. Conf. Vibrations at Surfaces, Namur, Belgium (September 1980) to be published.

19. L. H. Dubois and G. A. Somorjai, Surface Sci. 91, 514 (1980).

20. M. Adnot, J. Fusy and A. Cassuto, Surface Sci. 72, 467 (1978).

21. M. A. Barteau and R. J. Madix, Surface Sci. 97, 101 (1980).

22. R. W. Joyner and M. W. Roberts, Chem. Phys. Letters 60, 459 (1979).

23. E. Whalley, "The Hydrogen Bond in Ice", Ch. 29 of The Hydrogen Bond: Recent Developments in Theory and Experiments 3, P. Schuster, G. Zundel and C. Sandorfy, Eds., North-Holland Publishing Co., Amsterdam (1976) p. 115.

24. R. H. Hauge, J. W. Kauffman and J. L. Margrave, J. Am. Chem. Soc. 102, 6005 (1980).

25. D. W. Turner, C. Baker, A. D. Baker and C. R. Brundle, Molecular Photoelectron Spectroscopy, John Wiley and Sons, London (1970) pp. 77-81.

26. H. R. Oswald, Helv. Chim. Acta 48, 600 (1965).

27. T. E. Madey and J. T. Yates, Jr., Chem. Phys. Letters 51, 77 (1977).

28. P. F. Meier, R. H. Hauge and J. L. Margrave, J. Am. Chem. Soc. 100, 2108 (1978); also R. H. Huage, P. F. Meier and J. L. Margrave, Ber. Bunsenges. Phys. Chem. 82, 102 (1978).

29. W. McLean, J. A. Schulz, L. G. Pedersen and R. C. Jornagin, Surface Sci. 83, 354 (1979).

30. F. A. Cotton and G. Wilkinson, Advanced Inorganic Chemistry, Interscience Publishers, New York (1972) p. 713.

31. R. Eisenberg and C. D. Meyer, Acc. Chem. Res. 8, 26 (1975).

32. M. Poliakoff and J. J. Turner, J. Chem. Soc. A, 654 (1971); M. Poliakoff and J. J. Turner, Chem. Comm., 1008 (1970).

33. J. R. Norton, J. P. Collman, G. Dolcetti and W. T. Robinson, Inorganic Chem. 11, 382 (1972).

34. J. Müller and S. Schmitt, J. Organomet. Chem. 97, C54 (1975).

35. E. E. Mercer, W. A. McAllister and J. R. During, Inorganic Chem. 5, 1881 (1966).

36. (a) A. Ortega, A. Garbout, F. M. Hoffmann, W. Stenzel, R. Unwin, K. Horn and A. M. Bradshaw, Proc. 4th Int. Conf. Solid Surfaces and 3rd Eur. Conf. Surface Sci., Cannes, France (September 1980) 1125.
    (b) P. Hollins and J. Pritchard, Surface Sci. 89, 486 (1979).

37. G. E. Thomas and W. H. Weinberg, Phys. Rev. Letters 41, 1181 (1978).

38. S. Bhaduri, B. F. G. Johnson, J. Lewis, D. J. Watson and C. Zuccaro, J. Chem. Soc. Chem. Comm., 477 (1977).

39. B. F. G. Johnson, private communication.

40. K. Christmann, R. J. Behm, G. Ertl, M. A. Van Hove and W. H. Weinberg, J. Chem. Phys. 70, 4168 (1979).

41. T. F. Koetzle, J. Muller, D. L. Tipton, D. W. Hart and R. Bau, J. Am. Chem. Soc. 101, 5631 (1979).

42. R. Bau, R. G. Teller, S. W. Kirtley and T. F. Koetzle, Acc. Chem. Res. 12, 176 (1979).

43. A. M. Baró, H. Ibach and H. D. Bruchmann, Surface Sci. 88 (1979) 384.

44. W. Eberhardt, W. W. Plummer and J. Dinardo, J. Vacuum Sci. Technol. (March/April 1981), to be published.

Chapter 1

THE INTERACTION OF OXYGEN WITH THE Rh(111) SURFACE

1. Introduction.
2. Experimental Details.
3. Experimental Results.
    - 3.1. Oxygen Thermal Desorption Spectra.
    - 3.2. Oxygen Auger Spectra.
    - 3.3. LEED Studies of Irreversible Thermal Ordering and Disordering of Oxygen on Rh(111).
    - 3.4. Kinetic Studies of Oxygen Ordering Using LEED.
4. Discussion.
    - 4.1. General Behavior of Oxygen on Group VIII Metals.
    - 4.2. Kinetics of Oxygen Adsorption at 170 K.
    - 4.3. Oxygen Penetration into Rh(111).
    - 4.4. Thermal Desorption of O_2 from Rh(111).
    - 4.5. LEED Data for Oxygen on Rh(111).

Surface Science 82 (1979) 22–44
© North-Holland Publishing Company

THE INTERACTION OF OXYGEN WITH THE Rh(111) SURFACE [a]

P.A. THIEL [b], J.T. YATES, Jr. [c] and W.H. WEINBERG [d]
Division of Chemistry and Chemical Engineering, California Institute of Technology, Pasadena, California 91125, USA

Received 31 August 1978; manuscript received in final form 26 October 1978

The adsorption of oxygen on Rh(111) at 100 K has been studied by TDS, AES, and LEED. Oxygen adsorbs in a disordered state at 100 K and orders irreversibly into an apparent (2 × 2) surface structure upon heating to $T \geqslant 150$ K. The kinetics of this ordering process have been measured by monitoring the intensity of the oxygen $(1, \overline{1/2})$ LEED beam as a function of time with a Faraday cup collector. The kinetic data fit a model in which the rate of ordering of oxygen atoms is proportional to the square of the concentration of disordered species due to the nature of adparticle interactions in building up an island structure. The activation energy for ordering is 13.5 ± 0.5 kcal/mole. At higher temperatures, the oxygen undergoes a two-step irreversible disordering ($T \geqslant 280$ K) and dissolution ($T \geqslant 400$ K) process. Formation of the high temperature disordered state is impeded at high oxygen coverages. Analysis of the oxygen thermal desorption data, assuming second order desorption kinetics, yields values of 56 ± 2 kcal/mole and 2.5 ± 10^{-3} cm^2 s^{-1} for the activation energy of desorption and the pre-exponential factor of the desorption rate coefficient, respectively, in the limit of zero coverage. At non-zero coverages the desorption data are complicated by contributions from multiple states. A value for the initial sticking probability of 0.2 was determined from Auger data at 100 K applying a mobile precursor model of adsorption.

1. Introduction

The interaction of oxygen with Group VIII transition metal surfaces is important in understanding both partial and total oxidative catalysis over these surfaces. However, the interaction is so complex that the experimental work reported to date leaves many questions to be answered before a consistent detailed atomic model for the oxygen + metal system can be developed. In this paper, we report the results of a study of the interaction of oxygen with the Rh(111) surface based on low-energy

---

[a] Supported by the Army Research Office (Durham) under Grant No. DAHCO4-75-0170.

[b] National Science Foundation Predoctoral Fellow.

[c] Sherman Fairchild Distinguished Scholar. Permanent address: National Bureau of Standards, Washington, DC 20234, USA.

[d] Camille and Henry Dreyfuss Foundation Teacher–Scholar, and Alfred P. Sloan Foundation Fellow.

electron diffraction (LEED), thermal desorption mass spectrometry (TDS), and Auger electron spectroscopy (AES).

Tucker [1,2] has studied LEED patterns formed by oxygen on Rh(110) and Rh(100) surfaces. However, later studies have suggested that these early experiments were carried out on a contaminated surface [3]. The adsorption of small molecules, including oxygen, on Rh(100) and Rh(111) surfaces has been reported by Castner et al. [4]. The present study is a more detailed examination of the interaction of oxygen with Rh(111) than has been reported previously.

In section 2, a description of the experimental apparatus and procedures is presented. The experimental data are presented in section 3, and their interpretation is discussed in section 4.

2. Experimental details

The ultra-high vacuum (UHV) apparatus, crystal preparation and cleaning procedures, and measurement techniques for the LEED data have been described elsewhere [5]. The system was equipped with a single-pass cylindrical mirror electron energy analyzer for Auger spectroscopy. It was equipped also with 4-grid LEED optics and a movable Faraday cup collector. Gases were admitted to the UHV chamber and exposed to the crystal by adjusting a variable leak valve until the desired steady state pressure was obtained, as measured with a Bayard–Alpert gauge. All oxygen exposures are reported in Langmuirs (Torr s $\times 10^6$, L), corrected for the sensitivity of the ion gauge to oxygen relative to nitrogen. Thermal desorption spectra were measured with the crystal rotated 185° from the quadrupole mass spectrometer (QMS), except for several line-of-sight measurements. The QMS was operated at an electron energy of 70 eV and an emission current of 2.0 mA in all measurements. Research grade O_2 (>99% purity) from Matheson was used in all experiments. The measured pumping speed of the system was 980 l/s for CO and 1750 l/s for H_2, using an estimated value for the system volume of 50 l.

3. Experimental results

3.1. Oxygen thermal desorption spectra

Representative thermal desorption spectra for oxygen on the clean Rh(111) surface are shown in fig. 1B. The crystal was exposed to O_2 at temperatures below 170 K and was heated to 1240 K at a rate of ~24 K/s during each flash. The oxygen Auger intensity was recorded after each exposure (fig. 1A) to give an indication of the amount of oxygen which had been adsorbed, and it was recorded after each desorption experiment (fig. 1C) to show that the crystal had returned to its original condition. We believe that the small residual oxygen Auger feature remaining after

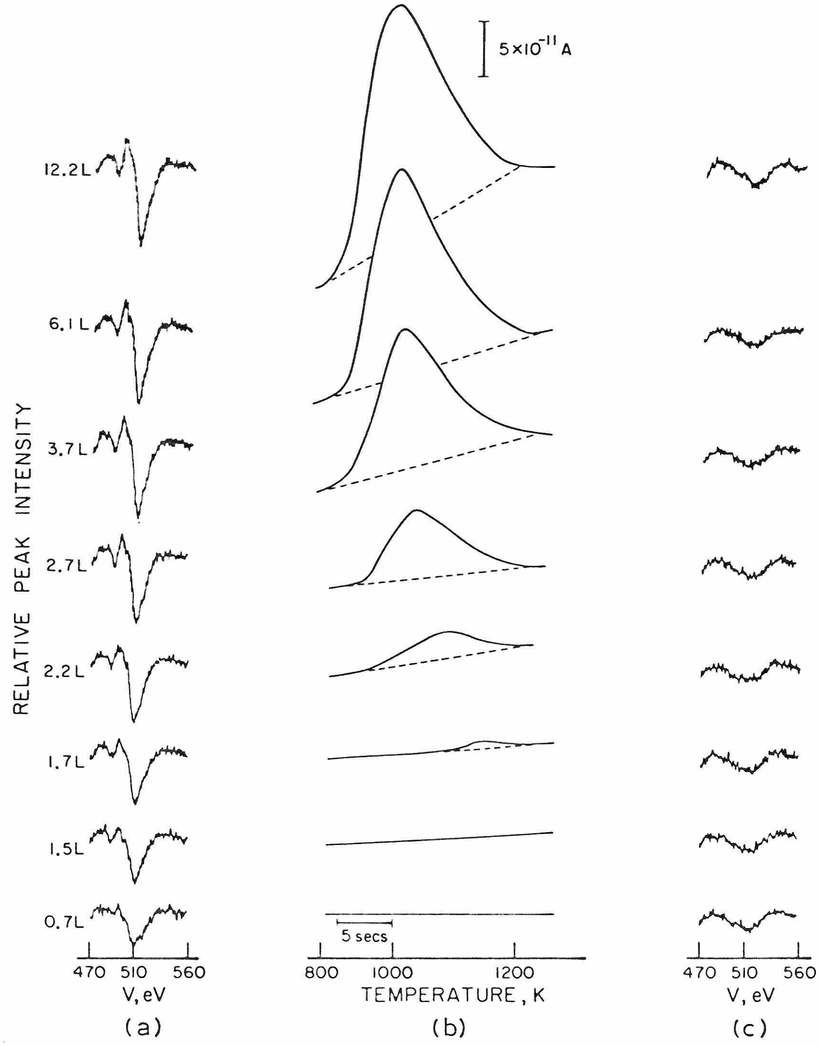

Fig. 1. Thermal desorption of O_2 from Rh(111). The Auger spectra were taken with V_e = 2000 eV, I_e = 4.1–4.3 μA, V_{mod} = 1.2 eV, sensitivity = 10X.

desorption is due to subsurface oxygen as will be discussed later. In fig. 2, the oxygen Auger intensity, taken as the peak-to-peak amplitude, and the yield of thermally desorbed O_2 are plotted as functions of O_2 exposure. These data show clearly that at low oxygen exposures, an appreciable amount of oxygen adsorbs on the crystal and disappears upon heating to 1240 K, but not by means of O_2 desorption.

We investigated the possibility that atomic oxygen (M = 16 amu) or volatile rhodium oxides (RhO: M = 119 amu; RhO_2: M = 135 amu; Rh_2O_3: M = 254 amu) were being evolved during the thermal desorption, but no such species were ob-

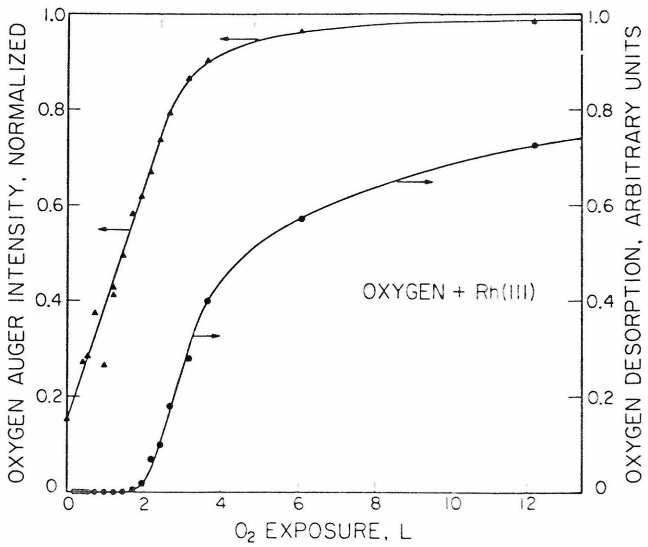

Fig. 2. Oxygen thermal desorption peak areas and oxygen Auger peak intensities as a function of O_2 exposure. All values were normalized to an asymptotic value obtained by extrapolating intensity as a function of $1/\epsilon$ to $1/\epsilon = 0$, where $\epsilon = O_2$ exposure. $T = 170$ K.

served. The appropriate mass peaks were monitored during oxygen desorption with the crystal directly in line-of-sight with the mass spectrometer and approximately 1 cm removed. The rhodium oxide mass peaks were monitored with the resolution of the mass spectrometer fully degraded. This effectively increased the sensitivity by a factor of three. However, no evidence for the evolution of atomic oxygen or volatile rhodium oxides from the crystal was observed. This precludes the possibility that the absence of oxygen thermal desorption at low O_2 exposures is due to desorption of species with mass other than $M = 32$ amu.

On the basis of the above experiments, it appears that competition between two modes of oxygen depletion occurs during thermal desorption of oxygen: dissolution into the bulk and desorption as molecular oxygen, with dissolution being the predominant depletion mode at low coverages. On the basis of the Auger data of fig. 2, at least 40% of the saturation coverage of oxygen must adsorb before O_2 desorption is observed. This "threshold effect" means that the thermal desorption peak areas can only be interpreted as effective desorption coverages, not as total relative oxygen coverages. Experimentally, it was observed that a high exposure to O_2 and subsequent heating could be followed by a low O_2 exposure and heating, with no desorption resulting from the second exposure. This indicates that the desorption behavior at low exposures cannot be due to formation of a permanent surface or subsurface oxide which remains unchanged during the desorption measurement. In repeating these experiments on two separate Rh(111) crystals, the O_2 exposure required to produce measurable O_2 desorption varied only from 1.3 to

1.6 L. If oxygen is depleted by dissolution into the bulk at low coverages, one would expect the desorption threshold to be somewhat sensitive to previous O_2 exposure and heating cycles, as was observed.

It should be noted that the thermal desorption peak areas were estimated on the assumption that the rising background during the final stages of heating could be represented by a straight line, the position of which was determined empirically. The validity of this procedure is supported by the observation that desorption spectra following low O_2 exposures were straight lines as in the 1.2 L O_2 exposure experiment shown in fig. 1B. Backgrounds are shown as dashed lines in the desorption spectra of this figure. It should be noted also that a small, sharp, first order O_2 desorption peak was observed consistently at 158 K. The magnitude of this peak scaled approximately with exposure and was less than 10% of the area of the high temperature peak. This peak could be due either to adsorption on the Ta support wires or to O_2 desorption from molecularly adsorbed oxygen on the Rh(111) crystal. At ~150 K, an undissociated O_2 desorption state has been seen for O_2 adsorption on Pt(100) [6].

The O_2 thermal desorption spectra exhibit apparent second order behavior; the peak shifts from ~1160 to 1038 K with increasing coverage. On the assumption that desorption obeys second order kinetics, the activation energy and pre-exponential factor for each desorption peak were calculated using the method of Chan et al. [7]. This method involves measuring the peak width and the temperature at which the maximum rate of desorption occurs. The results are shown in figs. 3 and 4. The calculated kinetic parameters vary dramatically with coverage, which demonstrates

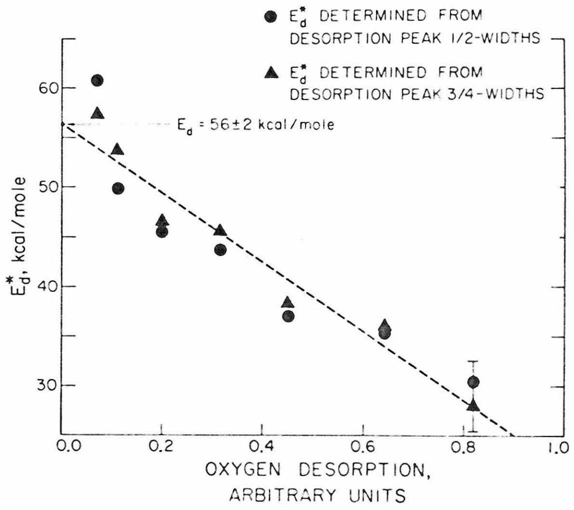

Fig. 3. Effective oxygen energy of desorption, $E_d^{*(2)}$, as a function of oxygen desorption intensity for second-order desorption kinetics. Error bars were estimated on the basis of a worst-case error of 5 K in *each* peak temperature measurement.

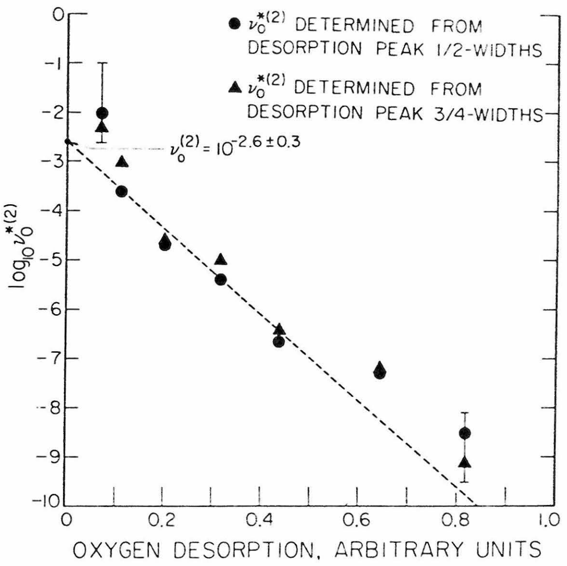

Fig. 4. Effective second-order pre-exponential, $\nu_0^{*(2)}$, as a function of oxygen desorption intensity. Error bars were estimated on the basis of a worst-case error of 5 K in *each* peak temperature measurement.

that the desorption spectra do not represent a simple second order process. The effective pre-exponential factor, $\nu_0^{*(2)}$, varies from 1.5 X 10^{-9} cm^2 s^{-1} at high coverage to 2.5 X 10^{-3} cm^2 s^{-1} at zero oxygen surface coverage, where the latter value has been obtained from a linear extrapolation of the logarithm of $\nu_0^{*(2)}$ to zero surface coverage. The effective energy of desorption, $E_d^{*(2)}$, may be extrapolated linearly to a value of 56 ± 2 kcal/mole at zero surface coverage; at high coverage, the measured value of $E_d^{*(2)}$ was 29 kcal/mole. The errors in the kinetic parameters are based on the statistical scatter in the experimental data with respect to a linear least squares fit to the data.

The kinetic parameters which were calculated by extrapolation to zero surface coverage are reasonable for second order O_2 desorption. At higher coverages, the anomalous kinetic parameters are related to desorption peak broadening. This may be caused by the occurrence of unresolved site-dependent desorption states, or by strong interactional effects within the overlayer. In either case, the original assumption of simple second order kinetics for a single state is clearly invalid. Therefore, the calculated kinetic parameters shown in figs. 3 and 4 have no straightforward physical meaning, except in the limit of zero coverage: $E_d^{(2)}$ = 56 ± 2 kcal/mole and $\nu_0^{(2)}$ = 2.5 X 10^{-3} cm^2 s^{-1}.

For O_2 exposures $\leqslant$2.4 L at a crystal temperature $\leqslant$170 K, a value of the sticking coefficient, S_0, was calculated on the basis of the Auger data of fig. 2. The result is S_0 = 0.16 ± 0.02, where the error is estimated on the basis of the scatter in

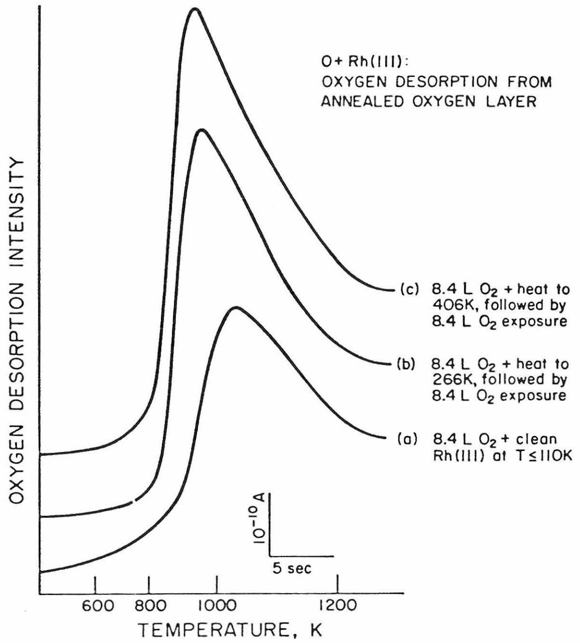

Fig. 5. O_2 thermal desorption spectra following 8.4 L O_2 exposure to annealed O + Rh(111).

the data relative to a linear least squares fit. Errors in absolute calibration of the Bayard–Alpert gauge could lead to a factor of two uncertainty in S_0. The value of S_0 measured is very comparable to values of S_0 reported for the other Group VIII transition metals. (See, for example, refs. [8–11].)

When oxygen is adsorbed on top of an annealed oxygen overlayer, the shape of the O_2 thermal desorption peak changes distinctly, with the leading edge becoming much sharper and the peak maximum moving to lower temperatures. This effect is illustrated in fig. 5 and will be discussed more fully in a later section.

3.2. Oxygen Auger spectra

Adsorbed oxygen also exhibited behavior indicative of dissolution into Rh(111) at temperatures below those at which desorption occurred. A high-sensitivity study of the oxygen Auger intensity as a function of annealing temperature showed a definite decrease at temperatures below the onset of desorption. Following exposure to 3.1 L O_2 at temperatures below 140 K, the crystal was heated to successively higher temperatures, and the Auger spectrum was recorded after the crystal had recooled. Representative oxygen Auger spectra are shown in fig. 6 for various final heating temperatures. The intensity, measured as the peak-to-peak amplitude of the differential 510 eV oxygen transition relative to the 303 eV Rh transition, began to

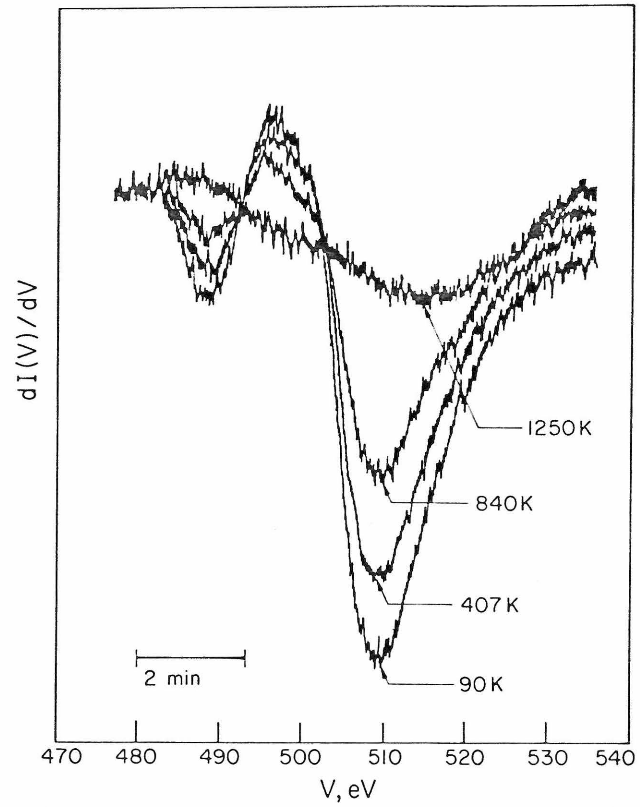

Fig. 6. Oxygen Auger spectrum as a function of heating following 3.1 L O_2 exposure. I_e = 3.3 μA, V_e = 2000 eV, V_{mod} = 1.2 eV, sensitivity = 40X.

decrease near 390 K and reached 50% of its original value upon heating to 800 K, where desorption begins for high oxygen coverages. This is illustrated in fig. 7B, where the normalized oxygen : rhodium Auger peak intensity ratio is plotted as a function of the temperature to which the crystal with the adsorbed overlayer was heated. A viable explanation for the systematic decrease in the O : Rh Auger peak intensity ratio above 400 K is that the oxygen penetrates the crystal at relatively low temperatures. This is supported by other data which will be discussed.

The line shape of the oxygen Auger transition resulting from chemisorption of oxygen on the Rh(111) surface was distinctly different from the line shape of the residual oxygen Auger transition following a high temperature anneal in vacuum, as shown in fig. 6. Chemisorbed oxygen exhibited a major peak at 510 eV and a smaller peak at 448 eV. The positions of these peaks were invariant upon heating to temperatures up to the onset of desorption, although the intensity decreased during the course of this treatment. The residual Auger signal shows a broad maximum at ~515 eV. The oxygen Auger peak shown in fig. 6 after heating to 1250 K is typical

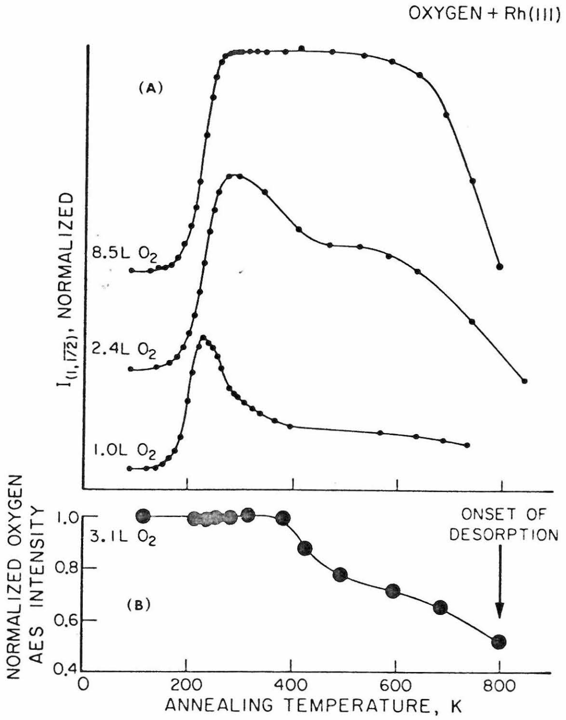

Fig. 7. Effects of annealing on oxygen overlayer following adsorption at $T \leqslant 120$ K. (A) Intensity of oxygen (1, $\overline{1/2}$) spot as a function of annealing temperature. (B) Normalized value of the oxygen : rhodium Auger peak intensity ratio as a function of annealing temperature.

of our Rh(111) surface and represents 0.3–0.6% of the intensity of the 303 eV Rh peak. The maximum O : Rh Auger peak intensity ratio observed was ~5%, following a 12.2 L O_2 exposure at $T \leqslant 170$ K. Heating the crystal to 1660 K in vacuo did not change the residual oxygen Auger intensity. It was unaffected also by heating the crystal to 670 K in 3×10^{-7} Torr H_2 for 1 min or to 500 K in 5×10^{-7} Torr CO for 15 min. Furthermore, it was unchanged following a series of H_2 or CO exposures at $T \leqslant 170$ K and subsequent heating. It is interesting to note that in experiments on two separate crystals, this residual oxygen AES peak was absent or very small when the crystal was at room temperature, but appeared or intensified when the crystal was cooled to near liquid nitrogen temperature. This phenomenon may be related to temperature-dependent surface segregation of bulk oxygen, although it was not studied in detail.

If one assumes that this small residual oxygen Auger intensity is due to oxygen uniformly distributed throughout the near surface region of the Rh crystal, then the amount of dissolved oxygen present is on the order of 1 at%. This number represents a crude upper limit, since it ignores the effect of primary electron beam attenuation and secondary electron emission in the bulk. The calculation assumes an escape depth of 10 Å for 500 eV electrons [12] and a saturation surface coverage of 4×10^{14} cm^{-2}.

A study of the oxygen Auger intensity as a function of time showed that electron beam damage could not account for the observed variation in oxygen Auger intensity with annealing temperature. At a beam voltage of 2000 eV and a beam current of 4.3 μA (measured using the commercial Varian gun control unit output), the net change in the O : Rh intensity ratio was less than 5% over a period of 60 min. On the basis of these results, as well as the observed constancy in the O : Rh Auger intensity ratio at temperatures below 390 K (fig. 7B), it is concluded that electron stimulated desorption of oxygen cannot be invoked as an explanation for the results shown in figs. 6 and 7B.

3.3. LEED studies of irreversible thermal ordering and disordering of oxygen on Rh(111)

The LEED pattern characteristic of the clean Rh (111) surface exhibited hexagonal symmetry, as reported previously [2–5]. A (2 × 2) LEED pattern was observed for oxygen adsorbed on the Rh(111) surface. All O_2 exposures were made at $T \leqslant 120$ K, and the intensity of the oxygen overlayer LEED pattern was observed to have a marked dependence upon the temperature to which the crystal was heated following exposure to O_2. A detailed study of the intensity of the oxygen overlayer LEED pattern as a function of heating temperature indicated that a complex, irreversible ordering-disordering phenomenon was occurring. No pattern other than the (2 × 2) formed as a result of oxygen adsorption following annealing at temperatures up to 1250 K.

Experimentally, the crystal was exposed to between 1.0 and 8.5 L of O_2 at $T \leqslant 120$ K. The crystal was then heated to successively higher temperatures. The intensity of the oxygen $(1, \overline{1/2})$ beam was measured with the Faraday cup when the crystal had recooled to $T \leqslant 105$ K after each heating cycle, thus eliminating Debye–Waller effects in our intensity measurements. In fig. 7A, we show the intensity as a function of heating temperature following exposures of 1.0, 2.4 and 8.5 L O_2. The data show that the ordering–disordering phenomenon is coverage dependent and appears to occur in at least two distinct stages: the oxygen orders between 150 and 280 K, then undergoes a disordering/depletion process at higher temperatures. Both processes are irreversible as indicated by the following two experiments:

Experiment A. Following a 2.4 L O_2 exposure, the crystal was heated stepwise to 467 K, which is just at the leading edge of the intensity plateau for the 2.4 L exposure in fig. 7A. The crystal was then annealed at 280 K for ten minutes. The oxygen overlayer LEED intensity increased from 63% to 69% of the value of the maximum ordered intensity as a result of this prolonged heating. With the electron beam off, this LEED intensity was stable to within 1% over a twenty minute period at 90 K, indicating that electron impact effects are unimportant in the LEED measurements.

Experiment B. The crystal was heated stepwise to 739 K following a 1.0 L O_2 exposure. The crystal was then annealed at 245 K for 8 min. When the crystal was recooled to $T \leqslant 105$ K, the oxygen $(1, \overline{1/2})$ beam intensity, $I_{(1,\overline{1/2})}$, had increased from 33% to 39% of the value of the maximum ordered intensity.

In both of these experiments, the small increases in $I_{(1,1/2)}$ over long periods of heating are insignificant compared to the major effects which were observed upon heating the crystal to successively higher temperatures, and do not detract from our general conclusion that the order → disorder transition is irreversible.

It is important to note that, following an 8.5 L O_2 exposure and subsequent stepwise heating, the intensity of the ordered oxygen LEED beams remained constant between 280 and 530 K, whereas the intensity of the oxygen LEED beams resulting from 1.0 to 2.4 L O_2 exposures dropped sharply between 280 and 400 K. This indicates that the disorder/depletion process occurs in two steps, the first step being inhibited at high coverages. We propose that between 280 and 400 K the ordered layer disorders irreversibly, and that the extent to which disordering occurs depends upon the coverage of ordered material, i.e., upon the number of unfilled adsites remaining on the crystal surface after ordering occurs. This is followed by dissolution into the near surface region at temperatures between 400 and 800 K. Detailed studies of the high temperature disordering process will be reported in the following paper [13], in which the energy of activation for the disordering process was measured to be 8.2 ± 0.3 kcal/mole.

Examination of the O : Rh Auger intensity ratio as a function of heating temperature in fig. 7B supports this two-step model, since the O : Rh Auger intensity ratio only begins to decrease at temperatures above 400 K following a 3.1 L O_2

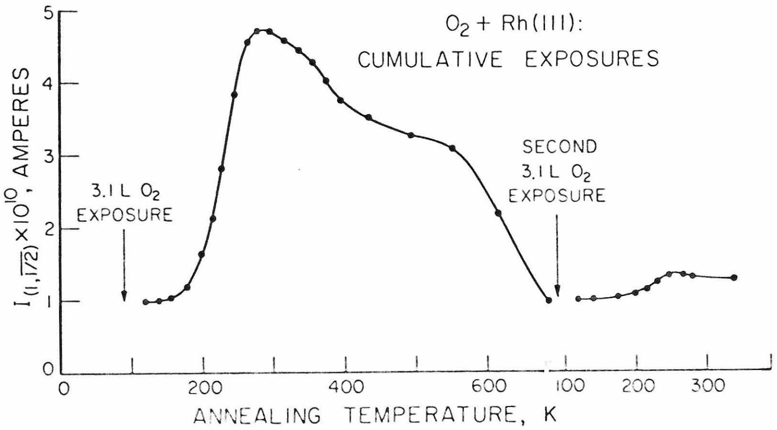

Fig. 8. Effect of annealing oxygen overlayer (3.1 L O_2 exposure) to 690 K, then re-exposing to 3.1 L O_2 at $T \leqslant 118$ K, on the intensity of the oxygen $(1, \overline{1/2})$ spot.

exposure. At 400 K, $I_{(1,\,\overline{1/2})}$ for a 3.1 L O_2 exposure has already decreased to 76% of its maximum value due to irreversible thermal disordering.

The result of exposing the crystal to 3.1 L O_2, heating successively to temperatures up to 775 K, then re-exposing to 3.1 L O_2 is shown in fig. 8. Either the capacity of the crystal for further adsorption was reduced greatly by the initial O_2 exposure and heat treatment, or more oxygen was adsorbed but was prevented from ordering by the initial treatment. On the basis of the oxygen AES intensity as a function of exposure and the desorption data of fig. 2, and on the basis of hydrogen–oxygen coadsorption experiments to be discussed in a separate paper [14], the latter explanation is more plausible.

3.4. Kinetic studies of oxygen ordering using LEED

The kinetics of the ordering process between 150 and 280 K were studied in detail by monitoring the intensity of the oxygen (1, $\overline{1/2}$) beam as a function of time, while the crystal was maintained at constant temperature (± 1.4 K) following exposure to 2.4 L O_2 at temperatures below 120 K. The oxygen (1, $\overline{1/2}$) beam intensity as a function of time is shown in fig. 9, with the intensities normalized to their asymptotic values. The asymptotic intensities were measured after each intensity–time curve had been recorded by heating the crystal to 280 K, recooling to the temperature of the kinetic measurement, and recording the intensity at that tem-

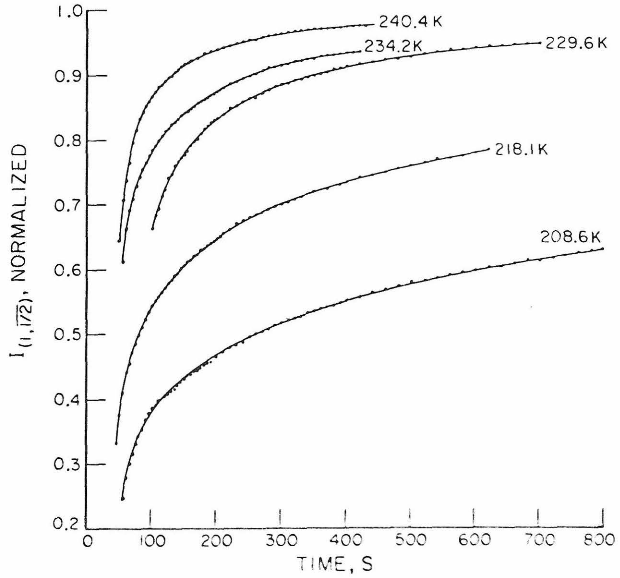

Fig. 9. Kinetic data for oxygen ordering on Rh(111): intensity of the oxygen (1, $\overline{1/2}$) spot as a function of time at constant temperature for T = 208.6, 218.1, 229.6, 234.2 and 240.4 K.

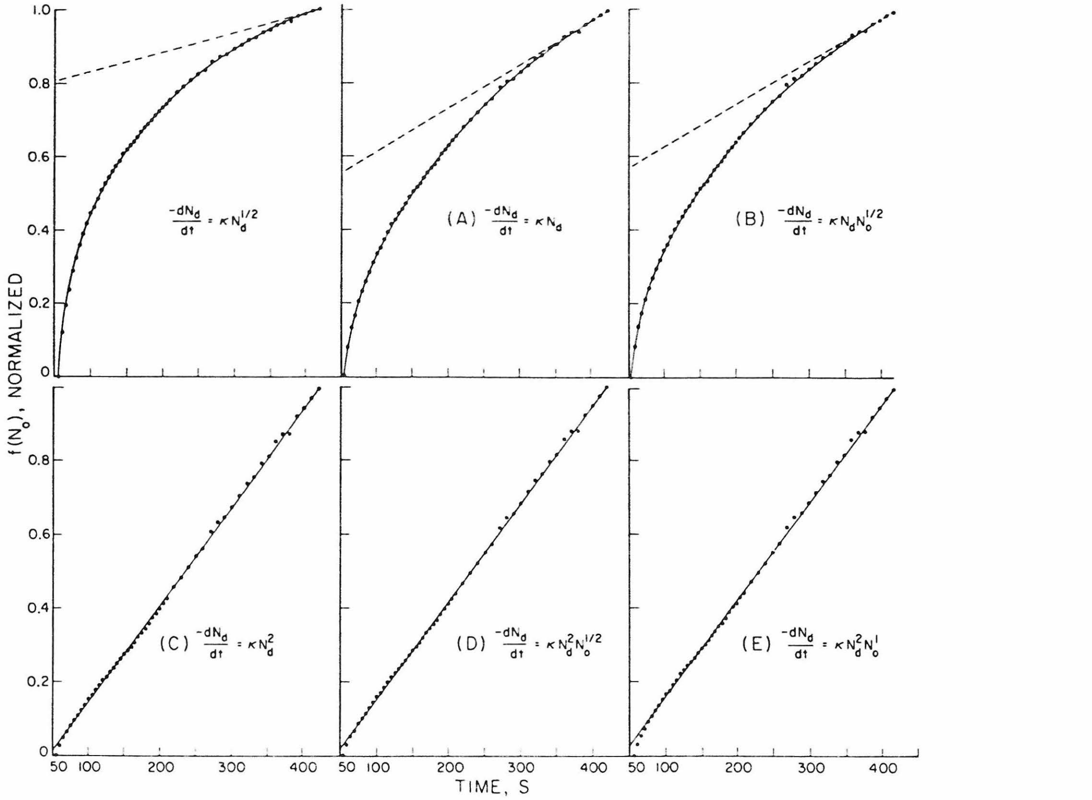

Fig. 10. Integrated kinetic data as a function of time for six kinetic models. The integrated kinetic function for each model, $f(N_0)$, corresponds to the appropriate function listed in the Table multiplied by a normalization factor for purposes of comparison.

perature. In this way, our measurement of the asymptotic intensity relative to the kinetic intensity curves was unaffected by Debye–Waller effects or changes in magnetic field due to variations in heating current.

In treating the kinetic data, several different kinetic models were tested. The integrated kinetic functions are shown in fig. 10 for six different kinetic models. It is apparent that the rate laws which are second order in concentration of disordered species, N_d, linearize the experimental data best. The goodness of fit of the experimental data, and the activation energy calculated for any particular kinetic model, are insensitive to the functional dependence of $I_{(1,\ \overline{1/2})}$ on the concentration of ordered species, N_0. We assumed therefore that $I_{(1,\ \overline{1/2})}$ is proportional to N_0^2, as kinematic scattering theory predicts. The proportionality constant was calculated with the assumption that the maximum value of $I_{(1,\ \overline{1/2})}$ represented 4×10^{14} atoms/cm^2 following a 2.4 L O_2 exposure, i.e., that the (2 × 2) pattern observed represents a p(2 × 2) structure rather than three independent p(2 × 1) domains rotated 120° with respect to one another. (The pre-exponential factor is the only kinetic parameter which depends upon the value of the proportionality constant, and the goodness of fit of any given kinetic model to the kinetic ordering data is independent of the value of this constant.)

In fitting the data to kinetic models, we assumed that

$$N_0 = CI_t^{1/2}\,, \tag{1}$$

$$N_d = CI_\infty^{1/2} - CI_t^{1/2}\,, \tag{2}$$

where I_∞ is the experimentally determined asymptotic value of $I_{(1,\,\overline{1/2})}$, I_t is the value of $I_{(1,\,\overline{1/2})}$ at any time t, and C is the proportionally constant. In addition, we assumed that the oxygen overlayer is completely disordered following adsorption at $T \leqslant 120$ K, i.e., $N_d = CI_\infty^{1/2}$ at $t = 0$. It was shown that the linearity of fit of the data in the three lower plots in fig. 10 is sensitive to the assumption that $N_d = 0$ for $I_t = I_\infty$. This supports the basic assumptions in the models, eqs. (1) and (2).

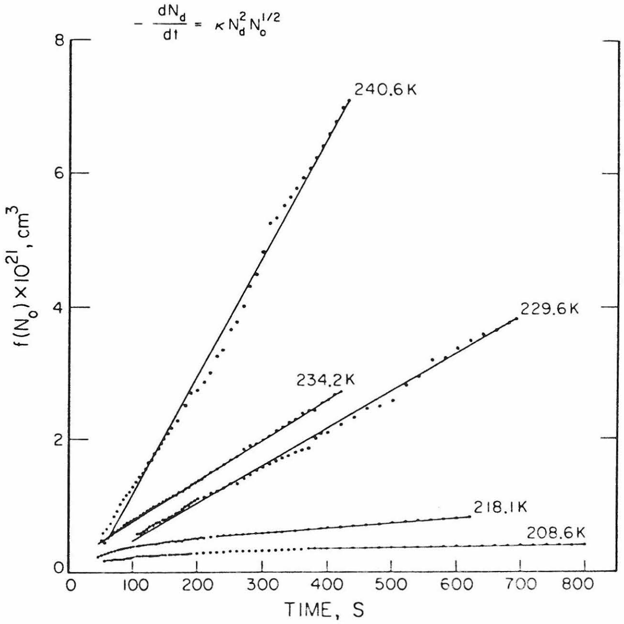

Fig. 11. Integrated form of the kinetic data as a function of time for all data, for the particular case of the rate of ordering = $\kappa N_d^2 N_0^{1/2}$, where $\kappa = \kappa^{(0)} \exp(-E_a/kT)$ by definition. In calculating these values, it was assumed that $I_t^{1/2} = C^{-1} N_0$ where $C^{-1} = 2.1 \times 10^{-14}$ cm^2 for the normalized data. Thus,

$$f(N_0) = \frac{1}{N_\infty}\left[\frac{N_t^{1/2}}{N_\infty - N_t} - \frac{1}{2N_\infty^{1/2}} \ln\left(\frac{N_\infty^{1/2} - N_t^{1/2}}{N_\infty^{1/2} + N_t^{1/2}}\right)\right],$$

where N_t = the value of N_0 at time t, and $N_\infty = 4 \times 10^{14}$ cm^{-2}.

Table 1
Rate of oxygen ordering on Rh(111): kinetic equations and parameters for five kinetic models

	Rate low	Integrated form used in data analysis	E_a (kcal/mole)	$\kappa^{(0)}$
(A)	$\frac{-dN_d}{dt} = \kappa^{(0)} N_d \exp\left(-\frac{E_a}{kT}\right)$	$\ln\left(\frac{I_\infty^{1/2}}{I_\infty^{1/2} - I_t^{1/2}}\right) = \kappa t$	ca. 5.8 ± 0.3	$10^{+2.8\pm0.7}$ s^{-1}
(B)	$\frac{-dN_d}{dt} = \kappa^{(0)} N_d N_0^{1/2} \exp\left(-\frac{E_a}{kT}\right)$	$\frac{-1}{CI_\infty^{1/4}} \ln\left(\frac{I_\infty^{1/4} - I_t^{1/4}}{I_\infty^{1/4} + I_t^{1/4}}\right) = \kappa t$	ca. 5.5 ± 0.5	$10^{-4.5\pm0.9}$ cm s^{-1}
(C)	$\frac{-dN_d}{dt} = \kappa^{(0)} N_d^2 \exp\left(-\frac{E_a}{kT}\right)$	$\frac{1}{C}[(I_\infty^{1/2} - I_t^{1/2})^{-1} - (I_\infty^{1/2})^{-1}] = \kappa t$	13.9 ± 0.8	$10^{-2.7\pm0.7}$ cm^2 s^{-1}
(D)	$\frac{-dN_d}{dt} = \kappa^{(0)} N_d^2 N_0^{1/2} \exp\left(-\frac{E_a}{kT}\right)$	$\frac{1}{C^{3/2} I_\infty^{1/2}} \left\{ \frac{I_t^{1/4}}{I_\infty^{1/2} - I_t^{1/2}} - \frac{1}{2I_\infty^{1/4}} \ln\left(\frac{I_\infty^{1/4} - I_t^{1/4}}{I_\infty^{1/4} + I_t^{1/4}}\right) \right\} = \kappa t$	13.5 ± 0.9	$10^{-10.3\pm0.9}$ cm^3 s^{-1}
(E)	$\frac{-dN_d}{dt} = \kappa^{(0)} N_d^2 N_0 \exp\left(-\frac{E_a}{kT}\right)$	$\frac{1}{C^2 I_\infty} \left\{ \frac{I_t^{1/2}}{I_\infty^{1/2} - I_t^{1/2}} - \frac{I_0^{1/2}}{I_\infty^{1/2} - I_0^{1/2}} + \ln\left(\frac{I_t^{1/2}}{I_\infty^{1/2} - I_t^{1/2}}\right) - \ln\left(\frac{I_0^{1/2}}{I_\infty^{1/2} - I_0^{1/2}}\right) \right\} = \kappa t, \quad I_0 \neq 0$	13.2 ± 0.7	$10^{-17.9\pm0.7}$ cm^4 s^{-1}

The activation energies, E_a, and pre-exponential factors, $\kappa^{(0)}$, calculated for five different models are given in table 1. The errors in the kinetic parameters are estimated statistically on the basis of the scatter in the kinetic rates. Note that models (C) through (E), all of which have an N_d^2 dependence in the rate law, yield values for the activation energy of ordering which are identical within the error of the measurement: 13.5 ± 0.5 kcal/mole. For models (A) and (B), the integrated kinetic data were not linear functions of time, as is apparent in fig. 10. Therefore, the rate of ordering of the oxygen at various temperatures was estimated by fitting empirically a straight line to the last points in the kinetic plots, and the kinetic parameters given for these models are based on this approximation. In fig. 11, we show the integrated kinetic data as a function of time for all temperatures, assuming a rate law which is second order in N_d and half order in N_0. This kinetic model is appealing intuitively since the $N_0^{1/2}$ factor is consistent with an island growth model, although there is no other justification for choosing this model over one which has a different dependence on N_0. It should be noted that model (E) is physically unreasonable under the assumption that the oxygen overlayer is completely disordered following adsorption at $T \leqslant 120$ K. Inspection of the integrated form of the kinetic rate law for model (E) in table 1 shows that if $I_0 = 0$, an infinite time is required for the ordering process to occur.

The rate of ordering at each temperature was determined from the slope of a least squares fit to the integrated kinetic data. The fitted lines for this particular model are shown in fig. 11. The slight nonlinearity of the integrated data at low temperatures and short times may be due to the physical sharpening of the oxygen $(1, \overline{1/2})$ spot as ordering occurs. This effect was observed visually and may be thought of as an instrumental artifact related to the acceptance angle of the Faraday cup. The Arrhenius plot for this kinetic ordering model is shown in fig. 12. It should be noted that although the kinetic data only span a 32 K temperature range, due to the narrow temperature range over which the ordering phenomenon occurs, they represent a 90-fold change in rate.

A qualitative comparison of the intensity–voltage (I–V) beam profiles of the oxygen $(1, \overline{1/2})$ LEED beam after the crystal had been heated to several different temperatures shows that the local atomic structure of the oxygen responsible for the ordered overlayer remained unchanged during the annealing process. Following an exposure to 2.4 L O_2 at temperatures below 120 K, the Rh(111) crystal was heated successively to 279, 470 and 708 K, then recooled to $T \leqslant 105$ K. After each cycle, the intensity of the oxygen $(1, \overline{1/2})$ beam was monitored as a function of voltage. The results are shown in fig, 13. It appears that the ordered (2 × 2) oxygen overlayer is undergoing depletion, not structural rearrangement, during the annealing process.

An upper limit for the cross section, Q, for disordering of the (2 × 2) structure by electron impact was estimated by measuring the change in $I_{(1, \overline{1/2})}$ as a function of time during electron bombardment with the LEED gun (62 eV, 0.7 μA, 1 mm^2 area) at 90 K. A 14% decrease in $I_{(1, \overline{1/2})}$ occurred after 2300 sec under these con-

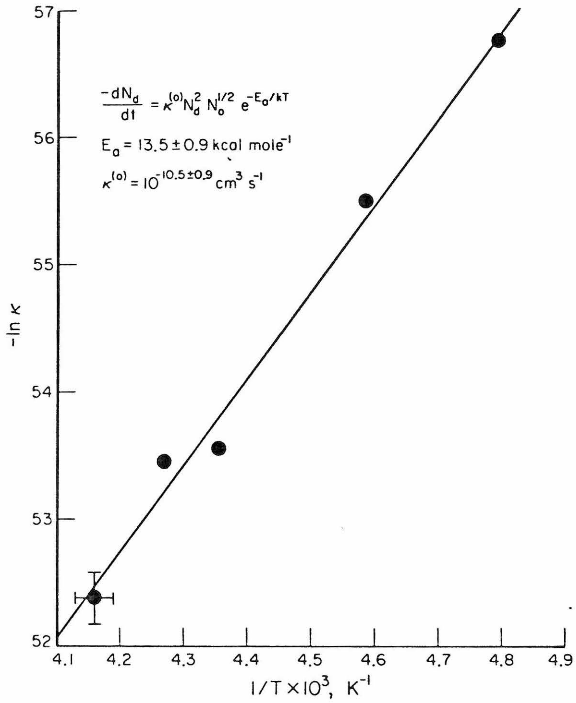

Fig. 12. Arrhenius plot of $-\ln \kappa$ as a function of T^{-1} for the ordering data of fig. 11. Error bars were estimated on the basis of a constant temperature deviation of ±1.4 K during the ordering process, whereas in fact the temperature oscillated ±1.4 K about the mean temperature. Thus, the error bars shown are worst-case values.

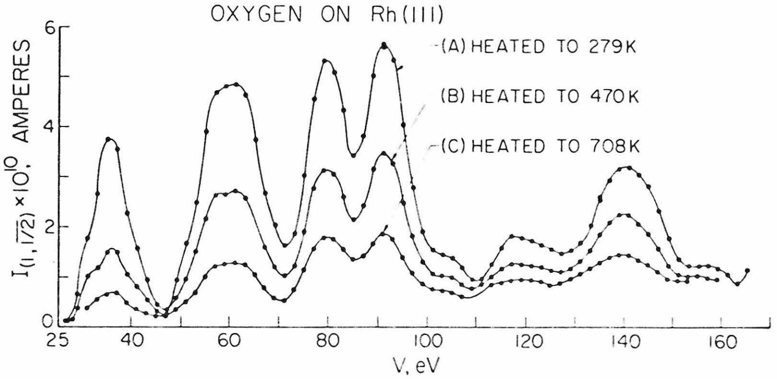

Fig. 13. Intensity as a function of voltage profiles for oxygen (1, $\overline{1/2}$) LEED beam following heating to various temperatures. Oxygen exposure: 2.4 L at $T \leqslant 120$ K. The data shown are uncorrected for variation in the primary electron beam current (collected by the crystal) as a function of beam voltage.

ditions. A 5% decrease in $I_{(1,\ \overline{1/2})}$ was observed after 1500 sec with the electron beam off, and the origin of this small effect is not understood. On the basis of these data, an upper limit for the value of Q was calculated to be 1×10^{-19} cm^2. To investigate the possibility that the slow decrease in $I_{(1,\ \overline{1/2})}$ in the absence of the electron beam was due to a slow reaction with background H_2 at 90 K, $I_{(1,\ \overline{1/2})}$ was monitored as a function of time at a steady state pressure of 6×10^{-8} Torr H_2. This caused the intensity of the oxygen $(1, \overline{1/2})$ beam to decrease by 2% over a period of 120 sec, a definite but small effect. It is concluded that background H_2 at 1×10^{-10} Torr pressure could not have caused the slight decrease in $I_{(1,\ \overline{1/2})}$ in the absence of electron bombardment. These data demonstrate the stability of $I_{(1,\ \overline{1/2})}$ with time during the course of our experiments.

We observed also that the ordering of the oxygen overlayer with temperature occurred in the absence of an electron beam. After exposing the crystal to 2.4 L O_2 at 140 K and heating to 280 K with the electron beam off, the electron beam was turned on, and $I_{(1,\ \overline{1/2})}$ immediately rose to a value which was maintained within 1% for 140 sec while the electron beam was on. Thus, the electron beam does not have an observable ordering effect.

4. Discussion

4.1. General behavior of oxygen on group VIII metals

The chemisorptive properties of the Group VIII transition metals when exposed to oxygen have stirred much interest and investigation. This is due to the importance of oxygen and oxygen-containing molecules as surface species in hetergeneous catalysis, and due to the complexity of oxygen chemistry on these metals. Oxygen is both chemically active with respect to most clean Group VIII metal surfaces, and the adsorptive behavior of oxygen is quite sensitive to the geometrical structure of the surface. Nickel, which forms epitaxial oxides readily, has been studied most extensively [15,16]; more recently, ruthenium [8,17,18], palladium [9,19,20], iridium [10,21,22] and platinum [6,11,23,24] have come under study with respect to the chemisorption of oxygen. In general, the following phenomena have been observed and are relevant to the present discussion:

(i) At room temperature, oxygen forms an apparent (2 × 2) structure on the hexagonally close packed surfaces Ni(111) [16], Ir(111) [10], Ru(001) [8], Pd(111) [9] and Pt(111) [11]. On Ni(111) [16] and Ru(001) [8], apparently it undergoes a reversible order–disorder transition at temperatures above 300 K. When oxygen is adsorbed at temperatures below room temperature on the Ir(111), Ru(001) and Pd(111) surfaces the crystal must be heated to approximately room temperature before the oxygen (2 × 2) pattern is observable. There is speculation as to whether this "(2 × 2)" pattern represents a p(2 × 2) structure or a structure consisting of three independent p(2 × 1) domains rotated 120° to each other.

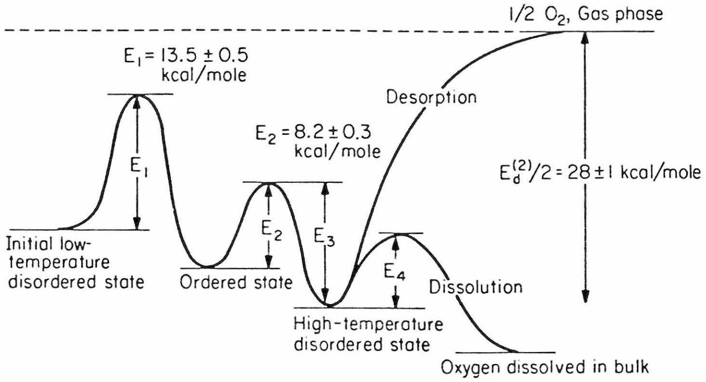

Fig. 14. Energy levels of adsorbed oxygen species on Rh(111).

All of these previous results are consistent with the observations reported in this paper, except the apparent reversibility of the order–disorder transition above 300 K on other surfaces. The definite irreversible behavior on Rh(111) reflects the fact that activation energies for forward processes (see fig. 14) are less than activation energies for processes occurring in the reverse direction.

(ii) On any particular metal, the adsorption and desorption data differ significantly for different crystallographic orientations. Perhaps the most striking example is palladium: the Pd(111) surface shows a great tendency to dissolve oxygen into the bulk [9], whereas the (110) surface is reportedly inert to formation of bulk oxides [19]. On the Pt(100) surface, the sticking coefficient of oxygen varies by at least three orders of magnitude between the active (1 X 1) surface and the inert, reconstructed (5 X 20) surface [11]. Norton et al. [15] have observed from ultraviolet photoemission spectra that, at 295 K, oxygen adsorbs on Ni(111) into sites of constant electronic potential since the oxygen 1s binding energy remains constant at 529.7 eV throughout chemisorption and nucleation processes, whereas, on Ni(100) and Ni(110) surfaces, the O 1s binding energy decreases substantially during these processes until it reaches the value characteristic of NiO formation, 529.7 eV. These are but a few examples of the "structure sensitivity" of oxygen chemisorption.

(iii) Single crystal and polycrystalline surfaces of the Group VIII transition metals tend to form surface, subsurface, and bulk oxides to varying degrees. Both Pd(111) and polycrystalline Pd surfaces reportedly have a high capacity for dissolution of oxygen into the bulk [9,20]. Klein et al. [17] and Reed et al. [18] report evidence for incorporation of oxygen into Ru(101) and Ru(100) crystals, respectively, at elevated temperature. Madey et al. [8] do not see evidence for this phenomenon on the Ru(001) surface, which is structurally similar to Rh(111). Evidence for growth of an epitaxial oxide at temperatures above 800 K has been observed on the Pt(110) surface [24], and the formation of near surface oxides on

Ir(110) and Ir(111) has also been observed [10,21,22]. Often the data show the presence of two types of chemisorbed oxygen, depending upon the oxygen coverage and/or the temperature. There have been some data indicating adsorption of molecular oxygen at low temperatures [6,21]. The oxygen thermal desorption, LEED, and AES data presented in this paper are consistent with this general picture for oxygen chemisorption on the Group VIII metals, and they provide more insight into the detailed processes which occur on the Rh(111) surface than has been available on most other surfaces.

4.2. Kinetics of oxygen adsorption at 170 K

The long linear initial region of the oxygen AES intensity as a function of O_2 exposure suggests that at low temperatures oxygen adsorption on Rh(111) occurs with a constant sticking coefficient. This constant rate of adsorption is exhibited over 80% of the coverage range as the disordered oxygen layer is filled. This behavior implies that a mobile second layer of adsorbed oxygen is formed during adsorption with high sticking coefficient and with a lifetime sufficiently long to permit migration to occur to fill first layer chemisorption sites. Such behavior is often found for low temperature adsorption processes, e.g., Xe on W(111) [25,26] and O_2 on W(111) [26].

4.3. Oxygen penetration into Rh(111)

The oxygen Auger data of figs. 6 and 7B show clearly that oxygen begins to penetrate the Rh(111) surface at temperatures below the onset of desorption. Therefore, during oxygen thermal desorption, part of the chemisorbed oxygen must be diffusing into the near surface and bulk regions of the Rh(111) crystal before desorption begins. One would expect the rate of oxygen dissolution to be limited by the rate of diffusion from the near surface region into the bulk. This rate of diffusion is apparently slow enough that, following exposures of $\gtrsim 1.6$ L O_2, the near surface region effectively reaches steady state saturation with respect to oxygen. The remaining chemisorbed oxygen desorbs as molecular O_2. Oxygen desorption from the near surface region may occur also. This phenomenon has been discussed by Conrad et al. [9] in terms of concentration gradients to explain their observations on the Pd(111) surface. Their results for the Pd(111) surface are strikingly similar to the present results for the Rh(111) surface. Desorption of oxygen from the near surface region could account for much of the variation in O_2 desorption parameters shown in figs. 3 and 4; if this is occurring during the desorption measurement, then the thermal desorption peaks at high coverage effectively are broadened by the desorption of O_2 from multiple states. This is consistent with the shape of the desorption peaks of fig. 5 following oxygen adsorption on an annealed oxygen/Rh(111) surface. Chemisorbed oxygen may be contributing to the low temperature side of the desorption peak, and relatively more chemisorbed oxygen would be expected to desorb following oxygen exposure to an annealed oxygen covered surface than following exposure to a clean Rh(111) surface, since in the former case the near surface region would already have a high concentration of dissolved oxygen. Campbell et al. [20] have concluded that oxygen penetration into Pd polycrystalline foils at high O_2 pressures (4×10^{-1} to 2×10^{-3} Torr) occurs from an oxygen saturated surface and that the rate of dissolution is limited by the process in which chemisorbed oxygen moves out of the surface layer into the Pd bulk. This is based on their observation that the rate of oxygen uptake on a relatively clean surface is independent of the oxygen pressure within the pressure range cited above.

4.4. Thermal desorption of O_2 from Rh(111)

Assuming second order desorption kinetics for oxygen, we find that the effective pre-exponential factor of the desorption rate coefficient varies over six orders of magnitude (1.5×10^{-9} to 2.5×10^{-3} cm^2 s^{-1}), and that the effective activation energy of desorption varies by 27 kcal/mole (29 to 56 kcal/mole). Only the values of the desorption kinetic parameters near zero coverage are thought to have fundamental significance since the analysis cannot be done for unresolved states [7]. In the limit of zero surface coverage, $E_d^{(2)} = 56 \pm 2$ kcal/mole, and $\nu_0^{(2)} = 2.5 \times 10^{-3}$ cm^2 s^{-1} for oxygen desorption; it is possible that this limit represents O_2 desorption from the near surface region. Within the error of our measurement, this is the same value as reported by Conrad et al. [9] for O_2 desorption from Pd(111): 55 kcal/mole for low oxygen coverages ($\theta \leqslant 0.15$) on "pretreated" Pd(111) surfaces. Other values of $E_d^{(2)}$ which have been reported for geometrically similar surfaces, assuming a constant value of the pre-exponential factor, are the following: 80 kcal/mole for Ru(001) at low oxygen coverage [8] and 65 kcal/mole for Ir(111) in the limit of zero coverage [10].

4.5. LEED data for oxygen on Rh(111)

The LEED data for oxygen on the Rh(111) surface support the following conclusions:

(i) The oxygen adsorbs as a disordered species at ~100 K and orders into an apparent (2 × 2) structure between 150 and 280 K. The kinetics of the oxygen ordering process are second order with respect to the concentration of disordered species, which indicates, within the framework of an ordered island nucleation model, that three-adatom interactions may be important in this process. To the best of our knowledge, this is the first experimental demonstration of such an effect. Three-body interactions have come under theoretical scrutiny recently in terms of interpreting phase transitions in ordered overlayers. Einstein [27] has calculated three-adatom interaction effects for a c(2 × 2) ordered overlayer and concluded that, at low temperatures, these interaction energies may be an important factor in determining island shapes at coverages below saturation. The activation energy for the oxygen ordering process is 13.5 ± 0.5 kcal/mole, which is comparable to that estimated for the oxygen ordering process on Ir(111) at room temperature, 16–19 kcal/mole [10]. The migration of oxygen on Ru also has been observed directly by field emission microscopy [17]. Boundary migration occurs above ~250 K with an activation energy of 14 kcal/mole. The ratio of $E_a/E_d^{(2)}$ for the O/Rh(111) system, 0.24, is also comparable to the value of this ratio, 0.19, reported for oxygen on W(100) [28].

(ii) The structure of the ordered (2 X 2) oxygen overlayer remains constant during the disordering and depletion processes which occur above room temperature. We have measured $I-V$ profiles for several of the oxygen (2 X 2) beams and are performing currently a dynamical LEED calculation to determine the structure of the ordered oxygen overlayer.

(iii) The ordered oxygen overlayer undergoes an irreversible disordering process between 280 and 400 K which is coverage-dependent. At high coverage (8.5 L O_2 exposure), apparently there is not a sufficient number of unoccupied adsites on the Rh(111) surface for the disordering phenomenon to take place. A detailed study of this disordering process will be reported in a subsequent paper [13].

(iv) Oxygen penetration into the bulk occurs between 390 and 800 K, based on LEED, AES, and thermal desorption data. The oxygen Auger peak shape is modified significantly when penetration into the bulk occurs. The presence of bulk oxygen prevents thermal ordering of oxygen chemisorbed following thermal disordering and penetration.

Thermodynamically, these data support the energy diagram shown in fig. 14. This energy diagram is drawn so that the transition from the ordered state to the high temperature disordered state is irreversible, which implies that E_3 must be greater than both E_2 and E_4. The fact that the order–disorder transition is apparently reversible on Ni(111) and Ru(001) suggests that on these surfaces E_2 may be similar to the energy of activation measured for E_1, assuming that E_1 is a simple energy of migration; and that the energy level of the high temperature disordered state relative to the ordered (2 X 2) oxygen state may be lower on Rh(111) than on the Ni or Ru surfaces.

Acknowledgment

One of us (J.T.Y.) acknowledges partial support of equipment facilities from the Division of Physical Research, Department of Energy. Primary support was derived from the Army Research Office under Grant No. DAHCO4-75-0170.

References

[1] C.W. Tucker, J. Appl. Phys. 37 (1966) 4147.
[2] C.W. Tucker, J. Appl. Phys. 37 (1966) 3013.

[3] J.T. Grant and T.W. Haas, Surface Sci. 21 (1970) 76.
[4] D.G. Castner, B.A. Sexton and G.A. Somorjai, Surface Sci. 71 (1978) 519.
[5] C.-M. Chan, P.A. Thiel, J.T. Yates, Jr. and W.H. Weinberg, Surface Sci. 76 (1978) 296.
[6] M. Alnot, J. Fusy and A. Cassuto, Surface Sci. 72 (1978) 467.
[7] C.-M. Chan, R. Aris and W.H. Weinberg, Appl. Surface Sci. 1 (1978) 360.
[8] T.E. Madey, H.A. Engelhardt and D. Menzel, Surface Sci. 48 (1975) 304.
[9] H. Conrad, G. Ertl, J. Küppers and E.E. Latta, Surface Sci. 65 (1977) 245.
[10] V.P. Ivanov, G.K. Boreskov, V.I. Savchenko, W.F. Egelhoff, Jr. and W.H. Weinberg, Surface Sci. 61 (1976) 25.
[11] C.R. Helms, H.P. Bonzel and S. Kelemen, J. Chem. Phys. 65 (1976) 1773.
[12] C.J. Powell, Surface Sci. 44 (1974) 29.
[13] J.T. Yates, Jr., P.A. Thiel and W.H. Weinberg, Surface Sci. 82 (1979) 45.
[14] P.A. Thiel, J.T. Yates, Jr. and W.H. Weinberg, Surface Sci., 90 (1979) 121.
[15] P.R. Norton, R.L. Tapping and J.W. Goodale, Surface Sci. 65 (1977) 13.
[16] A.R. Kortan, P.I. Cohen and R.L. Park, J. Vacuum Sci. Technol. (March/April 1979).
[17] R. Klein and A. Shih, Surface Sci. 69 (1977) 403.
[18] P.D. Reed, C.M. Comrie and R.M. Lambert, Surface Sci. 64 (1977) 603.
[19] G. Ertl and P. Rau, Surface Sci. 15 (1969) 443.
[20] C.T. Campbell, D.C. Foyt and J.M. White, J. Phys. Chem. 81 (1977) 491.
[21] J.L. Taylor, D.E. Ibbotson and W.H. Weinberg, Surface Sci. 79 (1979) 349.
[22] H. Conrad, J. Küppers, F. Nitschké and A. Plagge, Surface Sci. 69 (1977) 668.
[23] H.P. Bonzel and R.Ku, Surface Sci. 40 (1973) 85.
[24] R. Ducros and R.P. Merrill, Surface Sci. 55 (1976) 227.
[25] M.J. Dresser. T.E. Madey and J.T. Yates, Jr., Surface Sci. 42 (1974) 533.
[26] J.T. Yates, Jr. and N.E. Erickson, Surface Sci. 44 (1974) 489.
[27] T.L. Einstein, Phys. Rev. B16 (1977) 3411.
[28] R. Gomer and J.K. Hulm, J. Chem. Phys. 27 (1957) 1363.

Chapter 2

THE CHEMISORPTION OF HYDROGEN ON Rh(111)

Surface Science 84 (1979) 427–439
© North-Holland Publishing Company

THE CHEMISORPTION OF HYDROGEN ON Rh(111) *

J.T. YATES, Jr. ** P.A. THIEL *** and W.H. WEINBERG †
Division of Chemistry and Chemical Engineering, California Institute of Technology, Pasadena, California 91125, USA

Received 2 January 1979; manuscript received in final form 27 February 1979

The chemisorption of H_2 on the (111) surface of Rh has been studied using thermal desorption mass spectrometry and low-energy electron diffraction. No evidence for the formation of an ordered hydrogen overlayer has been detected between 100 and 400 K. Hydrogen adsorbs dissociatively following Langmuir $[(1-\theta)^2]$ adsorption kinetics. Thermal desorption spectra at all coverages suggest that a mobile precursor is involved in the desorption step. In the limit of zero coverage, $E_d^{(2)} = 18.6$ kcal/mole and $\nu_0^{(2)} = 1.2 \times 10^{-3}$ cm^2/sec. No differences in H_2 and D_2 desorption kinetics are observed, suggesting that zero-point energy effects do not play a major role in determining desorption rates.

1. Introduction

Rhodium is an active heterogeneous catalyst for a number of reactions involving hydrogen. Examples include the hydrogenation of olefins [1], deuterium exchange with hydrocarbons [2] and with NH_3 [3], benzene hydrogenation [4], ketone reduction [5], catalytic reduction of CO to methane [6], and the oxidation of hydrogen [7,8]. For this reason, it is important to understand the dynamics of hydrogen chemisorption on and hydrogen desorption from rhodium. In this paper, we report the behavior of hydrogen on Rh(111), the most closely packed plane of this fcc metal.

The structure of the Rh(111) surface has been determined previously using low-energy electron diffraction (LEED) [9,10]. The Rh surface is unreconstructed and unrelaxed to within 5%. The effective Debye temperature of Rh(111) has also been measured using LEED and was found to be near 200 K in the surface region [9]. A detailed study of adsorption of O_2 on Rh(111) has been carried out recently [11]

---

* Supported by the Army Research Office (Durham) under Grant No. DAHCO4-75-0170.

** Sherman Fairchild Distinguished Scholar. Permanent address: National Bureau of Standards, Washington, DC 20234, USA

*** National Science Foundation Predoctoral Fellow.

† Camille and Henry Dreyfus Foundation Teacher–Scholar, and Alfred P. Sloan Foundation Fellow.

as well as a study of the catalytic reaction of $H_2(g)$ with adsorbed oxygen on Rh(111) [7]. Thermal desorption mass spectrometry has been used to study the nonreactive interaction of chemisorbed hydrogen and oxygen on Rh(111) [12]. A detailed study of the interaction of H_2 with Rh(111) has not been reported previously, however. Castner et al. [13] have reported H_2 desorption spectra from Rh(111), in which the temperature at which the maximum rate of desorption occurs, disagrees by over 100 K with the measurements reported in this study. This discrepancy is due to the fact that, in their work, the H_2 *adsorption* was carried out at 300 K. Moreover, they did not analyze the kinetic desorption parameters. Earlier thermal desorption measurements for hydrogen adsorbed on polycrystalline Rh filaments [14] are in excellent agreement with our results. A further study of H_2 adsorption kinetics and H_2–D_2 exchange on polycrystalline Rh has been reported recently [15] and it too agrees with our results where comparisons are possible.

2. Experimental details

The apparatus and the Rh(111) crystal preparation procedures have been described previously [7,9,11]. Facilities were available for LEED, Auger spectroscopy, and mass spectrometry. The Rh(111) crystal was cleaned by a combination of ion bombardment and O_2 treatments followed by heating in vacuum to 1240 K. Subsequent experiments involving higher temperature heating (1565 K) showed no effect on the desorption spectra. All H_2 pressures during adsorption were measured with a Bayard–Alpert gauge and are reported using the appropriate gauge sensitivity S ($S_{H_2}/S_{N_2} = 0.5$). The mass spectrometer was calibrated against the Bayard–Alpert gauge for both H_2 and D_2 (sensitivity for H_2, 141 A/Torr; sensitivity for D_2, 95 A/Torr). The assumed sensitivity of the mass spectrometer to HD was the mean of the H_2 and the D_2 sensitivity. The measured pumping speed of the vacuum chamber for H_2 was 1750 l/s using an estimated system volume of 50 l. The pumping speeds for HD and D_2 were assumed to be $(2/3)^{1/2}$ and $(1/2)^{1/2}$, respectively, of that found for H_2.

3. Experimental results

3.1. H_2 adsorption kinetics

The rate of adsorption of H_2 on Rh(111) at 175 K was measured by exposing the crystal to H_2 and then carrying out thermal desorption measurements following evacuation of the system. The data have been fitted to two kinetic rate expressions for dissociative and non-dissociative Langmuir adsorption, as shown in figs. 1A and 1B, respectively. The linearity of the fit in fig. 1A and the non-linearity of the fit in fig. 1B indicate that the adsorption rate is proportional to $(1 - \theta)^2$, and

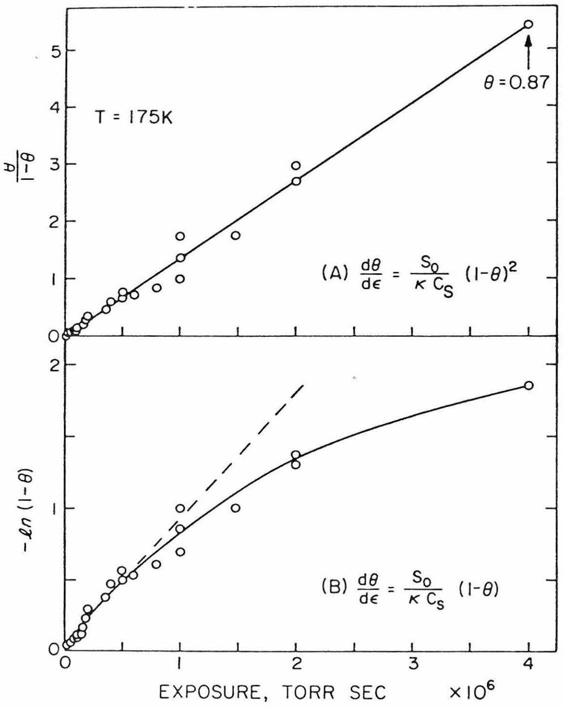

Fig. 1. Langmuir plots for hydrogen adsorption on Rh(111). The data have been plotted in terms of kinetic rate expressions for dissociative adsorption (A) and non-dissociative adsorption (B). The expressions involve the coverage relative to saturation, θ; the exposure, ϵ; and the initial sticking coefficient, S_0. The parameter $\kappa \equiv (2\pi mkT)^{1/2}$, where m is the molecular weight, k is the Boltzmann's constant, and T is the gas temperature.

this demonstrates the sensitivity for discrimination between the two models. The probability of adsorption of H_2 at 175 K on an empty site is 0.65 ± 0.03, assuming a saturation coverage $C_s = 1.58 \times 10^{15}$ cm^{-2} (one H atom per surface Rh atom). It must be remembered, however, that inaccuracies in absolute ionization gauge calibration may lead to as much as a 50% error in this type of measurement. In fig. 2, the fractional hydrogen coverage, θ, has been plotted as a function of H_2 exposure.

In addition, in fig. 2, various theoretical curves are shown for comparison. In these representations, a parameter K is varied between 0.1 and 2.8. This parameter is defined by Kisliuk [16] as

$$K \equiv P_b'/(P_a + P_b) ,$$

where P_b' is the probability of desorption of a precursor molecule from a site occupied by a chemisorbed atom, P_a is the probability of chemisorption at a site unoccupied by a chemisorption atom, and P_b is the probability of desorption of the

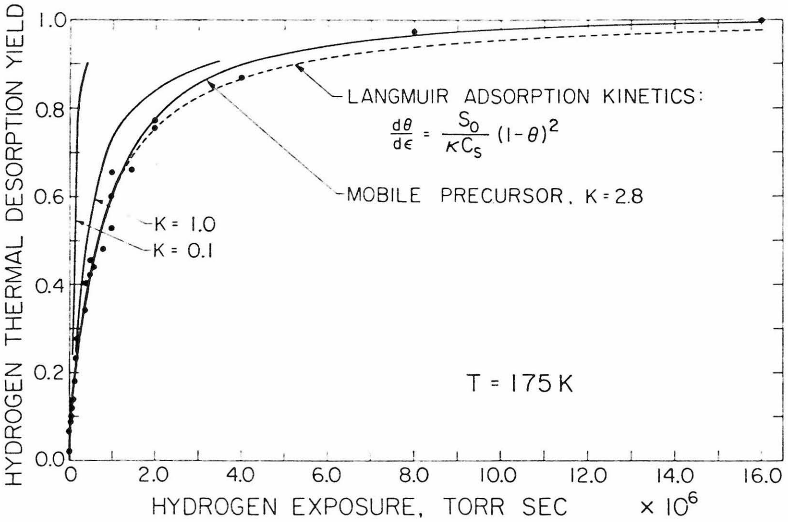

Fig. 2. Hydrogen coverage as a function of exposure on Rh(111). Theoretical plots for a mobile precursor adsorption state are shown for various values of K (see definition in text).

precursor from a site unoccupied by a chemisorbed atom. As K increases, the migration lifetime for the precursor is reduced due to its higher probability of desorption from an occupied site; and, in the limit of large K, the behavior approaches the Langmuir kinetics shown by the dashed line in fig. 2. We cannot distinguish experimentally between dissociative adsorption with a mobile precursor corresponding to $K \gtrsim 2$ and the limiting dissociative Langmuir kinetics. The data shown in fig. 2 are thus consistent with a mobile precursor model in which the lifetime of the precursor is very short but not necessarily zero.

3.2. Thermal desorption of H_2

Thermal desorption spectra were measured over a wide range of hydrogen coverages, and representative desorption spectra are shown in fig. 3. At the lowest hydrogen coverages, approximately 3% of saturation, a single desorption peak near 390 K is observed. As coverage increases, the peak shifts to lower temperatures and broadens. At the highest hydrogen coverages, the main desorption peak occurs at 275 K. In addition, a small desorption peak near 150 K appears at $\theta \gtrsim 0.5$. Two H_2 desorption states at ~150 K and 300 K were also seen by Mimeault and Hansen [14] on polycrystalline Rh in a ratio of approximately 1 : 2. The lower ratio found here suggests that the low temperature state in our study on Rh(111) may originate from another crystal plane present on the crystal edge or from surface defects.

The kinetics of H_2 desorption in the main state shown in fig. 3 have been

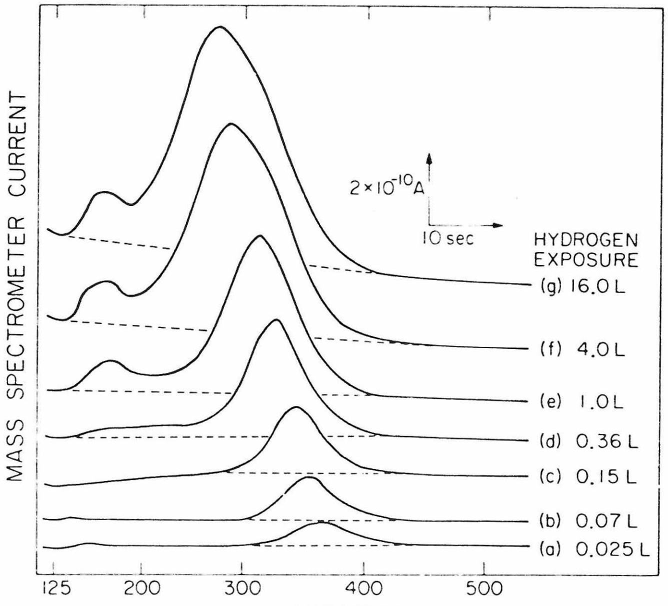

Fig. 3. Experimental thermal desorption spectra for hydrogen from Rh(111). The heating rate is 6.3 ± 0.5 K/sec.

analyzed using the method of Chan et al. [17]. This method permits the calculation of the *effective* pre-exponential factor, $\nu_0^{*(2)}$, and the *effective* activation energy for desorption, $E_d^{*(2)}$, for second-order kinetics at various coverages, using the desorption peak temperature, T_p, and the desorption peak width at half-maximum. The results of this analysis are presented in fig. 4. It may be seen that *extreme* variations in both $\nu_0^{*(2)}$ and $E_d^{*(2)}$ are observed as the initial hydrogen coverage is increased.

3.3. Thermal desorption of H_2 and D_2

The desorption spectra for hydrogen and deuterium are compared in fig. 5 for full coverages of each molecule adsorbed in separate experiments on Rh(111). Two observations may be made from the comparison of these data:

(1) There is no discernible difference in desorption kinetics for H_2 and D_2: the desorption traces are accurately superimposable.

(2) The curves are equal in area. This is a result of the fortuitous ratio of mass spectrometer sensitivity for H_2 and D_2 (1.48) which cancels the ratio of pumping speeds (1.4) expected on the basis of kinetic theory. Thus, the saturation coverages are identical for hydrogen and deuterium.

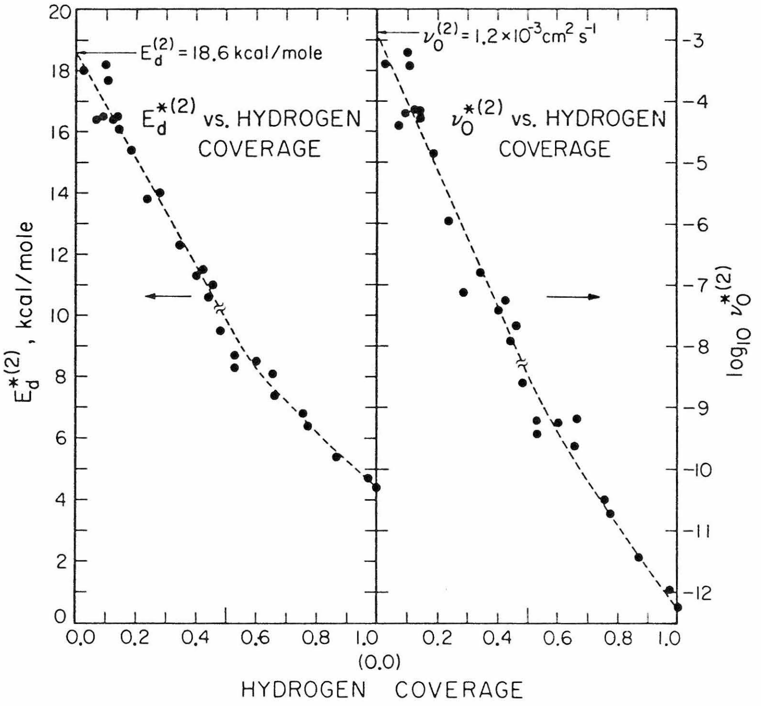

Fig. 4. Effective kinetic parameters for desorption of H_2 from Rh(111).

3.4. Isotopic mixing between adsorbed hydrogen and deuterium

The isotopic mixing between hydrogen and deuterium was studied by the simultaneous adsorption of these two gases from an H_2/D_2 gas mixture containing each isotopic species at a partial pressure of 2×10^{-8} Torr as measured with the Bayard–Alpert gauge. The gauge was then turned off during the main adsorption period to prevent isotopic mixing on the hot filament. The experimental desorption traces for successive experiments are shown in fig. 6A. We have computed the experimental value of the equilibrium coefficient, K_{eq}, for the reaction $H_2(g) + D_2(g) \rightleftharpoons 2HD(g)$, using the isotopic intensities for desorption in the temperature region 200 to 350 K and by correcting for mass spectrometer sensitivity and for variation in mean lifetime of each isotopic species in the vacuum chamber. The experimental values of the calculated K_{eq} are shown as dark points in fig. 6B. The theoretical K_{eq} is plotted as the dashed line in fig. 6B [18]. Systematic errors are responsible for the high values of the points; however, there is a clear suggestion of the expected temperature dependence of K_{eq} in the experimental data.

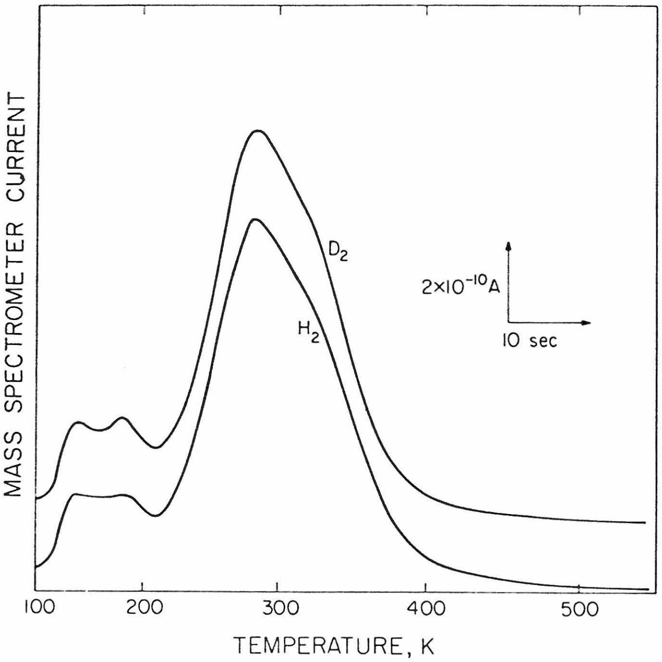

Fig. 5. Comparison of full coverage thermal desorption spectra for hydrogen and deuterium adsorbed on Rh(111).

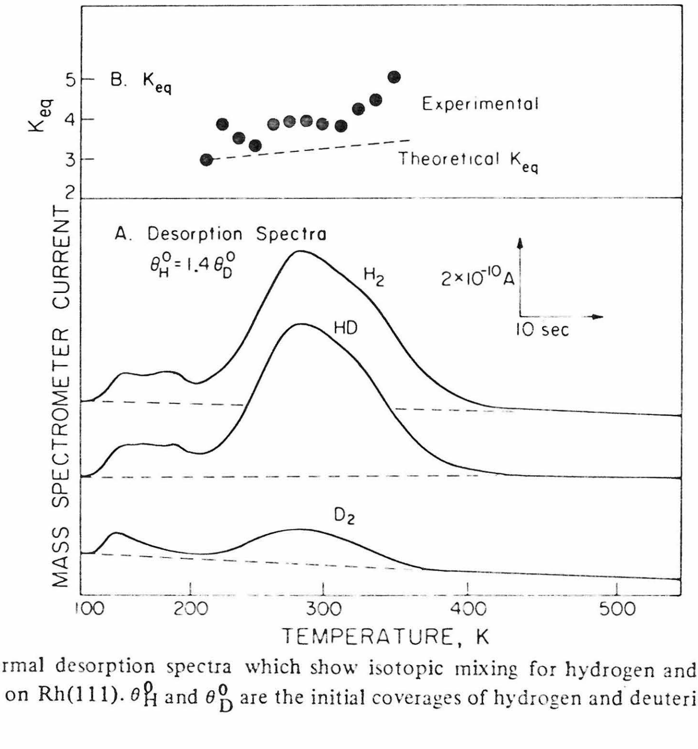

Fig. 6. Thermal desorption spectra which show isotopic mixing for hydrogen and deuterium adsorption on Rh(111). θ_H^0 and θ_D^0 are the initial coverages of hydrogen and deuterium, respectively.

3.5. LEED study of H_2 chemisorption

An attempt was made to observe the presence of extra LEED beams following the adsorption of H_2 at 100 K. In separate experiments, the crystal was exposed to 16 L and 2 L of H_2, then heated to 400 K in steps, and cooled back to ~100 K. No extra LEED beams were observed at any stage in these measurements, which were carried out at an incident electron beam energy of 24 eV and at 0.4 μA beam current. The lack of observation of a new LEED pattern following adsorption of hydrogen on Rh(111) may be due to one of the following factors:

(1) Hydrogen does not form ordered structures on Rh(111) under these experimental conditions.
(2) Hydrogen forms an ordered (1×1) overlayer.
(3) Electron scattering from the ordered hydrogen overlayer is very small.

It should be noted that the third explanation is unlikely in view of the fact that hydrogen causes the formation of an observable (2×2) LEED pattern following adsorption on Ni(111) at low temperature [19].

4. Discussion

4.1. Kinetics of hydrogen adsorption

The adsorption of H_2 on Rh(111) at 175 K follows the expected kinetic rate law for dissociative chemisorption [20], namely, the rate of adsorption is proportional to $(1-\theta)^2$. This behavior suggests that the rate determining step in chemisorption involves the interaction of a H_2 molecule with two Rh sites leading to dissociative chemisorption. Although such behavior is commonly observed in the adsorption of diatomic molecules, it is not universal. For example, O_2 chemisorption on Rh(111) occurs via $(1-\theta)$ kinetics at 335 K, suggesting that dual Rh sites are unnecessary in the rate determining step. This is possibly a consequence of the transient existence of O_2 molecular complexes at single sites [7,11].

4.2. Kinetics of hydrogen desorption

The thermal desorption of H_2 from Rh(111) is complex as indicated by the desorption spectra of fig. 3. The meaningful parameters to be derived from the analysis of these spectra are the values of $E_d^{*(2)}$ and $\nu_0^{*(2)}$ in the limit of zero coverage (fig. 4). These limiting values are in remarkably good agreement with the zero coverage H_2 desorption parameters measured by Mimeault and Hansen [14] for polycrystalline Rh [Rh(111): $E_d^{(2)} = 18.6$ kcal/mole and $\nu_0^{(2)} = 1.2 \times 10^{-3}$ cm^2/sec; Rh(poly): $E_d^{(2)} = 18.5$ kcal/mole and $\nu_0^{(2)} = (1.3 \pm 0.2) \times 10^{-3}$ cm^2/sec].

It is clear from fig. 4 that effects which reduce $\nu_0^{*(2)}$ and $E_d^{*(2)}$, the effective desorption parameters, occur as coverage increases. This may be seen in a com-

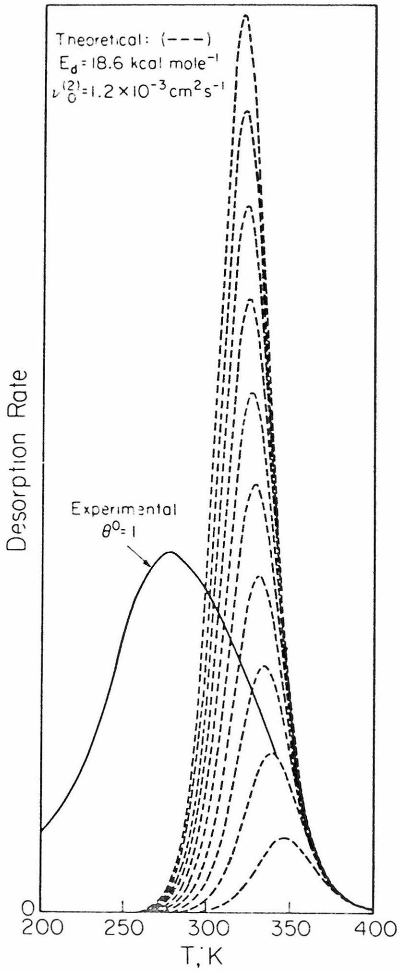

Fig. 7. Comparison of experimental H_2 desorption spectrum with theoretical spectra for second-order thermal desorption involving constant activation energy and pre-exponential factor. C_s = 1.58 × 10^{15} cm^{-2}.

parison of a series of theoretical thermal desorption traces generated using the zero coverage rate parameters with the full coverage experimental curve (fig. 7). This comparison illustrates clearly the failure of a simple second-order model having constant $\nu_0^{(2)}$ and $E_d^{(2)}$, in agreement with the results of fig. 4.

Two explanations may be suggested to explain these results:

(1) A mobile precursor state of H_2 [21] may be involved in the desorption process. Desorption kinetics via this state would be expected to cause a drastic reduction in the values of $\nu_0^{*(2)}$ and $E_d^{*(2)}$ as the initial hydrogen coverage is increased.

(2) Repulsive interactional effects between adsorbed H species would be expected

to produce a coverage dependent decrease in $E_d^{*(2)}$ and, possibly, $\nu_0^{*(2)}$.

We have investigated the involvement of a mobile precursor state in desorption by employing the ideas of Gorte and Schmidt [21]. For a single precursor, H_2^*, the sequence of elementary steps

$$2\,\mathrm{H(ads)} \underset{k_a}{\overset{k_d}{\rightleftharpoons}} \mathrm{H}_2^* \xrightarrow{k^*} \mathrm{H_2(g)}\,, \tag{1}$$

is proposed. In the steady state approximation, where $k_a \gg k^*$, the rate of desorption, $R_d = -d\theta/dt$, is given by

$$-R_d = \frac{k^* k_d}{k_a}\,\frac{\theta^2}{(1-\theta)^2} = \nu^{(2)}C_s\,\frac{\theta^2}{(1-\theta)^2}\exp\left(\frac{-E_d}{kT}\right). \tag{2}$$

We have integrated eq. (2) and computed theoretical desorption spectra for $\nu^{(2)}C_s \equiv \nu_0^{(2)} = 1.2 \times 10^{-3}$ cm^2/sec and $C_s = 1.58 \times 10^{15}$ cm^{-2} ≡ the number of Rh atoms cm^{-2}. This procedure produces theoretical thermal desorption peaks which are much broader than those shown in fig. 7. By analyzing these theoretical desorption peaks, values of the effective pre-exponential factor, $\nu_0^{*(2)}$, and the effective activation energy may be determined [17] as was done previously with the actual experimental data. In the experimental data analysis, as shown in fig. 4, a break in the linear curves occurs at $\theta \simeq 0.5$. We believe that this is due to the onset of additional complexities in desorption ultimately leading to the asymmetric desorption feature which develops its maximum at 275 K at higher hydrogen coverages. We

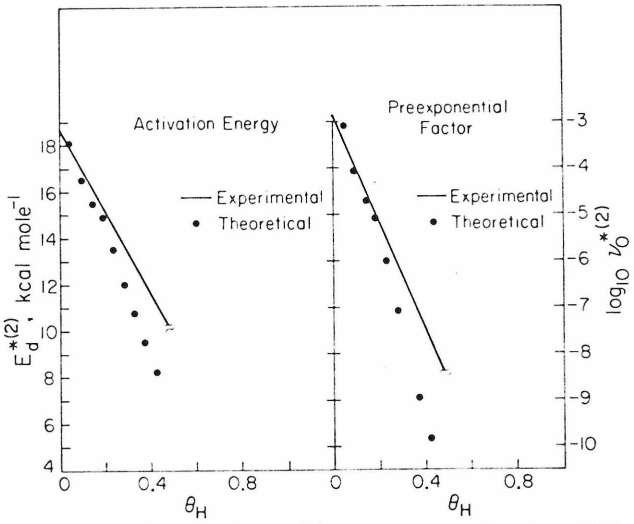

Fig. 8. Comparison of experimental (———) and theoretical (●) values of kinetic parameters for thermal desorption of H_2 from Rh(111). The theoretical values were calculated assuming both a mobile precursor to desorption and that saturation of one distinct state occurs at a total relative coverage of $\theta_H = 0.5$.

have therefore employed the mobile precursor model only up to $\theta = 0.5$ and have normalized the theoretical desorption data to this value by setting $\theta = 1$ in eq. (2) at the experimental value of $\theta = 0.5$. In fig. 8, comparison of the theoretical points and the linear least-squares fit to the experimental data taken from fig. 4 indicates that the rapid initial decrease in both $E_d^{*(2)}$ and $\nu_0^{*(2)}$ may in fact be expected on the basis of the mobile precursor model.

Repulsive hydrogen–hydrogen interactions may also be present leading to a decrease in $E_d^{*(2)}$ and possibly to the development of the asymmetry of the desorption peak as θ increases above ~0.5. It is not physically reasonable to attribute the entire coverage dependent desorption behavior to repulsive interactional effects, however [22].

4.3. Comparison of adsorption and desorption kinetics

Gorte and Schmidt [21] have pointed out that the mobile precursor state should be expected to participate in both adsorption and desorption processes although differences in the temperature of the two processes may of course influence the magnitude of the rate coefficients involved. In particular, the *absence* of evidence for a mobile precursor in low temperature adsorption implies that it will *not* be present in desorption at higher temperatures. In the work described here for H_2 on Rh(111), the adsorption measurements suggest that the precursor model may be operative at 175 K, whereas the desorption measurements indicate more strongly that a precursor exists at ~350 K. At the present time, we cannot explain why the desorption kinetic measurements are more strongly suggestive of the precursor than are the adsorption kinetic measurements.

4.4. Comparison with hydrogen desorption kinetics from other metals

For both fcc(111) and hcp(001) surfaces (surfaces which expose a hexagonal arrangement of substrate atoms), there appear to be strong similarities in H_2 desorption behavior. Although details differ, for low hydrogen coverages, $E_d^{(2)} \simeq 20$ kcal/mole and $\nu_0^{(2)} \simeq 10^{-2}$ to 10^{-4} cm^2/sec are typical values for the desorption parameters [23], in good agreement with our limiting behavior on Rh(111) [21]. As coverage increases, the appearance of two or more overlapping desorption peaks is a common feature of all hexagonal surfaces, although the degree of overlap varies from metal to metal.

5. Summary

The following features of hydrogen chemisorption on Rh(111) have been found: (1) Hydrogen adsorbs dissociatively following Langmuir $[(1-\theta)^2]$ kinetics at 175 K. The sensitivity of the measurement of adsorption kinetics is insufficient to discriminate between strict Langmuir adsorption and adsorption via a short-lived mobile precursor state.

(2) Ordered hydrogen superstructure formation is not observed by LEED.

(3) Hydrogen thermal desorption is complex. Evidence exists for the presence of a mobile precursor state during desorption, leading to very large coverage dependent variations in $\nu_0^{*(2)}$ and $E_d^{*(2)}$. At zero coverage, $E_d^{(2)} = 18.6$ kcal/mole and $\nu_0^{(2)} = 1.2 \times 10^{-3}$ cm^2/sec.

(4) No differences in H_2 and D_2 thermal desorption kinetics are observed, suggesting that zero-point energy effects do not play a major role in determining desorption rates.

Acknowledgments

We thank Dr. C.-M. Chan for computing the theoretical thermal desorption spectra. One of us (J.T.Y.) acknowledges partial support from the Department of Energy, Division of Basic Energy Sciences.

References

[1] O. Beeck, Disc. Faraday Soc. 8 (1950) 118.
[2] J.R. Anderson and C. Kemball, Proc. Roy. Soc. (London) A223 (1954) 361.
[3] C. Kemball, Proc. Roy. Soc. (London) A214 (1952) 413.
[4] G.C. Bond, Catalysis by Metals (Academic Press, London, 1962) p. 320.
[5] G.C. Bond, ibid, p. 337.
[6] G.A. Mills and F.W. Steffgen, Catalysis Rev. 8 (1974) 159.
[7] J.T. Yates, Jr., P.A. Thiel and W.H. Weinberg, Surface Sci. 82 (1979) 45.
[8] G.C. Bond, Catalysis by Metals (Academic Press, London, 1962) p. 447.
[9] C.-M. Chan, P.A. Thiel, J.T. Yates, Jr. and W.H. Weinberg, Surface Sci. 76 (1978) 296.
[10] F.R. Shepherd, P.R. Watson, D.C. Frost and K.A.R. Mitchell, J. Phys. C, submitted; see also Proc. 7th Intern. Vacuum Congr. and 3rd Intern. Conf. on Solid Surfaces, Vienna, 1977, p. A2725.
[11] P.A. Thiel, J.T. Yates, Jr. and W.H. Weinberg, Surface Sci. 82 (1979) 22.
[12] P.A. Thiel, J.T. Yates, Jr. and W.H. Weinberg, Surface Sci., submitted.
[13] D.G. Castner, B.A. Sexton and G.A. Somorjai, Surface Sci. 71 (1978) 519.
[14] V.J. Mimeault and R.S. Hansen, J. Chem. Phys. 45 (1966) 2240.
[15] S.M. Edwards, R.P.H. Gasser, D.P. Green, D.S. Hawkins and A.J. Stevens, Surface Sci. 72 (1978) 213.
[16] P. Kisliuk, J. Phys. Chem. Solids 3 (1957) 95; 5 (1958) 78.
[17] C.-M. Chan, R. Aris and W.H. Weinberg, Appl. Surface Sci. 1 (1978) 360.
[18] R. Fowler and E.A. Guggenheim, Statistical Thermodynamics (Cambridge University Press, London, 1956) p. 169.
[19] J. Behm, K. Christmann and G. Ertl, Solid State Commun. 25 (1978) 763.
[20] D.O. Hayward and B.M.W. Trapnell, Chemisorption (Butterworths, London, 1964) p. 92.
[21] R. Gorte and L.D. Schmidt, Surface Sci. 76 (1978) 559.
[22] E.D. Williams, S.L. Cunningham and W.H. Weinberg, J. Chem. Phys. 68 (1978) 4688.

[23] For examples see the following references:
Pd(111): H. Conrad, G. Ertl and E.E. Latta, Surface Sci. 41 (1974) 435;
Pt(111): K. Christmann, G. Ertl and T. Pignet, Surface Sci. 54 (1976) 365; R.W. McCabe and L.D. Schmidt, Surface Sci. 65 (1977) 189;
Ni(111): K. Christmann, R.J. Behm, G. Ertl, M.A. Van Hove and W.H. Weinberg, J. Chem. Phys. 70 (1979) (to appear in May 1, 1979 issue);
Ru(001): L. Danielson, M.J. Dresser, E.E. Donaldson and T. Dickinson, Surface Sci. 71 (1978) 559.

Chapter 3

THE CATALYTIC REACTION BETWEEN ADSORBED OXYGEN AND HYDROGEN ON Rh(111)

Surface Science 82 (1979) 45–68
© North-Holland Publishing Company

THE CATALYTIC REACTION BETWEEN ADSORBED OXYGEN AND HYDROGEN ON Rh(111) [a]

J.T. YATES, Jr. [b], P.A. THIEL [c] and W.H. WEINBERG [d]
Division of Chemistry and Chemical Engineering, California Institute of Technology, Pasadena, California 91125, USA

Received 31 August 1978; manuscript received in final form 13 October 1978

The adsorption rate for O_2 on Rh(111) at 335 K exhibits Langmuir $(1 - \theta)$ kinetics rather than the expected $(1 - \theta)^2$ dependence. Adsorption occurs with a sticking coefficient near unity on empty sites, producing a mixture of ordered and disordered domains. At $\theta \leqslant 0.5$, the intensity of the $(1, \overline{1/2})$ overlayer beam increases in proportion to θ^2 as expected for ordered oxygen island formation. Extensive ordering occurs only in the very last stages of monolayer formation. The reaction of the ordered-O layer with H_2(g) to produce H_2O takes place rapidly above 275 K in the 10^{-8}–10^{-6} Torr range and can be followed quantitatively by observation of the $(1, \overline{1/2})$ LEED beam intensity. The reaction accurately exhibits kinetics which are first order in H_2 pressure, implying an efficient trapping mechanism for adsorbed hydrogen on the ordered-O layer. The activation energy for reaction is 5.3 ± 0.3 kcal/mole; each reaction event leads to a loss of order from a ~300 Å^2 domain. This suggests that near saturation coverage, extensive disordering occurs for small decreases in ordered oxygen coverage during reaction with H_2(g) and is consistent with the massive ordering behavior seen in the final stages of oxygen adsorption. The reaction of H_2(g) with *disordered* oxygen species follows approximate half-order kinetics in P_{H_2} as expected for a mechanism which does not involve hydrogen atom trapping.

1. Introduction

Rhodium is an active catalyst for various types of reactions, in many cases rivaling or exceeding Pt in activity. The classes of reactions catalyzed efficiently by Rh are the hydrogenation of olefins [1], deuterium exchange with hydrocarbons [2] and NH_3 [3], benzene hydrogenation [4], ketone reduction [5], methanation [6], nitrogen oxide reduction [7], and the oxidation of hydrogen [8]. Despite the

---

[a] Supported by the Army Research Office (Durham) under Grant No. DAHC04-75-0170.
[b] Sherman Fairchild Distinguished Scholar.
[c] National Science Foundation Predoctoral Fellow.
[d] Camille and Henry Dreyfus Foundation Teacher–Scholar, and Alfred. P. Sloan Foundation Fellow.

diverse catalytic activity of Rh, the *catalytic* properties of the metal in single crystal form have not been examined previously using modern methods of surface science.

In a previous paper [9] we have reported a study of adsorption of oxygen on Rh(111). It was found that oxygen adsorbs in a disordered layer at ~100 K and undergoes an activated ordering process beginning near 200 K. On further heating, activated disordering begins near 300 K, followed by penetration of adsorbed oxygen into the bulk at temperatures near 400 K. This previous work [9] forms a sound basis for the investigation of the catalytic reduction of adsorbed oxygen on Rh(111) using $H_2(g)$, to produce H_2O. This reaction occurs at room temperature and at low H_2 pressures which are readily accessible in an ultra-high vacuum system. We have employed a combination of Low-Energy Electron Diffraction (LEED), Auger Electron Spectroscopy (AES), and Thermal Desorption Mass Spectrometry (TDS) to determine the kinetic and structural features of this reaction.

The structure [10,11] of Rh(111) and the effective Debye temperature [10] have been measured previously using LEED. In addition, the structures of both Rh(110) [12] and Rh(100) [13] have been determined using LEED. In all cases, the Rh surfaces are unreconstructed, and unrelaxed to within 5%. The results of hydrogen chemisorption [14] and oxygen–hydrogen coadsorption [15] on Rh(111) will be reported elsewhere, as will a determination of the structure of oxygen on Rh(111) [16].

2. Experimental details

The ultra-high vacuum apparatus consisted of an ion-pumped stainless steel chamber equipped with a titanium sublimation pump. The base pressure, following bakeout, was $<1 \times 10^{-10}$ Torr. The system was equipped with a four grid post-acceleration display LEED apparatus containing a movable Faraday cup for LEED intensity measurements. The Faraday cup aperture subtended an angle of 4.6×10^{-3} steradians. In addition, the system contained a Bayard–Alpert gauge, a quadrupole mass spectrometer, a single pass cylindrical mirror Auger electron spectrometer, and an ion gun. The Rh(111) crystal was mounted on a rotatable manipulator using 0.025 cm Ta heating wires welded to the back face of the crystal. A W/26%Re–W/5%Re thermocouple was used to monitor the crystal temperature.

The preparation and Ar^+ bombardment plus oxygen-cleaning procedure for the Rh(111) crystal (in which the crystal was heated to 1240 K in vacuum to remove residual oxygen) have been described previously [9,10]. In the present work, however, the crystal was heated to a higher temperature (1565 K) in vacuum during cleaning. The Auger spectrum of the clean Rh(111) surface resulting from the 1565 K treatment was identical to that obtained after the 1240 K treatment. A small residual 515 eV oxygen Auger peak showed the same temperature-dependence as discussed in a previous paper [9]. In separate experiments, in which an O_2-cleaned crystal was ground to half its original thickness, it was found that prior O_2 treatments (2×10^{-7} Torr, 1230 K, plus repeated room-temperature O_2 exposures) had effectively removed traces of dissolved boron from the entire bulk of the Rh single crystal disk [10]. Boron contamination in single crystal Rh is well known. All gas pressures and exposures reported here have been corrected for gauge sensitivities relative to nitrogen.

3. Results

3.1. Adsorption of O_2 at 335 K

The coverage-exposure relationship for O_2 on Rh(111) at 335 K is shown in fig. 1. These data were obtained by exposing the crystal to O_2 (using a Bayard–Alpert gauge to measure exposure) and then using Auger spectroscopy to measure both the Rh (303–293 eV) and the O (510–497 eV) peak-to-peak amplitudes. The relative coverages of chemisorbed oxygen, θ, were determined using the O/Rh

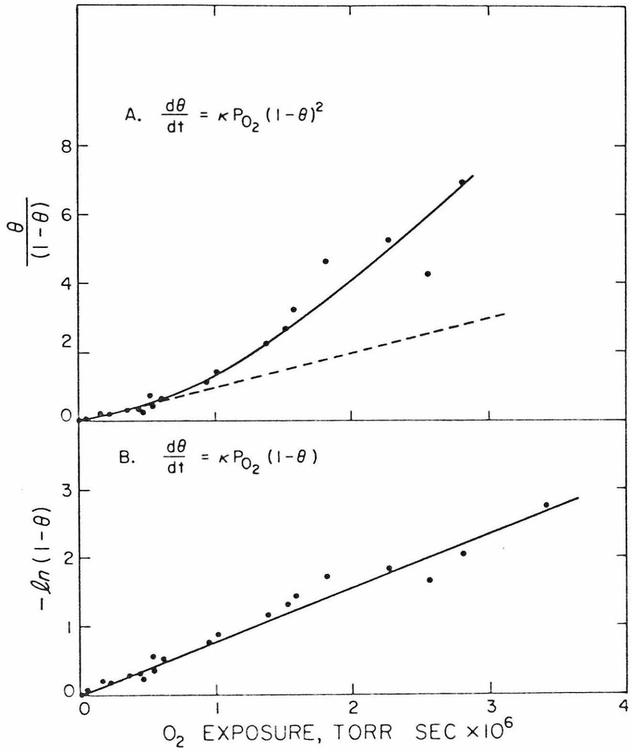

Fig. 1. Langmuir plots for O_2 adsorption on Rh(111) at $T = 335$ K. The oxygen coverage, θ, was measured by Auger spectroscopy. In the kinetic rate expressions for adsorption, t is the time of exposure at a given pressure of oxygen, P_{O_2}, and κ is a proportionality constant related to the initial sticking probability and the translational velocity of D_2.

intensity ratio, correcting the data slightly for systematic variations in attenuation of the rhodium signal by the overlayer. This was done by plotting the rhodium Auger amplitudes as a function of the oxygen Auger amplitudes and determining the linear least squares fit to these data. The individual O/Rh Auger amplitude ratios were thus corrected by a factor determined from the linear fit. The fractional oxygen coverage was then computed for each of the O_2 exposures. This procedure effectively compensates for small variations in electron emission current during the Auger measurement as well as for attenuation of the Rh Auger transition by an overlayer of adsorbed oxygen. When $\theta = 1$, a 22% attenuation of the Rh (293 eV) peak was observed. It was shown that electron impact on the oxygen layer did not cause measurable loss of the O Auger signal in times equivalent to those used in this measurement.

The experimental data have been fitted to a Langmuir model as shown by the plots of fig. 1. In this type of construction, the criteria for acceptance of a proposed model are a linear representation of the data and an intercept of zero, i.e. the origin represents one point on the line. A comparison of a $(1 - \theta)$ and a $(1 - \theta)^2$ model for the rate of oxygen adsorption clearly favors the $(1 - \theta)$ model, fig. 1B, in view of the nonlinearity of fig. 1A. A plot of the oxygen coverage as a function of exposure on Rh(111) is shown in fig. 2, where the solid line is a least squares $(1 - \theta)$ fit to the data. In order to calculate an approximate value for the sticking coefficient for O_2 on an empty site, a model describing the overlayer lattice structure is necessary. As will be discussed later, either a (2 X 2) overlayer or a surface containing three (2 X 1) overlayer domains will yield the (2 X 2) LEED pattern observed.

Assuming a saturation coverage of 4.0×10^{14} atoms/cm^2 [(2 X 2) overlayer], the sticking coefficient on an empty site in the Langmuir model is 0.44. For three (2 X 1) domains, the saturation coverage is 8.0×10^{14} atoms/cm^2, and the sticking

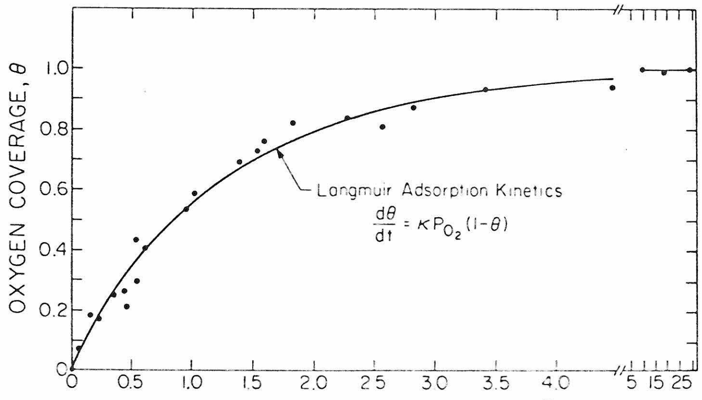

Fig. 2. Kinetics of O_2 adsorption on Rh(111) at $T = 335$ K.

coefficient on an empty site is near unity. It must be remembered that absolute errors of 50% are possible in a measurement of this type.

The O_2 coverage–exposure relationship, shown in fig. 2, differs from similar measurements on Rh(111) previously made at $T \leqslant 170$ K. The 170 K plot displayed a long initial linear region. This may be due to an adsorption mechanism in which initial adsorption at low temperatures occurs on both covered and uncovered sites with high sticking coefficient, followed by filling of the vacant sites from the mobile second layer [9].

3.2. LEED behavior upon O_2 adsorption at 335 K

In view of the fact that oxygen forms a (2 X 2) overlayer, we have studied the intensity of the $(1, \overline{1/2})$ LEED beam, $I_{(1,\overline{1/2})}$, as a function of oxygen exposure, and the result is shown in fig. 3. An initial ordering region is observed below 1.5 L O_2 exposure, followed by a region in which the intensity decreases. At exposures above 3 L, a final ordering region is observed in which a twenty-fold increase in the $(1, \overline{1/2})$ beam intensity is observed. It should be noted, by comparison with the experimental adsorption kinetics curve, that the final ordering region occurs over a wide exposure range very near the oxygen saturation coverage. This observation implies that a massive cooperative ordering effect takes place in the final stages of chemisorption, induced by the addition of a small number of oxygen atoms to a nearly saturated layer at this temperature.

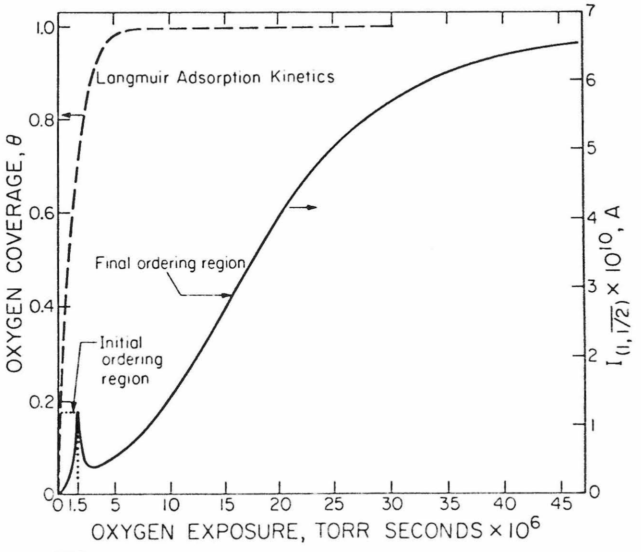

Fig. 3. Oxygen $(1, \overline{1/2})$ LEED beam intensity as a function of O_2 exposure at $T = 335$ K. (The Langmuir adsorption curve is taken from fig. 2.)

By orienting the Faraday cup slightly off of the center of the $(1, \overline{1/2})$ beam, it was apparent that sharpening of the $(1, \overline{1/2})$ beam is a major cause of the final intensity increase. Thus, in fig. 4, the relative attenuation of the $(1, \overline{1/2})$ beam current when the detector is at the edge of the $(1, \overline{1/2})$ beam during O_2 exposure appears to be greater in the final ordering region than in the initial ordering region.

We have examined the quantitative relationship between $I_{(1, \overline{1/2})}$ and oxygen coverage in the initial ordering region. The results are shown in fig. 5. Here the intensity is plotted as a function of θ^2. Up to a relative coverage of ~0.45, $I_{(1, \overline{1/2})}$ increases linearly with θ^2, as shown by data from three separate experiments carried out over a five-fold range in adsorption rate, which is proportional to P_{O_2}. This behavior agrees with theoretical predictions for electron diffraction from two-dimensional periodic structures in either kinematic or dynamic theories [17]. However, above $\theta \simeq 0.45$, significant departures from this behavior are observed. At a value of θ near 0.65, a sharp maximum in $I_{(1, \overline{1/2})}$ occurs and a subsequent 65% decrease in measured intensity is observed prior to entering the final ordering region shown in fig. 3.

It was considered important to establish whether the complex behavior of $I_{(1, \overline{1/2})}$ was accompanied by changes in either the local adsorption site symmetry or a surface phase transition [conversion from a (2×2) overlayer to a three-fold degenerate (2×1) lattice]. Therefore, as shown in fig. 6, the intensity–voltage $(I-V)$ characteristics of the $(1, \overline{1/2})$ beam were studied at two different oxygen coverages corresponding to the exposures labeled A and B in the inset. There is no detectable change in the $I-V$ characteristics of this LEED beam in going from the initial ordering region to the final ordering region. Also, the $I-V$ curves are identical to those of the ordered structures produced by heating an oxygen overlayer which had been adsorbed at ~100 K. These curves have been described previously [9]. On this basis, we conclude that the ordered LEED structure produced on Rh(111)

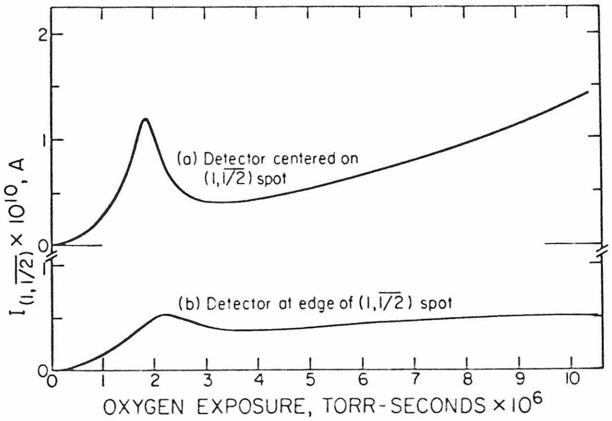

Fig. 4. Intensity of oxygen $(1, \overline{1/2})$ LEED beam as a function of O_2 exposure at T = 335 K.

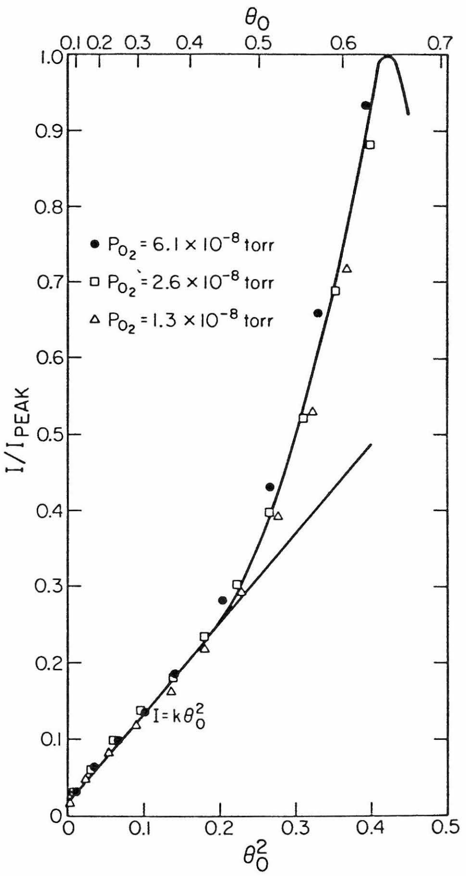

Fig. 5. Intensity of oxygen $(1, \overline{1/2})$ LEED beam as a function of oxygen coverage at $T = 335$ K. The data represent three rates of O_2 adsorption.

originates from a single overlayer lattice structure and is independent of temperature or coverage.

3.3. Use of LEED intensity to measure the rate of change of oxygen coverage in the high coverage region

As shown by the data in fig. 7, the rate of change of *intensity* of the $(1, \overline{1/2})$ beam is directly proportional to the rate of change of *coverage* in the final ordering region. In fig. 7, the adsorption of O_2 at 6.1×10^{-8} Torr has been interrupted in three separate experiments. When $P_{O_2} = 0$, the $(1, \overline{1/2})$ beam ceases to intensify. This proves that the intensification observed in the final ordering region is not controlled by a slow thermal process. A second experiment involving $P_{O_2} = 2.6 \times 10^{-8}$ Torr produces an intermediate rate of intensification of $I_{(1, \overline{1/2})}$. In these three

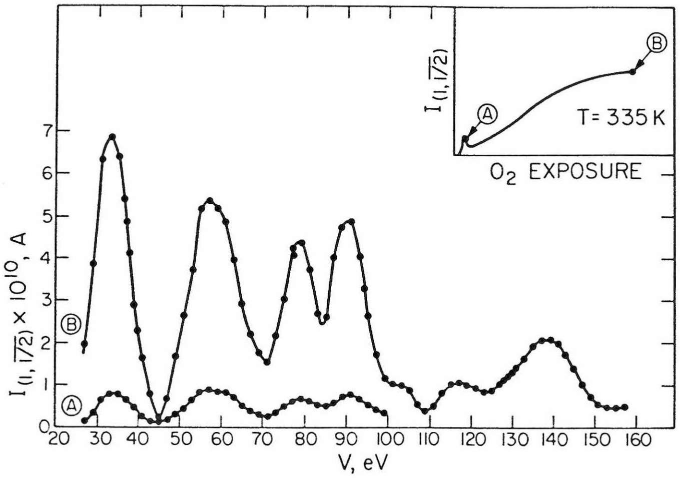

Fig. 6. Intensity–voltage curves for oxygen $(1, \overline{1}/2)$ LEED beam at two O_2 exposures on Rh(111). Oxygen exposure at A = 2 × 10^{-6} Torr sec. Oxygen exposure at B = 38 × 10^{-6} Torr sec.

experiments, the slope is directly proportional to P_{O_2} and hence to the *rate* of oxygen adsorption. These data suggest that in this region, $I_{(1,\,\overline{1/2})}$ may be used to study the rate of change of surface oxygen coverage in the ordered layer. Separate experiments involving use of an interrupted primary electron beam (V_e = 62 eV; I_e = 0.7

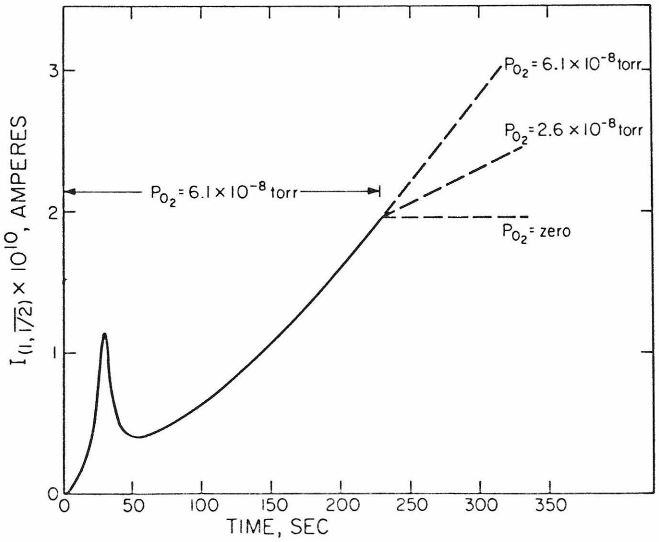

Fig. 7. Intensity behavior of oxygen $(1, \overline{1/2})$ LEED beam upon change of P_{O_2}.

μA) indicate that there is no kinetic effect which can be related to electron impact processes during O_2 adsorption.

3.4. Onset temperature for the reaction of ordered oxygen with $H_2(g)$

An ordered oxygen layer was produced on Rh(111) by adsorption of O_2 (8.2 L) at 100 K, followed by heating in vacuo to 300 K. This produced the characteristic (2 X 2) LEED pattern [9]. The crystal containing the ordered layer was cooled to 90 K, and H_2(g) was admitted to a pressure of 4×10^{-7} Torr. The crystal was heated successively to various temperatures, then cooled back to 90 K where the intensity of the $(1, \overline{1/2})$ LEED beam was measured. As shown in fig. 8, the first evidence of loss of ordered oxygen occurs at 275 K. At higher temperatures, a monotonic drop in $I_{(1, \overline{1/2})}$ is observed; complete removal of ordered material has occurred near 400 K. This result is indicative of an activated process for the reaction of ordered oxygen with H_2(g), since coadsorption studies of oxygen and hydrogen on Rh(111) show that the two species coexist on the surface below 275 K [9].

3.5. Reaction of $H_2(g)$ with ordered oxygen on Rh(111)

We have investigated the kinetics of the reaction of an ordered oxygen overlayer on Rh(111) with H_2(g) by measurements of $I_{(1, \overline{1/2})}$, as shown in fig. 9. The

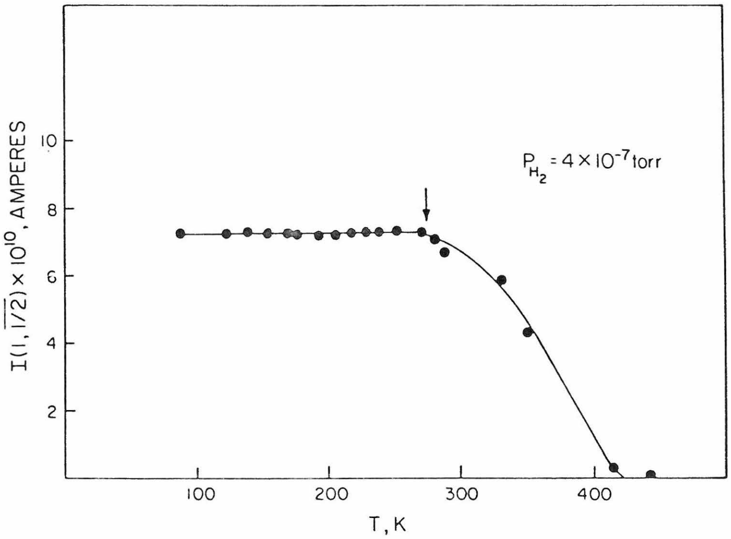

Fig. 8. Onset temperature for reaction of ordered oxygen with H_2(g). Initial O_2 exposure is 8.2×10^{-6} Torr sec at 100 K, followed by heating to 300 K to produce ordered oxygen overlayer.

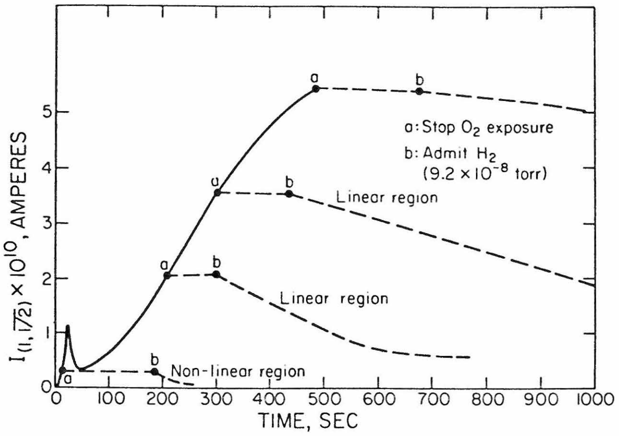

Fig. 9. Reaction of ordered oxygen with H_2 in various regions of oxygen coverage at T = 335 K on Rh(111). The O_2 exposures were carried out at $P_{O_2} = 6.1 \times 10^{-8}$ Torr to the various points labeled a.

ordered oxygen layer was produced by exposure to O_2, and the adsorption was interrupted at various points (labeled a) as shown. Following periods of 100 to 200 s, $H_2(g)$ was admitted at point b, and $I_{(1,\,\overline{1/2})}$ was monitored. In the two experiments carried out in the middle of the final ordering region, long linear plots of $I_{(1,\,\overline{1/2})}$ as a function of time were obtained. However, for the experiment in which the O_2 exposure was halted during the *initial* ordering region, non-linear behavior was observed, as shown. Also, at higher values of $I_{(1,\,\overline{1/2})}$, reaction of ordered oxygen with $H_2(g)$ yields a slightly nonlinear curve as shown by the experiment at highest $I_{(1,\,\overline{1/2})}$. It is interesting to note also that the initial slopes of the three curves in

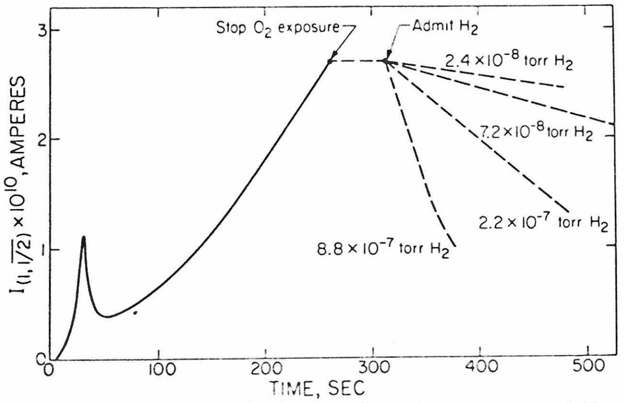

Fig. 10. Reaction of ordered oxygen with H_2 at various H_2 pressures and T = 335 K. The O_2 exposure was carried out at $P_{O_2} = 6.1 \times 10^{-8}$ Torr.

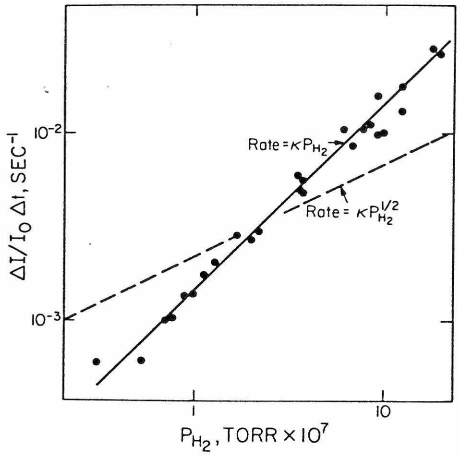

Fig. 11. Kinetics of reaction of ordered oxygen with $H_2(g)$ on Rh(111) at T = 335 K.

the final ordering region decrease as the initial value of I increases. We have not attempted to fit these typical curves to models, but have been satisfied rather to employ the initial slope of the linear curve as a measure of the depletion rate for adsorbed ordered oxygen on Rh(111).

Fig. 10 demonstrates the use of the intensity of the $(1, \overline{1/2})$ oxygen beam to measure the kinetics of depletion of ordered oxygen by reaction with $H_2(g)$. A sequence of typical experiments is shown for various values of P_{H_2} at 335 K. Starting at identical values of $I_{(1,\ \overline{1/2})}$, each experiment results in a linear region of intensity loss. In the log-log plot of fig. 11, the initial rates of intensity loss are plotted as a function of P_{H_2} for 26 experiments. It is clear that the reaction rate is proportional to the first power of P_{H_2} over almost a 100-fold range in P_{H_2}, and that the data cannot be fitted to half-order kinetics in P_{H_2}.

3.6. Activation energy for the reaction $H_2(g)$ + O(ads., ordered)

We have employed the technique discussed above to determine the temperature dependence of the $H_2(g)$ + O(ads., ordered) reaction on Rh(111). Fig. 12 illustrates the method. Oxygen was adsorbed at 317 K until the intensity, $I_{(1,\ \overline{1/2})}$, rose to the same value as in previous experiments, at which point adsorption was interrupted. The crystal temperature was adjusted to a higher temperature in a time period of ~20 s and then hydrogen was admitted. At this point it was impossible to monitor the decrease in intensity of the $(1, \overline{1/2})$ spot due to the effects of a strong magnetic field resulting from the heating current and also due to a reduction of beam intensity at elevated temperatures (Debye–Waller effect). Following an appropriate reaction time, the heating current was interrupted, and the crystal was cooled rapidly to 317 K which resulted in the rise in beam intensity beyond 370 sec in fig. 12. The

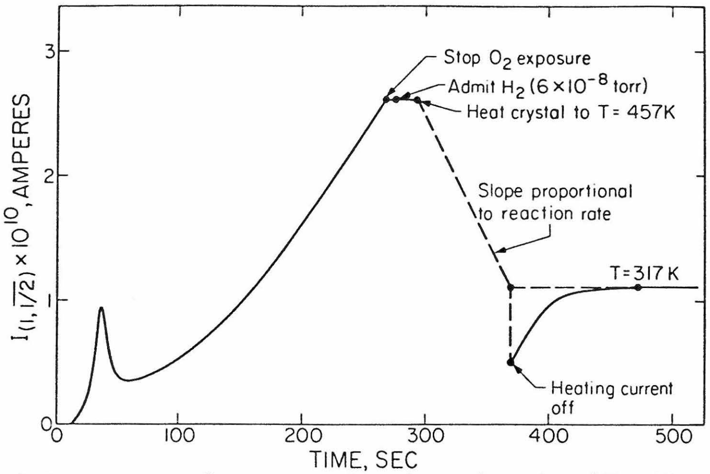

Fig. 12. Typical measurement of temperature dependence of reaction of H_2 with ordered oxygen on Rh(111). The dashed lines represent a geometrical construction based upon the experimental data (solid lines).

geometrical construction shown by dashed lines was used to deduce the rate of intensity change during reaction. Although this method is subject to some error due to the time required to reach constant elevated temperature initially (~20 s), and the time required to cool finally to near the initial temperature (~80 s), these effects are somewhat compensating. These sources of error become less serious at temperatures below the temperature of the experiment shown in fig. 12, which is the maximum temperature employed (457 K).

It has been shown previously that a "high-temperature" disordering process

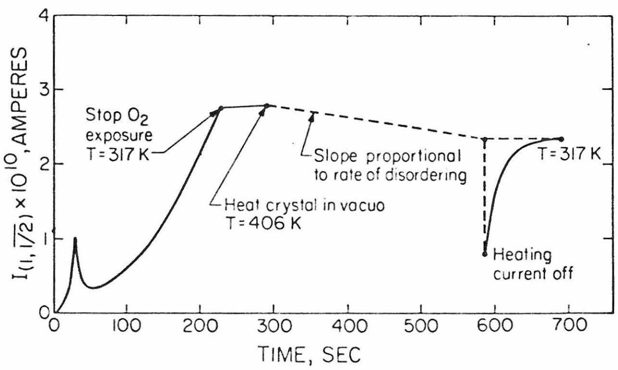

Fig. 13. Typical measurement of temperature-dependent disordering rate for ordered oxygen overlayer on Rh(111). The dashed lines represent a geometrical construction based upon the experimental data (solid lines).

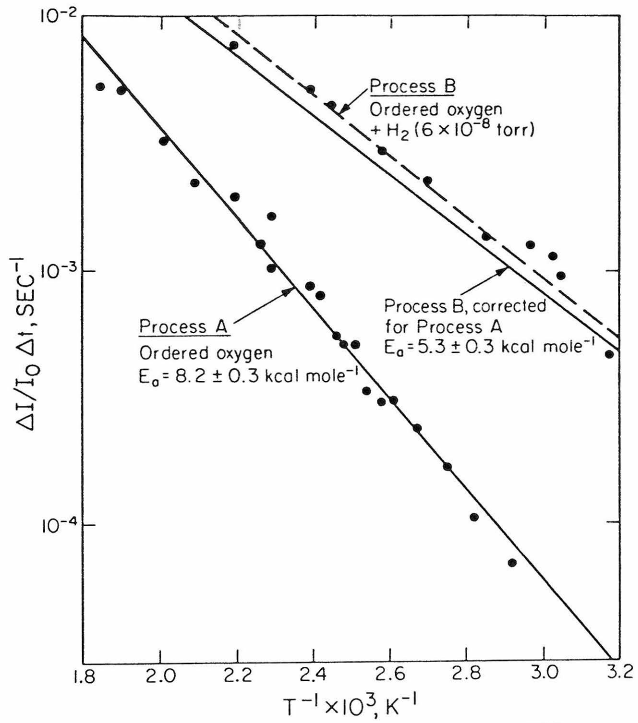

Fig. 14. Arrhenius plots of rates of disappearance of oxygen (1, $\overline{1/2}$) beam intensity from Rh(111). The activation energies and their uncertainties are based upon a linear least-squares fit to the data. Process A is the activated oxygen disordering. Process B is the activated H_2 reaction with ordered oxygen.

occurs for ordered oxygen layers on Rh(111) above ~300 K [9]; thus, the loss of intensity discussed above for reaction of $H_2(g)$ with the ordered oxygen layer contains a contribution from thermal disordering which must be subtracted. In order to measure the kinetics of the "high-temperature" disordering effect, a procedure similar to that shown in fig. 12 was employed. This is shown in fig. 13, where heating in vacuo was carried out to induce the disordering process.

Arrhenius plots for these two processes are shown in fig. 14. Process A, the activated thermal disordering of the ordered oxygen overlayer, exhibits an $E_a = 8.2 \pm 0.3$ kcal mole^{-1}. Process B, the activated reaction of ordered oxygen with H_2, is the main contributor to the rate process indicated by the upper dashed line. When the small correction due to the contribution from Process A is made, the solid line results. This yields an activation energy of 5.3 ± 0.3 kcal mole^{-1} for the reaction between $H_2(g)$ and ordered oxygen.

3.7. Use of Auger spectroscopy to measure the rate of removal of adsorbed oxygen by $H_2(g)$

It was feasible to employ Auger spectroscopy to carry out crude measurements of the rate of reaction of *total* adsorbed oxygen on Rh(111) with $H_2(g)$. The spectrometer was arranged to scan the peak maxima for chemisorbed oxygen between 510 eV and 497 eV rapidly. (Typical spectra for chemisorbed oxygen on Rh(111) are shown in ref. [9].) As indicated in the bottom of fig. 15, the peak-to-peak amplitude decreased systematically upon admission of H_2. Semi-logarithmic plots of the Auger intensity as a function of time for various values of P_{H_2} were generally linear near the initial region as shown in typical results displayed at the top of fig. 15. The measured rates are associated with the loss of *all* chemisorbed oxygen from the surface when this method of measurement is employed. A log-log plot of the kinetic results for 29 experiments over a 100-fold range of hydrogen pressure is shown in fig. 16. The scatter in the data is related to the difficulty of determining the best linear fits to the semi-logarithmic data, as exemplified in fig. 15. Two regions are evident in the plot of fig. 16. Below a hydrogen pressure of $\sim 10^{-7}$ Torr, the data best fit a *one-half order kinetic expression* as shown by the solid line. The dashed line clearly indicates that a fit to first-order kinetics in hydrogen pressure is inap-

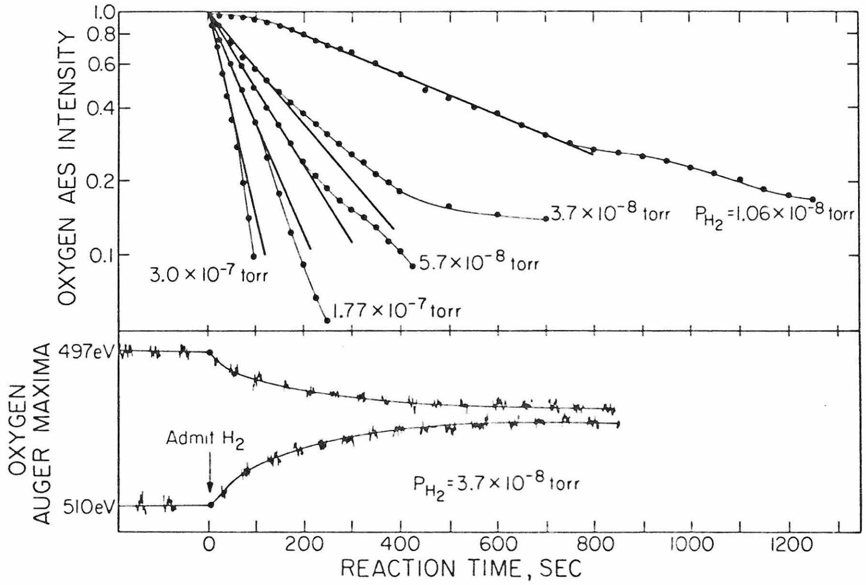

Fig. 15. Upper panel: Typical data showing rate of reaction of $H_2(g)$ with oxygen adsorbed on Rh(111) at $T = 335$ K. The straight lines drawn on the semi-logarithmic plots were used to estimate the rate coefficients (first-order in oxygen coverage).
Lower panel: Variation in peak-to-peak amplitude in oxygen Auger intensity as a function of time during exposure to hydrogen at 335 K.

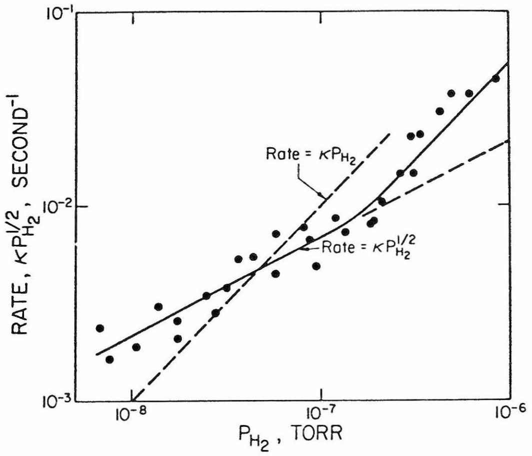

Fig. 16. Kinetics of reaction of total surface oxygen on Rh(111) with $H_2(g)$ at $T = 335$ K.

propriate in the low pressure region. The second region of fig. 16, above ~10^{-7} Torr hydrogen pressure, suggests a conversion to a reaction process which exhibits first-order kinetics in the hydrogen pressure.

3.8. Detection of deuterated water by reaction of H_2–D_2 mixture with adsorbed oxygen on Rh(111)

In order to distinguish between Eley–Rideal and Langmuir–Hinshelwood mechanisms for the interaction of hydrogen with adsorbed oxygen on Rh(111),

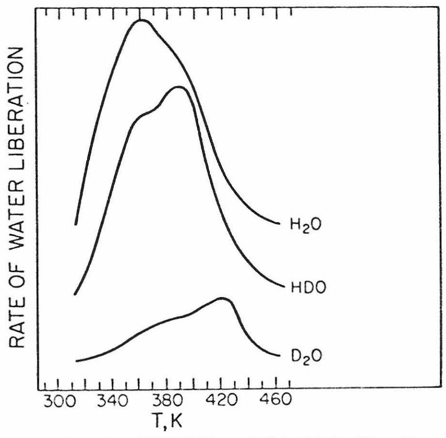

Fig. 17. Water liberation upon heating Rh(111) and O(ads) in H_2–D_2 mixture. The curves were measured in $P_{H_2} = P_{D_2} = 5 \times 10^{-8}$ Torr.

a series of experiments involving a 1 : 1 mixture of H_2 and D_2 were carried out. For an Eley–Rideal mechanism, no HDO products would be expected. A high coverage of chemisorbed oxygen was adsorbed on Rh(111) (oxygen exposure = 11 L, $T = 335$ K). The H_2–D_2 mixture was admitted to a pressure of 1×10^{-6} Torr; this caused the background production of all three isotopic water molecules within the vacuum system. Following stabilization of the partial pressure of each isotopic water species, the Rh(111) crystal was heated with a reproducible temperature program, and thermal evolution of the three isotopic water molecules was observed on top of their large background levels in the vacuum system. The "desorption spectra" are shown in fig. 17, corrected for background effects. It is evident that all three isotopic water molecules are produced, suggesting that dissociative adsorption of H_2 precedes reaction with chemisorbed oxygen (Langmuir–Hinshelwood mechanism).

4. Discussion

4.1. Kinetics of O_2 adsorption on Rh(111)

The observation at 335 K of an O_2 adsorption rate proportional to $(1 - \theta)$ is unexpected for the dissociative adsorption of a diatomic molecule into a mobile chemisorbed layer, where a $(1 - \theta)^2$ dependence would be appropriate [18]. Several general explanations for this observation may be suggested:

(1) The dissociation of O_2 on Rh(111) does not require the presence of neighboring pairs of empty atomic lattice sites but can occur at a single position.

(2) The rate controlling step for adsorption of O_2 involves the interaction of an O_2 *molecule* with a single atomic site. Subsequent dissociation is not rate controlling.

(3) Molecular oxygen is the chemisorbed species at 335 K.

We can eliminate the third explanation on the basis of two observations: (a) thermal desorption mass spectrometry of oxygen from the (111) surface of Rh [9] indicates that O_2 desorbs above ~800 K with an activation energy of ~56 kcal mole^{-1} in the limit of zero oxygen coverage. This large activation energy, as well as the observation of second order desorption kinetics, precludes the possibility of desorption from an undissociated state; (b) the occurrence of irreversible dissociation above the temperature of adsorption (335 K) may be excluded by virtue of the observation of invariant LEED I–V curves for adsorbed oxygen on Rh(111) from 280 to 700 K [9].

A more attractive model involves the interaction of an O_2 molecule with a *single* atomic site during adsorption and possibly dissociation [suggestions (1) and (2) above]. This is, in fact, likely, based on the interatomic O–O distance (1.21 Å) in O_2 compared to the Rh–Rh nearest neighbor spacing (2.69 Å). A number of "peroxo" dioxygen complexes involving π-bonded O_2 and transition metal atoms have been reported and studied spectroscopically [19,20]. Typical O–O distances in these ionic peroxo complexes are 1.4–1.5 Å, and they exhibit O_2 vibrational frequencies near 860 cm^{-1}. Non-ionic peroxo complexes with metal atoms isolated in inert matrices have been studied for several transition metals (Ni, Pd, Pt), and exhibit O_2 vibrational features near 1000 cm^{-1} [21]. We do not believe that the postulated peroxo surface complexes are stabilized for long times during O_2 adsorption on Rh(111), but instead may exist as intermediates for lifetimes long enough to control the adsorption kinetics yielding a $(1 - \theta)$ dependent rate. The involvement of end-on "superoxo" O_2–M complexes as intermediates formed prior to dissociation on the Rh(111) surface cannot be excluded.

4.2. LEED behavior upon O_2 adsorption

A complex intensity behavior for the $(1, \overline{1/2})$ LEED beam occurs as oxygen coverage increases at 335 K. The expected θ^2 dependence of intensity is observed for $\theta \leqslant 0.45$ as shown by the data in fig. 5. This behavior is expected for island formation with net pairwise attractive forces operating [22]. However, above this point in coverage, the measured intensity increases more rapidly than θ^2 and then decreases sharply above $\theta = 0.65$. The final ordering region is associated with sharpening of the $(1, \overline{1/2})$ LEED beam, suggesting that for the more diffuse beams encountered at lower exposures, the Faraday cup may have collected only a fraction of the beam current. Thus, the complex intensity–exposure behavior exhibited in fig. 3 may be due in part to coverage-dependent beam sharpening effects. We do not believe that conversion from a (2 × 2) to three (2 × 1) overlayer domains [both yielding a (2 × 2) LEED pattern] is occurring as coverage increases, due to the observed invariance of the LEED *I–V* beam profiles over the entire coverage range (fig. 6).

In summary, we propose the following general picture for the intensity–exposure behavior observed for O_2 adsorption on Rh(111):
(1) $\theta \leqslant 0.45$: island growth with net pairwise attractive interactions;
(2) $0.45 \lesssim \theta \lesssim 0.65$: three- or more-body attractive interactions giving accelerated ordering;
(3) $0.65 \lesssim \theta \lesssim 0.90$: net many-body repulsive interactions giving loss of order;
(4) $0.90 \lesssim \theta \lesssim 1$: final filling in of empty sites with optimally ordered overlayer.

It is of interest to note that Madey et al. [23] observed very similar intensity-exposure behavior for O_2 adsorption on Ru(001); at the maximum point in the initial ordering region, a break in the work function-coverage relationship was observed suggesting that two binding sites for adsorbed oxygen may occur at coverages beyond that corresponding to the break point. However, other measurements (thermal desorption, sticking coefficient, and LEED) could not detect the change in binding suggested by the break in the work-function curves.

From the viewpoint of this paper, the final ordering region of fig. 3 is of central importance. We have demonstrated three characteristics of the LEED intensity behavior in this region:

(1) The rate of change of intensity is related to the O_2 adsorption rate, and not to the existence of slow thermal processes.

(2) In a limited part of the final ordering region, the rate of change of intensity is directly proportional to the rate of O_2 adsorption, and hence to the rate of change of oxygen coverage.

(3) Small changes in θ lead to very large changes in the degree of order in this region.

Thus, we have demonstrated that the observation of the intensity of the $(1, \overline{1/2})$ LEED beam is a very sensitive method for studying the kinetic behavior of the almost fully oxygen-covered Rh(111) surface.

4.3. The reaction of $H_2(g)$ and ordered adsorbed oxygen on Rh(111)

Below 275 K, and at a H_2 pressure of 4×10^{-7} Torr, there is no detectable reaction of hydrogen with ordered oxygen (fig. 8). However, the oxygen adsorbate is able to undergo local site-to-site motion at temperatures above ~150 K, as judged by studies of thermal ordering by LEED [9]. We therefore believe that the reaction between H_2 and ordered oxygen above 275 K proceeds via an activated process which does not involve directly the mobility of adsorbed oxygen.

In fig. 11, it is seen that the rate of reaction of H_2 with ordered oxygen is first order in P_{H_2}. This result can be understood by means of a simple kinetic scheme in which the following reactions are involved:

$$H_2(g) + 2* \underset{k_2}{\overset{S_{H_2}}{\rightleftharpoons}} 2\,H(ads)\,, \tag{1}$$

$$H(ads) + O(ads) \underset{k_4}{\overset{k_3}{\rightleftharpoons}} OH(ads) + *\,, \tag{2}$$

$$OH(ads) + H(ads) \underset{k_6}{\overset{k_5}{\rightleftharpoons}} H_2O(g) + 2*\,. \tag{3}$$

We assume in reaction (1) that the sites (*) active for dissociative adsorption of H_2 behave as "trap sites" within the ordered oxygen overlayer, *and that from these sites the back reaction, k_2, is unlikely*. We assume further that reactions k_4 and k_6 are unlikely. Using the steady-state approximation, where the quantities in square brackets are surface concentrations,

$$d[OH]/dt = k_3[H][O] - k_5[OH][H] \simeq 0\,, \tag{4}$$

$$d[H]/dt = 2F_{H_2}S_{H_2} - k_3[H][O] - k_5[OH][H] \simeq 0\,, \tag{5}$$

where F_{H_2} is the incident H_2 flux, and S_{H_2} is the reactive sticking coefficient for H_2 on an ordered oxygen layer.

From eqs. (4) and (5), we obtain the rate of H_2O production, R_{H_2O},

$$R_{H_2O} = k_5 [OH] [H] = F_{H_2} S_{H_2} \,. \qquad (6)$$

According to eq. (6), H_2 adsorption is rate determining for H_2O production, and first-order kinetics in the hydrogen pressure are predicted. R_{H_2O} is dependent on the oxygen coverage only insofar as the sticking coefficient, S_{H_2}, depends on oxygen coverage. The postulate that trap sites within the ordered oxygen overlayer effectively trap and dissociate adsorbing H_2 molecules and prevent the hydrogen recombination step, k_2, suggests that S_{H_2} is proportional to the ordered oxygen coverage.

A schematic view of both a (2 X 2) and a (2 X 1) domain for oxygen adsorbed on Rh(111) is shown in fig. 18, where the oxygen adsorbate atoms, shown with their effective covalent radii, are located arbitrarily in on-top sites on the Rh(111) lattice. For either the (2 X 2) or (2 X 1) case, a number of hydrogen-trap sites are geometrically possible for the small H_2 molecule.

The activation energy for the disappearance of the ordered oxygen layer by reaction with $H_2(g)$ is 5.3 ± 0.3 kcal mole^{-1} (fig. 14). According to eq. (6), the elementary step associated with this activation energy must be the initial adsorption of reactive H_2. The measured activation energy is higher than expected for dissociative adsorption of hydrogen on a *clean* Rh(111) surface where H_2–D_2 isotopic mixing is observed at temperatures as low as ~150 K [14]. Thus, it seems that the "trap sites" envisioned within this ordered oxygen overlayer are not only effective in stabilizing the dissociation fragments from H_2 but also raise the activation energy for the H_2 dissociation above that found for clean Rh(111).

The rate data of fig. 11 permit a calculation of the cross section for the depletion of ordered oxygen by reaction with $H_2(g)$. Let σ_0 be the coverage of the

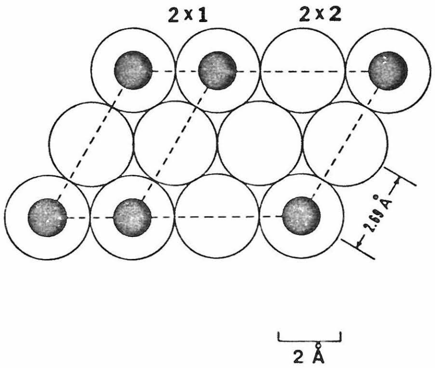

Fig. 18. Schematic view of a (2 X 2) and a (2 X 1) oxygen domain. The location of the oxygen atoms on the Rh(111) substrate has been selected arbitrarily. Either a (2 X 2) or three degenerate (2 X 1) domains could yield the observed (2 X 2) LEED pattern.

ordered oxygen. Then,

$$-d\sigma_0/dt = k_1 F_{H_2} \sigma_0 \,, \tag{7}$$

where k_1 is the rate coefficient for the hydrogen-induced disordering process. From the LEED intensity measurements,

$$-\Delta I/I_0 \Delta t \simeq -d\sigma_0/\sigma_0 \, dt = k_1 F_{H_2} \tag{8}$$

The data of fig. 11 indicate that at 335 K, k_1 is 1.09×10^{-17} cm^2. From the data of fig. 14, E_a is 5.3 kcal mole^{-1} for the process. Thus, we may write

$$k_1 = 1.09 \times 10^{-17} \text{ cm}^2 = A \exp(-E_a/kT) \,, \tag{9}$$

$$A = 3.14 \times 10^{-14} \text{ cm}^2 = 314 \text{ Å}^2 \,. \tag{10}$$

This large value for A means that for every *successful* reaction event an ordered oxygen domain of ~300 Å^2 area is destroyed. The (2 × 2) structure shown in fig. 18 occupies an area of only 25.1 Å^2, so that disordering of ~12 of these domains must occur upon the removal of a single adsorbed oxygen atom by reaction with H_2. This picture is entirely consistent with the conclusion reached from O_2 adsorption studies, that extensive ordering takes place for very small increases in oxygen coverage in the final ordering region (fig. 3).

4.4. Further kinetic studies of the reaction of $H_2(g)$ with adsorbed oxygen on Rh(111)

Kinetic studies of the reaction of $H_2(g)$ with ordered oxygen using LEED have been especially informative regarding the nature of this reaction. However, we know that at temperatures near 335 K, we are dealing with a *mixture* of ordered and disordered adsorbed oxygen on Rh(111) [9]. Therefore, as shown in fig. 15, we have employed Auger spectroscopy to measure the total rate of oxygen depletion during reaction with H_2. It is clear from the data at the top of fig. 15 that the rate of *total* oxygen depletion during reaction exhibits complex behavior, as evidenced, for example, by the induction period seen at lowest hydrogen pressures. Similar induction periods have been observed for the reaction of $H_2(g)$ with adsorbed oxygen on Pt(100), using XPS to monitor the oxygen coverage [24]. We have chosen to use the linear section of these curves to deduce the rate of reaction. As shown in fig. 16 at the lower values of P_{H_2}, approximate *half-order* kinetics in P_{H_2} are observed over a ten-fold range of P_{H_2}. This is in distinct contrast to the accurate *first-order* P_{H_2} kinetics observed for the depletion of *ordered* adsorbed oxygen. A kinetic model to explain this behavior is advanced below. We assume that the reaction of disordered oxygen dominates the overall rate and that a measurement of the kinetics of *total* oxygen removal is, to a good approximation, a measure of the kinetics of depletion of disordered oxygen. For disordered oxygen, the elementary reaction sequence is again given by eqs. (1)–(3). We assume in reaction (1) that the sites ($*$), which are active for dissociative adsorption of H_2, do not behave as trap-sites but instead permit the reverse reaction, k_2, to occur. In addition, reactions k_4 and k_6 are considered to be unlikely just as in the model for the reaction kinetics of ordered oxygen. Using the steady-state approximation,

$$d[OH]/dt = k_3[H][O] - k_5[OH][H] \simeq 0\,, \tag{11}$$

$$d[H]/dt = 2F_{H_2}S_{H_2} - k_2[H]^2 - k_3[H][O] - k_5[OH][H] \simeq 0\,. \tag{12}$$

From these expressions,

$$[OH] = k_3[O]/k_5\,, \tag{13}$$

$$[H] = \frac{-k_3[O]}{k_2} + \frac{1}{2}\left[\frac{4k_3^2[O]^2}{k_2^2} + \frac{8F_{H_2}S_{H_2}}{k_2}\right]^{1/2}. \tag{14}$$

Two limiting cases (a) and (b) exist:

(a) $[8F_{H_2}S_{H_2}/k_2] \gg [4k_3^2[O]^2/k_2^2]$ (high pressure limit).

Then,

$$[H] = (2S_{H_2}/k_2)^{1/2}\,F_{H_2}^{1/2}\,. \tag{15}$$

(b) $[8F_{H_2}S_{H_2}/k_2] \ll [4k_3^2[O]^2/k_2^2]$ (low pressure limit).

Then,

$$[H] = \frac{-k_3[O]}{k_2} + \frac{k_3[O]}{k_2}\left[1 + \frac{2F_{H_2}S_{H_2}k_2}{k_3^2[O]^2}\right]^{1/2} \simeq \frac{F_{H_2}S_{H_2}}{k_3[O]}\,. \tag{16}$$

We obtain for the rate of H_2O production, R_{H_2O},

$$R_{H_2O} = k_5[OH][H] = k_3[O][H]\,. \tag{17}$$

Substituting the value of [H] in the high pressure limit,

$$R_{H_2O} = k_3[O]\left(\frac{2S_{H_2}}{k_2}\right)^{1/2} F_{H_2}^{1/2}\,, \tag{18}$$

and in the low pressure limit

$$R_{H_2O} = F_{H_2}S_{H_2}\,. \tag{19}$$

This treatment predicts that first-order kinetics in P_{H_2} will be obtained at lower pressures while one-half order kinetics will occur at high pressures. We see just the *opposite* behavior experimentally (fig. 16).

A rational explanation for this behavior is that the 10^{-8}–10^{-7} Torr region should be considered a high pressure limit for the reaction of disordered oxygen, and therefore in this range the reaction exhibits half-order kinetics in P_{H_2}. The low pressure region is therefore below our range of observation, i.e., below 10^{-8} Torr hydrogen pressure.

The reason for the conversion to first-order kinetics above ~2×10^{-7} Torr H_2 pressure may lie in the fact that the rate of removal of ordered oxygen is proportional to P_{H_2}, whereas the rate of removal of disordered oxygen is proportional to P_{H_2}. Hence, as P_{H_2} increases, a proportionally greater contribution from the reaction involving ordered oxygen occurs.

It can be shown as follows that our kinetic measurement indicates the coexistence of appreciable amounts of disordered and ordered oxygen at 335 K. Let θ_d denote the fractional coverage of disordered oxygen, and θ_0 denote the fractional coverage of ordered oxygen. Then

$$d\theta_d/dt = -k_d P_{H_2}^{1/2} \theta_d \,, \tag{20}$$

$$d\theta_0/dt = -k_0 P_{H_2} \theta_0 . \tag{21}$$

Below $P_{H_2} = 2 \times 10^{-7}$ Torr, from the data of fig. 16,

$$k_d = 21.5 \text{ sec}^{-1} \text{ Torr}^{-1/2} .$$

Also, from fig. 11,

$$k_0 = 1.48 \times 10^4 \text{ sec}^{-1} \text{ Torr}^{-1} .$$

From eqs. (20) and (21),

$$\frac{d\theta_d/dt}{d\theta_0/dt} = 1.45 \times 10^{-3} \left(\frac{1}{P_{H_2}^{1/2}} \right) \frac{\theta_d}{\theta_0} . \tag{22}$$

If we assume that at the value of P_{H_2} where the kinetics switch from one-half order to first-order in P_{H_2}, the rates of reaction of disordered and ordered oxygen are equal, then we may calculate θ_d/θ_0. Letting $P_{H_2} = 1 \times 10^{-7}$ Torr, the breakpoint, we obtain for the ratio of disordered and ordered oxygen

$$\theta_d/\theta_0 \simeq 0.2 . \tag{23}$$

This calculation, while not to be considered too literally, suggests that significant amounts of both disordered and ordered oxygen coexist on the Rh(111) surface at 335 K, and that the complex kinetics observed in fig. 16 may therefore be due to the differing contribution of the disordered and ordered oxygen to the overall reaction as P_{H_2} is varied.

5. Summary

The following features of the adsorption of O_2 on Rh(111) and its subsequent reaction with H_2 have been determined:

(1) Oxygen adsorbs on Rh(111) following Langmuir kinetics in which single Rh atomic sites are involved in the rate-determining step at 335 K.

(2) Initially, an oxygen island-growth mechanism exists, yielding a (2 × 2) LEED

pattern which may originate from either a (2 X 2) or three (2 X 1) ordered domains. At intermediate O_2 exposures, complex interactional effects produce maxima and minima in the LEED intensity–exposure relationship.

(3) At oxygen coverages near saturation, the addition of small numbers of adsorbate atoms results in massive ordering, suggesting that a close balance of attractive and repulsive forces between adsorbate atoms is made finally net repulsive by the filling in of the last empty sites to yield the best-ordered overlayer.

(4) A significant structural factor exists in the catalytic reaction of adsorbed oxygen and $H_2(g)$ and Rh(111). The kinetics of the reaction of ordered and disordered oxygen are entirely different, with ordered oxygen exhibiting trap sites for adsorbed hydrogen atoms. Reaction of oxygen adatoms with $H_2(g)$ causes extensive disordering of the ordered layer, consistent with observation (3) above.

(5) The activation energy for the reaction of $H_2(g)$ with ordered oxygen is 5.3 kcal mole^{-1} and reflects the activation energy for H_2 adsorption on the oxygen-covered Rh(111).

(6) The Langmuir–Hinshelwood reaction mechanism is operative for the reaction of $H_2(g)$ with adsorbed oxygen on Rh(111) to yield H_2O.

(7) LEED intensity measurements have been shown to be an effective way to monitor the kinetics of a catalytic reaction involving an ordered adsorbate as a reactant.

Acknowledgments

One of us (J.T.Y.) acknowledges partial support of equipment facilities from the Division of Physical Research, Department of Energy. Primary support of this research was derived from the Army Research Office.

References

[1] O. Beeck, Disc. Faraday Soc. 8 (1950) 118.
[2] J.R. Anderson and C. Kemball, Proc. Roy. Soc. (London) A223 (1954) 361.
[3] C. Kemball, Proc. Roy. Soc. (London) A214 (1952) 413.
[4] G.C. Bond, Catalysis by Metals (Academic Press, London, 1962) p. 320.
[5] G.C. Bond, Catalysis by Metals (Academic Press, London, 1962) p. 337.
[6] G.A. Mills and F.W. Steffgen, Catalysis Rev. 8 (1974) 159.
[7] M. Shelef, Catalysis Rev. 11 (1975) 1.
[8] G.C. Bond, Catalysis by Metals (Academic Press, London, 1962) p. 447.
[9] P.A. Thiel, J.T. Yates, Jr. and W.H. Weinberg, Surface Sci. 82 (1979) 22.
[10] C.-M. Chan, P.A. Thiel, J.T. Yates, Jr. and W.H. Weinberg, Surface Sci. 76 (1978) 296.
[11] F.R. Shepherd, P.R. Watson, D.C. Frost and K.A.R. Mitchell, J. Phys. C. 11 (1978) 4591.
F.R. Shepherd, P.R. Watson, D.C. Frost and K.A.R. Mitchell, in: Proc. 7th Intern. Vacuum Congr. and 3rd Intern. Conf. on Solid Surfaces, Vienna, 1977, p. A2725.
[12] D.C. Frost, S. Hengrasmee, K.A.R. Mitchell, F.R. Shepherd and P.R. Watson, Surface Sci. 76 (1978) L585.

[13] K.A.R. Mitchell, F.R. Shepherd, P.R. Watson and D.C. Frost, Surface Sci. 64 (1977) 737.
[14] J.T. Yates, Jr., P.A. Thiel and W.H. Weinberg, Surface Sci. 84 (1979) 427
[15] P.A. Thiel, J.T. Yates, Jr. and W.H. Weinberg, Surface Sci. 90 (1979) 121.
[16] C.A. Sobrero, E.D. Williams & W.H. Weinberg, in preparation.
[17] G. Ertl and J. Küppers, Low Energy Electrons and Surface Chemistry (Verlag Chemie, Weinheim, 1974) pp. 152–155.
[18] D.O. Hayward and B.M.V. Trapnell, Chemisorption (Butterworths, London, 1964) pp. 161–163.
[19] L. Vaska, Accts. Chem. Res. 9 (1976) 175.
[20] A.B.P. Lever and H.B. Gray, Accts. Chem. Res. 11 (1978) 348.
[21] G.A. Ozin and A. Van der Voet, Accts. Chem. Res. 6 (1973) 313.
[22] G. Ertl and J. Küppers Low Energy Electrons and Surface Chemistry (Verlag Chemie, Weinheim, 1974) pp. 216–220.
[23] T.E. Madey, H.A. Engelhardt and D. Menzel, Surface Sci. 48 (1975) 304.
[24] P.R. Norton, R.L. Tapping and J.W. Goodale, J. Vacuum Sci. Technol. 14 (1977) 446; P.R. Norton, J. Catalysis 36 (1975) 211.

Chapter 4

THE CO-ADSORPTION OF OXYGEN AND HYDROGEN ON Rh(111)

Surface Science 90 (1979) 121–132
© North-Holland Publishing Company

THE CO-ADSORPTION OF OXYGEN AND HYDROGEN ON Rh(111) †

P.A. THIEL *, J.T. YATES, Jr. ** and W.H. WEINBERG ***
Division of Chemistry and Chemical Engineering, California Institute of Technology, Pasadena, California 91125, USA

Received 3 January 1979; manuscript received in final form 15 May 1979

The co-adsorption of oxygen and hydrogen on Rh(111) at temperatures below 140 K has been studied by thermal desorption mass spectrometry, Auger electron spectroscopy, and low-energy electron diffraction. The co-adsorption phenomena observed were dependent upon the sequence of adsorption in preparing the co-adsorbed overlayer. It has been found that oxygen extensively blocks sites for subsequent hydrogen adsorption and that the interaction splits the hydrogen thermal desorption into two states. The capacity of the oxygenated Rh(111) surface for hydrogen adsorption is very sensitive to the structure of the oxygen overlayer, with a disordered oxygen layer exhibiting the lowest capacity for hydrogen chemisorption. Studies with hydrogen pre-adsorption indicate that a hydrogen layer suppresses completely the formation of ordered oxygen superstructures as well as O_2 desorption above 800 K. This occurs with only a 20% reduction in total oxygen coverage as measured by Auger spectroscopy.

1. Introduction

It has been shown recently that the properties of a chemisorbed layer of oxygen on Rh(111) are complex, involving activated, irreversible order–disorder transitions of the adsorbed overlayer, as well as activated dissolution of a large fraction of the oxygen into the subsurface region of the crystal [1].

The kinetics of the interaction of hydrogen gas with chemisorbed oxygen on Rh(111) have been studied in detail as well [2]. It has been found that an ordered overlayer of oxygen [(2 × 2) LEED pattern] reacts efficiently above 275 K with hydrogen gas via a kinetic rate law involving P_{H_2} rather than $P_{H_2}^{1/2}$. The activation energy for this reaction is 5.3 kcal/mole. A possible model to explain these kinetics involves the presence of trap-sites for hydrogen within the ordered oxygen overlayer. Because of this unusual phenomenon, we have carried out a thermal desorp-

---

† Supported by the National Science Foundation under Grant No DMR77-14976.

* National Science Foundation Predoctoral Fellow.

** Sherman Fairchild Distinguished Scholar. Permanent Address: National Bureau of Standards, Washington, DC 20234, USA.

*** Camille and Henry Dreyfus Foundation Teacher–Scholar.

tion study of the interaction of chemisorbed hydrogen and oxygen on Rh(111), and the results of this investigation are reported here. In addition to using thermal desorption mass spectrometry, we have employed Auger spectroscopy and LEED as auxilliary tools in this work.

In section 2, a description of the experimental apparatus and procedures is presented. The experimental data are presented and discussed in section 3, and the results are summarized in section 4.

2. Experimental details

The experimental apparatus and cleaning procedures for the Rh(111) crystal have been described in detail elsewhere [1–3]. It should be noted that the experiments described here were performed on two Rh(111) crystals which were heated to different maximum temperatures (1240 and 1565 K) in the course of cleaning. The characteristic features of the Auger spectra from these two clean Rh(111) surfaces were identical, as were the adsorption and desorption properties of pure oxygen and hydrogen. The crystal was exposed to gases while it was being cooled with liquid nitrogen. The temperature of adsorption in all experiments was between 90 and 140 K, unless otherwise specified. All gas exposures are reported in langmuirs, L, where 1 langmuir $\equiv 1 \times 10^{-6}$ Torr s. Gas pressures during adsorption experiments were measured with a Bayard–Alpert ionization gauge, and all exposures reported have been corrected for the sensitivity of the gauge to either hydrogen or oxygen relative to nitrogen.

3. Experimental results

3.1. Hydrogen and oxygen adsorption on clean Rh(111)

The relationship between gas exposure and surface coverage for both oxygen and hydrogen has been reported in detail elsewhere [1,4], and these results are summarized in fig. 1. At 170 K, oxygen adsorbs with a constant sticking coefficient up to about 80% of saturation coverage, as evidenced by the initial linearity of the curve in fig. 1a. In contrast to this, hydrogen chemisorbs via langmuir kinetics, following a $(1 - \theta)^2$ rate law as shown in fig. 1b.

Thermal desorption mass spectrometry has been applied to the study of pure H_2 desorption from Rh(111) [4]. It has been found that in the limit of zero hydrogen coverage, the activation energy for second-order desorption is 18.6 kcal/mole, and the pre-exponential factor of the desorption rate coefficient is 10^{-3} cm^2/s. However, upon increasing the initial hydrogen coverage the thermal desorption peak broadens and shifts to lower temperature yielding, at saturation, an asymmetric main desorption peak and a low temperature shoulder as shown in spec-

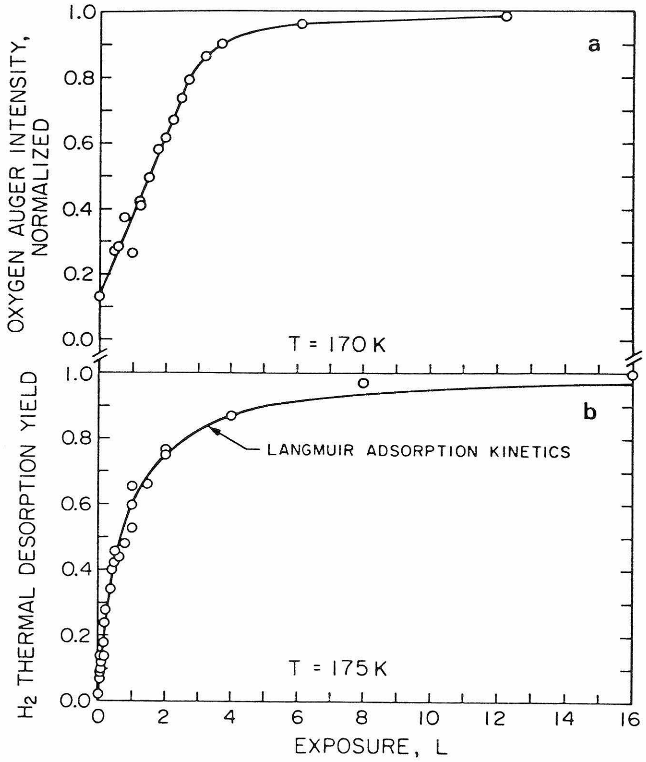

Fig. 1. Relationships between coverage and exposure for oxygen and hydrogen on clean Rh(111). The peak-to-peak amplitudes of the differential 510 eV oxygen Auger transition as a function of O_2 exposure are shown in (a). The linear part of the curve at exposures below 4 L implies a mobile precursor model for the adsorption kinetics. The thermal desorption yield of H_2 is shown as a function of H_2 exposure in (b). The data fit a model for dissociative adsorption in which the lifetime of the precursor is very short or zero [4]. The curve shows the theoretical adsorption kinetics for a model with no mobile precursor.

trum (a) of fig. 2. The coverage-dependent behavior of the main desorption peak is consistent with H_2 desorption via a mobile-precursor intermediate [4,5].

The results presented below are divided into two major sections (3.2 and 3.3) on the basis of the order of chemisorption of oxygen and hydrogen. It has been found that the order of chemisorption is of major importance to subsequent desorption of various products.

3.2. Oxygen adsorption followed by hydrogen adsorption

3.2.1. Thermal desorption of hydrogen

A series of H_2 thermal desorption spectra from Rh(111) pre-covered with vary-

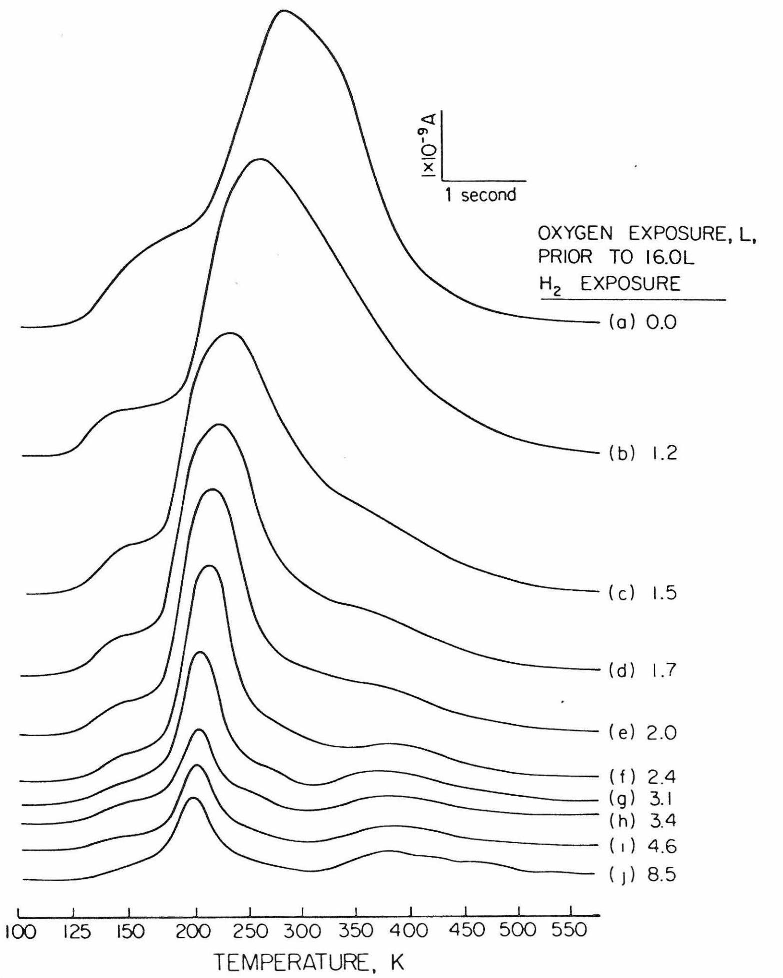

Fig. 2. Thermal desorption spectra for hydrogen from Rh(111) which was pre-exposed to oxygen, as indicated, followed by 16 L of H_2.

ing coverages of oxygen is shown in fig. 2. The Rh crystal was exposed to oxygen at temperatures between 100 and 140 K, under which conditions the oxygen adsorbed as a disordered layer [1]. It can be seen that systematic changes in the nature of the H_2 desorption spectra occur as the pre-exposure to O_2 increases. The heating rate used in these experiments was 44 ± 6 K/s and was linear within the given limits of uncertainty between crystal temperatures of 150 and 550 K. The crystal was heated to 1240 K following each thermal desorption experiment, and the desorption spectrum of hydrogen from the clean Rh(111) surface produced by this thermal cleaning was reproducibly similar to that shown in spectrum (a) of fig. 2. It can be seen

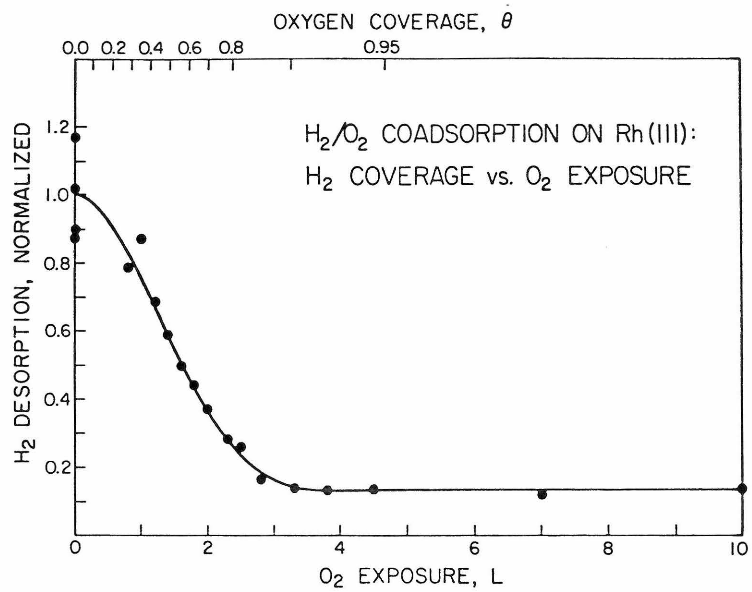

Fig. 3. Thermal desorption yield of hydrogen relative to the amount which desorbs following a 16 L exposure of H_2 on clean Rh(111), as a function of the amount of oxygen pre-adsorbed. These data correspond to the experimental spectra of fig. 2.

that pre-adsorbed oxygen blocks adsorption of hydrogen and causes the hydrogen to desorb in two distinct states at approximately 200 and 380 K. Qualitatively similar behavior has been observed previously for the co-adsorption of oxygen and hydrogen on the (111) surface of W [6].

The relative coverage of hydrogen is shown as a function of oxygen pre-exposure in fig. 3. The fractional oxygen coverage is shown on the upper abscissa. Within experimental error, it can be seen that over most of its range, the saturation hydrogen coverage decreases linearly with increasing oxygen coverage, suggesting that site exclusion by adsorbed oxygen occurs in low temperature co-adsorption.

3.2.2. Influence of annealing of the oxygen layer on subsequent hydrogen chemisorption

Our previous studies of oxygen chemisorption on Rh(111) have shown that major changes occur in the oxygen overlayer upon heating. The initially disordered oxygen begins to order at approximately 150 K; near 300 K, thermally induced disordering takes place, followed by oxygen dissolution above 400 K [1]. These effects are also discernible by means of H_2 co-adsorption experiments as shown in fig. 4. A Rh(111) surface saturated with oxygen was heated to temperatures between 230 and 700 K for 1–2 sec, then recooled and exposed to 16 L H_2. The thermal desorption spectra of hydrogen which resulted from these co-adsorbed over-

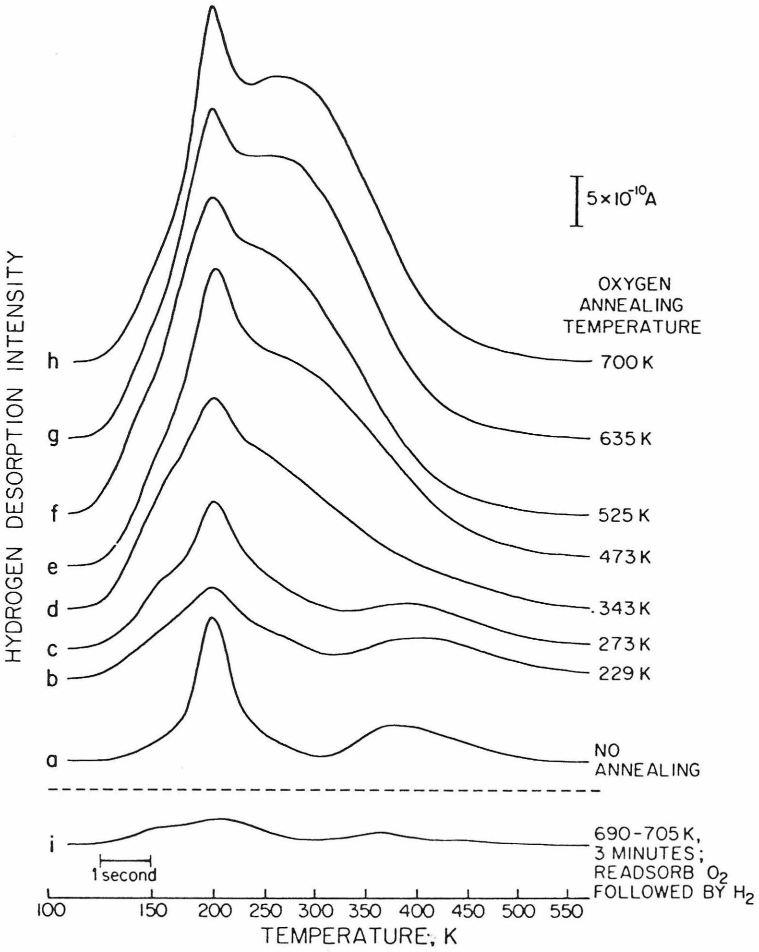

Fig. 4. Thermal desorption spectra of H_2 from an annealed overlayer of oxygen on Rh(111). The Rh(111) surface was saturated with oxygen (12 L), then annealed to the temperature indicated and re-exposed to 16 L of H_2 at $T \leqslant 180$ K in (a) through (h). In spectrum (i) the annealed oxygen-covered surface was re-exposed to 5 L of O_2, followed by 16 L of H_2 at $T \leqslant 180$ K.

layers are shown in fig. 4. It is obvious that the desorption spectrum of H_2 is extremely sensitive to the effects of annealing the oxygen overlayer, even to temperatures as low as 230 K.

The dominant effect seen in fig. 4 is the development of a major hydrogen desorption feature at 280 K. This feature first becomes prominent for oxygen layers annealed above approximately 350 K and therefore may be associated with the onset of oxygen dissolution into Rh [1], freeing additional sites for hydrogen

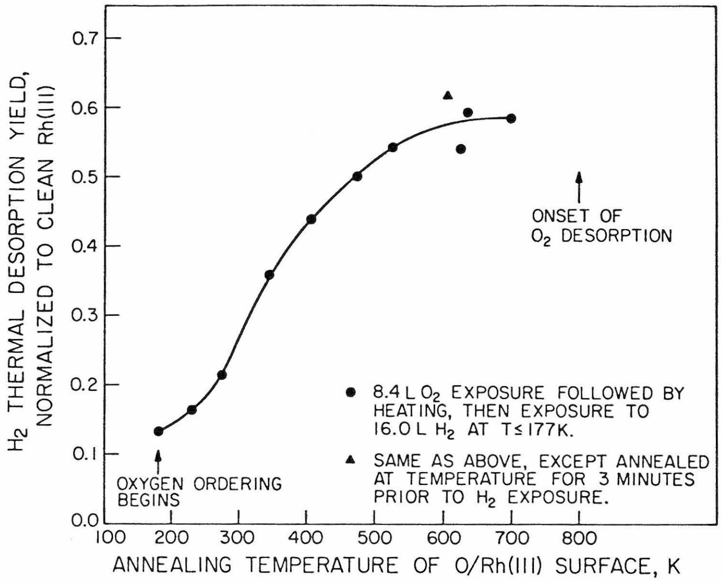

Fig. 5. Amount of hydrogen which thermally desorbs, relative to desorption from clean Rh(111), as a function of the temperature to which a pre-adsorbed overlayer of oxygen is heated. These data correspond to the experimental data of fig. 4.

chemisorption. This effect is seen also in fig. 5 where the saturation coverage of hydrogen is shown as a function of the annealing temperature of the oxygen overlayer. A monotonic increase in hydrogen capacity extends over the temperature region associated with oxygen ordering and also the region associated with oxygen penetration into the bulk. However, at the plateau on this curve, the surface exhibits a decreased capacity (0.6) for hydrogen adsorption compared to clean Rh(111).

It has been demonstrated that an oxygen overlayer on Rh(111) may be depleted by two mechanisms: (1) Solution of oxygen above 400 K, and (2) desorption of oxygen above 800 K [1]. The thermal desorption results in fig. 5 suggest that approximately equal quantities of adsorbed oxygen disappear by means of these two reactions as judged by the capacity of the surface to chemisorb H_2 following completion of each reaction.

3.2.3. Water production

Very small amounts of water were detected by thermal desorption following co-adsorption of hydrogen and oxygen. Following the co-adsorption of hydrogen and oxygen, desorption of water (M = 18 amu) was observed near 295 K upon heating the crystal at a linear rate of 5.9 ± 0.4 K/s. The yield of water as a function of oxygen exposure is shown in fig. 6. The maximum yield of H_2O, at 0.5 L O_2 exposure, represents only 0.1% of the integrated intensity of the H_2 desorption peak result-

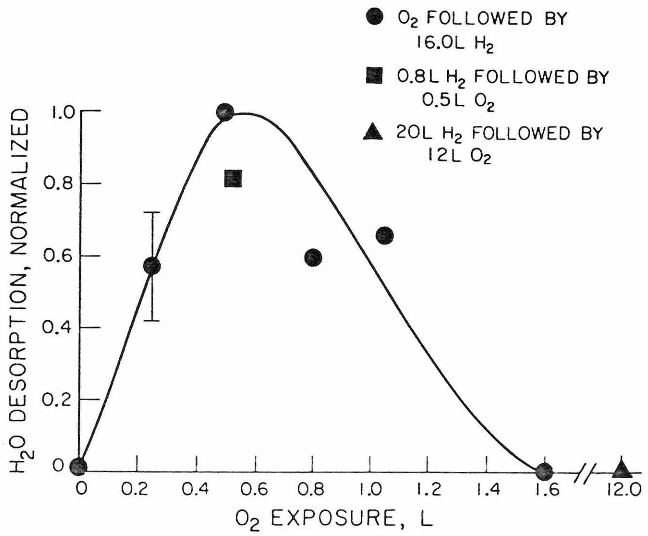

Fig. 6. Production of water from a co-adsorbed overlayer of hydrogen and oxygen on Rh(111) which results from heating the crystal. The maximum rate of H_2O desorption occurred at 295 K.

ing from a 16 L H_2 exposure, corrected for relative mass spectrometer sensitivities and the calculated difference in pumping speed between H_2O and H_2. The yield of H_2O falls to near zero at 1.6 L O_2 exposure. Obviously, the amount of H_2O which was produced as a result of the low temperature co-adsorption of hydrogen and oxygen was very small relative to the major effects illustrated in figs. 2 and 4.

3.2.4. Thermal desorption of oxygen

When a clean Rh(111) surface was exposed to 12 L O_2 followed by 20 L H_2, the desorption spectrum of oxygen was essentially unchanged in peak area and peak shape relative to oxygen desorbing from clean Rh(111) [1]. This co-adsorption sequence is similar to the treatment of the Rh(111) surface prior to the desorption spectrum of H_2 shown in curve (j) of fig. 2, where major changes in the desorption characteristics of H_2 are evident. This result is not surprising since all hydrogen has desorbed prior to O_2 desorption. The results demonstrate again, however, that extensive oxygen depletion (to form water) does not occur in the co-adsorption (transient) experiment. In contrast, the continuous reaction of chemisorbed oxygen with $H_2(g)$ at approximately 10^{-7} Torr leads to extensive oxygen depletion above 280 K in several hundred sec [2].

3.3. Hydrogen adsorption followed by oxygen adsorption

3.3.1. Thermal desorption of oxygen

Pre-adsorption of hydrogen on Rh(111) did not prevent the subsequent adsorp-

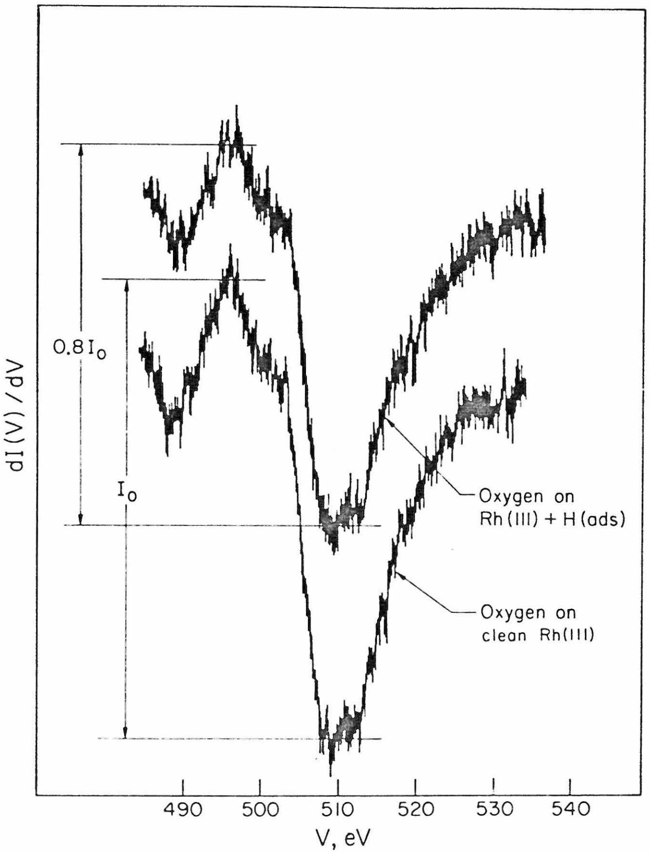

Fig. 7. Differential Auger spectra following a 12 L exposure of O_2 to clean and hydrogen-covered (20 L exposure of H_2) Rh(111). The peak-to-peak amplitude of the 510 eV oxygen transition on the hydrogen-saturated surface is 80% as intense as the transition on the clean surface. The magnitudes of the two spectra shown are normalized to the 303 eV Rh transition.

tion of oxygen, as demonstrated in fig. 7 by the peak-to-peak amplitude of the oxygen 510 eV differential Auger transition relative to the major 303 eV Rh transition. The Auger data were measured on a Rh(111) surface which was saturated with hydrogen (20 L) and then exposed to an amount of oxygen which would saturate the clean surface (12 L). At saturation, 80% as much oxygen is adsorbed on the hydrogen-covered surface as on the clean Rh(111) surface.

The amount of oxygen which desorbed upon heating was quite sensitive to pretreatment of the Rh(111) surface with hydrogen, however. In a series of experiments, the Rh(111) crystal was treated with a range of H_2 exposures, then exposed to 12 L of O_2. The results of the thermal desorption of oxygen from these surfaces are shown in fig. 8, where the oxygen desorption peak areas are displayed as a func-

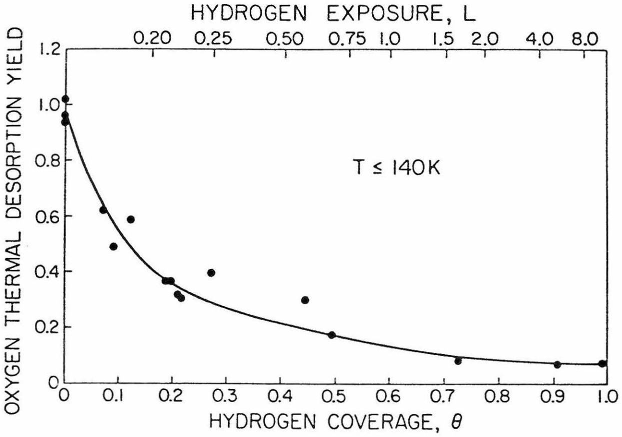

Fig. 8. Amount of oxygen which thermally desorbs following a 12 L exposure of O_2 as a function of the amount of hydrogen which is pre-adsorbed. The values for the oxygen thermal desorption yield are shown relative to O_2 desorption from clean Rh(111) following the same oxygen exposure.

tion of the preadsorbed hydrogen coverage. In the limit of saturation of the surface with hydrogen, the desorption yield of oxygen drops to 7% of its value on the clean Rh(111) surface. No evolution of water was observed during thermal desorption from these co-adsorbed overlayers, as shown by the triangular datum point of fig. 6.

3.3.2. Observation of ordered oxygen LEED patterns

Oxygen adsorbed on clean Rh(111) at 100 K causes formation of a sharp (2 X 2) LEED pattern when the crystal is heated above 150 K, as has been described in detail elsewhere [1]. Similar experiments were performed to determine whether the ordering behavior of oxygen is modified on a Rh(111) surface pre-exposed to H_2, as follows: the clean Rh crystal was exposed to 20 L of H_2 and then to 12 L of O_2. The crystal was heated sequentially to various temperatures up to 700 K, and recooled to at least 125 K after each heating cycle. The LEED pattern was examined each time after the crystal had recooled, both visually and with a Faraday cup positioned appropriately. *No evidence for formation of the ordered oxygen (2 X 2) lattice was found at any temperature* when a pre-exposure to hydrogen was carried out, even after the hydrogen had been desorbed from the surface.

3.3.3. Thermal desorption of hydrogen

Thermal desorption of hydrogen from a Rh(111) surface treated as described above caused small changes in peak shape [spectra were similar to curve (b) of fig. 2] and a 10–30% attenuation of the 2 amu desorption peak area, relative to desorption from clean Rh(111). This may be due either to displacement of hydrogen or production of water during the oxygen exposure. The temperature at which the maximum rate of desorption occurred was unchanged to within ±15 K.

4. Summary

Several features of the oxygen-hydrogen interaction on Rh(111) are prominent in the experiments reported here. It has been found that the order of addition of hydrogen and oxygen to Rh(111) profoundly affects subsequent thermal behavior of the mixed adsorbate system.

4.1. Oxygen adsorption followed by hydrogen adsorption

(1) Oxygen blocks sites extensively for subsequent H_2 chemisorption. The hydrogen which does chemisorb is split into two states, one of which desorbs at slightly higher temperatures than observed for pure hydrogen. A site exclusion mechanism, induced by oxygen chemisorption, is indicated by comparison of coverages of the two adsorbates.

(2) It has been shown that the capacity for hydrogen adsorption on oxygen-covered Rh(111) is very sensitive to the structure of the oxygen overlayer. A disordered oxygen overlayer exhibits the lowest capacity for H_2 chemisorption, whereas oxygen ordering by annealing leads to enhanced hydrogen capacity. Partial penetration of oxygen into the bulk above 400 K leads to further enhancement of the capacity of the surface to adsorb hydrogen.

(3) Interactional effects between the co-adsorbed species are not due to the reaction of hydrogen and oxygen to form H_2O since the yield of H_2O is very small compared to the mutual effect of the co-adsorbed adatoms on each other.

4.2. Hydrogen adsorption followed by oxygen adsorption

(1) The various thermally induced processes observed for pure oxygen overlayers on Rh(111) are significantly influenced by the pre-adsorption of hydrogen.

(a) Pre-adsorbed hydrogen prevents completely the ordering of oxygen which is subsequently adsorbed.

(b) The maximum coverage of oxygen on a saturated overlayer of hydrogen is reduced only by approximately 20%, and co-adsorption in this manner reduces the coverage of hydrogen by only 10–30%.

(c) Desorption of molecular oxygen above 800 K is suppressed extensively by hydrogen pre-adsorption.

These results are consistent with a model in which only a part of the total adsorbed oxygen can thermally desorb, a large fraction penetrating into the bulk of the Rh crystal [1].

Acknowledgement

We are grateful for primary support of this work by the National Science Foundation (Grant No. DMR77-14976). One of us (J.T.Y.) acknowledges partial support from the Department of Energy, Division of Basic Energy Sciences.

References

[1] P.A. Thiel, J.T. Yates, Jr. and W.H. Weinberg, Surface Sci. 82 (1979) 22.
[2] J.T. Yates, Jr., P.A. Thiel and W.H. Weinberg, Surface Sci. 82 (1979) 45.
[3] C.-M. Chan, P.A. Thiel, J.T. Yates, Jr. and W.H. Weinberg, Surface Sci. 76 (1978) 296.
[4] J.T. Yates, Jr., P.A. Thiel and W.H. Weinberg, Surface Sci. 84 (1979) 427.
[5] R. Gorte and L.D. Schmidt, Surface Sci. 76 (1978) 559.
[6] T.E. Madey, Surface Sci. 29 (1972) 571.

Chapter 5

THE CHEMISORPTION OF CO ON Rh(111)

Surface Science 84 (1979) 54–64
© North-Holland Publishing Company

THE CHEMISORPTION OF CO ON Rh(111) *

P.A. THIEL **, E.D. WILLIAMS **, J.T. YATES, Jr. *** and W.H. WEINBERG ‡
Division of Chemistry and Chemical Engineering, California Institute of Technology, Pasadena, California 91125, USA

Received 5 January 1979; manuscript received in final form 4 February 1979

The adsorption of CO on Rh(111) has been studied by thermal desorption mass spectrometry and low-energy electron diffraction (LEED). At temperatures below 180 K, CO adsorbs via a mobile precursor mechanism with sticking coefficient near unity. The activation energy for first-order CO desorption is 31.6 kcal/mole ($\nu_d = 10^{13.6}$ s^{-1}) in the limit of zero coverage. As CO coverage increases, a $(\sqrt{3} \times \sqrt{3})R30°$ overlayer is produced and then destroyed with subsequent formation of an overlayer yielding a (2 × 2) LEED pattern in the full coverage limit. These LEED observations allow the absolute assignment of the full CO coverage as 0.75 CO molecules per surface Rh atom. The limiting LEED behavior suggests that at full CO coverage two CO binding states are present together.

1. Introduction

The adsorption of CO on the hexagonally close-packed surfaces of the Group VIII transition metals appears to follow a general pattern [1–12] which may be characterized as follows: (1) The CO is associatively adsorbed, and the energy of adsorption is between 27 and 35 kcal/mole. (2) The CO forms ordered hexagonal arrays which are highly symmetrical with respect to the substrate and which compress continuously as coverage increases. (3) A second low-temperature desorption peak or shoulder appears in the thermal desorption spectra at high CO coverages, although there is some disagreement concerning the existence of a second peak on Pt(111) [10–12]. This desorption behavior may be attributed partly to repulsive adsorbate–adsorbate interactions and partly to the population of lower energy binding sites at high coverage, but the origin of multiple CO desorption states on

---

* Supported by the Army Research Office (Durham) under Grant No. DAHC04-75-0170.

** National Science Foundation Predoctoral Fellow.

*** Sherman Fairchild Distinguished Scholar. Permanent address: National Bureau of Standards, Washington, DC 20234, USA.

‡ Camille and Henry Dreyfus Foundation Teacher–Scholar, and Alfred P. Sloan Foundation Fellow.

Table 1
LEED structures for saturation CO coverages on some Group VIII transition metal surfaces of hexagonal symmetry

Surface	Reference	T (K)	Saturation LEED structure	CO–CO spacing (Å)	θ = CO/Rh
Ni(111)	[1]	200	$(\frac{1}{2}\sqrt{7} \times \frac{1}{2}\sqrt{7})$ R19.1°, compressed c(4 × 2)	3.3	0.57
Ru(001)	[4]	110	$(5\sqrt{3} \times 5\sqrt{3})$ R30°, compressed $(2\sqrt{3} \times 2\sqrt{3})$ R30°	3.35	0.65
Rh(111)	This work	<125	(2 × 2)	3.11	0.75
Pd(111)	[7]	200	Compressed c(4 × 2)	3.16 ± 0.03	0.63 ± 0.01
Ir(111)	[8]	~300	$(2\sqrt{3} \times 2\sqrt{3})$ R30°	3.55	0.58
Pt(111)	[10]	170	Compressed c(4 × 2)	~3.4	~0.68

these metals is not understood completely. This general pattern has been observed for adsorption of CO on Ni(111) [1,2], Ru(001) [3,4], Rh(111) [5,6], Pd(111) [7], Ir(111) [8,9] and Pt(111) [10–12]. A summary of LEED results is given in table 1. All of these metal surfaces are distinguished by the formation of hexagonal lattices at high coverage and low temperature, and in many cases the CO molecules may be in low-symmetry binding sites, i.e., the registry of the overlayer with respect to the substrate is not preserved. At high CO coverages on Pt(111), Norton et al. [13] have observed distinct O(1s) and C(1s) features in the X-ray photoelectron spectrum which they attribute to two distinct forms of bound CO at saturation coverage. Furthermore, on Ni(111) [14,15], Pt(111) [16,17] and Pd(111) [18], two CO stretching frequencies are observed at saturation coverage, suggesting that two forms of CO binding may exist.

The adsorption of CO on the Rh(100) [6] and Rh(110) [19] surfaces, and on polycrystalline Rh surfaces [20] has also been studied. In the present paper, we report a more thorough study of the adsorption of CO on Rh(111) than has been reported previously, using low-energy electron diffraction (LEED) and thermal desorption mass spectrometry. The adsorption of CO on Rh(111) follows the general pattern outlined above, but with subtle distinctions which are discussed below.

In section 2, the experimental apparatus is described. In section 3, the experimental data are presented and discussed, and the results are summarized in section 4.

2. Experimental details

The experimental apparatus and the procedures used in cleaning the Rh(111) crystal have been described elsewhere [21,22]. It should be noted that the experiments described here were performed on two separate Rh(111) crystals which were heated to different maximum temperatures (1240 and 1565 K) in the course of cleaning. The characteristic features of the Auger spectra from these two clean Rh(111) surfaces were identical, as were the adsorption and desorption properties of pure H_2 and CO.

The base pressure, following bakeout, was $<1 \times 10^{-10}$ Torr. The system was equipped with a four-grid post-acceleration display LEED apparatus containing a movable Faraday cup for LEED intensity measurements. The Faraday cup aperture subtended an angle of 4.6×10^{-3} steradians.

All gas exposures are reported in langmuir (1 langmuir ≡ 1 L ≡ 1×10^{-6} Torr s), corrected for the sensitivity of the Bayard–Alpert ionization gauge to CO relative to N_2. Research grade CO from Matheson was used in all experiments. The pumping speed of the system for CO was measured to be 980 *l*/s, assuming a system volume of 50 *l*.

3. Experimental results and discussion

3.1. Thermal desorption of CO

Representative thermal desorption spectra for carbon monoxide on the clean Rh(111) surface are shown in fig. 1. The crystal was exposed to CO at $T \leqslant 180$ K and was heated to 635 K at a linear rate of 5.7 ± 0.6 K/s during each flash, while monitoring the intensity of the $M = 28$ amu peak mass spectrometrically. These spectra show a single desorption peak, with the peak temperature decreasing from 490 K at low coverage to 470 K at high coverage. A low temperature shoulder develops at $\theta/\theta_{max} \geqslant 0.5$, where θ/θ_{max} is the relative coverage. The coverage data

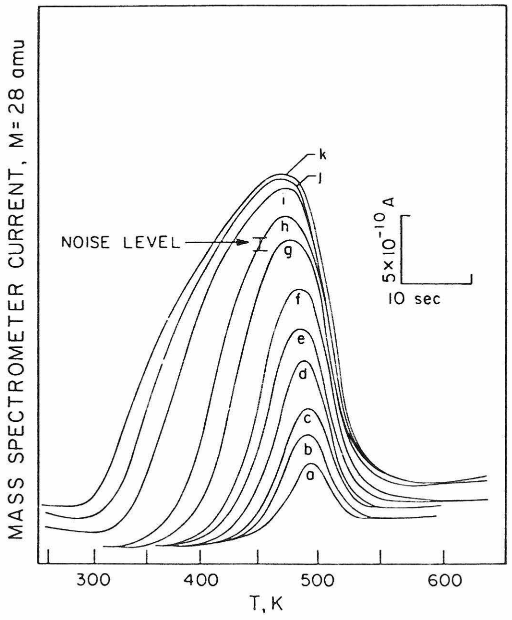

Fig. 1. Thermal desorption spectra of CO on Rh(111) at $T_{ads} \leqslant 180$ K, heating rate = 5.7 ± 0.6 K/s. The spectra shown correspond to the following exposures and coverages:

Spectrum	Exposure (L)	Coverage, θ/θ_{max}	Spectrum	Exposure (L)	Coverage, θ/θ_{max}
a	0.19	0.05	g	1.4	0.49
b	0.29	0.09	h	1.9	0.63
c	0.38	0.12	i	2.9	0.83
d	0.57	0.20	j	3.8	0.87
e	0.76	0.25	k	9.5	0.94
f	1.0	0.34			

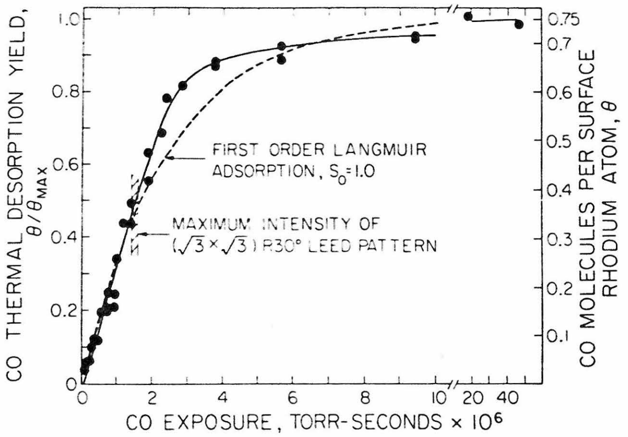

Fig. 2. CO coverage as a function of exposure, $T_{ads} \leqslant 180$ K. For values of $\theta/\theta_{max} \leqslant 0.75$, the solid line is a linear least-squares fit to the data. Above $\theta/\theta_{max} = 0.75$, the solid line is an empirical fit to the data.

as a function of exposure shown in fig. 2 were obtained by integration of the desorption peaks represented in fig. 1, where baselines of the desorption spectra were taken as empirically determined straight lines. The number of adsorbed CO molecules per surface Rh atom, θ, shown as the right-hand ordinate in fig. 2, is based on LEED data to be discussed later.

The relationship between coverage and exposure of fig. 2 is linear up to $\theta/\theta_{max} = 0.75$, implying that adsorption occurs via a mobile precursor. For values of $\theta/\theta_{max} \leqslant 0.7$, the data is fit best by a straight line with $S_0 = 0.76 \pm 0.04$. A comparison to a Langmuir adsorption model with $S_0 = 1$ is shown by the dashed line. It may be seen that below $\theta/\theta_{max} \simeq 0.5$, the two models are indistinguishable. However, the full range of the data favors clearly the mobile precursor model of adsorption.

On the assumption that desorption of CO from Rh(111) follows first-order kinetics, the activation energy and pre-exponential factor of the desorption rate coefficient were calculated for each desorption spectrum in the range $\theta/\theta_{max} \leqslant 0.25$. The method of analysis involves measuring the peak width and the temperature at which the maximum rate of desorption occurs [23]. The results are shown in fig. 3, where the straight lines represent empirical least-squares fits to the data. In the limit of zero coverage, the activation energy of desorption, E_d, is 31.6 ± 1 kcal/mole, and the pre-exponential factor, ν_d, is $10^{13.6\pm0.3}$ s^{-1}. The stated uncertainties in the values of the kinetic parameters at $\theta = 0$ are based upon statistical analyses of the scatter in the data relative to the linear least-squares fits of fig. 3.

Both these adsorption parameters are reasonable for first-order desorption and are comparable to values reported for CO adsorbed on other Group VIII metal surfaces [1–12]. In particular, the value of E_d is identical within experimental error to

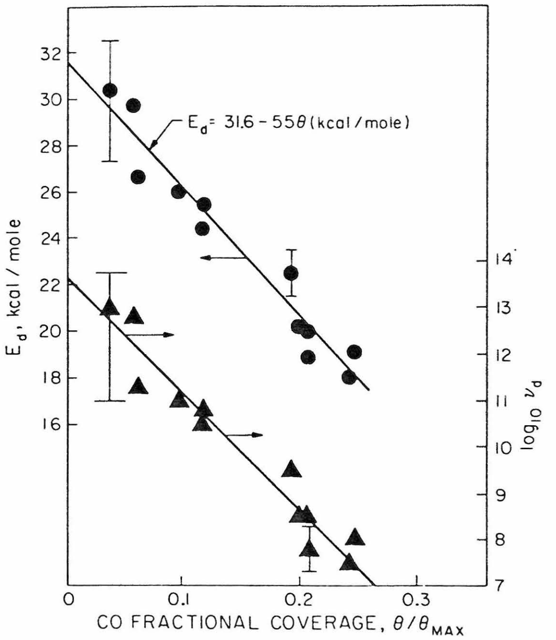

Fig. 3. Energy of activation and pre-exponential factor for desorption rate coefficient of CO from Rh(111) at low coverages. The lines are linear least-squares fits to the experimental data. In the limit of zero coverage, $E_d = 31.6 \pm 1$ kcal/mole, $T \leqslant 180$ K, and $\nu_d = 10^{13.6 \pm 0.3}$ s^{-1}. The error bars shown were estimated from the experimental uncertainty in determining the peak half-width and the peak temperatures.

that reported for low coverages of CO on Rh(110), 31 kcal/mole [19], and also to that reported for CO adsorption on polycrystalline Rh, 32 kcal/mole [20]. Both of the latter values of E_d were calculated with the assumption that $\nu_d = 10^{13}$ s^{-1}.

It should be noted that the rapid drop in E_d, given by $E_d = 31.6 - 55\theta$ kcal/mole from the linear regression analysis, cannot be explained in terms of repulsive dipole–dipole interactions at higher coverages, which would only contribute approximately -2θ kcal/mole to the drop in E_d with increasing coverage [24,25]. For $\theta > 0$, the desorption parameters of fig. 3 have no straightforward physical meaning, and may be due to overlap of the two unresolved desorption features at low coverage which become more evident at higher coverages. However, the construction in fig. 3 is useful in estimating limiting kinetic parameters at zero coverage; and it may be used empirically even at high coverages.

3.2. LEED data

A progression of LEED patterns due to the formation of ordered CO overlayers was observed with increasing CO coverage on Rh(111) at $T \leqslant 125$ K. At low expo-

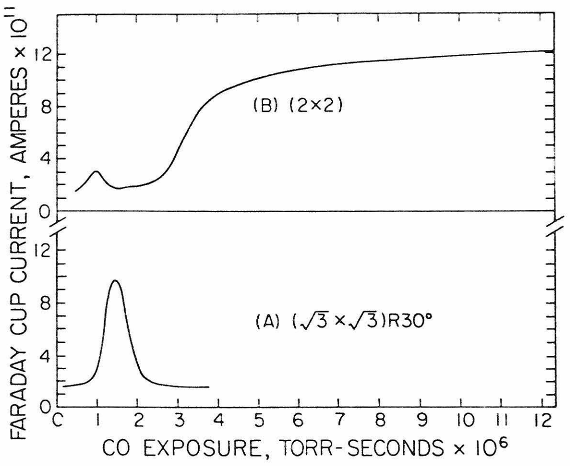

Fig. 4. Intensity of CO LEED patterns as a function of CO exposure at $T \leqslant 125$ K. (A) ($\sqrt{3} \times \sqrt{3}$)R30° pattern, $I_e = 0.1$ μA, $V_e = 27$ eV. (B) (2 × 2) pattern; $I_e = 0.1$ μA, $V_e = 24$ eV.

sures to CO, a diffuse ring forms inside the Rh beams and then sharpens into a ($\sqrt{3} \times \sqrt{3}$)R30° pattern. As the exposure is increased, the ($\sqrt{3} \times \sqrt{3}$)R30° spots blur, and then a split (2 × 2) pattern appears and becomes sharp. Further exposure to CO causes the split spots to coalesce into the half-order beams of a (2 × 2) pattern which gradually increase in intensity as saturation is approached.

In figs. 4A and 4B are shown the intensities of the ($\sqrt{3} \times \sqrt{3}$)R30° and (2 × 2) LEED beams as functions of exposure to a constant background pressure of CO. These spectra were recorded by positioning the LEED Faraday cup appropriately and monitoring the cup current during the exposure. The incident electron beam was defocused, and a beam current, I_e, of 0.1 μA was used to obviate electron beam damage. Incident beam voltages, V_e, of 27 and 24 eV were used in the experiments of figs. 4A and 4B, respectively. The shape of the curve of fig. 4A and the position of the peak maximum were invariant, within experimental error, over a three-fold range of CO background pressures (3×10^{-9} to 10×10^{-9} Torr). Further, the formation of both these patterns was independent of whether the electron beam was on during the exposure. For example, in one experiment the electron beam was turned off after 2.7 L CO exposure and turned on again after 3.8 L CO exposure, while recording an intensity-exposure curve for the (2 × 2) pattern as shown in fig. 4B. In the absence of the incident electron beam, the intensity of the half-order beam had risen to the same value as in fig. 4B at 3.8 L exposure, where the intensity was monitored continuously with the beam on. This indicates that in our experiments, the formation of the (2 × 2) ordered CO overlayer on Rh(111) does not result from electron beam damage during the exposure, as has been reported for formation of the (2 × 2) CO structure on the hexagonal Ru(001) surface [3].

As can be seen in fig. 4A, the $(\sqrt{3} \times \sqrt{3})R30^\circ$ pattern reaches its maximum intensity at an exposure of 1.5 L of CO. The optimum absolute coverage for a $(\sqrt{3} \times \sqrt{3})R30^\circ$ structure with one admolecule per unit cell is $\theta = 1/3$. This is in good agreement with the results of the thermal desorption experiments shown in fig. 2, relative to the absolute coverage at saturation.

The intensity-exposure curve for the (2×2) pattern (fig. 4B) exhibits a small peak at an exposure of 1 L, well before the growth in intensity due to the formation of the final (2×2) structure. There are two reasonable possibilities for the source of this peak. First, the initial diffuse intensity of the $(\sqrt{3} \times \sqrt{3})R30^\circ$ pattern may spread as far as the position of the (2×2) beam (a defocused incident electron beam was used for these measurements), causing a spurious increase in intensity at the (2×2) beam position. Second, a very faint, true (2×2) pattern, corresponding to a coverage of $\theta = 1/4$, may form prior to the $(\sqrt{3} \times \sqrt{3})R30^\circ$ pattern. If this second possibility is the correct one, it would be worthy of further study as a source of information about the nature of the CO–CO interaction.

As noted previously [6], the continuous convergence of the split (2×2) beams with increasing coverage indicates that the CO molecules form a hexagonal structure with its unit cell rotated 30° from the Rh unit cell. The splitting of the (2×2) spots results from the continuous contraction of the size of the CO unit cell as coverage increases. The usual alternative analysis of a (2×2) LEED pattern as due to three domains of a (2×1) structure thus is precluded in this case. At saturation coverage, the CO unit cell is a $(\frac{2}{3}\sqrt{3} \times \frac{2}{3}\sqrt{3})R30^\circ$ structure with one atom per unit cell, which is equivalent to a (2×2) structure with three atoms per unit cell. This structure has a optimum coverage of $\theta = 3/4$. This fact has been used to correlate the relative coverages determined from thermal desorption with absolute coverages as shown in fig. 2. Of course, the coverage determined from the LEED pattern corresponds to that of a perfectly ordered overlayer on a perfect surface. Application of this value to a real system will be uncertain to the extent that adsorption on surface defects and local disorder (as at domain boundaries) are important.

If the CO molecules occupy distinct binding sites on the Rh surface, the saturation (2×2) structure would have high symmetry. Two possible (2×2) structures for CO on Rh(111) are shown in fig. 5. In the structure of fig. 5A, two molecules per unit cell are in three-fold sites and one is in an on-top site [6]. A structure with one CO molecule per unit cell in a bridged site and two in positions slightly displaced from three-fold sites is also possible, as shown in fig. 5B. No à priori determination of the correct CO overlayer structure can be made on the basis of these LEED results. However, it is possible to postulate structures, as shown in fig. 5, that involve CO in two distinct adsorption sites which should be detectable by various surface spectroscopies.

A comparison of the LEED and spectroscopic data for CO on Rh(111), Pt(111) and Ru(001) is of interest. Both on Pt(111) [10] and Rh(111), the CO overlayer at saturation is in registry with the substrate, whereas this is not the case, for example, for CO on Ru(001) [4]. On Pt(111), two distinct CO stretching modes have been

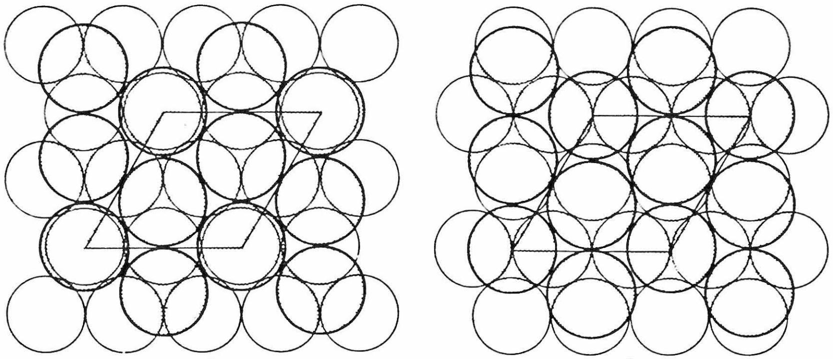

Fig. 5. Two possible orientations of the (2 × 2) CO overlayer with respect to the rhodium substrate. The diameter of the Rh atoms, shown as open circles, is 2.69 Å. The diameter of the CO molecules, shown as shaded circles, is arbitrarily shown as their nearest neighbor distance of 3.11 Å. (A) One-third of the CO molecules are in on-top sites, two-thirds in three-fold sites. (B) One-third of the CO molecules are in bridge sites, two-thirds in low-symmetry sites.

observed [16], whereas on Ru(001) only a single mode has been observed which shifts to higher frequency with increasing coverage [26,27]. Based on the LEED results, CO on Rh(111) should be more similar to CO on Pt(111) than CO on Ru(001) insofar as its surface vibrational structure is concerned. The spectroscopic data which suggest the existence of two discrete states on Pt(111) [13, 16, 17] imply that two states may be found on Rh(111) also, consistent with the saturation structures postulated in fig. 5.

The formation of a highly symmetrical CO overlayer at saturation coverages on Rh(111) indicates that the CO–Rh interaction is stronger, relative to the CO–CO repulsion on Rh, than the CO–Ru interaction is, relative to the CO–CO repulsion on Ru, where "coincidence lattices" are formed at saturation. This is consistent with the observation that the absolute coverage at saturation, θ, is 0.75 on Rh and is 0.65 on Ru at low temperature. These coverages correspond to CO–CO spacings of 3.11 Å on Rh and 3.35 Å on Ru at saturation. The minimum CO–CO distance observed on Rh(111) is somewhat smaller than observed on the hexagonal surfaces of other metals [1–10], but in good agreement with the value of 3.17 Å for CO on Rh(100) at room temperature [6]. The CO–Rh interaction is strong enough to cause formation of CO lattices which are more closely packed at saturation than on Ru(001) and in which the CO molecules are located in highly symmetrical adsorption sites. The balance between substrate–adsorbate attraction and adsorbate–adsorbate repulsion on Rh(111) is thus in subtle contrast to the balance of these interactions on the structurally similar Ru(001) surface.

4. Summary

The major conclusions of our work may be summarized as follows:
(1) CO adsorbs on Rh(111) at $T \leqslant 180$ K via a mobile precursor state with a sticking coefficient near unity.
(2) Thermal desorption mass spectrometry has been used to measure, in the limit of zero coverage, $E_d = 31.6$ kcal/mole and $\nu_d = 10^{13.6}$ s^{-1} with first-order desorption kinetics.
(3) As CO coverage is increased, a $(\sqrt{3} \times \sqrt{3})R30^\circ$ LEED pattern is produced and reaches a maximum intensity at the optimal coverage of one CO molecule per three Rh atoms.
(4) Beyond $\theta = 1/3$, the $(\sqrt{3} \times \sqrt{3})R30^\circ$ LEED pattern converts to a split (2×2) pattern which in the saturation limit develops into a (2×2) pattern corresponding to 0.75 CO molecules per Rh atom.
(5) The surface structures corresponding to the (2×2) overlayer may involve two CO binding states having different site conformations.

Acknowledgment

Major support of this research was derived from the Army Research Office under Grant No. DAHC04-75-0170. Additional support was made available by the National Science Foundation (P.A.T. and E.D.W.), and the Alfred P. Sloan and Camille and Henry Dreyfus Foundations (W.H.W.). One of us (J.T.Y.) acknowledges partial support of equipment facilities from the Department of Energy, Division of Basic Energy Science.

Note added in proof

We have shown recently that the maximum in the diffracted beam intensity at 1 L in fig. 4B is due to a $p(2 \times 2)$ superstructure corresponding to a fractional coverage of CO of 0.25.

References

[1] H. Conrad, G. Ertl, J. Küppers and E.E. Latta, Surface Sci. 57 (1976) 475.
[2] K. Christmann, O. Schober and G. Ertl, J. Chem. Phys. 60 (1974) 4719.
[3] T.E. Madey and D. Menzel, Proc. 2nd Intern. Conf. on Solid Surfaces, Japan. J. Appl. Phys. Suppl. 2, Pt. 2 (1974) 229.
[4] E.D. Williams and W.H. Weinberg, Surface Sci. 82 (1979) 93.
[5] J.T. Grant and T.W. Haas, Surface Sci. 21 (1970) 76.
[6] D.G. Castner, B.A. Sexton and G.A. Somorjai, Surface Sci. 71 (1978) 519.

[7] G. Ertl and J. Koch, Z. Naturforsch. 25a (1970) 1306;
H. Conrad, G. Ertl, J. Koch and E.E. Latta, Surface Sci. 43 (1974) 462.
[8] C.M. Comrie and W.H. Weinberg, J. Chem. Phys. 64 (1976) 250.
[9] J. Küppers and A. Plagge, J. Vacuum Sci. Technol. 13 (1976) 259.
[10] G. Ertl, M. Neumann and K.M. Streit, Surface Sci. 64 (1977) 393.
[11] R.W. McCabe and L.D. Schmidt, Surface Sci. 65 (1977) 189.
[12] R.W. McCabe and L.D. Schmidt, Surface Sci. 66 (1977) 101.
[13] P.R. Norton, E.B. Selkirk and J.W. Goodale, J. Vacuum Sci. Technol, 16 (1979) 457.
[14] J.C. Bertolini, G. Dalmai-Imelik and J. Rousseau, Surface Sci. 68 (1977) 539.
[15] W. Erley, H. Ibach and H. Wagner, Ned. Tijdschr. Vacuümtech. 16e (1978) 154.
[16] H. Froitzheim, H. Hopster, H. Ibach and S. Lehwald, Appl. Phys. 13 (1977) 147.
[17] H.J. Krebs and H. Lüth, Appl. Phys. 14 (1977) 337.
[18] A.M. Bradshaw and F.M. Hoffman, Surface Sci. 72 (1978) 513.
[19] R.A. Marbrow and R.M. Lambert, Surface Sci. 67 (1977) 489.
[20] C.T. Campbell and J.M. White, J. Catalysis 54 (1978) 289.
[21] C.-M. Chan, P.A. Thiel, J.T. Yates, Jr. and W.H. Weinberg, Surface Sci. 76 (1978) 296.
[22] J.T. Yates, Jr., P.A. Thiel and W.H. Weinberg, Surface Sci. 82 (1979) 45.
[23] C.-M. Chan, R. Aris and W.H. Weinberg, Appl. Surface Sci. 1 (1978) 360.
[24] D.H. Everett, Proc. Chem. Soc. 38 (1957) 38.
[25] E.D. Williams, S.L. Cunningham and W.H. Weinberg, J. Chem. Phys. 68 (1978) 4688.
[26] G.E. Thomas and W.H. Weinberg, Ned. Tijdschr. Vacuümtech. 16e (1978) 57.
[27] G.E. Thomas and W.H. Weinberg, J. Chem. Phys. 70 (1979) 1437.

Chapter 6

THE ADSORPTION OF NITRIC OXIDE ON Ru(001)

[*This chapter was published as a paper by P. A. Thiel, W. H. Weinberg and J. T. Yates, Jr. in* Chemical Physics Letters *67 (1979) 403.*]

Abstract

The influence of chemisorbed nitrogen and oxygen atoms on the subsequent adsorption of NO on Ru(001) at 150 K has been investigated by high resolution electron energy loss spectroscopy. The presence of the NO dissociation products can block adsorption of one of the two states of molecular NO which are populated on the clean Ru surface.

1. Introduction

The adsorption of nitric oxide on the Group VIII transition metals is a complex phenomenon, partly because molecular NO and its dissociation products can be adsorbed simultaneously on a given surface. For example, ultraviolet photoemission spectroscopy (UPS) has shown that adsorption of molecular NO is preceded in coverage by dissociation of NO on Ru(100) at 370 K (1). The situation is further complicated by the possibility that two distinct types of molecular NO adsorb on some surfaces. This has been observed in the case of adsorption of NO on Pt(111) by electron energy loss spectroscopy (EELS) (2), and on Ir(111) using UPS (3,4).

Previously, we have reported inelastic electron scattering measurements which show that two states of molecular NO are adsorbed on the hexagonally close-packed Ru(001) surface at 150 K (5). These states have been observed subsequently in XPS and UPS spectra (6). Molecular nitric oxide undergoes dissociation and conversion from one molecular state to another as the surface is heated. This has been explained in terms of a model in which the molecular NO can occupy two distinct types of sites on this surface. The dissociation products occupy the same sites as one of the molecular states of NO. In this paper, we present additional data from electron energy loss spectroscopy and thermal desorption mass spectrometry which provide further evidence that the two-site model is valid.

In Sec. 2, the experimental methods are presented; in Sec. 3, the experimental data are presented and discussed; and in Sec. 4, the results and conclusions are summarized.

2. Experimental Methods

The experiments were performed in a stainless steel vacuum system with a base pressure of 5×10^{-11} torr. The mechanical polishing and chemical cleaning procedure used in preparing the Ru(001) crystal have been reported elsewhere (5,7,8). Occasionally, the oxygen cleaning treatment and the NO exposures resulted in the formation of a tenacious surface oxide, as judged by the presence of a 64 to 74 meV loss (and gain) feature in the inelastic scattering spectrum (8,9). Heating the Ru crystal for total periods of up to 30 minutes at 1580 - 1660 K was required to remove this surface oxide. The crystal was exposed to NO through a directional beam doser. Exposures of NO, ε_{NO}, are reported in units of torr-s, where the pressure refers to the NO pressure in a gas storage bulb behind a glass capillary, and the time refers to the time of exposure. Relative coverages of NO are based on thermal desorption peak areas of N_2 and NO. Thermal desorption spectra were taken with a model UTI 100C, with an emission current of 2.0 mA. Isotopic $N^{15}O^{16}$ was used in the thermal desorption experiments to circumvent interference between N_2^{14} desorption from the Ru crystal and background CO, both of which cause mass peaks at 28 amu.

The electron spectrometer used in these energy loss measurements has been described fully (10). The energy of the incident electron beam was 4 eV. The full-width at half-maximum of the elastic peak varied from 14 to 16 meV, with 5×10^5 cps of elastic electrons reflected specularly from the clean surface. The energies of the loss features are accurate to within approximately ± 1 meV (± 8 cm^{-1}).

3. Experimental Results and Discussion

The frequencies of the two main loss features which are due to the N-O stretch of NO adsorbed molecularly on Ru(001) are shown in Fig. 1 as functions of coverage (exposure) of NO at approximately 150 K. Within the framework of the site-dependent model which has been proposed for this adsorption system (5,11), the loss feature at 171 - 189 meV (1379 - 1525 cm^{-1}) is due to the N-O vibration of NO adsorbed at a site of two- or three-fold coordination. At coverages greater than approximately 1/3 of saturation, a loss feature appears at 221 - 226 meV (1783 - 1823 cm^{-1}) which is due to NO bound linearly at an on-top site. These two forms will be referred to as "bridged" and "linear" NO, respectively. The frequency assignments are consistent with the infrared spectra of homogeneous metal clusters containing nitrosyl ligands in various coordination states (12 - 15).

A third loss feature at approximately 1150 cm^{-1} has been observed also. This feature is observed as a "transient", i.e., it apparently represents an adsorbate which is unstable on the Ru(001) surface at 120 K or above. The closest spectral analogy is to be found in the infrared spectra of cobalt complexes which contain the hyponitrite ligand, N_2O_2. These spectra are characterized by absorption bands between 925 and 1195 cm^{-1} (15). However, a firm assignment of the transient feature in the experiments reported here must await further clarification.

At lower energies, a feature at 64 - 71 meV (516 - 576 cm^{-1}) is observed also when linear NO is present on the surface. This is probably due to the Ru-N stretch of the linear form of NO (11). At temperatures where dissociation products and molecular NO are both present on the Ru(001) surface, this Ru-NO loss feature overlaps the Ru-O feature, which falls in the same frequency range (8,9).

Experimentally, thermally-induced dissociation of NO occurs at higher temperatures as the relative coverage increases. Within the framework of the two-site model of NO adsorption, this can be understood as follows: Upon heating, the bridged NO produces dissociation products which occupy multiple coordination sites on the Ru(001) surface. This is accompanied by conversion of the bridged form of NO to the linear form. At high NO coverages, dissociation is impeded due to the site competition between bridged molecular NO and its dissociation products. The two-site model is thus consistent with the observed coverage dependence of the activated dissociation of NO (5). It has been inferred from UPS data that there is a coverage-dependent activation barrier for dissociation of molecular NO on the (111) surface of Ni also (16).

Energy loss spectra are shown in Figs. 2 and 3 where the Ru(001) surface was treated sequentially as follows: (a) It was exposed to NO at 150 K; (b) It was heated to a temperature sufficient to dissociate the adsorbed NO; and (c) The surface prepared in (b) was exposed again to NO at 150 K. The initial relative (to saturation) coverage of NO in Fig. 2(a) is $\hat{\theta}_{NO} = 0.15$. The peak at 1379 cm^{-1} is due to bridged NO. The spectrum of Fig. 2(b) follows heating the surface to 250 K. In this spectrum, the peak at 64 meV (516 cm^{-1}) is due to chemisorbed oxygen. When this surface was then exposed to 43 torr-s NO at 150 K, spectrum (c) of Fig. 2 resulted, with peaks at 1412 and 524 cm^{-1}. It can be seen, by comparison with Fig. 3(a), that the presence of the dissociation products resulting from the small initial NO coverage does not significantly influence the subsequent adsorption of NO, on the basis of energy loss spectra. The dissociation products do not prevent the NO from adsorbing into the bridged state, where it would adsorb also at low coverages on the clean Ru(001) surface (5).

At a higher initial coverage of NO, $\hat{\theta}_{NO} = 0.32$, the results are quite different. The vibrational spectrum of the initial surface is shown in Fig. 3(a), with peaks at 1395 and 1113 cm^{-1}. Spectrum (b) of Fig. 3 follows heating to 311 K, which again leaves a surface where only chemisorbed nitrogen and oxygen atoms are present. The spectrum of Fig. 3(c) was taken after the surface with dissociation products had been exposed to 43 torr-s of NO at 150 K. It can be seen that the higher coverage of nitrogen and oxygen atoms resulting from the higher initial coverage of NO almost completely prevents subsequent adsorption of molecular NO into the bridged state. Rather, adsorption of linear NO occurs after this exposure, in contrast to the behavior shown in spectrum (c) of Fig. 2. Further exposure of this surface to NO leads only to a growth in the intensity of the feature at 222 meV (1791 cm^{-1}), which is due to linear NO, as shown in Fig. 3(d).

The experimental data of Figs. 2 and 3 provide strong support for the two-site model of adsorption of NO (5,11). The dissociation products of NO occupy the same sites on the Ru(001) surface as the bridged state of molecular NO. When the initial coverage of dissociation products is sufficiently high, as in Fig. 3, the surface is poisoned with respect to subsequent adsorption of bridged NO. At a lower initial coverage of N and O adatoms (Fig. 2), the NO can adsorb first into the (vacant) bridged sites, which are energetically preferred. This is consistent with previous results in which adsorption of NO at 280 K yielded a vibrational spectrum which showed only evidence for the presence of chemisorbed oxygen and linear NO on this surface (11).

These conclusions are reminiscent of those drawn from previous UPS studies of the adsorption of NO on Ru(100) at 370 K, in which dissociation of NO was shown to precede adsorption of molecular NO in coverage (1). This adsorption sequence has also been postulated to occur on polycrystalline Rh at room temperature on the basis of CO titration experiments (17).

At an initial relative coverage of NO of 0.15, dissociation of the bridged NO is complete by 250 K, as shown by spectrum (b) of Fig. 2. If one assumes that the (coverage-independent) value of the pre-exponential factor of the rate coefficient is $10^{13}s^{-1}$, then the activation energy for dissociation of this state is approximately 16 kcal/mole.

Thermal desorption experiments indicate that there is a minimum relative coverage below which no desorption of molecular NO occurs. Thermal desorption spectra of molecular $N^{15}O^{16}$ which follow exposure to various amounts of $N^{15}O^{16}$ at 150 K are shown in Fig. 4. The heating rate used in the desorption experiments was 21 ± 1 K/s. The maximum amount of $N^{15}O^{16}$ which desorbed represented only 5% of the total N^{15} which desorbed as mass 30. (This relative intensity may be subject to slight error due to preferential adsorption of $N^{15}O^{16}$ at the walls of the vacuum chamber.) The molecular $N^{15}O^{16}$ desorbs as a single first-order peak at 480 K, from which it follows that the value for the activation energy for desorption is 31 kcal/mole, assuming that the pre-exponential factor of the desorption rate coefficient is $10^{13}s^{-1}$. Below $\hat{\theta}_{NO} = 0.5$, no molecular $N^{15}O^{16}$ desorbs. The onset of desorption of molecular NO at intermediate relative coverages of NO has also been observed on Ni(111) (16), polycrystalline Rh (17), Ru(100) (18) and Ru(101) (19). In our experiments. desorption as molecular NO may occur only when the coverage-dependent activation energy for dissociation (5) becomes comparable to the activation energy for desorption. Another perspective is that desorption of some molecular NO above $\hat{\theta}_{NO} = 0.5$ may be necessary to free sites on the surface required for dissociation of the remaining NO.

4. Summary

The major conclusions from this investigation of NO adsorption on Ru(001) may be summarized as follows:

(1) Bridged NO dissociates with an activation energy of approximately 16 kcal/mole at low relative coverages.

(2) At a sufficiently high coverage of dissociation products, the Ru(001) surface is poisoned with respect to subsequent adsorption of bridged NO. Rather, adsorption into the linear state of NO occurs.

(3) Desorption of molecular NO begins to occur only at intermediate coverages, following adsorption at 150 K. This may be related to the coverage dependence of the activation energy for dissociation of bridged NO.

Acknowledgments

We wish to thank E. Umbach, S. Kulkarni, P. Feulner and D. Menzel for providing us with a preprint of ref. (6).

References

1. H. P. Bonzel and T. E. Fischer, Surface Sci. 51, 213 (1975).
2. H. Ibach and S. Lehwald, Surface Sci. 76, 1 (1978).
3. J. Kanski and T. N. Rhodin, Surface Sci. 65, 63 (1977).
4. P. A. Zhdan, G. K. Boreskov, A. I. Boronin, A. P. Schepelin, W. F. Egelhoff, Jr. and W. H. Weinberg, J. Catal. 60, 93 (1979).
5. G. E. Thomas and W. H. Weinberg, Phys. Rev. Letters 41, 1181 (1978).
6. E. Umbach, S. Kulkarni, P. Feulner and D. Menzel, Surface Sci. 88, 65 (1979).
7. G. E. Thomas and W. H. Weinberg, J. Chem. Phys. 70, 1437 (1979).
8. G. E. Thomas and W. H. Weinberg, J. Chem. Phys. 70, 954 (1979).
9. G. E. Thomas and W. H. Weinberg, J. Chem. Phys. 69, 3611 (1978).
10. G. E. Thomas and W. H. Weinberg, Rev. Sci. Instrum. 50, 497 (1979).
11. P. A. Thiel, W. H. Weinberg and J. T. Yates, Jr., J. Chem. Phys. 71, 1643 (1979).
12. J. R. Norton, J. P. Collman, G. Dolcetti and W. T. Robinson, Inorganic Chem. 11, 382 (1972).
13. J. Müller and S. Schmitt, J. Organomet. Chem. 97, C54 (1975).
14. R. Eisenberg and C. D. Meyer, Acc. Chem. Res. 8, 26 (1975).
15. K. G. Caulton, Coord. Chem. Rev. 14, 317 (1975), and references therein.
16. H. Conrad, G. Ertl, J. Küppers and E. E. Latta, Surface Sci. 50, 296 (1975).
17. C. T. Campbell and J. M. White, Appl. Surface Sci. 1, 347 (1978).
18. R. Klein and A. Shih, Surface Sci. 69, 403 (1977).
19. P. D. Reed, C. M. Comrie and R. M. Lambert, Surface Sci. 72, 423 (1978).

Figure Captions

Fig. 1: Energies of the nitrogen-oxygen vibrations of the two major states of molecular NO on Ru(001) at 150 K as functions of exposure and coverage. The error bars show the typical uncertainty in each individual frequency assignment, approximately ± 1 meV (± 8 cm^{-1}). In the proposed model, the lower curve represents the frequencies observed for bridged NO, and the upper curve represents the frequencies observed for linear NO.

Fig. 2: A series of energy loss spectra of molecular NO and its dissociation products adsorbed on Ru(001).

(a) Follows an exposure of ε_{NO} = 22 torr-s ($\hat{\theta}_{NO}$ = 0.15) at T = 150 K on clean Ru(001).

(b) Follows heating the surface represented in (a) to 250 K.

(c) Follows exposing the surface represented in (b) to 43 torr-s NO at 150 K.

Fig. 3: A series of energy loss spectra of molecular NO and its dissociation products adsorbed on Ru(001).

(a) Follows an exposure of ε_{NO} = 55 torr-s ($\hat{\theta}_{NO}$ = 0.32) at 150 K on clean Ru(001).

(b) Follows heating the surface represented in (a) to 311 K.

(c) Follows exposing the surface represented in (b) to 43 torr-s NO at 150 K.

(d) Follows exposing the surface represented in (c) to 43 torr-s NO at 150 K.

Fig. 4: Thermal desorption spectra of $N^{15}O^{16}$ following adsorption of $N^{15}O^{16}$ on Ru(001) at 150 K. The baselines of the desorption spectra are displaced relative to one another for clarity.

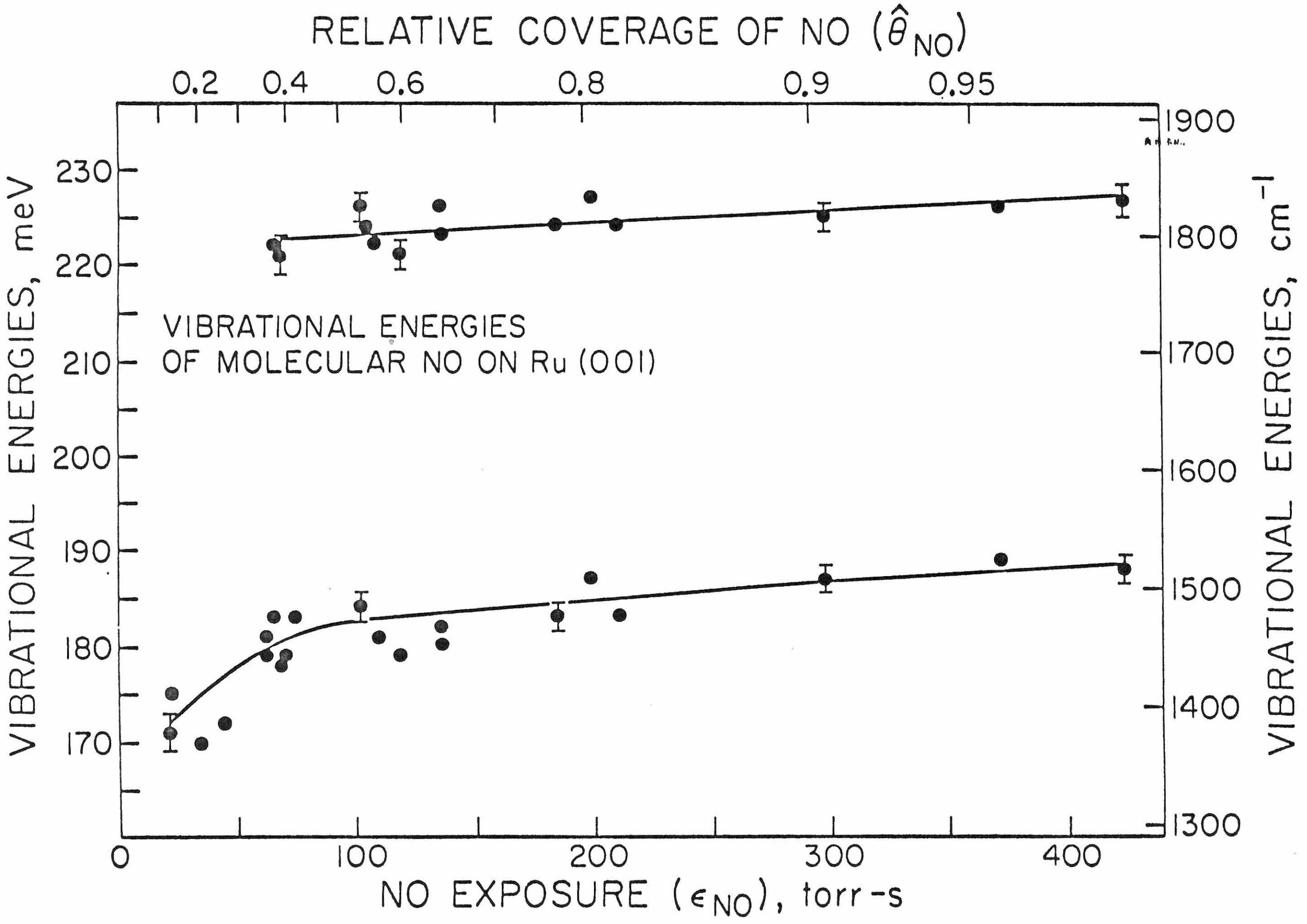
RELATIVE COVERAGE OF NO ($\hat{\theta}_{NO}$)
0.2
0.4
0.6
0.8
0.9
0.95
VIBRATIONAL ENERGIES, meV
230
220
210
200
190
180
170
VIBRATIONAL ENERGIES, cm^{-1}
1900
1800
1700
1600
1500
1400
1300
VIBRATIONAL ENERGIES
OF MOLECULAR NO ON Ru (001)
0
100
200
300
400
NO EXPOSURE (ϵ_{NO}), torr-s

Figure 1.

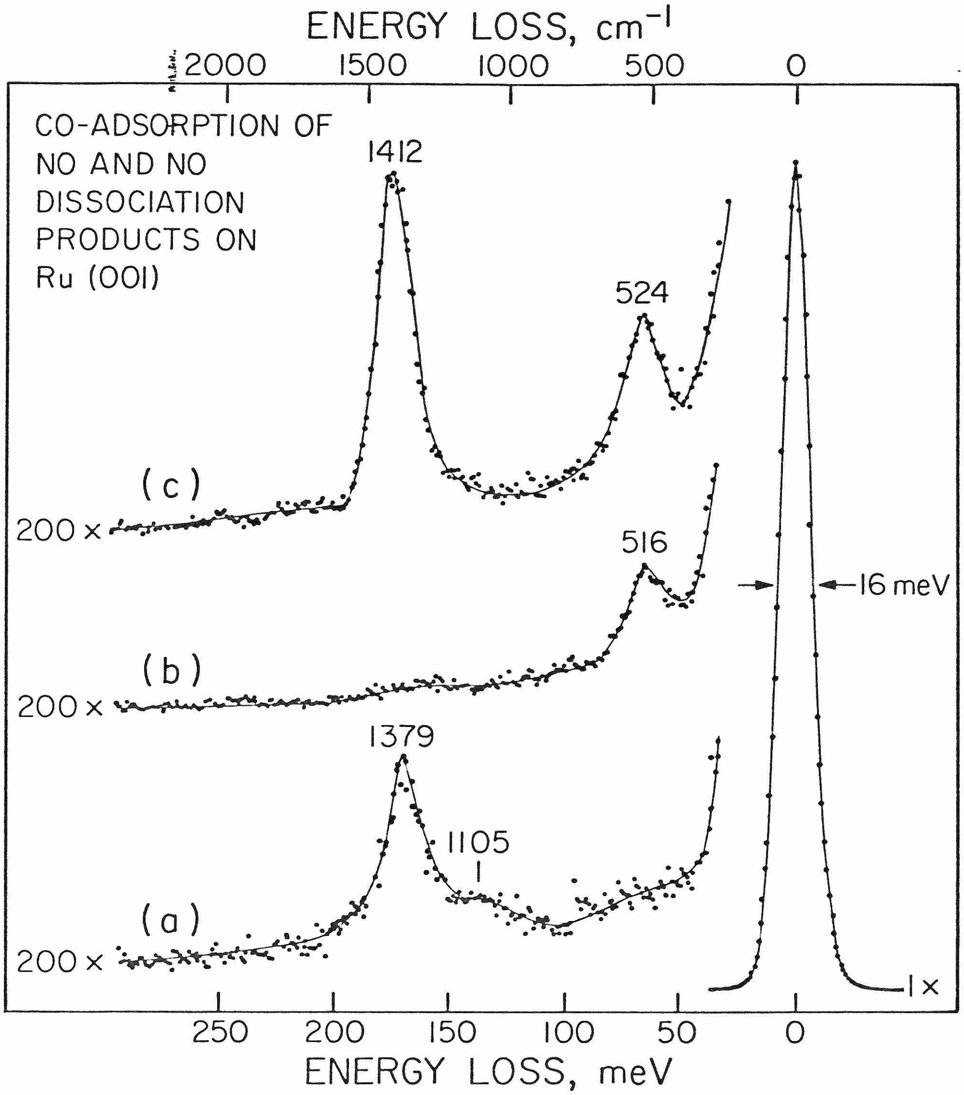
ENERGY LOSS, cm⁻¹
2000
1500
1000
500
0
CO-ADSORPTION OF NO AND NO DISSOCIATION PRODUCTS ON Ru (001)
1412
524
(c)
200 ×
516
16 meV
(b)
200 ×
1379
1105
(a)
200 ×
1 ×
250
200
150
100
50
0
ENERGY LOSS, meV

Figure 2.

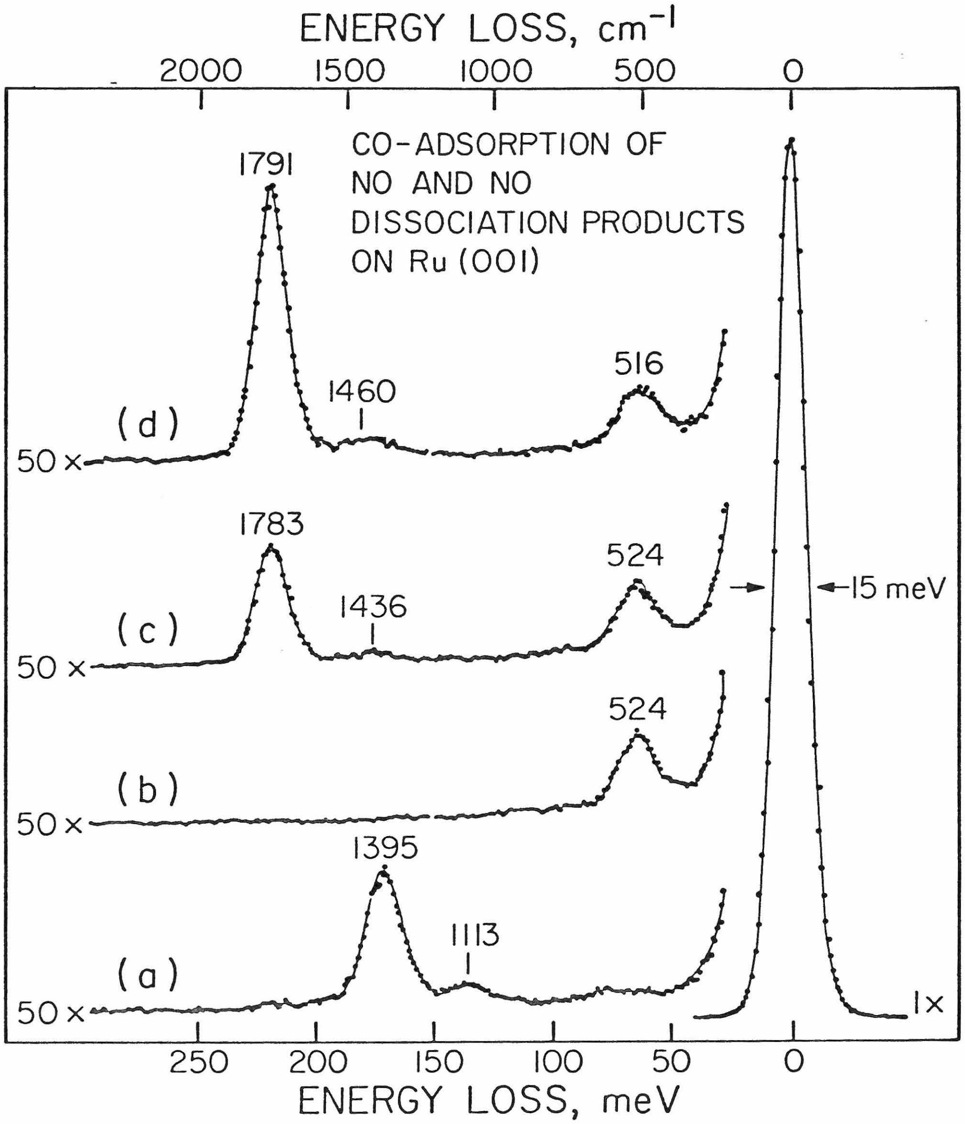
ENERGY LOSS, cm^{-1}
2000
1500
1000
500
0
CO-ADSORPTION OF
NO AND NO
DISSOCIATION PRODUCTS
ON Ru (001)
1791
1460
516
(d)
50 ×
1783
1436
524
(c)
50 ×
15 meV
524
(b)
50 ×
1395
1113
(a)
50 ×
1×
250
200
150
100
50
0
ENERGY LOSS, meV

Figure 3.

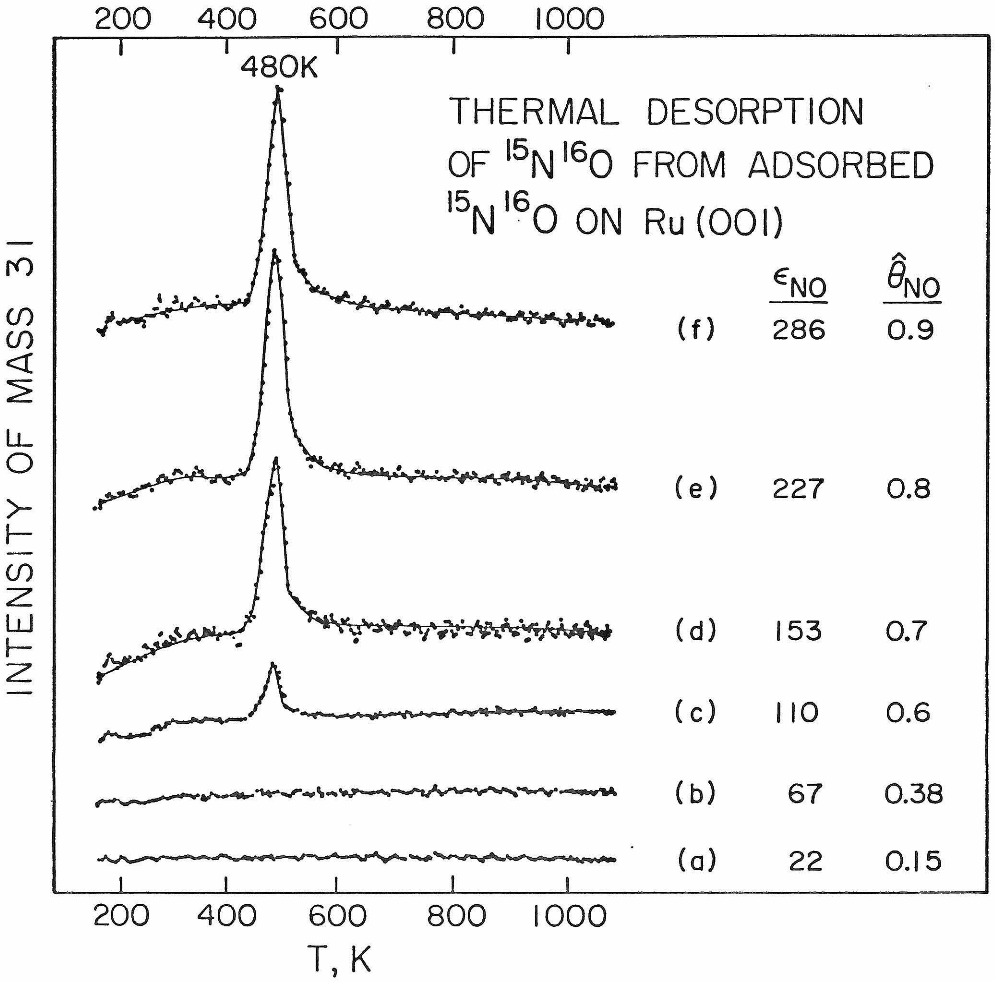

200
400
600
800
1000
480K
THERMAL DESORPTION OF $^{15}N^{16}O$ FROM ADSORBED $^{15}N^{16}O$ ON Ru(001)
ϵ_{NO}
$\hat{\theta}_{NO}$
(f) 286 0.9
(e) 227 0.8
(d) 153 0.7
(c) 110 0.6
(b) 67 0.38
(a) 22 0.15
INTENSITY OF MASS 31
T, K

Figure 4.

Chapter 7

A DETERMINATION OF ADSITE SYMMETRY ON SURFACES VIA ELECTRON ENERGY LOSS SPECTROSCOPY: CO-ADSORPTION OF CO AND NO ON Ru(001)

[*This chapter was published as a paper by P. A. Thiel, W. H. Weinberg and J. T. Yates, Jr. in* The Journal of Chemical Physics *71, (1979) 1643.*]

ABSTRACT

Electron energy loss spectroscopy has been used to study the vibrational energies of NO and CO co-adsorbed on the Ru(001) surface. Adsorption of CO competes directly with adsorption of one of the two molecular states of NO. This is interpreted in terms of the geometry of the adsorption sites for CO and NO and is consistent with models proposed previously for adsorption of CO and NO separately on the Ru(001) surface.

1. Introduction

The adsorption and dissociation of NO on the Ru(001) surface, as studied by high resolution electron energy loss spectroscopy (EELS), has been reported recently (1). The vibrational spectra of CO adsorbed on this hexagonally close-packed surface have been measured also (2,3). In this work, we report vibrational measurements of co-adsorbed overlayers of CO and NO on Ru(001) which demonstrate directly the occurrence of site competition between the two adsorbates. Furthermore, these data support and clarify the models of adsorption site geometries proposed previously for the single adsorbates (1 - 5).

The characterization of CO and NO co-adsorbed on the platinum group metals is important in elucidating the mechanisms involved in the oxidation of CO and simultaneous dissociation/reduction of NO over these surfaces. Few previous studies of the interaction between CO and NO on clean, well-characterized surfaces have been reported. On Pt(111) and Pt(110), Lambert and Comrie (6) have inferred from thermal desorption data that gaseous CO displaces molecular NO from the surface and also causes a conversion between two thermal desorption states of molecular NO. The high temperature state, which undergoes conversion and displacement, is the only one which is reactive in the oxidation of CO. Similarly, Campbell and White (7) report that adsorbed CO inhibits the oxidation of CO by NO at low temperature on polycrystalline Rh. They attribute this to the occupation of sites by CO which are required for NO adsorption and dissociation. Conrad et al. (8) have used UV-photoelectron spectroscopy to observe directly the displacement of molecular NO by gaseous CO from Pd(110) and polycrystalline Pd surfaces. Thus, it appears that adsorption of molecular NO and CO is competitive on these surfaces, at a temperature below that at which oxidation of CO occurs. The present study shows directly that a competitive mechanism is operative in co-adsorption on Ru(001) also.

2. Experimental Methods

The experiments were performed in a stainless steel vacuum system with a base pressure of 5 x 10^{-11} torr. The mechanical polishing and chemical cleaning procedures used in preparing the Ru(001) crystal have been reported previously (1 - 5). The crystal was exposed to NO through a directional beam doser and was exposed to CO by backfilling the vacuum system with gaseous CO. Relative coverages of NO are based on thermal desorption peak areas of N_2 and NO, and absolute coverages of CO are based on combined thermal desorption data and LEED observations (2,5). All exposures were performed with the crystal at temperatures between 120 K and 180 K, unless otherwise specified.

The electron spectrometer used in these energy loss measurements has been described fully elsewhere (9). The energy of the incident electron beam was 4 eV. The full-width at half-maximum of the elastic peak varied from 13 to 16 meV, with 5 x 10^5 cps of elastic electrons reflected specularly from the clean surface. The counting rate in the elastic channel decreased by a factor of 20 with increasing exposure to NO. A similar effect was also reported in the vibrational spectra of pure NO on Ru(001) (1). The energies of the loss features are accurate to within approximately ± 1 meV (± 8 cm^{-1}).

3. Results and Discussion

Energy loss spectra of NO and CO adsorbed separately on Ru(001) are shown in Fig. 1. The energy loss spectra shown in Fig. 1(A), for various coverages of NO at $120\ K \leq T \leq 180\ K$, are consistent with a model in which molecular NO adsorbs in two sites of different symmetry (1). The energy loss feature at 174 - 189 meV (1404 - 1525 cm^{-1}) is assigned to the N-O vibration of NO adsorbed at a site of two- or three-fold coordination, in analogy with doubly- and triply-coordinated nitrosyl ligands in homogeneous metal clusters (1,10,11). This form will be referred to as "bridged". The loss feature at 221 - 226 meV (1783 - 1823 cm^{-1}) can similarly be assigned to NO bound linearly in an on-top site (12). This form will be referred to as "linear". At low coverages,the NO adsorbs in the more strongly bound bridged form; at coverages greater than approximately 1/3 of saturation, the on-top site becomes populated.

A transient feature at approximately 1154 cm^{-1} occurred in some spectra. This feature was noted previously (1) and apparently represents an adsorbate which is unstable at $120\ K \leq T \leq 180\ K$ on Ru(001). In several cobalt complexes, the presence of the hyponitrite ligand, N_2O_2, is characterized by infrared bands between 925 and 1195 cm^{-1}, depending upon the nature of the anion and the other ligands (13). The exact nature of the transient species on the Ru(001) surface will require further clarification, however.

A low energy feature at 66 - 71 meV (533 - 576 cm^{-1}) is observed also. The frequency range for the Ru-O stretch of atomic oxygen on Ru(001), determined in separate studies (2,4), is 64 - 74 meV (516 - 596 cm^{-1}). However, in inorganic complexes the Ru-N vibration of those nitrosyl ligands with N-O frequencies above 1800 cm^{-1} is reported to occur in the range 570 - 638 cm^{-1} (14,15). In our spectra, the intensity of the low energy feature correlates with the appearance and growth in intensity of the loss feature above 1780 cm^{-1}, which is due to linear NO [Fig. 1(A)]. This suggests strongly that, at T ≤ 180 K, the vibrational feature at 66 - 71 meV is due to the Ru-NO stretch of linear NO. This assignment is supported by the fact that, at T ≤ 150 K, Umbach, et al. see no evidence for dissociation of NO on Ru(001) using X-ray photoelectron spectroscopy (16). At higher temperatures, where dissociation products and molecular NO are both present on the Ru(001) surface, the Ru-NO loss feature is unresolved from the Ru-O feature in our experiments.

Experimentally, thermally-induced dissociation of NO occurs at higher temperatures as the relative coverage increases. Within the framework of the two-site model of NO adsorption, this can be understood as follows: Upon heating, the bridged NO produces dissociation products which occupy multiple coordination sites on the Ru(001) surface. This is accompanied by conversion of the bridged form of NO to the linear form. This conversion is inhibited by the presence of a high initial coverage of linear NO. At high NO coverages, dissociation is impeded due to this site competition. The two-site model is thus consistent with the observed coverage dependence of the activated dissociation of NO (1).

Previous low-energy electron diffraction (LEED) data for CO on Ru(001) (5) indicate that adsorbed CO forms coincidence lattices at absolute coverages, θ_{CO}, greater than 1/3, in which many of the CO molecules are in low-symmetry adsorption sites. A $(\sqrt{3} \times \sqrt{3})R30^{o}$ LEED pattern is observed at $\theta_{CO} = 1/3$, however, and presumably corresponds to CO molecules adsorbed in sites of high symmetry.

The energy loss spectra for this system, represented in Fig. 1(B), show a single C-O stretching frequency which shifts with increasing coverage. At an adsorption temperature of 180 K, the frequency of the C-O vibration at saturation coverage is 252 meV (2033 cm^{-1}). The energy loss feature at approximately 55 meV (444 cm^{-1}) is assigned to the Ru-CO stretching vibration, and the feature at approximately 106 meV (855 cm^{-1}) is the first harmonic of this vibration. The C-O vibration occurs in the frequency range commonly assigned to CO bound linearly to a single metal atom, in spite of the observation of coincidence lattices in the LEED structure. This may be evidence that the Ru(001) surface is electronically and geometrically homogeneous with respect to adsorption of CO at high coverages, where CO-CO repulsive interactions predominate in the formation of the ordered overlayer (2,3,5a), although recently an alternative model has been proposed with CO bound exclusively in on-top sites which is also consistent with the LEED data (5b).

In Fig. 2, vibrational spectra are shown for four experiments in which the Ru surface, with four different initial coverages of CO, was exposed to various amounts of NO (17). It is apparent that for initial absolute coverages of CO, θ^{o}_{CO}, less than 0.3 [Fig. 2(A) and (B)], the subsequent adsorption of NO occurs with an attenuation of intensity of the linear NO loss feature [1791 - 1831 cm^{-1} in Fig. 1(A) and (B)] relative to the loss spectra of NO on clean Ru(001) which were obtained after equal NO exposures [Fig. 1(A)]. Qualitative comparison of the intensities of the loss features in Fig. 2(A) and (B) suggest that adsorption of NO may be accompanied by some displacement of CO from the surface for $\theta^{o}_{CO} \leq 0.3$. The observed variations in energy of the vibrational loss features may be due to changes in coverage of the individual adsorbates and/or interactions between different adsorbates. At $\theta_{CO}^{o} \geq 0.3$, adsorption of NO occurs only in the bridged sites [1395 - 1460 cm^{-1} in Fig. 2(C) and (D)]. The fact that NO can adsorb into the linear sites only below $\theta_{CO}^{o} \sim 0.3$ is evidence that the CO molecules in the $(\sqrt{3} \times \sqrt{3})R30^{o}$ lattice are adsorbed in the on-top sites.

In Fig. 3, vibrational spectra are shown for three experiments in which exposure to NO was followed by exposure to CO, the reverse of the exposure sequence of Fig. 2. The spectrum of Fig. 3(A) is to be compared with the spectrum of Fig. 1(A) which follows a 120 torr-s (<u>17</u>) NO exposure. It can be seen in Fig. 3(A) that exposure to CO causes displacement and/or conversion of the NO which would have yielded the loss feature at 1783 cm^{-1} (linear NO) in the absence of exposure to CO. In Fig. 3(B), the conversion/displacement is obviously more difficult due to the higher initial coverage of NO relative to the saturation coverage of NO on the clean surface, $\hat{\theta}_{NO} = 1$. Qualitative comparison of the relative peak intensities of Figs. 3(A) and (B) implies also that less CO adsorption occurs for the higher value of $\hat{\theta}_{NO}^{o}$.

Finally, the energy loss spectra of Fig. 3(C) clearly show that <u>conversion from linear to bridged NO occurs during adsorption of CO.</u> Whether displacement of NO by CO from the surface occurs also cannot be determined on the basis of these data. The surface represented by the spectrum at the bottom of Fig. 3(C) was prepared by exposing the Ru(001) crystal to NO at 280 K. At an exposure temperature between 120 K and 180 K, this 120 torr-s exposure (<u>17</u>) would have resulted in the spectrum of Fig. 1(A) and a relative surface coverage of $\hat{\theta}_{NO}^{o} = 0.6$. Exposure at the higher temperature allows dissociation of bridged NO to occur, resulting in the exclusive population of the linear molecular NO state at this coverage. This is consistent with the thermally activated dissociation experiments reported previously (1), where dissociation of low initial coverages of NO was complete by T = 316 K. Exposure to CO of the surface of Fig. 3(C), where only linear NO and dissociation products are present, results in the growth of the 1508 cm^{-1} loss feature (bridged molecular NO), the growth of the 2057 cm^{-1} feature (adsorbed CO), and a decrease in the intensity of the 1823 cm^{-1} feature (linear molecular NO) relative to the other two. The 548 cm^{-1} feature (Ru-O and Ru-NO stretching vibrations) becomes almost obscured by the 411 cm^{-1} feature (Ru-CO vibration) as the CO exposure increases.

The model proposed here for the competitive adsorption of CO and NO on Ru(001) has a close analogy in the reactions of two metal cluster compounds. The compound $Os_3(CO)_{12}$, which has 12 linear, singly-coordinated CO ligands, reacts with gaseous NO to form $Os_3(CO)_9(NO)_2$, in which three of the carbonyl ligands on one Os atom have been replaced by two singly-coordinated nitrosyl ligands. This compound can be reacted further with CO(g) to form $Os_3(CO)_{10}(NO)_2$, in which both nitrosyl ligands are now two-fold coordinated (bridged), and an Os-Os bond has been broken (18). The reaction sequence is illustrated in Fig. 4. This reaction proceeds similarly for the $Ru_3(CO)_{12}$ cluster (19). The conversion of the nitrosyl ligand by CO(g) from a single to a multiple coordination state with the metal is thus seen in both heterogeneous and homogeneous Ru systems.

4. Synopsis

The data presented in this paper demonstrate the validity of the two-site model for adsorption of NO on Ru(001) proposed earlier (1).

Adsorbed CO competes directly with NO for the adsites which are occupied by the linear form of NO. Adsorption of NO, followed by exposure to gaseous CO, causes at least partial conversion from the linear to bridged form of NO as adsorption of CO occurs. Adsorption of CO, followed by exposure to gaseous NO, prevents adsorption of linear NO at $\theta^{o}_{CO} \geq 0.3$. The fact that some NO can adsorb into the linear sites only below $\theta^{o}_{CO} = 0.3$ is evidence that the CO molecules in the $(\sqrt{3} \times \sqrt{3})R30^{o}$ overlayer are adsorbed in the on-top sites.

Acknowledgment

We would like to acknowledge useful discussions with Dr. Wayne Gladfelter and Dr. Dietrich Menzel.

References

1. G. E. Thomas and W. H. Weinberg, Phys. Rev. Letters, 41, 1181 (1978).
2. G. E. Thomas and W. H. Weinberg, J. Chem. Phys. 70, 954 (1979).
3. G. E. Thomas and W. H. Weinberg, J. Chem. Phys. 70, 1437 (1979).
4. G. E. Thomas and W. H. Weinberg, J. Chem. Phys. 69, 3611 (1978).
5. (a) E. D. Williams and W. H. Weinberg, Surface Sci. 82, 93 (1979).
   (b) J. P. Biberian and M. A. Van Hove, Proc. I.R.I.S. Conf. Vibrations at Surfaces, Namur (September 1980), to be published.
6. R. M. Lambert and C. M. Comrie, Surface Sci. 46, 61 (1974).
7. C. T. Campbell and J. M. White, Appl. Surface Sci. 1, 347 (1978).
8. H. Conrad, G. Ertl, J. Küppers and E. E. Latta, Faraday Discussions — Chem. Soc. 58, 116 (1974).
9. G. E. Thomas and W. H. Weinberg, Rev. Sci. Instrum. 50, 497 (1979).
10. J. R. Norton, J. P. Collman, G. Dolcetti and W. T. Robinson, Inorganic Chem. 11, 382 (1972).
11. J. Müller and S. Schmitt, J. Organomet. Chem. 97, C54 (1975).
12. R. Eisenberg and C. D. Meyer, Acc. Chem. Res. 8, 26 (1975).
13. H. Toyuki, Spectrochim. Acta 27A, 985 (1971); B. F. Hoskins and F. D. Whillans, J. Chem. Soc. Dalton, 607 (1973); see also K. G. Caulton, Coord. Chem. Rev. 14, 317 (1975) and references therein.
14. E. E. Mercer, W. A. McAllister and J. R. Durig, Inorganic Chem. 5, 1881 (1966).
15. M. S. Quinby and R. D. Feltham, Inorganic Chem. 11, 2468 (1972).
16. E. Umbach, S. Kulkarni, P. Feulner and D. Menzel, Surface Sci. 88, 65 (1979).

17. The NO exposure, ε_{NO}, is reported in units of torr-s where the pressure refers to the NO pressure in a gas storage bulb behind a glass capillary, and the time refers to the time of exposure.

18. S. Bhaduri, B. F. G. Johnson, J. Lewis, D. J. Watson and C. Zuccaro, J. Chem. Soc. - Chem. Comm. 477 (1977).

19. B. F. G. Johnson, private communication.

Figure Captions

Fig. 1: Electron energy loss spectra of CO and NO adsorbed separately on the Ru(001) surface, for various coverages. θ_{CO} is the absolute coverage of CO (number of CO admolecules per substrate unit cell), and $\hat{\theta}_{NO}$ is the coverage of NO relative to saturation. The CO exposures, ε_{CO}, are reported in Langmuirs (L), where $1\ L \equiv 1 \times 10^{-6}$ torr-s. The energies of individual loss features are given in cm^{-1}.

Fig. 2: Electron energy loss spectra of the Ru(001) surface following exposure to CO and subsequent exposure to NO, at $120\ K \leq T \leq 180\ K$. The energies of the individual loss features are given in cm^{-1}.

Fig. 3: Electron energy loss spectra of the Ru(001) surface following exposure to NO and subsequent exposure to CO at the temperatures indicated. The energies of the individual loss features are given in cm^{-1}.

Fig. 4: Illustration of the reaction of $Os_3(CO)_{12}$ with NO(g) and subsequent reaction with CO(g) (12).

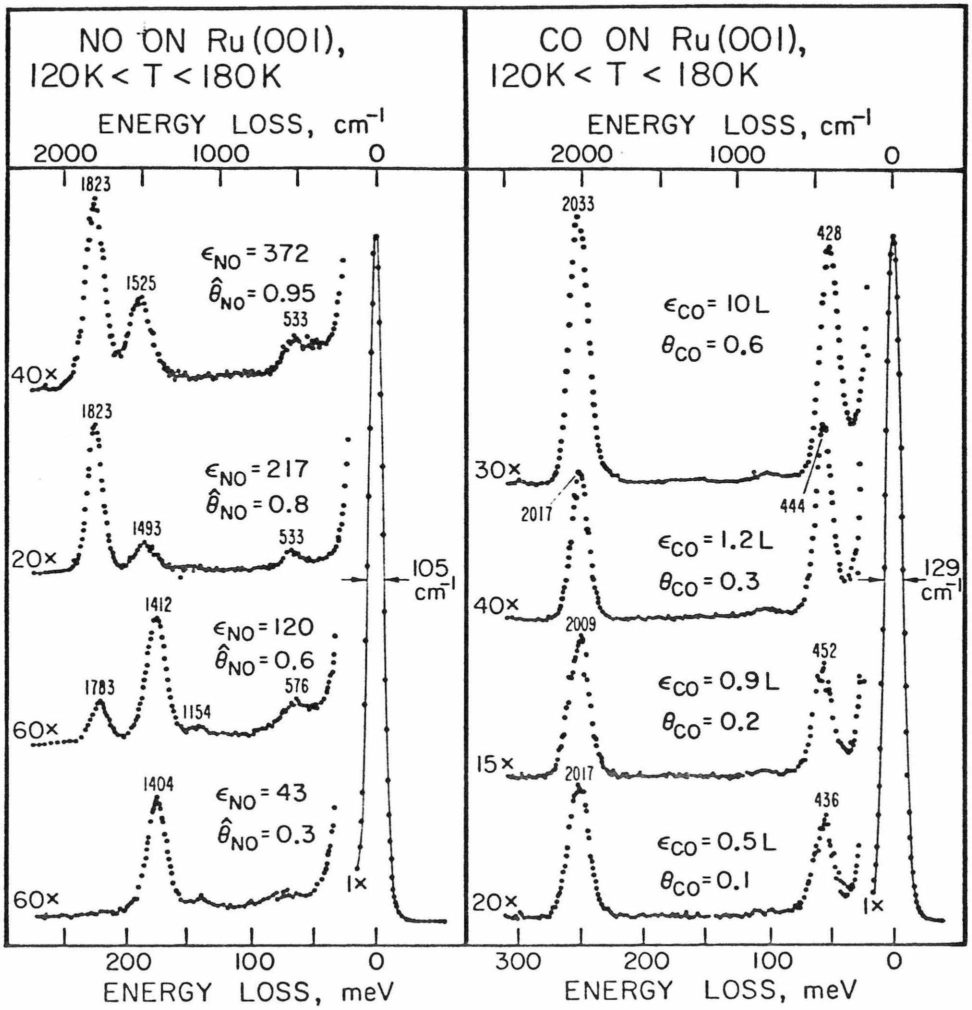
NO ON Ru(001),
120K < T < 180K
ENERGY LOSS, cm⁻¹
2000
1000
0
1823
ϵ_{NO} = 372
$\hat{\theta}_{NO}$ = 0.95
1525
533
40×
1823
ϵ_{NO} = 217
$\hat{\theta}_{NO}$ = 0.8
1493
533
20×
105 cm⁻¹
1412
ϵ_{NO} = 120
$\hat{\theta}_{NO}$ = 0.6
1783
576
1154
60×
1404
ϵ_{NO} = 43
$\hat{\theta}_{NO}$ = 0.3
60×
1×
200
100
0
ENERGY LOSS, meV
CO ON Ru(001),
120K < T < 180K
ENERGY LOSS, cm⁻¹
2000
1000
0
2033
428
ϵ_{CO} = 10 L
θ_{CO} = 0.6
30×
2017
444
ϵ_{CO} = 1.2 L
θ_{CO} = 0.3
40×
129 cm⁻¹
2009
452
ϵ_{CO} = 0.9 L
θ_{CO} = 0.2
15×
2017
436
ϵ_{CO} = 0.5 L
θ_{CO} = 0.1
20×
1×
300
200
100
0
ENERGY LOSS, meV

Figure 1.

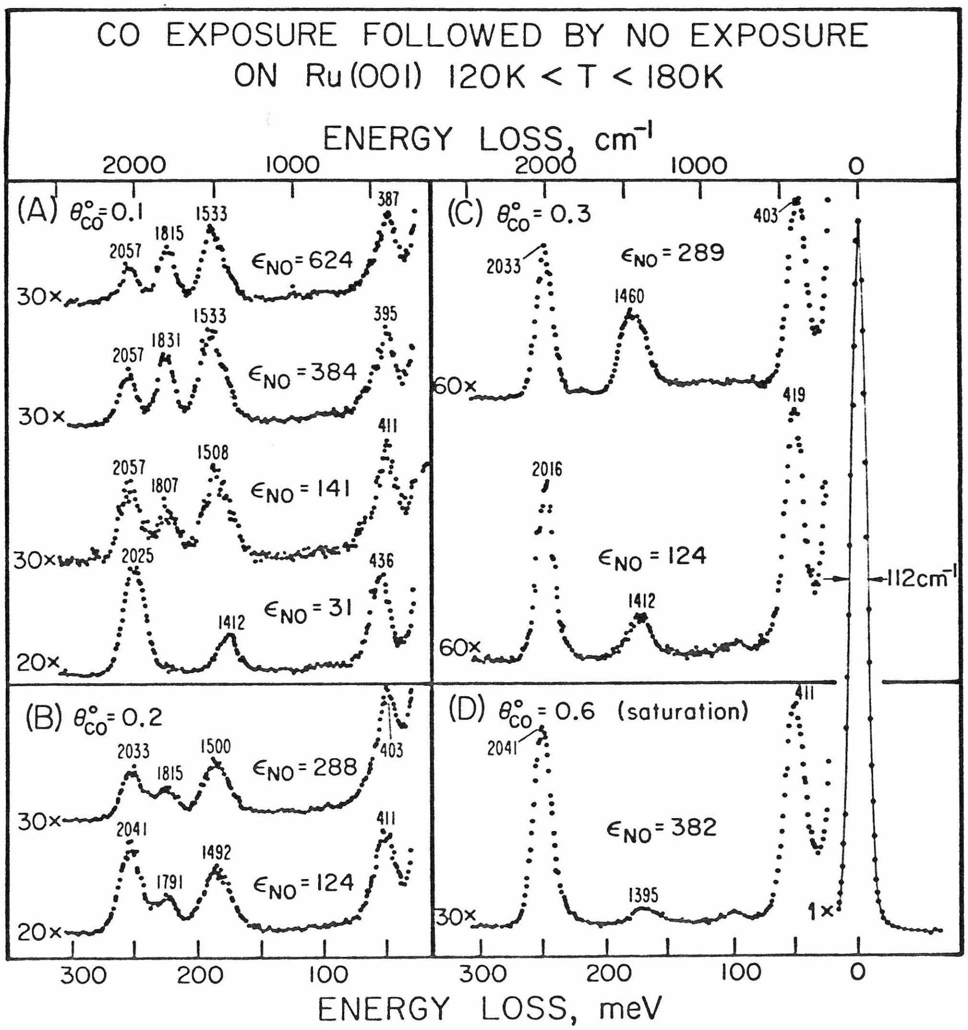
CO EXPOSURE FOLLOWED BY NO EXPOSURE
ON Ru(001) 120K < T < 180K
ENERGY LOSS, cm⁻¹
2000
1000
2000
1000
0
(A) θ°CO = 0.1
387
1533
1815
2057
εNO = 624
30×
1533
395
1831
2057
εNO = 384
30×
411
1508
2057
1807
εNO = 141
30×
2025
436
εNO = 31
1412
20×
(B) θ°CO = 0.2
2033
1500
1815
εNO = 288
403
30×
2041
411
1492
1791
εNO = 124
20×
(C) θ°CO = 0.3
403
2033
εNO = 289
1460
60×
419
2016
εNO = 124
112cm⁻¹
1412
60×
(D) θ°CO = 0.6 (saturation)
411
2041
εNO = 382
1395
30×
1×
300
200
100
300
200
100
0
ENERGY LOSS, meV

Figure 2.

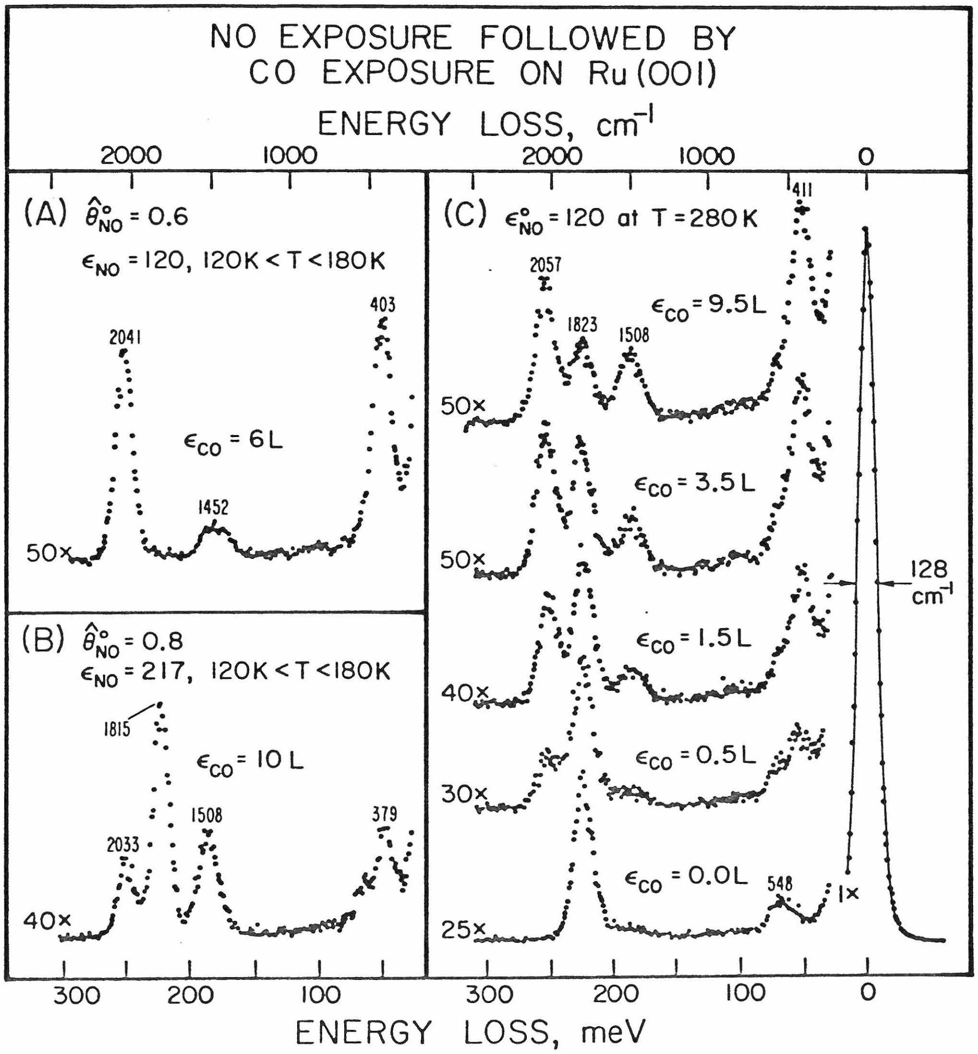
NO EXPOSURE FOLLOWED BY
CO EXPOSURE ON Ru(001)
ENERGY LOSS, cm⁻¹
2000
1000
2000
1000
0
(A) $\hat{\theta}^{\circ}_{NO} = 0.6$
$\epsilon_{NO} = 120$, 120K < T < 180K
2041
403
$\epsilon_{CO} = 6L$
1452
50×
(B) $\hat{\theta}^{\circ}_{NO} = 0.8$
$\epsilon_{NO} = 217$, 120K < T < 180K
1815
$\epsilon_{CO} = 10 L$
1508
379
2033
40×
(C) $\epsilon^{\circ}_{NO} = 120$ at T = 280K
411
2057
1823
1508
$\epsilon_{CO} = 9.5L$
50×
$\epsilon_{CO} = 3.5L$
50×
128 cm⁻¹
$\epsilon_{CO} = 1.5L$
40×
$\epsilon_{CO} = 0.5L$
30×
$\epsilon_{CO} = 0.0L$
548
1×
25×
300
200
100
300
200
100
0
ENERGY LOSS, meV

Figure 3.

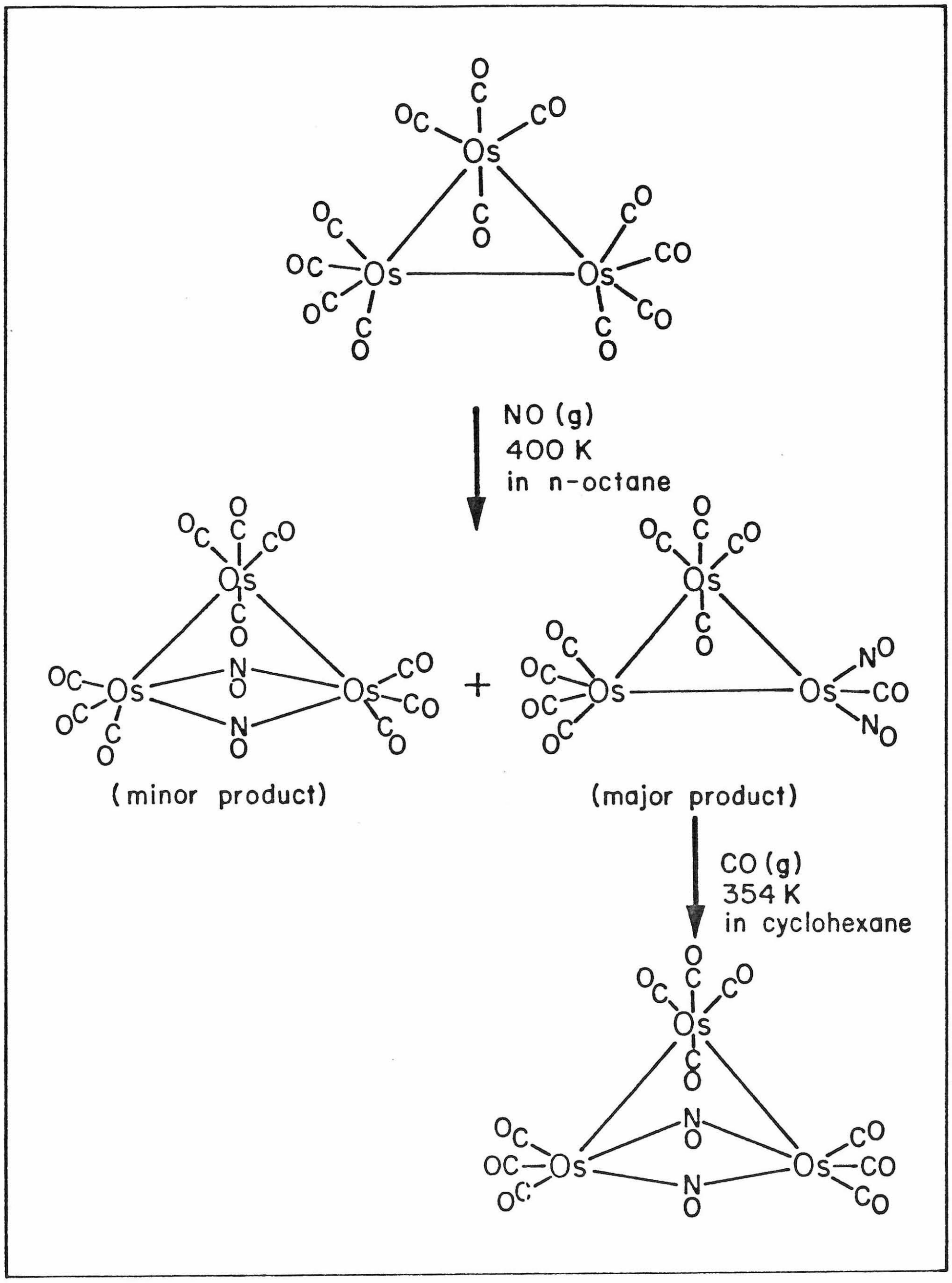
NO (g)
400 K
in n-octane
(minor product)
(major product)
CO (g)
354 K
in cyclohexane

Figure 4.

Chapter 8

ADSITE SYMMETRY AND VIBRATIONAL STRUCTURE OF NO AND H_2 CO-ADSORBED ON THE Ru(001) SURFACE

[*This chapter was published as a paper by P. A. Thiel and W. H. Weinberg in* The Journal of Chemical Physics *73 (1980) 4081.*]

Abstract

The co-adsorption of molecular nitric oxide and hydrogen on Ru(001) has been studied using electron energy loss spectroscopy. Previous work has shown that molecular nitric oxide occupies sites of single- and multiple- (probably three-fold) coordination. Competitive adsorption between hydrogen and the latter form of molecular NO is interpreted in terms of hydrogen preferentially adsorbing into three-fold symmetric sites. This is consistent with experimental results and theoretical calculations for other surfaces.

1. Introduction

In recent years significant progress has been made in the identification of adsorption sites which are preferentially occupied by atomic adsorbates on metal surfaces. By using surfaces which are crystallographically well defined, one can limit the number and type of high-symmetry sites which are available (in the absence of adsorbate-induced reconstruction), thus making the problem tractable. The most definitive experiments in this area have utilized profiles of the intensity as a function of incident energy (I-V profiles) of low-energy electron diffraction (LEED) beams (1-4), normal coordinate analyses of vibrational transitions observed in electron energy loss spectroscopy (EELS) (5-9), and analyses of order-disorder phase transitions (10-11). The results of such experiments to date, considering only the hexagonal surfaces of the Group VIII transition metals, indicate that hydrogen adsorbs in the three-fold hollow sites in an ordered (2x2) superstructure on Ni(111) (1,8,10), and also at saturation coverage on Pt(111) (9). From data available for other types of systems, hydrogen apparently occupies the two-fold bridge sites at maximum coverage on W(100) (5, 6, 7) and the hollow four-fold sites on Ni(100) (12). In the present study, the co-adsorption of molecular nitric oxide and hydrogen on Ru(001) was studied using EELS and thermal desorption mass spectrometry (TDS). The results are interpreted in terms of a site-competitive model, and the three-fold hollow sites are found to be the preferred adsorption sites of hydrogen on the Ru(001) surface.

2. Experimental Methods

The experimental chamber was a stainless steel ultrahigh vacuum system with a base pressure of 4×10^{-11} torr. The Ru crystal was cut from a boule supplied by Materials Research Corporation, which was oriented to within 1^{o} of the (001) plane, as determined by Laue back-reflection X-ray diffraction, and then cut with a rotating wire saw. The crystal was cleaned in vacuum by heating repeatedly to 1370 K in 5×10^{-8} torr O_2, followed by several minutes of annealing in vacuum at 1570 K. This cleaning procedure has been suggested by previous authors (13), and it was verified in our laboratory in a separate vacuum system equipped with LEED optics and a single-pass cylindrical mirror energy analyzer for Auger electron spectroscopy (14, 15). Occasionally, the oxygen cleaning treatment and exposures to nitric oxide resulted in formation of a tenacious surface oxide, as judged by the presence of a 64 to 74 meV loss (and gain) feature in the inelastic scattering spectrum (15, 16). Heating the Ru sample for total periods of up to 30 minutes at 1580-1600 K was required to remove this oxide. The crystal temperature was monitored with a 95% W/5% Re vs. 74% W/26% Re thermocouple spotwelded to the edge of the Ru disk, and the calibration scale of Sandstrom and Withrow (17) was used to correlate thermocouple voltage with temperature below 273 K. The crystal could be cooled using liquid nitrogen to approximately 150 K within 10 to 20 minutes after annealing at 1570 K. Unless otherwise specified, the temperature of the crystal during adsorption in all cases was between 120 K and 180 K. It was heated resistively by passing current through the two parallel Ta support wires, 0.025 cm in diameter, which were spotwelded on the back face of the crystal. An effusive molecular beam system (18) was used to expose the sample to NO. Exposures of NO, ε_{NO}, are expressed in units of torr-s, which is the product of the pressure in a gas storage bulb behind a glass capillary and the time of exposure. Thermal desorption peak areas of N_2 and NO provided a calibration of the coverage of NO relative to saturation, $\hat{\theta}_{NO}$. A similar procedure was used for the measurement of relative hydrogen coverages. Thermal desorption spectra were measured with a quadrupole mass spectrometer, model UTI 100C, using an emission current of 2.0 mA. The sample was exposed to H_2 by backfilling the entire vacuum system with the gas, and these exposures are reported in units of Langmuirs (1 L $\equiv$ 1 Langmuir $\equiv 1 \times 10^{-6}$ torr-s), corrected by a factor of two to compensate for the senstivity of the ionization gauge for H_2 relative to N_2 (19).

The electron spectrometer used in the energy loss measurements is based on the Kuyatt-Simpson hemispherical deflector design (20), and a complete description is available elsewhere (21). The energy of the incident beam of electrons was 4 eV, and the angle of incidence was 62^0 from the surface normal. In the specular direction, the count rate in the elastic channel was 5×10^5 cps. The half-width of the elastic peak varied from 10 to 16 meV. The energy assignments of the loss features have an accuracy of approximately ± 1 meV, where 1 meV $\equiv$ 8.066 cm^{-1}.

3. Results and Discussion

The vibrational spectra of nitric oxide chemisorbed on Ru(001) have been reported and discussed previously (22, 23, 24). They are characterized by two loss features in the range expected to encompass the nitrogen-oxygen stretching mode of molecularly adsorbed NO, i.e., between 1350 and 2000 cm^{-1}, in analogy with the infrared spectra of metal compounds containing nitrosyl ligands (25, 26, 27). The frequencies of both transitions increase with increasing coverage, as shown in Fig. 1. The high-frequency vibration, which appears at coverages greater than approximately one-third of saturation, varies in energy from 1783 to 1823 cm^{-1}. Since it is in the region usually associated with a terminal and linear M-N-O (formally NO^+) configuration (25, 26, 27), this vibration is reasonably assigned to molecular NO linearly bound to a single Ru atom.

The vibration at lower energies, which varies from 1379 to 1525 cm^{-1}, is due to a form of molecular NO which is populated first, at lowest coverages (cf., Fig. 1). In general, frequencies between 1525 and 1750 cm^{-1} are due to bent nitrosyls (formally NO^-) with M-N-O angles between 119^0 and 177^0, where M is a transition metal atom. Although correlations between vibrational frequencies and bonding configurations are not exact due to (at least in part) the variable electronic influence of the other ligands in the metal complex (25, 26, 28), it is apparent that the energy range observed for bent nitrosyl ligands (1525-1750 cm^{-1}) does not overlap the energy of the low-frequency vibration observed in the chemisorption experiments (1379-1525 cm^{-1}). The low-energy vibration of molecularly adsorbed NO may be assigned more satisfactorily to "bridged" NO adsorbed at a side of two- or three-fold coordination. In support of this assignment, each of the nitrosyl ligands in the compound $Ru_3(CO)_{10}(NO)_2$ is bound to two metal atoms, and the N-O vibrational frequencies lie between 1533 and 1500 cm^{-1}, depending slightly upon the solvent or matrix (29, 30, 31). In the compound $(C_5H_5)_3Co_3(NO)_2$, the nitrosyls are both bound to three cobalt atoms, and a strong absorption band due to the N-O stretching frequency is found at 1405 cm^{-1} (32). The three-fold symmetry of the Ru(001) surface, combined with the infrared frequencies discussed herein, suggests that the low-frequency state of molecular NO is adsorbed at a site of three-fold or, less probably, two-fold coordination.

In separate experiments, X-ray photoelectron spectroscopy (XPS) and ultraviolet photoelectron spectroscopy (UPS) have shown the existence of two discrete states of molecular NO adsorbed on Ru(001) also (33).

Other features, observed at 1154 cm^{-1}, 533-576 cm^{-1}, and 516-596 cm^{-1} are assigned to an unidentified molecular species [possibly N_2O_2 (23)], the Ru-NO stretch of the linear NO, and the Ru-O stretch of atomic oxygen (resulting from NO dissociation at elevated temperatures), respectively. A thorough discussion of these assignments has been given previously (22, 23, 24).

There is strong evidence that the bridged molecular NO, nitrogen adatoms and oxygen adatoms occupy identical types of surface sites. In previous experiments, it was found that the nitrogen and oxygen adatoms which are the dissociation products of NO can prevent subsequent adsorption of the bridged molecular NO (24), and that approximately twice as many adsorption sites are occupied by the dissociation products as by molecular NO (33). Ku, et al. (34) similarly concluded that N and O adatoms occupy identical adsorption sites on a Ru(101) surface following dissociative adsorption of NO at 363 K, based on the observation that exposure to O_2 or to NO caused the same sequence of LEED patterns to form at this temperature. Selective titration experiments supported their conclusion and led them further to posit that the N and O adatoms exist separately on the surface as islands (34).

The adsorption site of oxygen in a (2x2) overlayer superstructure has been determined on three hexagonal surfaces: Ni(111) (2,11); Rh(111) (3); and Ir(111) (4). I-V profile analyses (2,3,4) and also, in the case of Ni(111), an order-disorder phase transition analysis (11), have located the oxygen adatom at three-fold hollow sites in all cases. [For the sake of the present discussion, no distinction will be made between the two kinds of three-fold sites present on a (111) surface of an fcc crystal.] If this trend extends to the (001) surface of Ru also, the arguments given above lead to the conclusion that the bridged molecular NO is three-fold coordinated. The validity of the assumption that oxygen adsorption on Ru(001) is analogous to adsorption on Rh(111) is supported by the closeness of the metal-oxygen vibrational frequencies observed on these surfaces: 516-596 cm^{-1} (15,16) and 520 cm^{-1} (35), respectively. These frequencies are incompatible with oxygen coordinated to a single metal atom, for which a Ru-O vibrational frequency of 800-950 cm^{-1} is to be expected, by inspection of the infrared spectra of metal-oxy complexes (36).

Spectrum (a) of Fig. 2 represents a typical EEL spectrum of the clean Ru(001) surface. Spectrum (b) represents a clean surface which has been exposed to 20 L H_2. Note that no new vibrational features are detectable. Spectrum (c) follows exposure of the surface of (b) to 55 torr-s NO, and is to be compared with spectrum (d), where the clean

Ru(001) surface was exposed to the same amount of NO as in (c). Pre-exposure to a saturation coverage of H_2 obviously inhibits adsorption of some of the bridged NO and favors adsorption into the linear sites. A similar effect was noted for other exposures of NO.

These results are at variance with those reported by Umbach, et. al. (33), who concluded that pre-adsorbed hydrogen could essentially block adsorption of molecular NO in the linear state, which they designate as the v_2 state, based on XPS data. The reason for this discrepancy is unclear, particularly since other available data indicate a good correlation between these EELS and XPS experiments (22 - 24,33).

The absence of a loss feature which can be attributed to a Ru-H stretching mode [Fig. 2(b)] is surprising in view of the recent report that the symmetric Pt-H stretch occurs at 550 cm^{-1} on Pt(111) (9). In addition, a feature at 1230 cm^{-1} was attributed to the asymmetric stretch of hydrogen adsorbed at a site of three-fold symmetry, from an analysis of dipole-allowed and dipole-forbidden excitations (9). In transition metal hydrides, hydrogen atoms bound to a single metal atom cause absorption at 2200 - 1600 cm^{-1} in the infrared spectra, whereas edge-bridging hydrogen atoms are characterized by weak and broad absorption in the 1400 - 800 cm^{-1} range (37). This is compatible with the aforementioned assignment of a triply coordinated hydrogen atom at an even lower frequency. The Ru-H loss feature(s) in the present case may be unobserved due to a low dynamic dipole moment for this vibration.

In Fig. 3, thermal desorption spectra are shown following adsorption of hydrogen on a clean Ru(001) surface [Fig.3(a)], and a surface with pre-adsorbed nitric oxide [Fig. 3(b)]. The data of Fig. 3(a) are in good agreement with previously reported spectra for this adsorption system (38 - 40). The data of Fig. 3(b) indicate that a preexposure to nitric oxide of 55 torr-s [Fig. 2(d)] does not prevent adsorption during subsequent exposure to hydrogen, since 40 to 60% as much hydrogen desorbs in the experiment represented by Fig. 3(b) as from a saturated overlayer of hydrogen on the clean surface. This is consistent with the results of EELS experiments such as those shown in Fig. 4. Here, the surface was exposed to 55 torr-s of NO [Fig. 4(a)] to populate the bridged state, then to hydrogen [Fig. 4(b)]. Within experimental error, the results are identical when deuterium is used rather than hydrogen, as shown in Fig. 4(c). This precludes the possibility that any of the vibrations in Figs. 4(b) or (c) involve hydrogen atoms. The fact that the intensity of the loss feature which is associated with the linear NO has increased in Fig. 4(b) indicates that the hydrogen has displaced some of the bridged NO into the linear sites. The observation that hydrogen adsorbs competitively with the bridged molecular NO (Figs. 2 and 4) is thus consistent with its occupying the threefold sites, as it does also on the Pt(111) (9) and Ni(111) (1,8,10) surfaces.

It should be noted that UPS data indicate a significantly different type of bonding between hydrogen and Ni (41, 42) than between hydrogen and Pd (41, 42), Ir (43) or Pt (42). For the latter group of metals, this difference manifests itself as a large attenuation of photoemission from the d-band, indicating that hydrogen interacts primarily with the sp-band of Ni and the d-band of the other metals. In spite of this difference, recent ab initio calculations for hydrogen adsorption on Ni(111) (44) and Pd(111) (45) surfaces predict that the hydrogen atoms prefer the three-fold symmetric sites in both cases, and the results of these calculations are supported by comparison with experimental energy loss and photoemission data (8, 12, 41, 42, 44, 45).

4. Synopsis

Hydrogen adsorbs dissociatively and competitively with the bridged form of molecular NO on Ru(001), based on data from electron energy loss experiments. This is interpreted in terms of site competition for the three-fold hollow sites between these two species. This interpretation is consistent with all supporting data, as well as with models proposed for hydrogen chemisorption on other surfaces.

Acknowledgments

We would like to acknowledge valuable discussions with Dr. Thomas H. Upton and the financial support of the National Science Foundation (Grant No. CHE 77-16314).

References

1. K. Christmann, R. J. Behm, G. Ertl. M. A. Van Hove and W. H. Weinberg, J. Chem. Phys. 70, (1979) 4168).
2. P. M. Marcus, J. E. Demuth and D. W. Jepsen, Surface Sci. 53 (1975) 501.
3. C. A. Sobrero. E. D. Williams and W. H. Weinberg, in preparation.
4. C.-M. Chan and W. H. Weinberg, J. Chem. Phys. 71 (1979) 2788).
5. W. Ho, R. F. Willis and E. W. Plummer, Phys. Rev. Letters 40 (1978) 1463.
6. R. F. Willis, W. Ho and E. W. Plummer, Surface Sci. 80 (1979) 593.
7. M. R. Barnes and R. F. Willis, Phys. Rev. Letters 41 (1978) 1729.
8. W. Ho, PhD Thesis, University of Pennsylvania (1979).
9. A. M. Barő, H. Ibach and H. D. Bruchmann, Surface Sci. 88 (1979) 384.
10. E. Domany, M. Schick and J. S. Walker, Solid State Commun. 30 (1979) 331.
11. L. D. Roelofs, T. L. Einstein, P. E. Hunter, A. R. Kortran, R. L. Park and R. M. Roberts, J. Vac. Sci. Technol. 17 (1980) 000.
12. S. Andersson, Chem. Phys. Letters 55 (1978) 185.
13. T. E. Madey and D. Menzel, Jpn. J. Appl. Phys. 50, Suppl. 2, Part 2 (1974) 229.
14. E. D. Williams and W. H. Weinberg, Surface Sci. 82 (1979) 93.
15. G. E. Thomas and W. H. Weinberg, J. Chem. Phys. 70 (1979) 954.
16. G. E. Thomas and W. H. Weinberg, J. Chem. Phys. 69 (1978) 3611.
17. D. R. Sandstrom and S. P. Withrow, J. Vacuum Sci. Technol. 14 (1977) 748.

18. D. W. Goodman, T. E. Madey, D. M. Ono and J. T. Yates, Jr., J. Catal. 50 (1977) 279.

19. T. D. Flame and P. D. Ownby, J. Vacuum Sci. Technol. 8 (1971) 661.

20. C. E. Kuyatt and J. A. Simpson, Rev. Sci. Instrum. 38 (1967) 103.

21. G. E. Thomas and W. H. Weinberg, Rev. Sci. Instrum. 50 (1979) 497.

22. G. E. Thomas and W. H. Weinberg, Phys. Rev. Letters 41 (1978) 1181.

23. P. A. Thiel, W. H. Weinberg and J. T. Yates, Jr., J. Chem. Phys. 71 (1979) 1643.

24. P. A. Thiel, W. H. Weinberg and J. T. Yates, Jr., Chem. Phys. Letters 67 (1979) 403.

25. F. A. Cotton and G. Wilkinson, "Advanced Inorganic Chemistry", Interscience Publishers, New York, N.Y. (1972) 713-719.

26. R. Eisenberg and C. D. Meyer, Acc. Chem. Res. 8 (1975) 26.

27. K. Nakamoto, "Infrared and Raman Spectra of Inorganic and Coordination Compounds", John Wiley and Sons, New York, N.Y. (1978) 295-297.

28. E. E. Mercer, W. A. McAllister and J. R. During, Inorganic Chem. 5 (1966) 1881.

29. M. Poliakoff and J. J. Turner, Chem. Commun. (1970) 1008.

30. M. Poliakoff and J. J. Turner, J. Chem. Soc. A (1971) 654.

31. J. R. Norton, J. P. Collman, G. Dolcetti and W. T. Robinson, Inorganic Chem. 11 (1972) 382.

32. J. Müller and S. Schmitt, J. Organomet. Chem. 97 (1975) C54.

33. E. Umbach, S. Kulkarni, P. Feulner and D. Menzel, Surface Sci. 88 (1979) 65.

34. R. Ku, N. A. Gjostein and H. P. Bonzel, Surface Sci. 64 (1977) 465.

35. L. H. Dubois and G. A. Somorjai, Surface Sci. 91 (1980) 514.

36. W. P. Griffith, J. Chem. Soc. A (1969) 211.

37. H. D. Kaesz and R. B. Saillant, Chem. Rev. 72 (1972) 232.

38. L. R. Danielson, M. J. Dresser, E. E. Donaldson and J. J. Dickinson, Surface Sci. 71 (1978) 599.

39. J. A. Schwarz, Surface Sci. 87 (1979) 525.

40. J. Shimizu, K. Christmann and G. Ertl, J. Catal. 61 (1980) 412.

41. H. Conrad, G. Ertl, J. Küppers and E. E. Latta, Surface Sci. 58 (1976) 578.

42. J. E. Demuth, Surface Sci. 65 (1977) 369.

43. D. E. Ibbotson, T. S. Wittrig and W. H. Weinberg, J. Chem. Phys. 72 (1980) 0000.

44. T. H. Upton and W. A. Goddard III, Phys. Rev. Letters 42 (1979) 473.

45. S. G. Louis, Phys. Rev. Letters 42 (1979) 476.

Figure Captions

Fig. 1: Energies of the nitrogen-oxygen vibrations of the two major states of molecular NO on Ru(001) as functions of exposure and coverage (<u>24</u>). The error bars show the typical uncertainty in each individual frequency assignment, approximately ± 1 meV (± 8 cm^{-1}). The lower curve represents bridged NO, and the upper curve represents linear NO.

Fig 2: (a) Representative EEL spectrum of the clean Ru(001) surface.

(b) Vibrational spectrum following a 20 L exposure of H_2.

(c) Vibrational spectrum following an NO exposure of 55 torr-s on the hydrogen pre-treated surface of (b).

(d) Vibrational spectrum following an NO exposure of 55 torr-s on a clean Ru(001) surface, for comparison with (c).

Fig. 3: Thermal desorption of hydrogen from Ru(001). The spectra, taken in digital form, have been smoothed empirically.

(a) Desorption following various exposures of H_2 on clean Ru(001).

(b) Desorption following an H_2 exposure of 30 L on a surface which had been pre-treated with an NO exposure of 55 torr-s.

Fig. 4: Electron energy loss spectra of the Ru(001) surface following sequential exposure to NO [spectrum (a)] and then either H_2 [spectrum (b)] or D_2 [spectrum (c)].

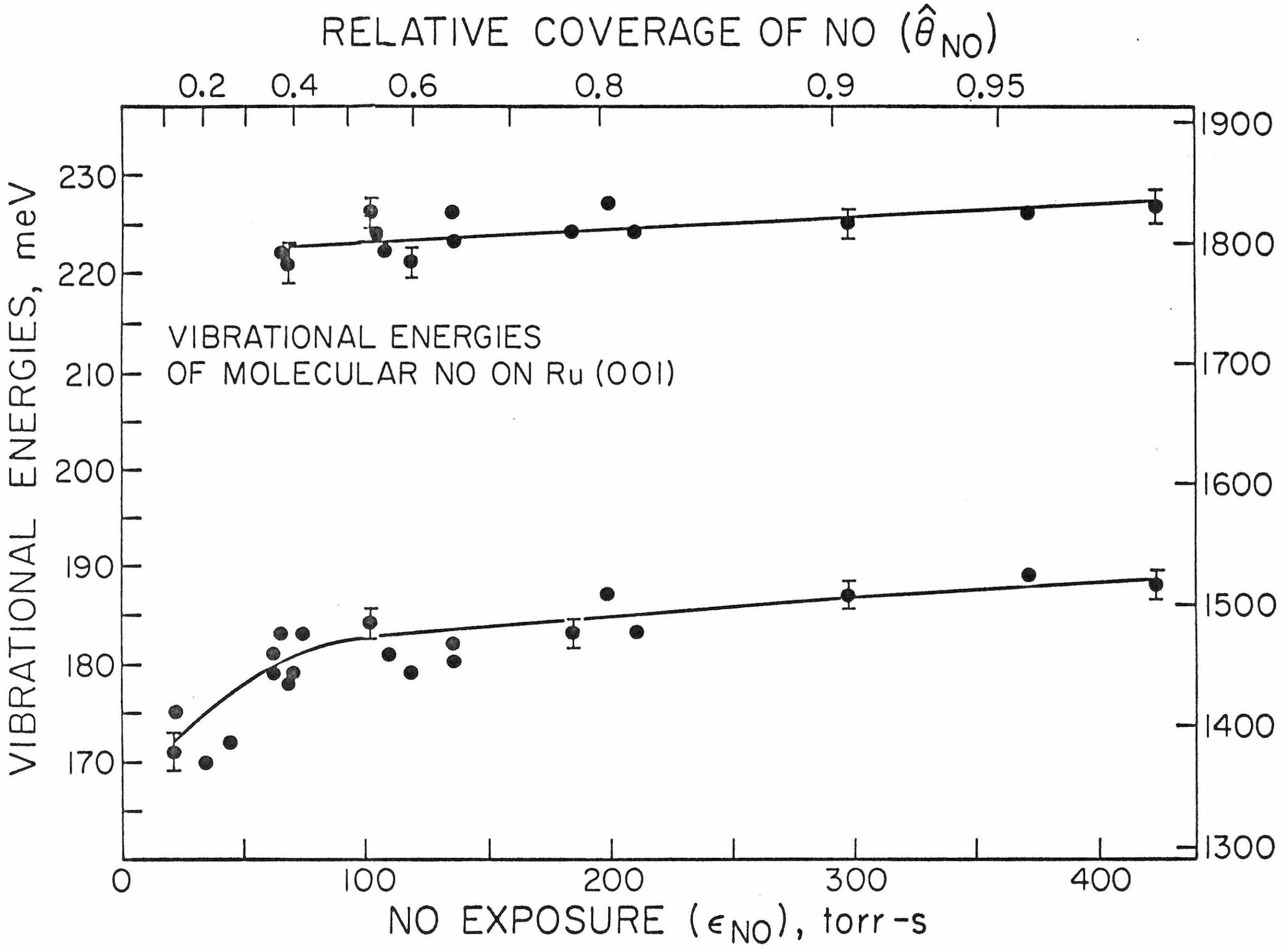
RELATIVE COVERAGE OF NO ($\hat{\theta}_{NO}$)
0.2
0.4
0.6
0.8
0.9
0.95
VIBRATIONAL ENERGIES, meV
230
220
210
200
190
180
170
VIBRATIONAL ENERGIES, cm^{-1}
1900
1800
1700
1600
1500
1400
1300
VIBRATIONAL ENERGIES
OF MOLECULAR NO ON Ru (001)
0
100
200
300
400
NO EXPOSURE (ϵ_{NO}), torr-s

Figure 1.

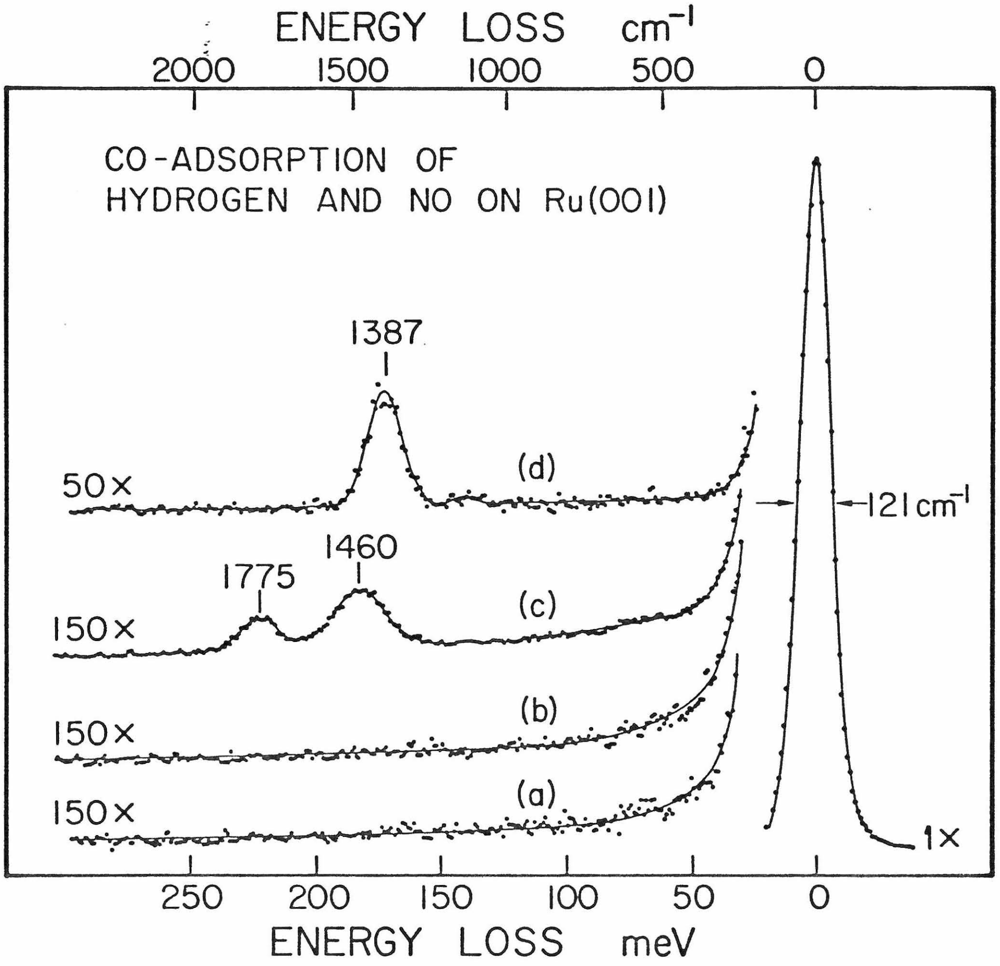
ENERGY LOSS cm^{-1}
2000
1500
1000
500
0
CO-ADSORPTION OF
HYDROGEN AND NO ON Ru(001)
1387
50×
(d)
121 cm^{-1}
1460
1775
150×
(c)
150×
(b)
150×
(a)
1×
250
200
150
100
50
0
ENERGY LOSS meV

Figure 2.

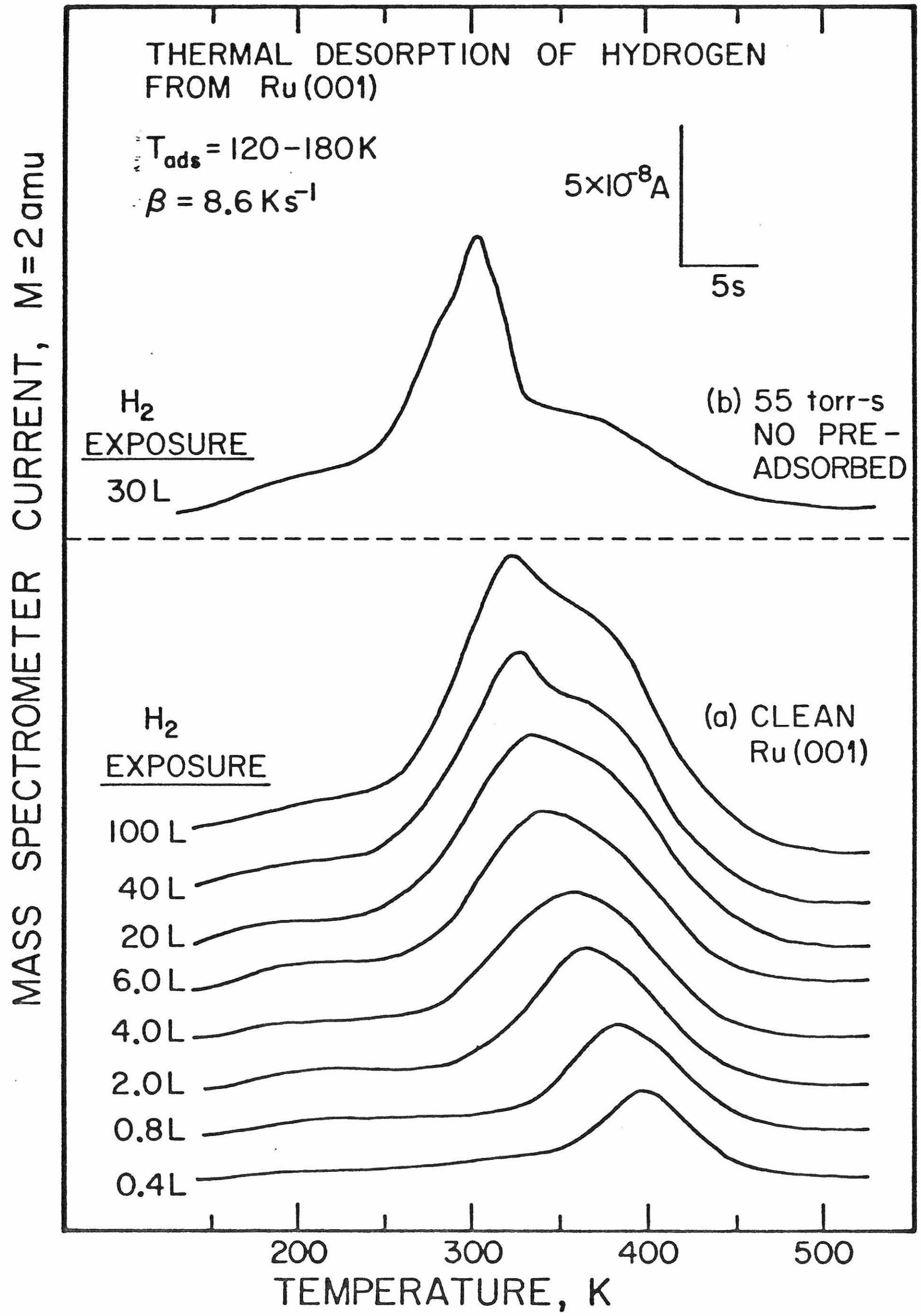
THERMAL DESORPTION OF HYDROGEN FROM Ru(001)
T_{ads} = 120-180K
β = 8.6 Ks^{-1}
5×10^{-8}A
5s
H_2 EXPOSURE
30 L
(b) 55 torr-s NO PRE-ADSORBED
H_2 EXPOSURE
100 L
40 L
20 L
6.0 L
4.0 L
2.0 L
0.8 L
0.4 L
(a) CLEAN Ru(001)
MASS SPECTROMETER CURRENT, M=2 amu
200
300
400
500
TEMPERATURE, K

Figure 3.

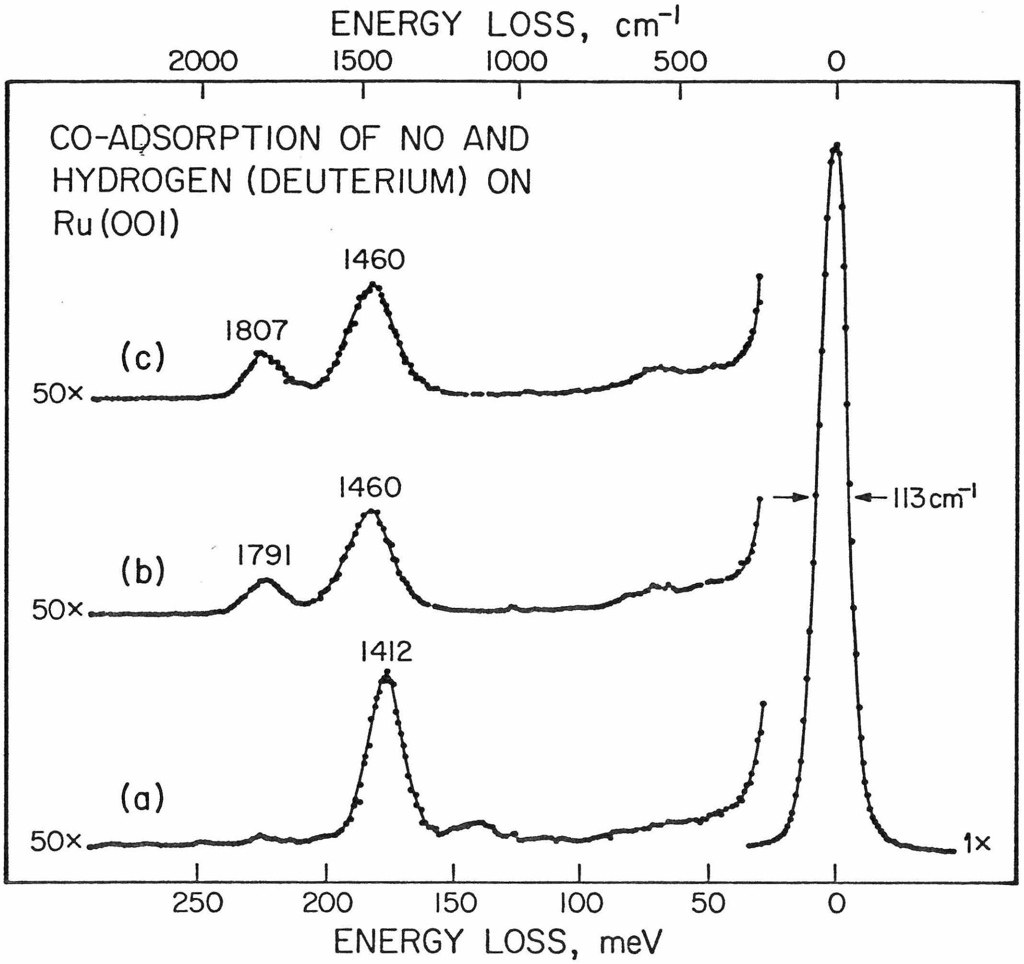
ENERGY LOSS, cm^{-1}
2000
1500
1000
500
0
CO-ADSORPTION OF NO AND
HYDROGEN (DEUTERIUM) ON
Ru(001)
1460
1807
(c)
50×
1460
1791
(b)
50×
113 cm^{-1}
1412
(a)
50×
1×
250
200
150
100
50
0
ENERGY LOSS, meV

Figure 4.

Chapter 9

THE ADSORPTION OF WATER ON THE (001) SURFACE OF RUTHENIUM

1. Introduction
2. Experimental Details
3. Results and Discussion
    - 3.1. Vibrational Spectra at 95 K
        - 3.1.1 The v_{OH} Mode
        - 3.1.2 The Intramolecular Deformation Mode, v_s
        - 3.1.3 Relative Intensities of the v_{OH} and v_s Features
        - 3.1.4 Librational and Translational Modes
        - 3.1.5 AREELS and the Scattering Mechanism
    - 3.2 Thermal Desorption Data
    - 3.3 Changes in Work Function
    - 3.4 LEED and ESDIAD Data
    - 3.5 Heating Experiments
    - 3.6 Vibrational Spectra at 165 K
        - 3.6.1 Frequencies and Assignments
        - 3.6.2 AREELS and the Scattering Mechanism
    - 3.7 Ultraviolet Photoemission Spectroscopy
    - 3.8 Exchange Between H_2O and D_2
4. Comparisons with Other Experiments
5. Summary

Abstract.

The properties of H_2O adsorbed on Ru(001) at 95 K have been studied using a variety of techniques. The geometrical properties of the overlayer, deduced from LEED and ESDIAD (1) data, indicate that layered, hydrogen-bonded clusters of H_2O molecules form which have specific orientation with respect to the hexagonal metal substrate. The vibrational, electronic and thermodynamic properties of the first two layers of H_2O molecules are distinct from the properties of ice multilayers. At an adsorption temperature of 165 K, only the first two layers are adsorbed, and the H_2O lattice is more well-ordered than at 95 K, which is an effect analogous to the irreversible vitreous-to-cubic phase transition which occurs at about this temperature in bulk ice. The inelastic electron scattering mechanism has been investigated and angle-resolved scattering experiments have enabled the resolution of overlapping vibrational features with different angular distributions of intensity. The scissoring mode frequency of chemisorbed water at 1510 cm^{-1} is indicative of bonding via electron donation from the $3a_1$ and/or $1b_1$ molecular orbitals of H_2O to the metal, and this may be related to the large H-O-H bond angle of $116 \pm 10^{\circ}$ which was derived from ESDIAD results (1).

1. Introduction

The properties of H_2O adsorbed on metallic surfaces are interesting from several points of view. Firstly, the interaction of water with metal surfaces is of fundamental importance in relation to electrochemical processes, and vacuum techniques provide the only direct means available for spectroscopically characterizing the water-metal interface without interference from the liquid medium. Chemically, H_2O is isovalent with H_2S and may serve also as a reference molecule in future studies of H_2S adsorption, which is important as an agent of hydrogen embrittlement and catalyst poisoning.

There are relatively few reported investigations of water adsorption on clean metal surfaces. Those which are most important to the discussion of the present results include the electron-stimulated desorption ion angular distribution (ESDIAD) and thermal desorption mass spectrometry (TDMS) measurements of Madey and Yates (1), who examined H_2O adsorbed on Ru(001). Also, very recently, Ibach and Lehwald (2) and Sexton (3) have used electron energy loss spectroscopy (EELS) and TDMS to investigate water adsorbed on Pt surfaces. In all cases there is evidence that interactions occur between water molecules at submonolayer coverages, which is not surprising in view of the well-known propensity of H_2O molecules for hydrogen-bond formation (e.g. 4 - 7).

In the present investigation, we have studied the adsorption of H_2O on Ru(001) using EELS, TDMS, low-energy electron diffraction (LEED) and ultraviolet photoelectron spectroscopy (UPS). Strong intermolecular interactions (i.e. hydrogen bonds) are evident in the vibrational and geometric properties of this adsorption system. In addition, the present investigation contains several unique features. It is the first detailed report of the scattering mechanism of the vibrational modes of H_2O molecularly adsorbed (8) on a metal surface, from which both dipolar and nondipolar scattering mechanisms are evident. This investigation of the scattering mechanism has facilitated the assignment of overlapping features with different angular distributions of intensities. It is also the first report of an irreversible phase transformation of water, analogous to the vitreous → cubic transformation of bulk ice, but studied on a molecular scale. Finally, it is one of the few cases in which EEL has been able to clarify a model proposed previously on the basis of ESDIAD and TDMS data (1). Thus, a uniquely detailed description of the properties of this adsorption system has been obtained.

2. Experimental

The experiments were performed on Ru(001) single crystals which were oriented, cut and polished as described elsewhere (9). Two separate stainless steel, ion pumped, ultrahigh vacuum systems were used in these experiments. The high resolution electron scattering experiments were performed in a chamber with a base pressure of 4×10^{-11} Torr; after a typical series of water exposures the residual pressure rose to a maximum value of 2×10^{-10} Torr. The crystals were exposed to gas by backfilling the entire vacuum chamber through a leak valve. Water was prepared by distillation at atmospheric pressure, followed by repeated freeze-thaw cycles under vacuum to remove impurities. Mass spectrometric analyses of the water prepared and introduced into the chambers in this manner indicated that initial displacement and/or fragmentation, possibly at chamber walls and ionization filaments, produced significant quantities of CO and H_2. After prolonged exposure to H_2O, the CO was eventually reduced to undetectable levels and the H_2 was at a constant level attributable to fragmentation of H_2O in the ionizer, i.e. the ion current at M = 2 amu was approximately 2% of the ion current at M = 18 amu, corrected for initial base pressure levels. All of the experimental results reported here were performed after the vacuum chamber had been "conditioned" in this manner. The LEED and Auger electron spectroscopy (AES) experiments were performed in a separate system with a base pressure of 6×10^{-11} Torr, using a second Ru(001) crystal. Both chambers were equipped with quadrupole mass spectrometers for monitoring gas purity and performing TDMS experiments; comparison of coverage-dependent TDMS features revealed that exposures of H_2O and CO within the two systems were approximately equivalent (±10%). Gas exposures were monitored with a nude Bayard-Alpert ionization gauge. All gas exposures are reported in units of Langmuirs, where $1 \text{ Langmuir} \equiv 1 \text{ L} \equiv 1 \times 10^{-6}$ Torr s, corrected for the ionization cross section of the gas relative to nitrogen (<u>10</u>). In the case of H_2O, the relative cross section is 0.9.

The crystals were spotwelded to two parallel Ta wires, 0.010" in diameter, and were heated resistively by passing current through these wires. The temperature was monitored using a 95%W/5%Re vs. 74%W/26%Re thermocouple, 0.003" in diameter, spotwelded to the edge or face of the crystals. Temperature was correlated with thermocouple voltage below

273 K using the calibration data of Sandstrom and Withrwow (11). Both crystals were cooled conductively with liquid nitrogen reservoirs. In the experimental system for EELS, the sample manipulator was a differentially pumped, rotatable cold finger(57), and the sample cooled from 1600 K to 100 K within five minutes, so that adsorption of background gases between cleaning and exposing the crystal to water was negligible. In some experiments the crystal temperature was maintained at 165 ± 5 K (ca. 165 K) during the exposure to H_2O, after which it cooled to 95 K within 20 s in the EELS apparatus, and to 115 ± 5 K (ca. 115 K) within approximately 90 s in the LEED apparatus. It was found that rapid cooling (to prevent slow desorption) and low base pressure (to prevent readsorption at lower temperature) were essential in obtaining reproducible thermal desorption data following exposures at 165 K.

The crystals were cleaned in several ways. AES showed that the surface was initially contaminated by sulfur, silicon and possibly carbon (12). These were removed by repeated thermal cycling between $\leq$400 K and 1100 K in a background pressure of 1×10^{-7} Torr O_2. In the EELS system, the surface was judged to be clean, following thermal cleaning in O_2, if the inelastic scattering spectrum was featureless. Residual oxygen was usually removed by heating the Ru crystal in vacuum to 1600 K, although both EELS and AES indicated that occasionally a more tenacious oxide formed (13) which was removed in one of two ways: (1) Prolonged heating at 1600 K in vacuum; or, occasionally, (2) Argon ion bombardment. The vibrational spectra of H_2O adsorbed on the clean Ru surface were invariant following cleaning via either of these two methods. Since the EELS and AES both indicated that some oxygen remained on the Ru surface following desorption of molecular H_2O, the crystal was heated to 1570 K following each exposure to H_2O.

The spectrometer used for the electron energy loss spectroscopy and the ultraviolet photoelectron spectroscopy has been described in detail elsewhere (14). The 4.0 eV beam of incident electrons had a full-width at half-maximum of 11 to 16 meV in these experiments. In most specular scattering experiments, the crystal was grounded and the electron beam was refocused slightly following adsorption of the gas. In the angle-resolved electron energy loss spectroscopy (AREELS) measurements, the crystal was usually biased to compensate for the change in work function resulting from adsorption of gas. All of the results reported here are independent of which of these methods was used, except for the intensities of the inelastic features relative to the intensity of the elastic beam in specular scattering. These ratios were found to vary also for scattering from a surface with adsorbed carbon monoxide, depending upon the bias voltage applied to the sample. Therefore, absolute scattering cross sections are not derived from these data; however, the relative intensities of various inelastic features of H_2O can be compared, since these were unaffected by the above experimental parameters. For reference in the AREELS data, typical angular distributions of a 4.0 and a 2.5 eV beam of electrons, elastically scattered from a clean Ru(001) surface at ground potential, are shown in Fig. 1. The broader distribution obtained at V_i = 2.5 eV may reflect the influence of relatively larger external electromagnetic fields at this energy.

A description of the system used in the LEED and AES experiments is available elsewhere (12). The LEED pattern which resulted from water adsorption was observed visually only in the range of incident beam energies between 16 and 60 eV, i.e. only the low-order spots were distinguishable. This explains why the pattern was not observed in another laboratory (1), where low beam voltages were not used. Incident beam currents below 1 μA were employed to minimize electron beam damage, which was evident nonetheless after observation periods of approximately 20 to 60 s.

3. Results and Discussion

3.1 Vibrational Spectra Following Adsorption at 95 K

The isolated water molecule is characterized by C_{2v} symmetry. There are three fundamental internal vibrations: the symmetric O-H stretch, the asymmetric O-H stretch, and the deformation, or scissoring (v_s) mode. Adsorption on a metal surface, or coordination with another atom, constrains the molecule so that the gas phase translational and rotational modes are "frustrated" and may be observed also in the vibrational spectra. Figure 2 illustrates the nine normal modes of a single water molecule adsorbed on a metal surface so that local C_{2v} symmetry is preserved, i.e. without regard for the additional symmetry which may be imposed by the substrate. The vibrational spectra of isolated water molecules (6,16,17), aquo-metallic complexes (18-23) and crystalline ice (6,24,25) have been studied extensively, and these results may be used to clarify the vibrational spectra of water adsorbed on metallic surfaces. In these compounds, the spectral region between 3150 and 3750 cm^{-1} corresponds to the symmetric and asymmetric O-H stretching modes, v_{OH}, and the region between 1500 and 1650 cm^{-1} corresponds to v_s. Absorption bands belo 900 cm^{-1} have been assigned to frustrated rotations ("librations") a frustrated translations.

The EEL spectra of H_2O adsorbed on Ru(001) exhibit features in similar energy ranges, as shown for various coverages of H_2O in Fig. Note that the spectrum of the clean metal surface is featureless, indicating the absence of contamination. Since the features due t tation of the v_{OH} and v_s modes are surprisingly weak, the range of e loss in which they occur is shown with an expanded ordinate scale ir Fig. 4.

3.1.1 The v_{OH} Mode

Within experimental uncertainty, the frequency ν_{OH} is const throughout the coverage range where it is observable in specular sca tering, 3350 ± 50 cm^{-1}. The large uncertainty associated with this value reflects the broadness and weakness of the feature in each ind vidual measurement, as well as the typical reproducibility of identic measurements. In specular scattering, the half-width of the OH stre mode is constant at approximately 500 cm^{-1}. It appears that several ferent v_{OH} features overlap in the specular scattering measurements. overlapping peaks contribute to the broadness of the composite featu can be distinguished using angle-resolved electron energy loss spect copy (AREELS), as discussed in Section 3.1.5 below.

The position of the O-H stretch at 3350 cm^{-1} is characteristic of intermolecular hydrogen bonding (e.g. 7). In crystalline ice, for example, hydrogen bonding results in infrared absorption between 3150 and 3380 cm^{-1} (24), compared to OH stretching frequencies between 3630 and 3750 cm^{-1} for isolated water molecules in the gas phase or in inert gas matrices (6,16,17). The invariance of the peak position in the EEL spectra from the lowest exposure at which it is distinguishable, approximately 0.2 L (cf. Fig. 3), to an exposure which produces epitaxial ice, 5.6 L, indicates that intermolecular hydrogen bonding occurs throughout this coverage range. In no case do we observe the low frequency O-H stretch which was reported at 2850 to 2870 cm^{-1} for H_2O adsorbed on Pt(100) (2).

3.1.2 The Intramolecular Deformation Mode, v_s

The feature in the EEL spectra which occurs at 1500 to 1640 cm^{-1} (cf. Fig. 4) is due to excitation of the "scissoring" mode, v_s. This is consistent with the isotopic frequency shift of 1.3 to 1.4 (ν_{H_2O}/ν_{D_2O}) which is observed for this mode in the corresponding EEL spectra of D_2O. Its appearance following exposures as low as 0.03 L, shown in Fig. 4, is evidence that water adsorbs molecularly throughout the coverage range studied, even when the feature due to the v_{OH} mode is undetectable.

The frequency of the deformation mode is shown in Fig. 5 as a function of increasing exposure (coverage) of H_2O. It has been shown experimentally that ν_s is lowered from its gas phase value, 1595 cm^{-1}, when the water molecule binds to a metal atom (21, 22). The relative downshift in frequency scales approximately with the strength of the metal-water bond (22), and is presumably due to transfer of some electron density to the metal atom from the H_2O molecule (22). Values of ν_s as low as 1498 cm^{-1} have been reported for metal-sulfate and metal-selanate-aquo complexes (21). It is noteworthy that electron transfer from molecular water to the metal has been postulated even for such a strongly basic metal as Li, based upon experiments with matrix isolated Li-H_2O adducts (23) and H_2O adsorbed on evaporated Li films (26).

The lowering of ν_s relative to its gas phase value may correlate with the relatively large H-O-H bond angle derived from ESDIAD data for the first chemisorbed layer of H_2O: 116 ± 10^0, to be compared with 104.5^0 for gaseous H_2O (6) and 109^0 for crystalline ice (6). [It should be remembered, however, that ESD ion angular distributions are subject to errors such as those due to the interaction of the escaping ion with its image charge in the metal and possible final-state effects (57).] As discussed in detail by other authors (22), a rationalization for the relationship between ν_s and the H-O-H bond angle is available from the photoelectron spectroscopy of water. Removal of an electron from either the $1b_1$ ("oxygen lone pair") or $3a_1$ ("oxygen-hydrogen nonbonding) orbitals of gaseous water causes an increase of the H-O-H bond angle and a concomitant decrease in ν_s (27). As a result of the ionization of these two orbitals, ν_{OH} either decreases (by 440 cm^{-1}) or remains constant, respectively. The decrease in ν_s and the possible widening of the H-O-H bond angle which is observed for H_2O chemisorbed on Ru(001) can be accounted for therefore by partial electron donation from the molecular $3a_1$ and/or $1b_1$ orbitals to the metal substrate. In crystalline ice, the ν_s mode causes a broad infrared absorption feature centered at 1650 cm^{-1} (6, 24), although this assignment is complicated by possible contributions from the overtone of the librational modes at 800 to 840 cm^{-1} (24, 25).

Therefore, it is proposed that the data of Fig. 5, following adsorption of H_2O at 95 K, reflect a smooth progression, from a state at low coverage ($\leq$2 L) in which a large fraction of the adsorbed water is bound directly to the Ru surface, to a state at higher coverage in which most of the water molecules are bound in an ice-like multilayer. Further evidence will be presented that the vibrational spectra at low coverage are particularly sensitive to the first layer of chemisorbed H_2O molecules.

3.1.3 Relative Intensities of ν_{OH} and ν_s Features

It has been proposed that a coverage-dependent structural transformation of H_2O clusters adsorbed on Pt(100) at 150 K is indicated by the change in the relative EEL spectral intensities of ν_s and ν_{OH} with coverage (2). In that case, the intensity ratio, $I(\nu_s)/I(\nu_{OH})$, decreased by a factor of 10^2 with increasing coverage of H_2O. It has been observed also that the ratio of the IR absorption coefficients for these two modes decreases by a factor of 12 with increasing size of matrix-isolated water clusters, which is attributed to hydrogen bond effects for water and other systems (7, 16).

The integrated intensities of the EEL features due to ν_{OH} and ν_s for H_2O adsorbed on Ru(001) at 95 K, and the ratio of these intensities, are shown in Fig. 6. Within experimental error, the relative intensities of the two features remain at a constant value at all coverages. To the extent that this ratio really reflects changes in the degree of intermolecular hydrogen bonding or the structure of the adsorbate cluster, these data indicate that no changes occur as coverage increases, up to and including the point of development of the ice multilayer. Although this is consistent with the conclusions of Section 3.1.1, it must be remembered that relative scattering cross sections in are strongly dependent on the scattering mechanism (28), with adsorbate orientation and admolecule-metal spacing being very important factors in dipolar scattering cross sections. Both dipolar and nondipolar excitations occur in this system making comparisons of relative intensities complex.

It has been reported that the integrated intensity of the absorption due to the O-H stretching mode absorption increases linearly with increasing exposure (coverage) also in IR reflectance experiments with H_2O adsorbed on Ru(001) (29).

3.1.4 Librational and Frustrated Translational Modes

The strongest features in the EEL spectra are those below 1000 cm^{-1}, as shown in Fig. 3. They are assigned both on the basis of their frequencies, shown in Fig. 7, and their isotopic frequency shifts, shown in Fig. 8. At very low exposures of H_2O, i.e. ≤ 0.08 L, there is a single loss feature in this energy range, illustrated clearly in Fig. 9, at 370 to 400 cm^{-1}. Adsorption of D_2O causes this feature to shift by a factor of 1.22 to 1.25 (cf. Fig. 8). As shown in Fig. 8, simple moment-of-inertia arguments for isolated water molecules predict ratios of 1.41 to 1.34 for the frequencies of the librational modes, whereas the frustrated translational mode perpendicular to the surface (the "metal-oxygen" stretching mode of chemisorbed H_2O) should shift in frequency by a factor of 1.04. Therefore, this feature is attributed to two overlapping peaks: a frustrated translational mode at 370 to 400 cm^{-1} and a librational mode, which change in frequency by different amounts upon deuteration. This assignment is supported by EELS measurements following adsorption at 165 K, in which the metal-oxygen vibration occurs at 370 to 400 cm^{-1}. A Ru-OH_2 vibration at this energy is also consistent with bonding through the oxygen atom to one or two metal atoms, based on an analogy with aquo-metal complexes. In the IR spectra of such complexes, this vibration occurs between 310 and 490 cm^{-1} (18,19). This assignment agrees also with the conclusion of Section 3.1.2 that, at low coverages of H_2O, the vibrational spectra are particularly sensitive to the H_2O molecules which are in direct contact with the metal surface.

Following higher exposures at 95 K, only the librational modes characteristic of H_2O aggregates are visible in the energy range below 1000 cm^{-1}. The librational modes of water molecules in aquo-metal complexes have been reported to occur in vibrational spectra at 450 to 890 cm^{-1} (18 - 20). Thus, the data of Fig. 7 indicate that the frequencies of the EEL features labelled ν_L' and ν_L'', at 440 to 890 cm^{-1} following exposures of H_2O greater than 0.08 L, are appropriate to their assignment as frustrated rotations. Furthermore, following exposures of H_2O (D_2O) greater than 0.08 L, the average experimental values of the isotopic frequency ratios (represented by the horizontal dashed lines of Fig. 8) are 1.40 and 1.37. This confirms the assignment of ν_L' and ν_L'' as librations.

An experimental investigation of the scattering mechanism which governs these losses [Section 3.1.5] leads to the conclusion that they are dipolar-enhanced features. This implies that they are subject to the "dipole selection rule" (30) in which a dipolar allowed vibration must have a nonzero component of e^* perpendicular to the surface, where e^* is the derivative of the dipole moment with respect to some internal coordinate. As shown in Fig. 2, none of the librational modes are dipolar allowed for a molecule adsorbed in a site with local C_{2v} symmetry. Figure 10(c-f) illustrates possible adsorption geometries in which the local symmetry is reduced to C_s or C_1 as a result of adsorption. In the latter two point groups, one or more of the librational modes, respectively, become dipolar active. We regard the configuration of Fig. 10(d) as a physically improbable model of chemisorbed H_2O, for the following reasons:

(1) For a strongly distorted configuration, one would expect the vibrational spectrum to be quite different from gas phase H_2O. However, all the EEL spectral features can be interpreted satisfactorily in terms of slightly perturbed modes of the gas phase molecule; and

(2) ESDIAD data (1) support a structure, even at lowest H_2O exposures, in which the O-H bonds are directed away from the metal surface, e.g. as in Fig. 10(a), (b), (c) or (e).

A configuration such as Fig. 10(f), with hydrogen bonding to the metal surface, is considered unlikely for the following additional reasons:

(3) There is no report of an H_2O ligand, in a metal complex or matrix isolated cluster, in which the H_2O molecule does not bind through the oxygen atom to the metal (18,22,23); and

(4) The vibrational frequencies of the modes which appear to be sensitive to the Ru-OH_2 interaction, ν_s and the metal-oxygen stretch, are consistent with bonding through the oxygen to the metal, as discussed previously.

Rather, a model in which clusters of H_2O molecules form, wherein molecules within successive layers can occupy a distribution of orientations relative to the surface (such as in Fig. 10) and are coupled via hydrogen bonds, provides an adequate and consistent explanation of the observed dipolar enhancement of the librational modes.

An exact assignment of ν_L' and ν_L'' in terms of the librational modes of Fig. 2 (ν_5, ν_6 or ν_7) is not possible due to the evidence that H_2O aggregates form. The two librational modes which are resolved clearly between exposures of 0.1 and 2.2 L in Figure 3 may represent vibrations of two distinct types of H_2O molecules or two different modes within the cluster. The assignment of multiple IR absorptions to specific H_2O librations is controversial even in the simpler systems which have been studied, i.e. aquo-metallic complexes (18-20).

At exposures greater than 3 L, the two low-frequency losses are replaced by a single broad feature at 780 ± 20 cm^{-1} which indicates the formation of an ice multilayer. This is confirmed also by TDS data. The observed frequency is similar to that of the corresponding feature in the IR spectra of ice (6,24). for which there is a broad, strong absorption band centered at 800 to 840 cm^{-1} which is assigned to frustrated rotations. Above 3 L also, a shoulder appears on the elastic peak at 280 cm^{-1}, as indicated in Fig. 7. This frequency is insensitive to deuteration, consistent with its assignment as a frustrated translation within an H_2O multilayer. In ice, for comparison, a frustrated O··· O translation causes absorption of far IR radiation at 230 cm^{-1} (6,24). The energy losses at low frequency thus show that ice formation occurs for exposures of H_2O greater than approximately 3 L.

3.1.5 AREELS and the Electron Scattering Mechanism

Typical angle-resolved inelastic scattering spectra, taken by rotating the electron energy analyzer along the polar angle, θ_s, are shown in Fig. 11. It is assumed that nondipolar scattering is distinguished in these measurements by a relatively isotropic distribution of scattered electrons away from the specular direction (31). These data show that the low-energy loss features decrease in intensity rapidly away from the specular direction, as does also the elastic peak, whereas v_{OH} and v_s do not. This has been illustrated in Fig. 12 by plotting the intensity of the inelastically scattered electrons at specific loss energies as functions of scattering angle. These data show that the librational modes are dipolar enhanced, as discussed previously. It is interesting to note that the lowest frequency loss feature changes from 440 to 520 cm^{-1} as $\Delta\theta_s$ changes from zero; again, this is consistent with the assignment of two overlapping features which decrease at different relative rates with respect to $\Delta\theta_s$, thereby causing the apparent change in frequency.

The scissoring mode, ν_s, is only enhanced in intensity by a factor of two in the specular direction, which may indicate that contributions from dipolar and nondipolar scattering are both significant in this feature. The origin of the nondipolar scattering mechanism is unknown. Possibilities include impact scattering (31) via interaction with the short-range potential of the dipole and a resonance-like scattering (35), which is known to occur in electron scattering from gas phase molecules.

In the data of Fig. 11, the shape of the feature assigned to ν_{OH} changes with decreasing $\Delta\theta_s$. The broad loss centered at 3370 cm^{-1} for $\Delta\theta_s = 0^0$ appears to split into a relatively sharp peak at 3520 cm^{-1} and a shoulder at 3240 cm^{-1}. In repeated AREELS experiments under various conditions of exposure, the shape of the ν_{OH} feature always changed with $\Delta\theta_s$, sometimes resolving into two features as shown in Fig. 11 and sometimes developing a high-frequency asymmetry centered at about 3500 cm^{-1}. The data of Fig. 11 can be explained if the ν_{OH} feature in specular scattering consists of at least three components, one of which (at approximately 3370 cm^{-1}) is dipolar allowed and two of which (at 3520 and 3270 cm^{-1}) are not. This hypothesis accounts for both the broadness of the ν_{OH} feature in specular scattering and for its change of shape in off-specular scattering, where the dipolar enhanced 3370 cm^{-1} feature would decrease rapidly in intensity. From IR reflectance spectra of H_2O adsorbed on Ru(001) under similar conditions, a broad band (half-width of 430 cm^{-1}) due to ν_{OH} is observed at exposures up to 2 L, centered at 3400 to 3450 cm^{-1} (29). Since the dipolar selection rule applies quite rigorously to IR reflectance measurements, it must be concluded that the IR absorption is due to dipolar allowed excitation(s), in agreement with our assignment of a dipolar allowed excitation in the EEL spectra at about 3370 cm^{-1}.

We tentatively assign the 3520 cm^{-1} feature as due to the O-H stretch of nonhydrogen bonded OH groups of molecular water, in agreement with water-oxygen co-adsorption experiments to be discussed elsewhere (32).

The origin of the EELS feature at 3270 cm^{-1} is uncertain, although it may contain contributions from multiple (impact) scattering involving $2\nu_s$, $\nu_s + 2\nu''_L$, and/or $4\nu''_L$. Such overtones and combinations have been postulated to occur in this frequency range in the IR spectra of ice and metal hydrates (6,33,34). Similarly, the broad features centered at 2270 to 2360 cm^{-1}, 4040 to 4090 cm^{-1}, 4790 to 4820 cm^{-1}, and 6440 to 6500 cm^{-1} (cf. Fig. 4 and Fig. 13) may be due to multiple loss events and/or true vibrational combinations involving ν_{OH}, ν_s and/or ν''_L.

Experiments were performed also to determine whether the resonance-like excitation of ν_{OH}, which has been observed in scattering from hydroxyl groups adsorbed on NiO(111) by Andersson and Davenport (35), occurs for H_2O on Ru(001) also. The evidence for the resonance-like behavior lay in the increase of the ν_{OH} scattering cross section with decreasing impact energy (35). In the case of NiO(111), the presence of 6 Å of insulating oxide may have been critical to electronic isolation of the resonant orbital, however. Following an exposure of 5.6 L of H_2O on Ru(001), the intensity of the

EEL feature due to v_{OH} relative to the other features in the spectrum (v_S and v_L) and also relative to the elastic peak was invariant within experimental error (±10%) for electron impact energies between 2.5 and 4.0 eV, with the crystal biased at -0.6 eV. Furthermore, the intensity of the first overtone of v_{OH} was less than 3% that of the fundamental mode, as shown in Fig. 13, assuming that the weak feature at approximately 6470 cm^{-1} is the first overtone of v_{OH} ($2\nu_{OH} = 6660$ cm^{-1}), lowered in frequency due to anharmonic effects. If this mode is instead a combination mode or multiple-loss mode, then the intensity of the first overtone of v_{OH} is even lower than 3% of the fundamental. For an impact energy of 4.0 eV, Andersson observed $I_1/I_2 \simeq 10$. Thus, both the relative intensity of the overtone and the impact energy dependence of the relative intensity are inconsistent with the resonant-like scattering behavior reported previously for OH groups on NiO (35).

3.2 Thermal Desorption Data

Typical thermal desorption (TD) spectra of H_2O are shown in Fig. 14 following various exposures of H_2O to the Ru(001) surface at 115 K. Three features are apparent at peak temperatures of 208 to 217 K, 177 to 188 K and 169 K. We will define these states as A, B and C, respectively. The TD spectra indicate that the highest-temperature state saturates first between 2 and 3 L. Based upon all the evidence accumulated for this system, we make the following assignments: the desorption feature A is due to chemisorbed water, i.e. water bound directly to the metal; B represents water molecules in a second, hydrogen bonded layer; and C is a consequence of desorption from an ice multilayer. These assignments have been proposed by other authors for H_2O desorption from Ru(001) (1). Since the TDMS features do not populate sequentially with increasing coverage (cf. Fig. 14) and since all available data show that clusters of H_2O molecules form on the surface at all exposures, no attempt has been made to assign absolute coverages on the basis of TD spectra alone. At this point, we note only that the total amount of H_2O adsorbed varies linearly with exposure at 115 K, as shown in Fig. 15. As discussed by previous authors (2,36), this implies a coverage-independent sticking probability of unity, and supports the aggregation model.

Desorption from an ice multilayer has been reported also in experiments with H_2O on Rh(111) (37), Pt(100) (2), Pt(111) (38) and Ir(110) (36) substrates. The temperature at which the maximum desorption rate occurs is insensitive to the metal substrate, as expected, occurring between 150 K and 170 K in all cases (2,36 - 38). Further, this desorption feature does not saturate with increasing exposure to H_2O at temperatures below 150 K. This behavior is evident in the data of Figs. 14 and 15.

A thermal desorption spectrum following saturation of the surface with H_2O at 165 K is shown in Fig. 13. At this temperature, a multilayer of ice does not form; only the A and B states are populated, and saturation is attained with an exposure of 2.2 L. The latter fact is clear from the data presented in Fig. 14. The achievement of saturation at 165 K with 2.2 L of H_2O is consistent with the conclusion from the vibrational data of Section 3.1.4 that, above 3 L exposures at 95 K, layers of epitaxial ice form. This is reflected also in the data of Fig. 6, where the intensities of ν_{OH} and ν_s following adsorption at 95 K diverge sharply from the intensities following adsorption at 165 K, between H_2O exposures of 1 and 2 L.

The EEL and UP spectra, to be discussed later, indicate that clusters of hydrogen bonded molecules still form at 165 K, and that the chemical composition of the overlayer is not significantly different than following adsorption at 95 K. This supports the proposed assignments of the A and B states. In addition, it was observed that the relative magnitude of the A state was extremely sensitive to traces of preadsorbed H_2 or CO, as would be expected if the A state is the first layer of chemisorbed molecules.

If one assumes that the preexponential factor of the desorption rate coefficient has a value between 10^{12} and 10^{14} s^{-1}, then the peak temperature of the A state at 210 K implies an activation energy for desorption of 12.1 ± 1.0 kcal/mole (39). For the B state at 180 K in Fig. 14, the corresponding value is 10.7 ± 0.8 kcal/mole. Alternatively, the half-width of the high-temperature edge of the A desorption peak can be used to derive unusually high values for the preexponential factor and the activation energy of desorption: 10^{22} s^{-1} and 21 kcal/mole, respectively, using the peak shape analysis of Chan et al. (40). Using the latter method, similar anomalous values have been reported for desorption from the chemisorbed state of H_2O on Rh(111) (37). The energy of desorption from an ice multilayer (the C state) has been found to be 11.5 kcal/mole on Ru(001) (1), 10 kcal/mole on Pt(111) (38), and 10.1 kcal/mole on Ir(110) (36). Attempts were made also to derive the heat of sublimation of the ice multilayer based upon the present experimental data; however, analyses of the shape of the low-temperature edge of desorption feature C in several sets of experimental data did not yield consistent or reasonable values. Based upon comparison of the TDS peak shapes obtained in two different experimental systems, it is concluded that desorption from crystal support wires may contribute significantly to the intensity of the C state at relatively low exposures, i.e. below 2.2 L of H_2O.

The value of 12 kcal/mole for the desorption energy from the first layer is in qualitative agreement with the observation that clusters of molecules form at all coverages at 95 K. It has been estimated that hydrogen bond strengths in ice are from 4 to 8 kcal/mole of O-H bond (6,7), so that adsorption of H_2O by formation of two hydrogen bonds appears to be only slightly less favored energetically than adsorption directly on the surface. The "second layer" represented by the B state may be additionally stabilized, relative to the ice multilayer, by a long-range interaction with the metal or by a synergistic strengthening of the hydrogen bonds formed with the first layer H_2O molecules, as suggested elsewhere (21).

It is also noteworthy that approximately equal amounts of H_2O desorb in the A and B states following saturation at 165 K, as shown in Fig. 14, implying that approximately equal amounts of first- and second-layer H_2O molecules are present under these conditions.

3.3 Changes in Work Function

The qualitative change in work function, $\Delta\phi$, was measured as a function of H_2O exposure by: (1) Measuring the bias potential required to create an "electron mirror" at the crystal, i.e. to reflect the total incident beam current; and (2) Measuring the bias potential required to maximize the elastically scattered beam, but without establishing condition (1) above. Although the absolute magnitude of $\Delta\phi$ measured via these two methods was different, qualitative features of $\Delta\phi$ were consistent. Following adsorption of H_2O at 95 K, the work function decreased monotonically up to exposures of approximately 2 L. At higher exposures, $\Delta\phi$ remained constant between -0.5 and -0.7 eV. A negative change in work function is usually assumed to indicate molecular adsorption via the oxygen atom, as discussed elsewhere (36,41). However, one would not expect the work function to decrease monotonically up to the work function of ice if successive layers fill in strict sequence. A monotonic decrease is more consistent with cluster formation at all coverages, in which case the sign of the change in work function is no longer a diagnostic for the configuration of the chemisorbed H_2O. The fact that $\Delta\phi$ saturates for exposures of H_2O greater than approximately 2 L, even though the total coverage is still increasing (cf. Fig. 15), is consistent with the condensation of multilayers above this exposure; at lower exposures, the additional water still interacts significantly with the metal substrate.

3.4 LEED and ESDIAD Data

Another set of experimental data which supports the formation of clusters comes from a combination of LEED and ESDIAD (1) data, as shown in Fig. 15. At exposures of 1.0 L or greater, we observe a faint and diffuse $(\sqrt{3} \times \sqrt{3})R30^0$ LEED pattern, arising from an ordered array of oxygen atoms with respect to the Ru substrate, as shown in Fig. 15(C). (Scattering from the hydrogen atoms is assumed to be insignificant in forming this pattern.) This pattern has been observed also following adsorption of H_2O near 100 K on the (111) surfaces of Rh (37), Ag (42) and Pt (38,42,43). Further, a hexagonal pattern of H^+ emission, Fig. 16(B), has been observed to result from electron bombardment (1) at a coverage of water which corresponds to the spectrum of Fig. 14 following exposure to 0.6 L of H_2O. This is based on a comparison of thermal desorption peak shapes between Fig. 14 and the data of Ref. (1). Under the assumptions that: (1) The pattern of H^+ emission reflects the initial orientation of the molecular O-H bonds; and (2) The C_2 axis of the gas phase molecule is perpendicular to the metal surface in the chemisorbed state, the hydrogen atoms must be positioned with respect to the oxygen atoms of the $(\sqrt{3} \times \sqrt{3})R30^0$ lattice as shown in Fig. 16(C). An intuitively appealing explanation of the physical forces which create this combination of orientations is available if a second layer of H_2O molecules is positioned within the $(\sqrt{3} \times \sqrt{3})R30^0$ unit cell, hydrogen bonded to at least two of the first layer H_2O molecules. Such a structure is suggested from an examination of the crystal structures of ices Ic and Ih (6, 7, 24). Two possible structures of this type are shown in Fig. 17. Thus, the combination of LEED and ESDIAD data further support the hypothesis that aggregates of hydrogen bonded H_2O molecules form at submonolayer coverages.

At lower coverages of H_2O, Madey and Yates observed that a diffuse halo formed, which they attributed to ESD from the chemisorbed H_2O and from which they derived an H-O-H bond angle of 116 ± 10^0 for the first chemisorbed layer. This pattern, as well as the centered hexagon of Fig. 16(B), were susceptible to electron beam damage and degraded within seconds under the experimental conditions employed (1). This is consistent with our observation that the $(\sqrt{3} \times \sqrt{3})R30^0$ LEED pattern is degraded rapidly by the LEED electron beam also, as discussed in Section 2.

At higher coverages of H_2O, a single beam of H^+ emission normal to the surface was observed in the ESDIAD experiment (1). The coverage at which this pattern emerged corresponds to coverages equal to or greater than 2.2 L in our experiments, again based upon the shapes of the thermal desorption spectra of Fig. 14 and Ref. 1. This pattern was attributed to emission from the O-H bonds of ice multilayers, oriented parallel to the surface normal (1). This agrees well with the data from our EELS, work function change and thermal desorption experiments, all of which show that multilayers of ice form at

95 K following exposures greater than 2.2 L of H_2O.

There is some evidence that the structure of Fig. 17(B) represents the top two layers of ice multilayers, whereas Fig. 17(A) shows the structure of the first two adsorbed layers. The configuration of Fig. 17(B) is identical to the arrangement of water molecules in crystalline ices. For an ice multilayer, the ESDIAD pattern shows only H^+ emission normal to the surface (1), as discussed above. Figure 17(B) almost certainly shows the (cyclohexane-like) structure of the top two layers of an ice multilayer, for which only the O-H bonds normal to the surface appear in the ESDIAD pattern. The "equatorial" O-H bonds are not visible. This suggests that the hexagonal beams of Fig. 16(B) cannot be accounted for by a structure such as shown in Fig. 17(B) for the first two chemisorbed layers of H_2O. Rather, a structure such as that of Fig. 17(A) must be postulated, with non-tetrahedral bonding around at least some of the oxygen atoms. The O-H bonds of the second H_2O layer which are shown perpendicular to the surface in Fig. 17(A) may also account for the normal emission in the hexagonal ESD pattern, shown in Fig. 16(B), or this center spot may result from patches of ice, as proposed originally (1). The fact that some of the chemisorbed H_2O molecules of Fig. 17(A) do not have classic tetrahedral bond orientation about the oxygen atom is in agreement with arguments by other authors that the traditional picture of sp^3 hybridization of the valence orbitals about the oxygen atoms in ice may be inaccurate (45).

The faint, diffuse $(\sqrt{3} \times \sqrt{3})R30^{o}$ LEED pattern is observed following adsorption at 165 K also, suggesting that ice multilayers are not necessary for its formation. The TD data of Fig. 14, which show that only the A and B desorption states are present under these conditions, thus imply that these are the two states involved in forming this pattern. This supports a structure such as that of Fig. 17(A) for the first two layers of adsorbed H_2O and predicts that the hexagonal ESD pattern of H^+ emission would be observed following adsorption of H_2O at 165 K also.

Strong support for this two-layer model comes from further analysis of the coverage data of Fig. 15. The absolute coverage of a lattice such as shown in Fig. 17(A), with two H_2O molecules per $(\sqrt{3} \times \sqrt{3})R30^{o}$ unit cell (one in each layer) is 2/3. If we assume that the probability of adsorption of water is unity at 95 K and at 165 K, as discussed in Section 3.2, then the exposure which is theoretically necessary to achieve a coverage of 2/3 is 2.3 L of H_2O. Experimentally, we observe that this is exactly the exposure required to saturate the surface at 165 K, 2.2 ± 0.2 L, as shown by the data of Fig. 15. The uncertainty in the experimental exposure required to achieve saturation at 165 K, ±0.2 L, corresponds to an uncertainty in the absolute coverage of ±0.07. Following higher exposures at 95 K, the work function data, EEL spectra, TD spectra and UP spectra all show uniformly that ice multilayers form. A working definition of "monolayer" can now be proposed: one monolayer is the number of molecules required to saturate the primitive $(\sqrt{3} \times \sqrt{3})R30^0$ lattice of the first chemisorbed layer, in the absence of cluster formation. Under this definition, one monolayer corresponds to an experimental exposure of 1.1 L H_2O at 95 K and a coverage of 5.5×10^{14} molecules cm^{-2}.

3.5 Thermally Induced Changes in Vibrational Spectra

Heating a surface covered with H_2O causes irreversible changes which do not simply reflect a change in coverage, because the vibrational spectra do not simply revert to lower-coverage forms. This is illustrated by the EEL spectra of Fig. 18 which show the vibrational energy range below 1400 cm^{-1}, following heating of the surface to the various temperatures indicated. The sample was re-cooled to 95 K before recording each spectrum. The initial exposure at 95 K was 0.6 L. Since the spectra which were measured following heating at 180 to 205 K do not resemble those following any exposure ≤ 0.6 L H_2O at 95 K, we performed a series of EELS experiments in which the H_2O was adsorbed at a slightly higher temperature of adsorption, 165 K, as discussed in the following section.

3.6 Vibrational Spectra at 165 K.

3.6.1 Frequencies and Assignments.

At an adsorption temperature of 165 K and at the equilibrium vapor pressures of H_2O used in these experiments ($\leq 1 \times 10^{-7}$ Torr), a multilayer of ice does not form on the Ru(001) surface; saturation is attained after a 2.2 L exposure of H_2O. The vibrational spectra obtained at 165 K differ markedly from those obtained at an adsorption temperature of 95 K, particularly for exposures of H_2O greater than 1 L, as shown in Fig. 19. The most noticeable differences are in the region below 1000 cm^{-1}. At saturation at 165 K, three modes are now resolved. Isotopic substitution reveals that the two modes at 940 and 710 cm^{-1} are librational modes with an average isotopic frequency ratio of 1.37, whereas the mode at 370 to 400 cm^{-1} is the frustrated translation of the molecule perpendicular to the metal surface, with an experimental isotopic frequency ratio of 1.05. These ratios are illustrated in Fig. 20. The observation of the Ru-OH_2 vibration at this frequency confirms the assignment of this mode discussed in Sections 3.1.4 and 3.1.5. In effect, the librational modes occur at higher frequency following adsorption at 165 K ($\nu_L' = 710$ cm^{-1} and $\nu_L'' = 940$ cm^{-1}) than following adsorption of an equal amount of H_2O at 95 K (following exposure to 2.2 L H_2O, $\nu_L' = 510$ cm^{-1} and $\nu_L'' = 850$ cm^{-1}; cf. Fig. 7). This enables clear resolution of the Ru-OH_2 vibration at 370-400 cm^{-1} in the former case. It is interesting to note that the relative intensity of the v_L' and v_L'' modes at saturation at 165 K is almost identical to their relative intensity in the data of Fig. 11 for $\Delta\theta_s = -6^o$, where variation of the scattering angle has also enabled resolution of the libration, v_L', from the Ru-OH_2 stretch [cf. Section 3.1.5]. This suggests that v_L' and v_L'' represent the same type of modes at 95 K as at 165 K, but they are shifted to higher frequencies at 165 K. A slightly more detailed analysis further supports this argument. The peak intensity of the librational mode at 940 cm^{-1} in Fig. 19

can be compared to the sum of the peak heights of the two modes at 710 and 400 cm^{-1}. The ratio of these intensities is 0.80 ± 0.05 following saturation at 165 K. This is identical to the ratio of the intensities of the v_L'' and v_L' features following exposures of 1.1 to 2.2 L H_2O at 95 K, shown in Fig. 3(B). This observation led to an attempt to deconvolute the v_L' feature of Fig. 3(B) in terms of other EEL spectral intensities. The results are shown in Fig. 21, where the loss spectra have all been normalized to the intensity of the v_L'' feature at 840 cm^{-1}. It is apparent that both the position and intensity of the v_L' feature at 485 cm^{-1} (curve a) can be reasonably well fit by the sum of the feature at 530 cm^{-1}, observed in the AREELS experiment of Fig. 11 at $\Delta\theta_s = -6^0$, and the Ru-OH_2 feature at 400 cm^{-1}, observed in the EELS experiment of Fig. 19 following saturation of the surface with H_2O at 165 K. This sum is shown in Fig. 21 as curve "b + c". This sum is fit less well by the sum of intensities shown as curve "b + c", where the vibrational spectra at 165 K have been shifted downward in frequency to align the v_L'' features (curve b), then added to the unshifted feature due to the Ru-OH_2 mode (curve c). The goodness of fit is obviously related to the separation between the two librational modes under this procedure. This separation is smaller at 165 K, 230 cm^{-1}, than the separation in the AREEL spectrum at 95 K, 300 cm^{-1}, causing curve "b + c" to fit the data more poorly. In any case, the arguments advanced previously regarding the assignment of the v_L' feature at 95 K as two overlapping features are supported well by the "deconvolution" analysis of Fig. 21. This further implies that the basic vibrational properties of the adsorbate layers prepared at 95 K and 165 K are very similar, with the same modes being observed in the two cases but at different frequencies.

Finally, it should be noted that the feature due to the Ru-OH_2 vibration is asymmetric, as shown in Fig. 21, and in some experiments a shoulder at 490 cm^{-1} was distinctly resolved. The origin of this small feature is unknown.

The values of ν_{OH} and ν_S are changed less markedly after adsorption at 165 K. The average value of ν_{OH} is slightly higher, 3460 ± 50 cm^{-1}, and at saturation ν_S = 1560 cm^{-1} (cf. Fig. 5). This value of ν_S, 40 cm^{-1} below the gas phase frequency, indicates that at saturation at 165 K the surface contains a relatively high fraction of chemisorbed H_2O molecules, consistent with the discussion of Section 3.1.2.

The differences in the vibrational spectra may be related to differences in the adsorbate lattice structure and differences in the relative distributions of chemisorbed H_2O molecules. This is supported by the following observations:

(1) There is a direct correlation between frequencies of librational modes and the degree of intermolecular hydrogen bonding. This is concluded from data on metal hydrates (18-21) and various ice polymorphs (24), wherein a decrease in the value of ν_{OH} is taken to mean an increase in the extent of hydrogen bonding. For H_2O adsorbed on Ru(001), the higher frequencies which we observe for ν_L' and ν_L'' thus indicate that the water lattice is more strongly hydrogen-bonded at 165 K, although this is inconsistent with the increase in ν_{OH}, from 3370 cm^{-1} at 95 K to 3460 cm^{-1} at 165 K. The

apparent change in ν_{OH} may be complicated by orientational effects and/or changes in relative scattering cross sections.

(2) In ice, there is an irreversible transition from vitreous ice to cubic ice at atmospheric pressure, variously reported to occur at temperatures between 140 and 160 K (6,27,46). While the arrangement of H_2O molecules in vitreous ice is subject to dispute (46), it is clear that in this temperature region the water molecules become sufficiently mobile within the lattice to achieve an energetically favored configuration. This supports a model in which, at an adsorption temperature of 165 K, the water molecules are sufficiently mobile to form a more well ordered, long-range hydrogen-bonded lattice than at 95 K on a Ru(001) substrate.

The vibrational spectra of Fig. 19 are quite similar to the spectra of Fig. 3(A) for equivalent exposures less than 2.2 L. One would expect this to be the case if clusters involving mainly the first two layers of H_2O molecules form at both temperatures below 2.2 L. Ice multilayers form with increasing exposure at 95 K, whereas at 165 K the first two layers form a well-ordered lattice which saturates the surface following an exposure of 2.2 L. This is strongly supported by the assignments of the thermal desorption features of Fig. 14 and by the coverage arguments presented in Section 3.4.

The fact that the array of water molecules is more well ordered at 165 K than at 95 K is reflected also by the fact that, for equal exposures, the elastically scattered electron intensity was always approximately an order of magnitude greater following adsorption at 165 K than at 95 K, which is a characteristic usually associated with ordered arrays of adsorbate molecules (47).

3.6.2 AREELS and the Scattering Mechanism

An investigation of the scattering mechanism for a surface saturated with H_2O at 165 K confirms that in this case, also, the librational modes are dipolar enhanced, whereas the O-H stretching mode is not. Figure 22 shows EEL spectra measured at various off-specular angles, and Fig. 23 shows the intensities of the features at specific frequencies as functions of scattering angle, $\Delta\theta_S$. It is apparent that the intensities of the librational modes decrease at approximately the same rate as the metal-oxygen mode, which must have a perpendicular component since the oxygen atom of chemisorbed H_2O binds directly to the metal. The angular distribution of the intensity of this frustrated translation can thus be used as a qualitative standard in judging dipolar enhancement. This confirms the dipolar enhancement of the frustrated rotations, in agreement with the situation at 95 K which was somewhat complicated by overlapping features at ν_L' (cf. Section 3.1.5).

In addition, the angular dependence of the intensity of the ν_L' mode of Fig. 12, relative to ν_L'', can now be explained in terms of the intensities of two modes, a librational mode and the Ru-OH_2 stretch, as discussed in the previous section. The intensity of this sum changes relative to the intensity of the mode at 900 cm^{-1} in Fig. 23 just as the intensities of

ν_L' and ν_L'' changed in Fig. 12, i.e. the relative intensities reverse as the analyzer moves away from the specular direction.

The shape of the loss due to ν_{OH} changes with scattering angle as occurs also at 95 K. At $\Delta\theta_s = -18^o$ there are distinct features at 3520 cm^{-1} and 3230 cm^{-1}. The assignments of these features have been discussed in Section 3.1.5.

3.7 Ultraviolet Photoelectron Spectroscopy

One possible explanation for the differences in the vibrational spectra measured at the two temperatures of adsorption is that at 165 K the adsorbed H_2O is chemically different, perhaps dissociated. However, the results of photoemission experiments, shown in Fig. 24, do not support the hypothesis that significant dissociation occurs at 165 K. In these experiments, photoelectron intensities were analyzed at two different exit angles for comparison. In the HeI photoelectron spectra of gaseous H_2O (25) and also of ice (48-50), three features are observed which are attributed to the antibonding O-H orbital ($1b_2$), the bonding O-H orbital ($3a_1$) and the nonbonding oxygen orbital ($1b_1$). Possible overlap of the latter feature with emission from the Ru substrate at 5 to 6.5 eV in these spectra makes identification of the $1b_1$ orbital ambiguous for exposures of 2 L or less. At higher exposures [cf. Fig. 24(D)] the UP spectrum resembles that of ice (48-50). Spectra B and C are virtually identical, even though they were measured following exposure of the surface to 2.2 L of H_2O at 95 K and following saturation with H_2O at 165 K, respectively. (As Fig. 15 shows, the total amount of H_2O adsorbed in these two cases is the same.) This measurement indicates that there are no major differences in the chemical composition of the adsorbate layers prepared under these two sets of conditions.

3.8 Isotopic Exchange between H_2O and D_2

Two measurements were performed to determine whether isotopic exchange between adsorbed H_2O and D_2 could be detected.

In the first experiment, the Ru(001) crystal was exposed to 1.1 L H_2O at 95 K followed by 5.0 L D_2 at 95 K. [Adsorption of some D_2 was evidenced by a factor of three increase in the elastically scattered intensity following exposure to D_2. Increases in reflectivity of up to a factor of ten are always observed after adsorption of H_2 (D_2) with an incident electron energy of 4.0 eV (<u>47</u>).] The resultant EEL spectrum showed no change, nor was a change observed after heating this surface slowly to 165 K in vacuum. In particular, no loss features appeared at the energies to be expected for ν_{OD} or $\nu_s(D_2O)$. The librational modes showed no change in frequency either, other than the shifts expected to result from heating to 165 K (cf. Section 3.6.1).

In the second experiment, the sample was exposed to a small amount (0.3L) of H_2O at 95 K, then exposed to 20 L D_2 at 95 K, and subsequently heated slowly to 165 K in a background pressure of 2×10^{-8} Torr D_2. Neither of these two treatments with D_2 caused changes in the vibrational spectra, including the frequencies of the librational modes, which would have been characteristic of OH-D exchange. The v_{OH} and v_s loss features were quite weak in this second experiment, and it is estimated that exchange of less than 50% of the total H_2O would have been below the experimental limits of detection in the v_{OD} and v_s (D_2O) features. However, it was expected that exchange might occur more readily in the second experiment due to the low initial coverage of H_2O and the constant background pressure of D_2, i.e. both Langmuir-Hinshelwood and Eley-Rideal mechanisms of exchange were facilitated. The fact that no exchange was evidenced in the EEL spectra indicates that H_2O does not exchange with D_2 below 165 K. This, in turn, indicates that there is no dynamic equilibrium established between molecular H_2O and its dissociation products under these conditions, which would be the case in a Langmuir-Hinshelwood reaction. This agrees with the conclusions of Sections 3.2 and 3.6 that only molecular H_2O is adsorbed at 165 K.

H_2O-D_2O mixing experiments were not feasible since it was impossible to introduce these two gases sequentially into the vacuum chamber without inducing significant cracking and mixing on the surfaces of the system, thereby making the source of any HDO adsorbed on the Ru surface questionable.

4. Comparisons with Other Experimental Data.

The properties of H_2O adsorbed on Ru(001) contain several unique features not revealed by previous investigations of related systems, as well as a number of similarities. The basic mode assignments of the EEL features as ν_{OH}, ν_s, ν_L and "combinations" thereof, are in general agreement with assignments proposed by other authors following adsorption of H_2O on W(100) (51), Pt(100) (2), Pt(111) (3) and Cu(100) (52). In all cases the position of the main ν_{OH} peak, 3330 to 3450 cm^{-1}, indicates intermolecular hydrogen bonding. Additional ν_{OH} features at 2870 and 3680 cm^{-1} were reported for H_2O on Pt(100) (2) and assigned to water hydrogen bonded to the Pt surface, and non-hydrogen bonded water molecules, respectively. These features may, however, be due to the relatively high defect density which is to be expected on this reconstructed surface, or other structural factors related to the reconstruction, since they were not observed for H_2O adsorbed on a Pt(111) crystal (3), nor were they observed in our experiments with the hexagonal Ru(001) surface. Presumably, Pt(111) and reconstructed Pt(100) are both hexagonal surfaces (2), although molecular beam scattering experiments indicate that corrugation of the latter surface may be significant (53), and alternative models have been proposed (54).

The librational modes in other systems occur between 560 and 920 cm^{-1}. In only one other case have two librational modes been distinctly resolved, for H_2O on reconstructed Pt(100) at 150 K (2); only one mode was identified for H_2O on Pt(111) at 100 K (3). The differences between the two sets of EELS data may be due to differences in the Pt substrates, as suggested above, or they may reflect the different temperatures of adsorption, as suggested by the results of the present study. The observation of the librational modes was also presumed to be consistent with cluster formation in both studies (2,3) although dipolar scattering was not verified.

The metal-oxygen frequency of chemisorbed H_2O occurs at 460 to 550 cm^{-1} on Pt(100) and Pt(111) surfaces (2,3), and a frustrated translation (an O····O stretch) within the ice lattice at 240 and 250 cm^{-1} (2, 3). These are to be compared with the corresponding frequencies of H_2O adsorbed on Ru(001): 370 to 400 cm^{-1}, and 280 cm^{-1}, respectively. The presence of the 240 cm^{-1} feature at a low coverage of H_2O on Pt(100) was used as evidence that clusters of H_2O formed even at a submonolayer coverage (2). The same conclusion regarding cluster formation was reached for H_2O on Pt(111), but the 250 cm^{-1} feature was only observed above a minimum exposure necessary to form ice (3). For H_2O on Ru(001), this feature is observed only for exposures of 3 L or greater, in agreement with the conclusion that it is characteristic of an ice multilayer [cf. section 3.1.4]. Its presence at lower exposures in our experiments cannot be excluded, however, since it could well be buried in the low-energy tail of the elastic peak if the relative intensity of the inelastic transition is too low, as may be seen in Fig. 3(B).

The frequency of the scissoring mode, ν_s, is much lower on Ru(001) than has been observed in other systems. On Pt(100) and Pt(111) surfaces it occurs at 1630 to 1650 cm^{-1} at all coverages investigated. As described in Section 3.1.2, this low frequency reflects a strong interaction between the metal and the chemisorbed water, probably due to electron transfer from the H_2O to the metal. This interaction must be stronger for Ru than for Pt to account for the differences in ν_s for the two metals.

The stronger interaction of H_2O with Ru than with Pt is also reflected in the thermal desorption spectra. The high-temperature desorption state attributed to desorption from the chemisorbed layer of H_2O occurs at 190 K on Rh(111) (37), 180 K on Pt(111) (38) and 208-217 K on Ru(001).

Desorption of H_2O at 210 - 220 K from Pt(111) (38) and Rh(111) (37) has been associated with preadsorption of oxygen and possible dissociation. However, we do not believe that oxygen (or other) contamination can account for desorption at 208 to 217 K in our experiments because of the various methods which were used in cleaning and verifying the cleanliness of the samples (cf. Section 2) and the fact that this feature is consistent with all of our other data. Rather, we propose that the presence of this feature reflects the relative strength of the interaction of chemisorbed H_2O with Ru(001). An unusually high-temperature desorption state has been observed for H_2O on clean Ir(110) at 310 K (36). This appears to be related to the microroughness of the reconstructed Ir substrate (36), further indicating the importance of the water-metal interaction in determining desorption temperatures.

Of the metal substrates which have been discussed thus far [Rh(111), Ir(110), Pt(100) and Pt(111)], Ru(001) is unique in that its ($\sqrt{3}$ x $\sqrt{3}$) unit cell lattice parameter, 4.59 Å [cf. Fig. 16(C)], provides quite a close match with the distance of closest approach of two non-hydrogen bonded H_2O molecules in crystalline ices Ic and Ih: 4.52 Å (55). This is to be compared with lattice parameters of 4.80 Å for Pt(111) and 4.66 Å for Rh(111). Undoubtedly, the Ru(001) surface provides a more "fitting" substrate for the adsorption of water clusters than does hexagonal Pt. This fact may be related to the unique properties of ν_s discussed above, since chemisorbed water molecules can maintain good registry with the Ru substrate, i.e. remain in specific, favorable adsorption sites, without introducing too much strain into the structure of the clusters or vice versa. The importance of a mismatch of the substrate lattice with the ice lattice has been noted by previous authors in a comparison of the LEED patterns of ice on Ag(111) and Pt(111) surfaces (42).

There have been two other specific models for the structures of H_2O clusters adsorbed in vacuum on metal surfaces (1, 2). The first, a model for H_2O on Ru(001), was based largely upon ESDIAD data (1). This model proposed that the hexagonal ESDIAD pattern was due to a single chemisorbed layer of H_2O molecules, oriented in islands with parallel molecular planes pointing toward nearest-neighbor Ru atoms. This model is difficult to rationalize; furthermore, it is inconsistent with our measurements which show that layered clusters form under all conditions. Ice-like layers, as shown in Fig. 17, provide an appealing and consistent explanation of the ESDIAD data. The other model was advanced by Ibach and Lehwald in an investigation of H_2O on Pt(100), based mainly upon EELS data. We do not feel that our model is in direct contradiction with theirs, because of the differences between Ru and Pt which have been discussed above. However, it must be pointed out that we have quite a complete set of data to elucidate the structure of H_2O on Ru(001), whereas the structural model for H_2O on Pt(100) was based largely upon a theoretical calculation of relative cluster stabilities (56). In this calculation, the free energy differences between various configurations of hydrogen-bonded H_2O clusters was relatively small; furthermore, the inevitable perturbation of the metal surface upon the theoretical stabilities of these clusters was ignored in choosing a specific one to model the EELS data (2). Three features of the EELS data were used to argue in favor of the "cyclic hexamer" model of H_2O on Pt(100) (2):

(1) The observation of v_{OH} at 2850 cm^{-1} to support hydrogen bonding to the surface;

(2) The fact that the relative intensities of v_s and v_{OH} changed by a factor of 100 with increasing coverage, possibly indicative of a structural transformation involving the hexamer clusters; and

(3) The disappearance of the metal-oxygen stretch at 440 cm^{-1}, at a coverage where the intensity ratio v_{OH}/v_s began to change, leaving only features due to librations at 560 to 920 cm^{-1}. This was attributed to the structural rearrangement of the clusters also, from a situation involving bonding to the metal surface through some of the oxygen atoms, to a a situation with complete hydrogen bonding of the chemisorbed layer to the metal, such as shown by Fig. 10(f).

As discussed in Sections 3.1.1 and 3.1.3, the first two points are not applicable to H_2O on Ru(001). We do observe behavior rather similar to point (3) above . However, we have verified that the metal-oxygen stretch is always present, merely obscured by overlap with an intense librational feature in some cases. This is confirmed by the isotopic substitution experiments of Section 3.1.4, the AREELS experiments of Sections 3.1.5 and 3.6.2 and the experiments following adsorption at 165 K of Section 3.6.1. We therefore conclude that none of our experiments supports the model proposed in Ref. (2), with water forming hydrogen bonds directly to the metal surface, for H_2O on Ru(001).

5. Summary.

On the basis of the experiments discussed herein, we present the following description of H_2O adsorbed on Ru(001).

Water adsorbs molecularly on Ru(001) at temperatures below 200 K. This is based upon the observation of ν_s in the EEL spectra, the TD spectra which show only desorption of molecular H_2O below 200 K, the UP spectra which show no major differences in chemical composition between 95 K and 165 K, and the absence of exchange between H_2O and D_2. The vibrational data are consistent with bonding to the Ru surface through the oxygen atom, by comparison with vibrational spectra of aquo-metallic complexes (18-21) and clusters (22). The value of ν_s at low coverage, 1510 cm^{-1}, is indicative of a relatively strong interaction with the metal via electron donation from the chemisorbed H_2O (22), and may be related to the relatively large H-O-H bond angle reported from ESDIAD experiments (1). The metal-oxygen stretch of chemisorbed H_2O occurs at 370 to 400 cm^{-1}, consistent with bonding to one or two metal atoms (18,19).

Self-aggregation of the H_2O molecules, via hydrogen bond formation, occurs under all conditions investigated. This conclusion is based upon the following:

(1) The coverage-independent value of ν_{OH} in the EEL spectra, 3370 $\pm$ 50 cm^{-1}, which is characteristic of intermolecular hydrogen bonding;

(2) The observation of dipolar enhanced librational modes in the EEL spectra, which can be rationalized in terms of hydrogen bonded clusters; and

(3) The observation of ESDIAD and LEED patterns which are indicative of hydrogen bonded clusters with specific long range order.

At exposures below 0.5 L H_2O at 95 K, the clusters are small and not well ordered. At higher exposures (coverages), up to 2.2 L, the clusters coalesce and achieve a long range order. Up to 2.2 L of H_2O, only the first two layers of H_2O molecules are being filled at 165 K; a small quantity of ice may form also in this range at 95 K. At the exposure of 2.2 L, the thermal desorption data indicate that the absolute coverage is 2/3, which is exactly the coverage of a $(\sqrt{3} \times \sqrt{3})R30^{0}$ lattice with an additional hydrogen bonded, second-layer H_2O molecule per unit cell, as shown in Fig. 17. Such a structure can be proposed independently, based solely upon the LEED and ESDIAD (1) data, which give information regarding the orientation of the water lattice with respect to the Ru substrate and the orientations of the O-H bonds of individual molecules.

The fact that long-range ordering occurs between exposures of 1.1 and 2.2 L is supported by the following observations:

(1) The EEL spectra at 95 K are relatively invariant in this exposure range (cf. Fig. 3), indicating that the vibrational properties of the clusters are no longer changing as a result of increasing size;

(2) The LEED pattern is first observable at approximately 1 L; and

(3) It is in this coverage range that the librational mode features

at 165 K diverge to higher frequencies relative to those at 95 K, which indicates a more well-ordered hydrogen bonded lattice at the higher temperature of adsorption.

The H_2O lattice saturates the surface following an exposure of 2.2 L at 165 K, which is consistent with the thermal desorption, work function change, UPS and EELS data, all of which verify that epitaxial ice forms above this coverage at 95 K. Evidently the properties of the first two H_2O layers are quite distinct from the properties of epitaxial ice.

The EELS, LEED and ESDIAD data support the structure of Fig. 17(A) as a model for the first two chemisorbed layers, whereas Fig. 17(B) almost certainly represents the top two layers of epitaxial ice.

Chemisorbed water interacts more strongly with the hexagonal Ru surface than with similar Pt surfaces (2, 3). This is apparent in the low values of ν_s and the high-temperature TD state at about 210 K which are observed for Ru(001). The lowering of ν_s in turn may be related in part to the relatively close match between the $(\sqrt{3} \times \sqrt{3})$ lattice parameter of the Ru(001) surface, 4.59 Å, and the corresponding oxygen-oxygen separation in crystalline ice at atmospheric pressure, 4.52 Å (56).
In other words, ice-like layers of hydrogen bonded H_2O molecules may form without displacing the lattice of chemisorbed H_2O molecules from favored adsorption sites, or vice versa.

Acknowledgments.

We wish to acknowledge valuable discussions with Dr. Alex Bradshaw, Dr. S. Holloway, Dr. Jürgen Sass, Ms. Ellen Williams and Dr. John Yates, Jr.

References.

1. T. E. Madey and J. T. Yates, Jr., Chem. Phys. Letters 51, 77 (1977); see also T. E. Madey and J. T. Yates, Jr., Proc. 7th Intern. Vac. Congr. and 3rd Intern. Conf. Solid Surfaces, Vienna, 1 (1977).
2. H. Ibach and S. Lehwald, Surface Sci. 9, 187 (1980).
3. B. A. Sexton, Surface Sci. 94, 435 (1980).
4. P. Schuster, G. Zundel and C. Sandorfy, Eds., The Hydrogen Bond: Recent Developments in Theory and Experiments, North-Holland Publishing Co., Amsterdam (1976).
5. F. Franks, Ed., Water: A Comprehensive Treatise, Plenum Press, New York (1972).
6. D. Eisenberg and W. Kauzmann, The Structure and Properties of Water, Oxford University Press, New York (1969).
7. G. C. Pimentel and A. L. McClellan, The Hydrogen Bond, Reinhold Publishing Corp., New York (1960).
8. In this report, the term "chemisorbed" H_2O will be used to designate only the first layer of H_2O molecules, in direct contact with the metal, as distinguished from molecules in successive hydrogen-bonded layers. "Ice" will be used to mean three or more monolayers of water.
9. G. E. Thomas and W. H. Weinberg, J. Chem. Phys. 70 954 (1979).
10. T. D. Flame and P. D. Ownby, J. Vacuum Sci. Technol. 8, 661 (1971).
11. D. R. Sandstrom and S. P. Withrow, J. Vacuum Sci. Technol. 14, 748 (1977).
12. E. D. Williams and W. H. Weinberg, Surface Sci. 82, 93 (1979).
13. The nature of the oxide formed on Ru(001) has been investigated in detail by the following authors: G. Praline, B. E. Koel, H.-I. Lee

and J. M. White, Appl. Surface Sci. 5, 296 (1980); also R. Klein, R. Siegel and N. E. Erickson, J. Vacuum Sci. Technol. 16, 489 (1979).

14. G. E. Thomas and W. H. Weinberg, Rev. Sci. Instrum. 50, 497 (1979).
15. G. Herzberg, Molecular Spectra and Molecular Structure II. Infrared and Raman Spectra of Polyatomic Molecules, Van Nostrand Reinhold Co., New York , pp. 106 and 281 (1945).
16. M. Van Thiel, E. D. Becker and G. C. Pimentel, J. Chem. Phys. 27, 486 (1957).
17. A. J. Tursi and E. R. Nixon, J. Chem. Phys. 52, 1521 (1970).
18. K. Nakamoto, Infrared and Raman Spectra of Inorganic and Coordination Compounds, Wiley-Interscience, New York, 226 (1978); and references therein.
19. J. R. Ferraro, Low-Frequency Vibrations of Inorganic and Coordination Compounds, Plenum Press, New York, 65-72 (1971).
20. J. A. Janik, "Incoherent Neutron Scattering Experiments on Hydrogen Bonded Systems", Ch. 19, V. 3 of Ref. 4, p. 891; and references therein.
21. H. R. Oswald, Helv. Chim. Acta 48, 600 (1965).
22. R. H. Hauge, J. W. Kauffman and J. L. Margrave, J. Am. Chem. Soc. 102, 6005 (1980).
23. P. F. Meier, R. H. Hauge and J. L. Margrave, J. Am. Chem. Soc. 100, 2108 (1978); also R. H. Hauge, P. F. Meier and J. L. Margrave, Ber. Bunsenges. Phys. Chem. 82, 102 (1978).
24. E. Whalley, "The Hydrogen Bond in Ice", Ch. 29, V. 3 of Ref. 4, p. 1425; see also F. Franks, "The Properties of Ice", Ch. 4 of Ref. 5, p. 115.
25. A. H. Hardin and K. B. Harvey, Spectrochim. Acta 29A, 1139 (1973).

26. W. McLean, J. A. Schulz, L. G. Pedersen and R. C. Jornagin, Surface Sci. 83, 354 (1979).

27. D. W. Turner, C. Baker, A. D. Baker and C. R. Brundle, *Molecular Photoelectron Spectroscopy*, John Wiley and Sons, London, 77-81 (1970).

28. F. M. Hoffmann, T. E. Felter, P. A. Thiel and W. H. Weinberg, J. Vacuum Sci. Technol. (March/April 1981), to be published.

29. J. K. Sass, Proc. 4th Int. Conf. Solid Surfaces and 3rd European Conf. Surface Sci. 2, 1426 (1980).

30. D. Šokčević, Z. Lenac, R. Brako and M. Šunjić, Z. Physik B 28, 273 (1977).

31. S. Y. Tong, C. H. Li and D. L. Mills, Phys. Rev. Letters 44, 407 (1980).

32. P. A. Thiel, F. M. Hoffmann and W. H. Weinberg, in preparation.

33. E. Whalley, Can. J. Chem. 55, 3429 (1977); and references therein.

34. B. K. Srivastava and D. P. Khandelwal, Solid State Commun. 19, 985 (1976); Y. S. Jain, J. Phys. Chem. Solids 37, 641 (1976).

35. S. Andersson and J. W. Davenport, Solid State Commun. 28, 677 (1978).

36. T. S. Wittrig, D. E. Ibbotson and W. H. Weinberg, Surface Sci. 102, in press (1981).

37. J. J. Zinck and W. H. Weinberg, J. Vacuum Sci. Technol. 17, 188 (1980).

38. G. B. Fisher and J. L. Gland, Surface Sci. 94, 446 (1980).

39. P. A. Redhead, Vacuum 12, 203 (1962).

40. C.-M. Chan, R. Aris and W. H. Weinberg, Appl. Surface Sci. 1, 360 (1978).

41. J. M. Heras and L. Viscido, Appl. Surface Sci. 4, 238 (1980).

42. L. E. Firment and G. A. Somorjai, Surface Sci. 84, 275 (1979); J. Chem. Phys. 63, 1037 (1975).

43. C. W. Tucker, Jr., J. Appl. Phys. 35, 1897 (1964).

44. T. E. Madey, private communication.

45. I. Olovsson and P.-G. Jönsson, "X-Ray and Neutron Diffraction Studies of Hydrogen Bonded Systems", Ch. 19, V. 2 of Ref. 4, p. 393; see also F. H. Stillinger, Science 209, 451 (1980).

46. L. C. Allen, "Structural Models for Vitreous Ice", in *The Physics and Chemistry of Ice*, E. Whalley, S. J. Jones and L. W. Gold, Eds., Royal Society of Canada, Ottawa (1973) 13 - 18.

47. P. A. Thiel, unpublished results.

48. I. Abbati, L. Braicovich and B. DeMichelis, Solid State Commun. 29 511 (1979).

49. M. J. Campbell, J. Liesegang, J. D. Riley, R. C. G. Leckey and J. G. Jenkin, J. El. Spec. Rel. Phen. 15, 83 (1979).

50. P. J. Page, D. L. Trimm and P. M. Williams, J. Chem. Soc. Far. Trans. I 70, 1769 (1975).

51. F. M. Propst and T. C. Piper, J. Vacuum Sci. Technol. 4, 53 (1967).

52. B. A. Sexton, J. Vacuum Sci. Technol. 16, 1033 (1979).

53. K. H. Rieder and T. Engel, private communication.

54. J. P. Biberian, Surface Sci. 97, 257 (1980).

55. R. W. G. Wyckoff, Crystal Structures, Vol. 1, Interscience, New York (1963) 322.

56. J. D. Bene and J. A. Pople, J. Chem. Phys. 52, 4858 (1970).

57. R. Unwin, K. Horn and P. Geng, Vakuumtechnik 29, 149 (1980).

Figure Captions

Figure 1: Intensity of the elastically scattered electron beam as a function of the change in polar angle, $-\Delta\theta_s$. (The geometry is shown in the inset.) V_i is the incident beam energy. The (circular) entrance aperture of the energy analyzer subtends an angle of $4.5^o (4.8 \times 10^{-3}$ steradians).

Figure 2: Normal modes of H_2O adsorbed with C_{2v} symmetry on a flat metal substrate, with the C_2 axis perpendicular to the metal surface. The symmetry designations are after Herzberg (15).

Figure 3: Electron energy loss spectra of H_2O adsorbed on Ru(001) at 95 K. The exposure of 5.6 L H_2O corresponds to approximately five monolayers of water (see Section 3.4), i.e. epitaxial ice

Figure 4: Electron energy loss spectra between 1000 and 4800 cm^{-1}, showing v_{OH} and v_s in detail.

Figure 5: Frequency of the scissoring mode of H_2O, ν_s, as a function of exposure of H_2O to Ru(001). The error bars are based upon worst-case estimates of the broadness of the v_s feature in individual experiments. The dark symbols show representative frequencies observed for D_2O, multiplied by 1.34.

Figure 6: Total intensities of the v_s and v_{OH} EELS peak as functions of H_2O exposure (top), and the ratio of the intensities, v_{OH}/v_s, as a function of H_2O exposure (bottom). The intensities were corrected for a background level of counts determined empirically.

Figure 7: Frequencies of the EELS features below 1000 cm^{-1} as functions of H_2O (D_2O) exposure at 95 K. The frequencies are labeled ν_L after the notation of Fig. 2.

Figure 8: Isotopic shifts of the low-energy vibrations below 1000 cm^{-1}. The loss in the range 370 to 550 cm^{-1} is labeled ν_L', and the loss between 710 and 890 cm^{-1} is designated ν_L''. The horizontal dashed lines show the average experimental values at exposures above 0.09 L at 95 K. In the lower right, I is defined as the moment of inertia and μ is the reduced mass. The coordinate axes are chosen after Herzberg (15).

Figure 9: EEL spectra of H_2O (D_2O) adsorbed on Ru(001) at 95 K, showing the low-energy region in detail.

Figure 10: Possible orientations of H_2O adsorbed on Ru(001). The point groups which describe the symmetries of these orientations are: (a) C_{2v}; (b) C_{2v}; (c) $C_s,\sigma(yz)$; (d) $C_s,\sigma(yz)$; (e) $C_s,\sigma(xz)$; and, (f) C_1.

Figure 11: Angle-resolved EEL spectra of the Ru(001) surface following exposure to 1.1 L H_2O at 95 K.

Figure 12: Intensities of the loss features of Fig. 11 as functions of change in the analyzer position from the specular direction which is defined as $\Delta\theta_s = 0^o$ ($\theta_s = \theta_i = 57^o$). The intensity plotted is the count rate at a single frequency, corrected for a background level determined empirically. In repeated AREEL experiments at this temperature and exposure, the ratio of the intensities of the features labelled v_L' and v_L'' always inverted as shown.

Figure 13: EEL spectrum of ice multilayers on Ru(001) showing the energy range below 7800 cm^{-1} in detail.

Figure 14: Thermal desorption spectra of H_2O from Ru(001). The heating rate is β, and is linear and constant within $\pm 1^o$ between 150 K and 250 K. The baselines of the curves have been displaced along the ordinate for clarity.

Figure 15: Integrated peak areas, $\int_t P_{H_2O}\, dt$, of the thermal desorption data corresponding to Fig. 14.

Figure 16: Structural information for H_2O on Ru(001) at 90 to 95 K. The ESDIAD data is from Ref. (1). The $(\sqrt{3} \times \sqrt{3})R30^o$ unit cell parameter, 4.59 Å, is reasonably close to the corresponding oxygen-oxygen distance of crystalline ices Ic and Ih, 4.52 Å (55).

Figure 17: Adsorption of a second-layer H_2O molecule, hydrogen-bonded to the chemisorbed H_2O, provides a model which is consistent with both the LEED and ESDIAD data of Fig. 16. Possible structures are shown here.

Figure 18: EEL spectra between 250 and 1400 cm^{-1}, showing the changes which result when a surface with 0.6 L H_2O at 95 K is heated to successively higher temperatures, as indicated.

Figure 19: Vibrational spectra following adsorption of H_2O on Ru(001) at 160 to 170 K, and re-cooling to 95 K.

Figure 20: Isotopic frequency shifts of low-energy vibrations of H_2O (D_2O) on Ru(001) at 165 K.

Figure 21: Curve a: EEL spectrum following exposure of Ru(001) to 1.6 L H_2O at 95 K, from Fig. 3(B), showing the v_L'' and v_L' features in detail.

Curve b: EEL spectrum following saturation of Ru(001) with H_2O at 165 K, from Fig. 19. The librational mode features have been shifted in frequency as indicated to align with v_L'' of curve a, and expanded to match the intensity of v_L'' in curve a.

Curve c: As in curve b, but not shifted in frequency.

Curve d: AREEL spectrum following exposure of Ru(001) to 1.1 L H_2O at 95 K, from Fig. 11. The loss spectrum has been normalized to the intensity of v_L'' in curve a. The tails of the individual loss features have been approximated by straight lines, as shown.

Figure 22: Angle-resolved EEL spectra of the Ru(001) surface following exposure to 3.3 L of H_2O at 165 K, i.e. at saturation at 165 K.

Figure 23: Intensities of electron energy loss features as functions of scattering angle, defined in Fig. 1, corresponding to the data of Fig. 21.

Figure 24: Photoemission spectra taken following exposure of the Ru(001) surface to H_2O. The angle of incidence of the HeI radiation is 80^0 from the surface normal. Experimental details are discussed elsewhere (13). The three molecular orbitals shown in the upper right panel are referenced to the $1b_2$ orbital in energy. From top to bottom, they are taken from (27), (48, 49), (50) and (38).

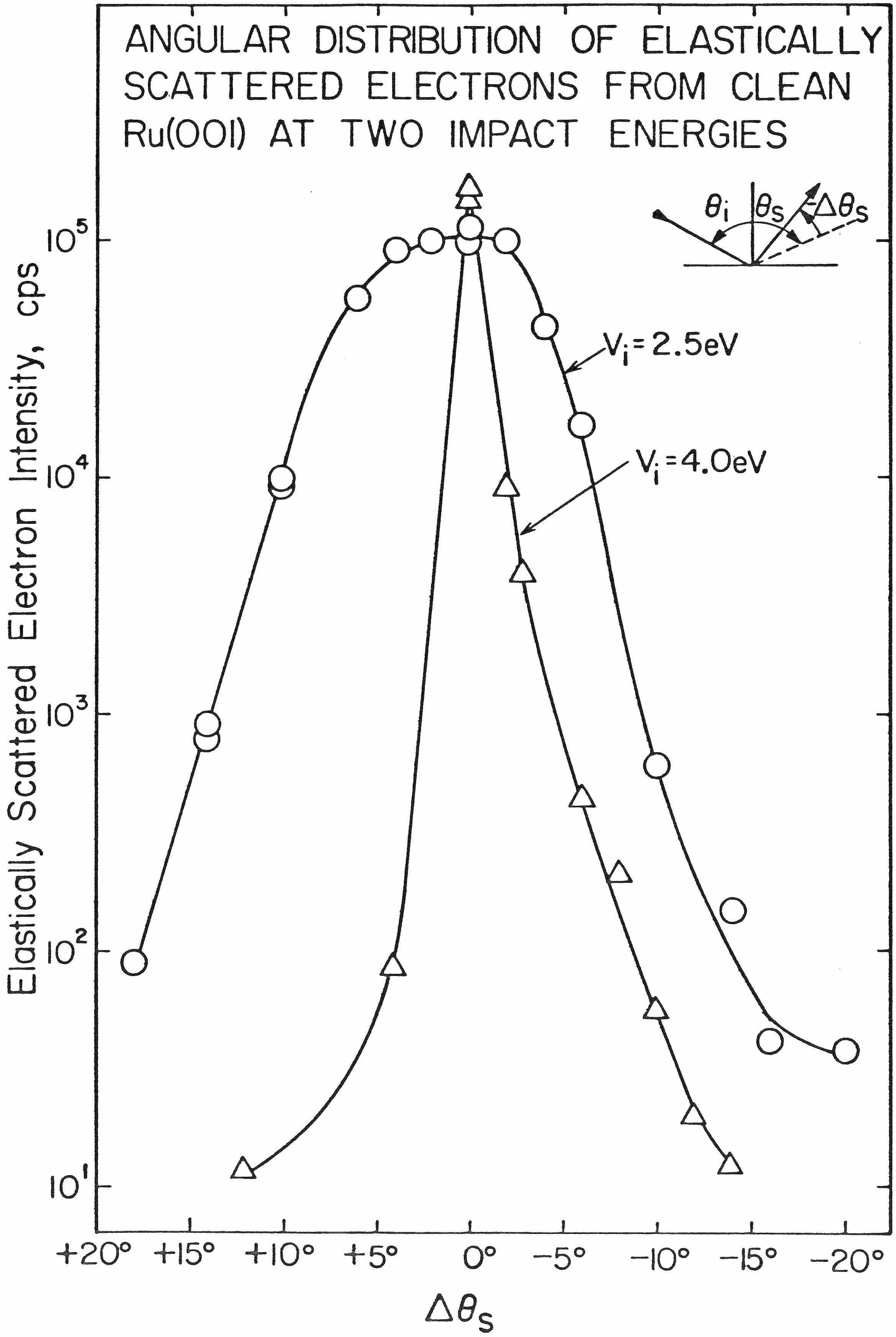
ANGULAR DISTRIBUTION OF ELASTICALLY SCATTERED ELECTRONS FROM CLEAN Ru(001) AT TWO IMPACT ENERGIES
θi
θs
Δθs
Vi = 2.5eV
Vi = 4.0eV
Elastically Scattered Electron Intensity, cps
10⁵
10⁴
10³
10²
10¹
+20°
+15°
+10°
+5°
0°
−5°
−10°
−15°
−20°
Δθs

Figure 1

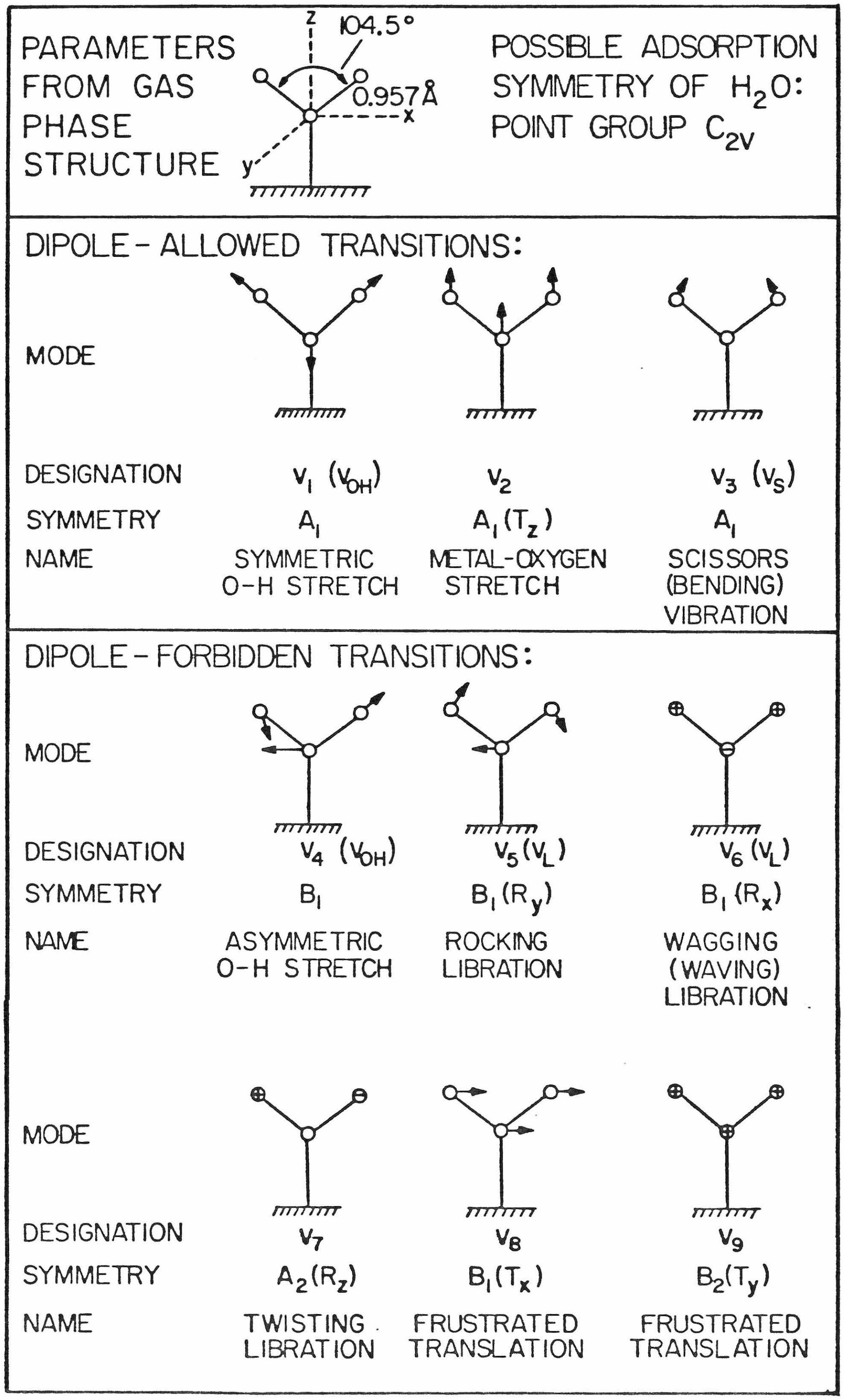
PARAMETERS FROM GAS PHASE STRUCTURE
z
104.5°
0.957Å
x
y
POSSIBLE ADSORPTION SYMMETRY OF H_2O: POINT GROUP C_{2v}
DIPOLE-ALLOWED TRANSITIONS:
MODE
DESIGNATION
SYMMETRY
NAME
ν_1 (ν_{OH})
A_1
SYMMETRIC O-H STRETCH
ν_2
$A_1(T_z)$
METAL-OXYGEN STRETCH
ν_3 (ν_S)
A_1
SCISSORS (BENDING) VIBRATION
DIPOLE-FORBIDDEN TRANSITIONS:
MODE
DESIGNATION
SYMMETRY
NAME
ν_4 (ν_{OH})
B_1
ASYMMETRIC O-H STRETCH
ν_5 (ν_L)
$B_1(R_y)$
ROCKING LIBRATION
ν_6 (ν_L)
$B_1(R_x)$
WAGGING (WAVING) LIBRATION
MODE
DESIGNATION
SYMMETRY
NAME
ν_7
$A_2(R_z)$
TWISTING LIBRATION
ν_8
$B_1(T_x)$
FRUSTRATED TRANSLATION
ν_9
$B_2(T_y)$
FRUSTRATED TRANSLATION

Figure 2

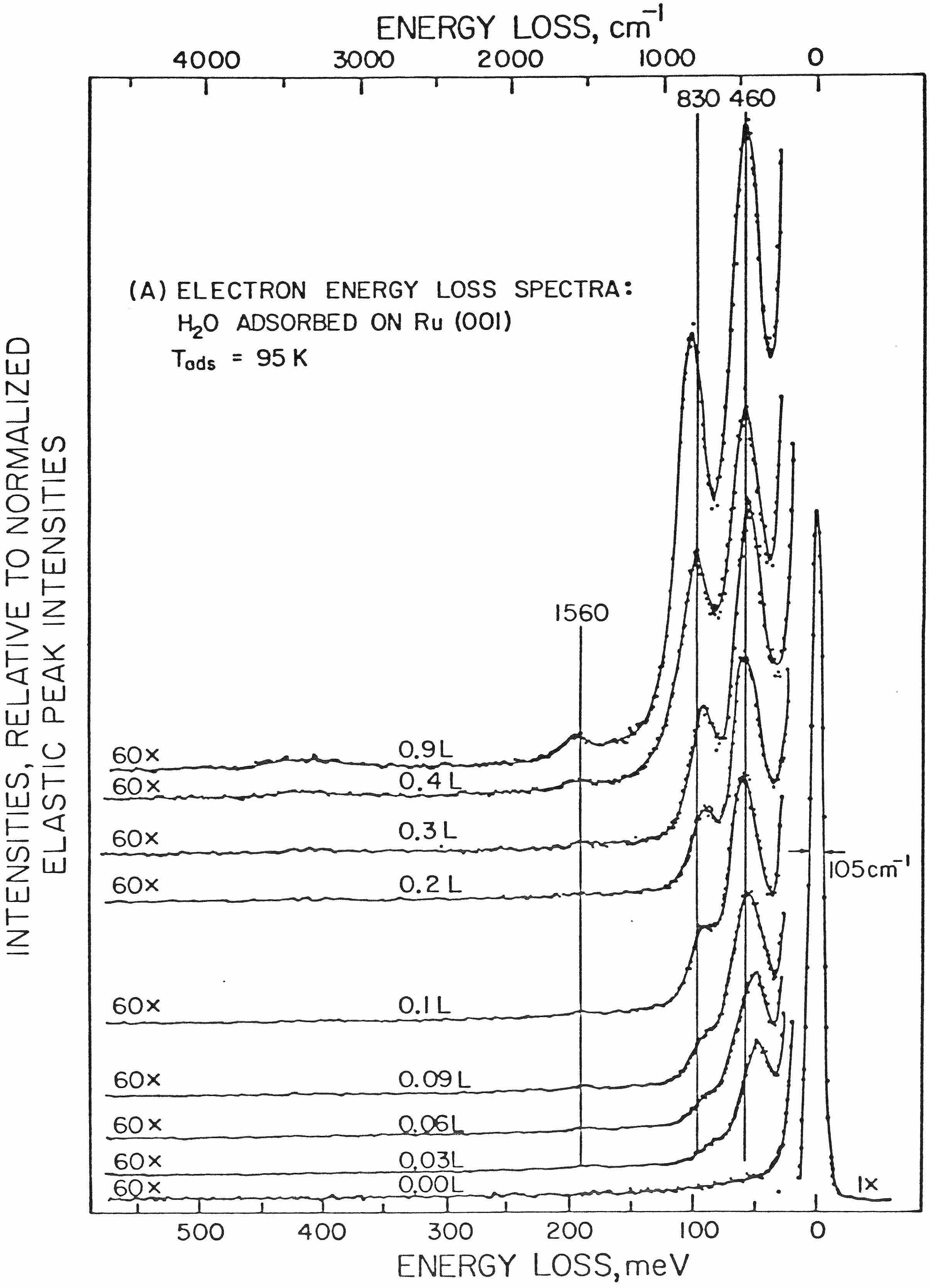
ENERGY LOSS, cm^{-1}
4000
3000
2000
1000
0
830
460
1560
(A) ELECTRON ENERGY LOSS SPECTRA:
H_2O ADSORBED ON Ru (001)
T_{ads} = 95 K
INTENSITIES, RELATIVE TO NORMALIZED ELASTIC PEAK INTENSITIES
60×
0.9L
60×
0.4L
60×
0.3L
60×
0.2L
105cm^{-1}
60×
0.1L
60×
0.09L
60×
0.06L
60×
0.03L
60×
0.00L
1×
500
400
300
200
100
0
ENERGY LOSS, meV

Figure 3(A)

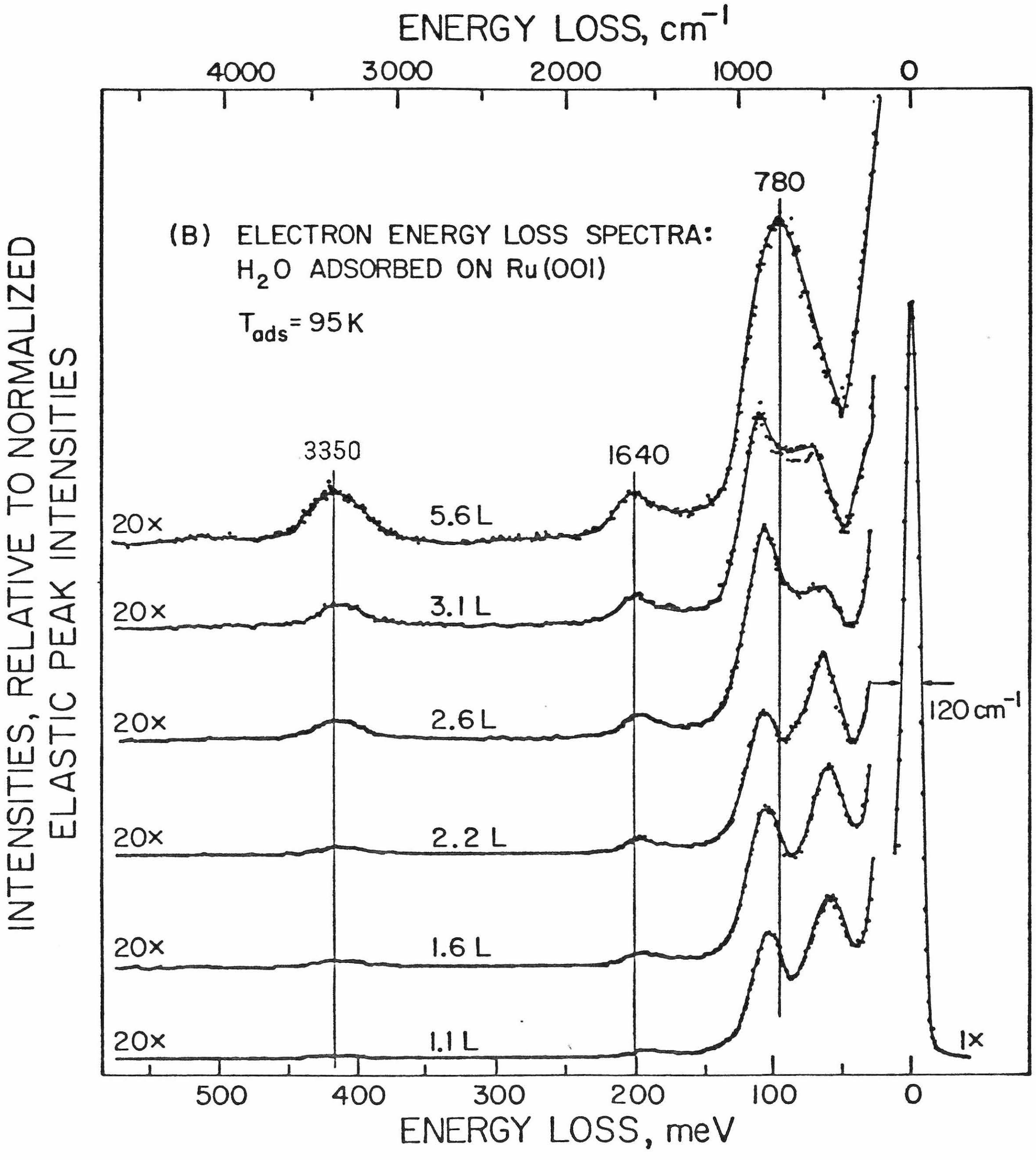
ENERGY LOSS, cm^{-1}
4000
3000
2000
1000
0
780
(B) ELECTRON ENERGY LOSS SPECTRA:
H_2O ADSORBED ON Ru(001)
T_{ads}= 95 K
3350
1640
20×
5.6 L
20×
3.1 L
20×
2.6 L
120 cm^{-1}
20×
2.2 L
20×
1.6 L
20×
1.1 L
1×
500
400
300
200
100
0
ENERGY LOSS, meV
INTENSITIES, RELATIVE TO NORMALIZED ELASTIC PEAK INTENSITIES

Figure 3(B)

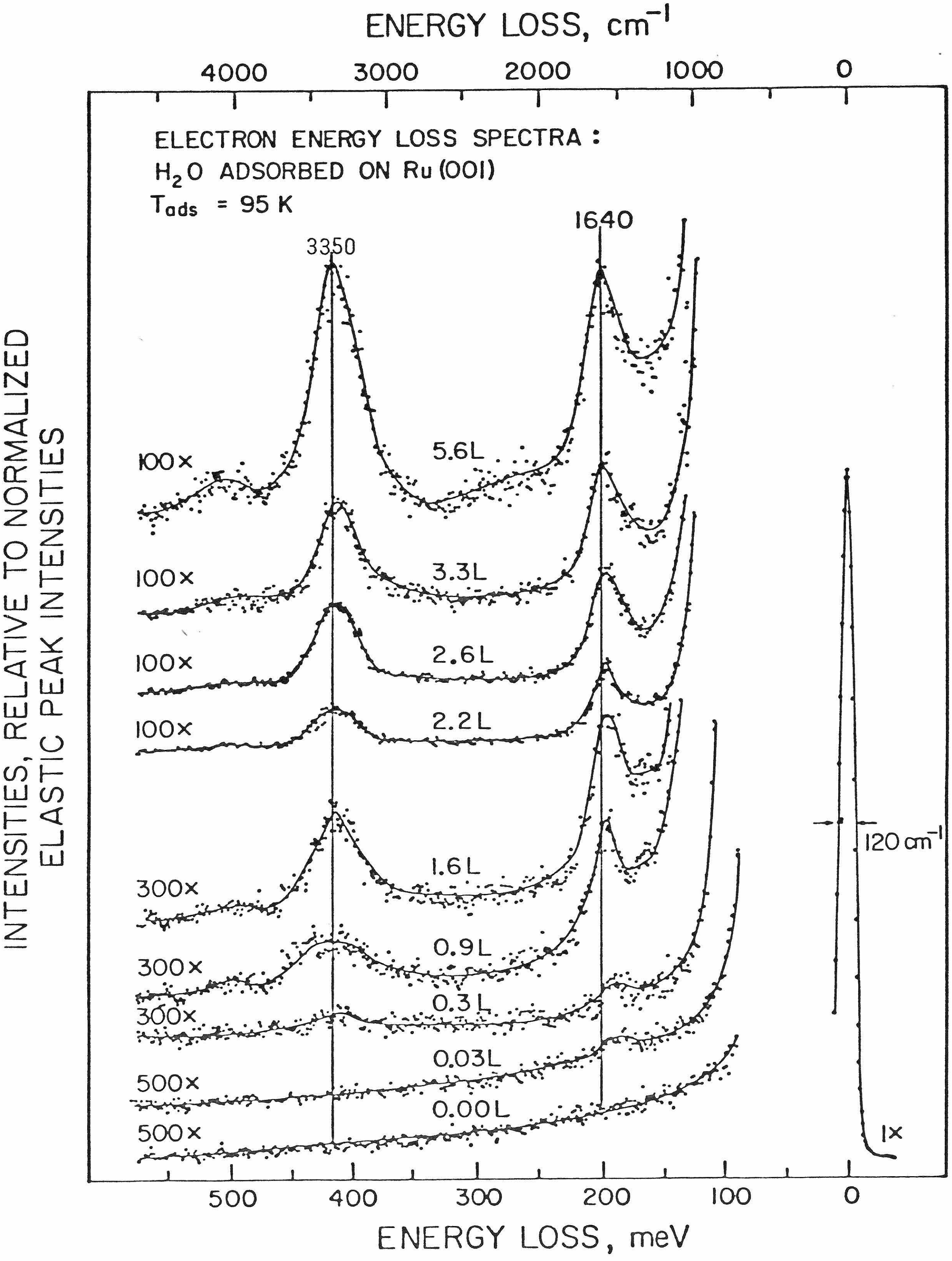
ENERGY LOSS, cm^{-1}
4000
3000
2000
1000
0
ELECTRON ENERGY LOSS SPECTRA:
H_2O ADSORBED ON Ru(001)
T_{ads} = 95 K
3350
1640
100×
5.6L
100×
3.3L
100×
2.6L
100×
2.2L
300×
1.6L
300×
0.9L
300×
0.3L
500×
0.03L
500×
0.00L
120 cm^{-1}
1×
500
400
300
200
100
0
ENERGY LOSS, meV
INTENSITIES, RELATIVE TO NORMALIZED ELASTIC PEAK INTENSITIES

Figure 4

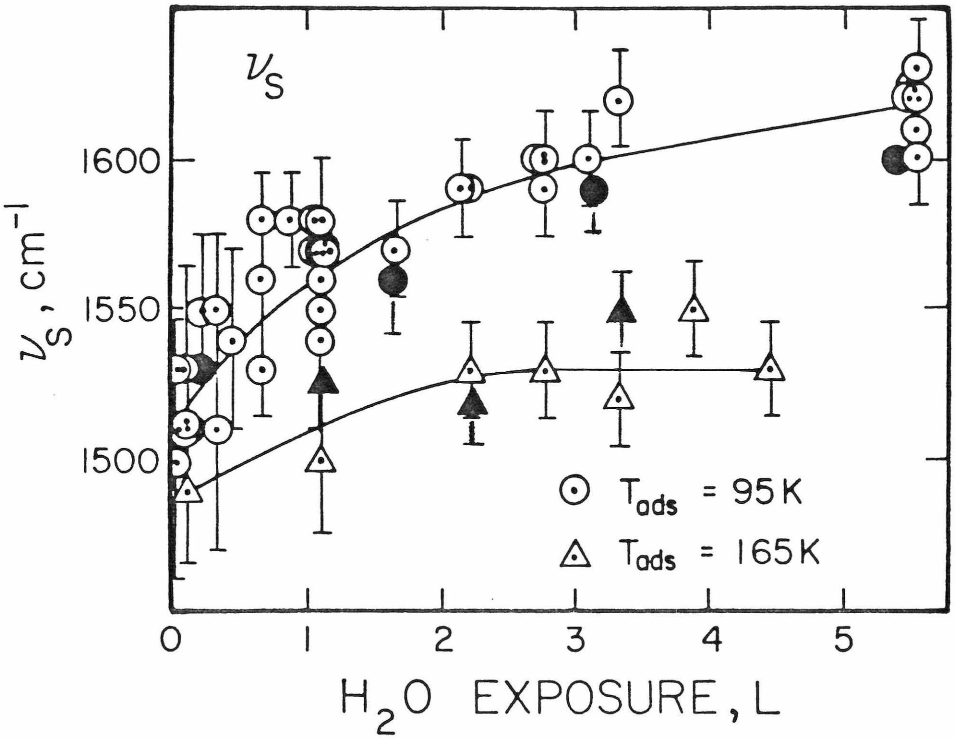
ν_S
ν_S, cm^{-1}
1500
1550
1600
0
1
2
3
4
5
H_2O EXPOSURE, L
⊙ T_{ads} = 95K
△ T_{ads} = 165K

Figure 5

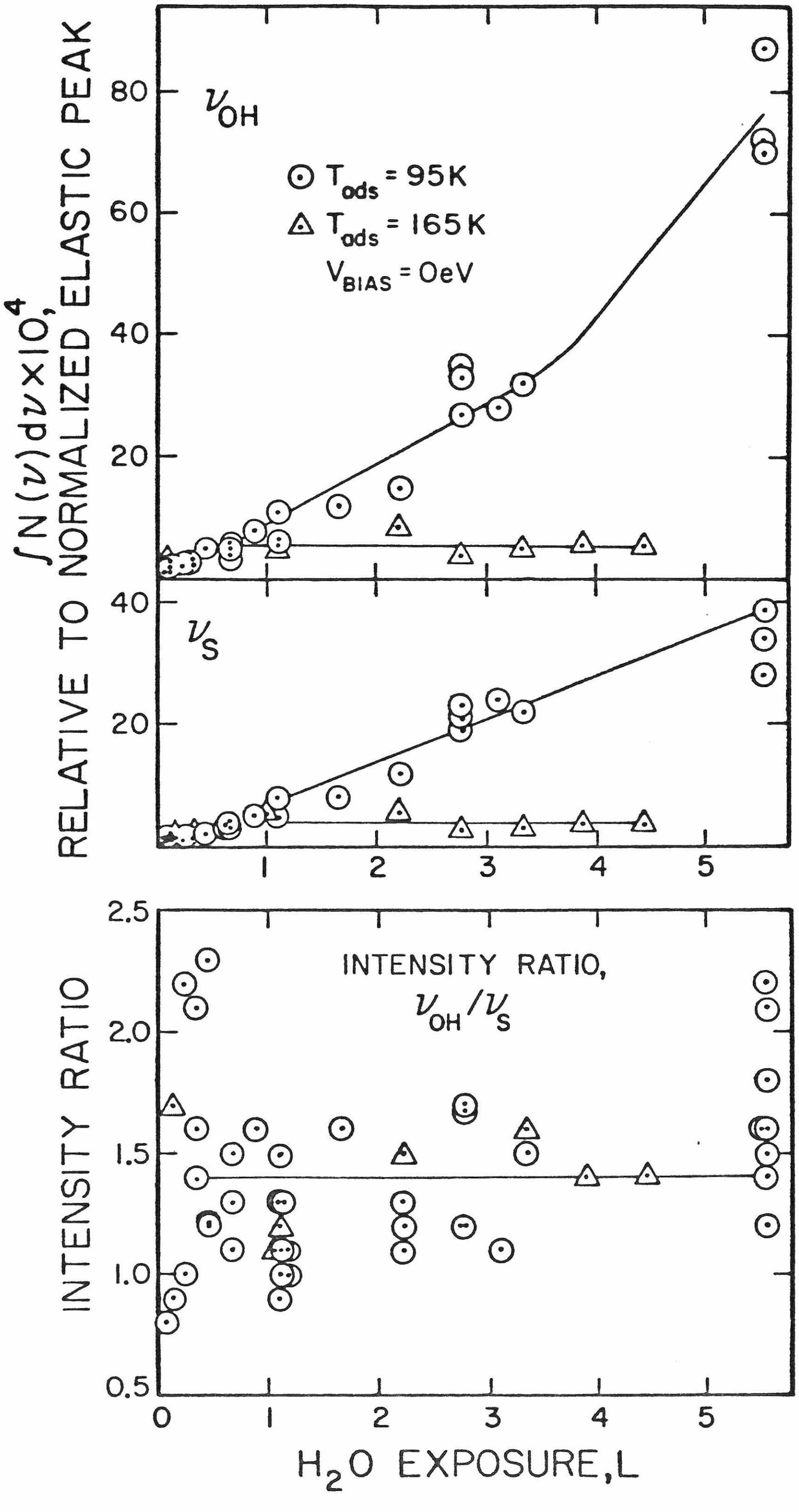
ν_{OH}
⊙ T_{ads} = 95K
△ T_{ads} = 165K
V_{BIAS} = 0eV
ν_S
INTENSITY RATIO, ν_{OH}/ν_S
$\int N(\nu)d\nu \times 10^4$, NORMALIZED ELASTIC PEAK RELATIVE TO
INTENSITY RATIO
H_2O EXPOSURE, L
80
60
40
20
40
20
2.5
2.0
1.5
1.0
0.5
0
1
2
3
4
5

Figure 6

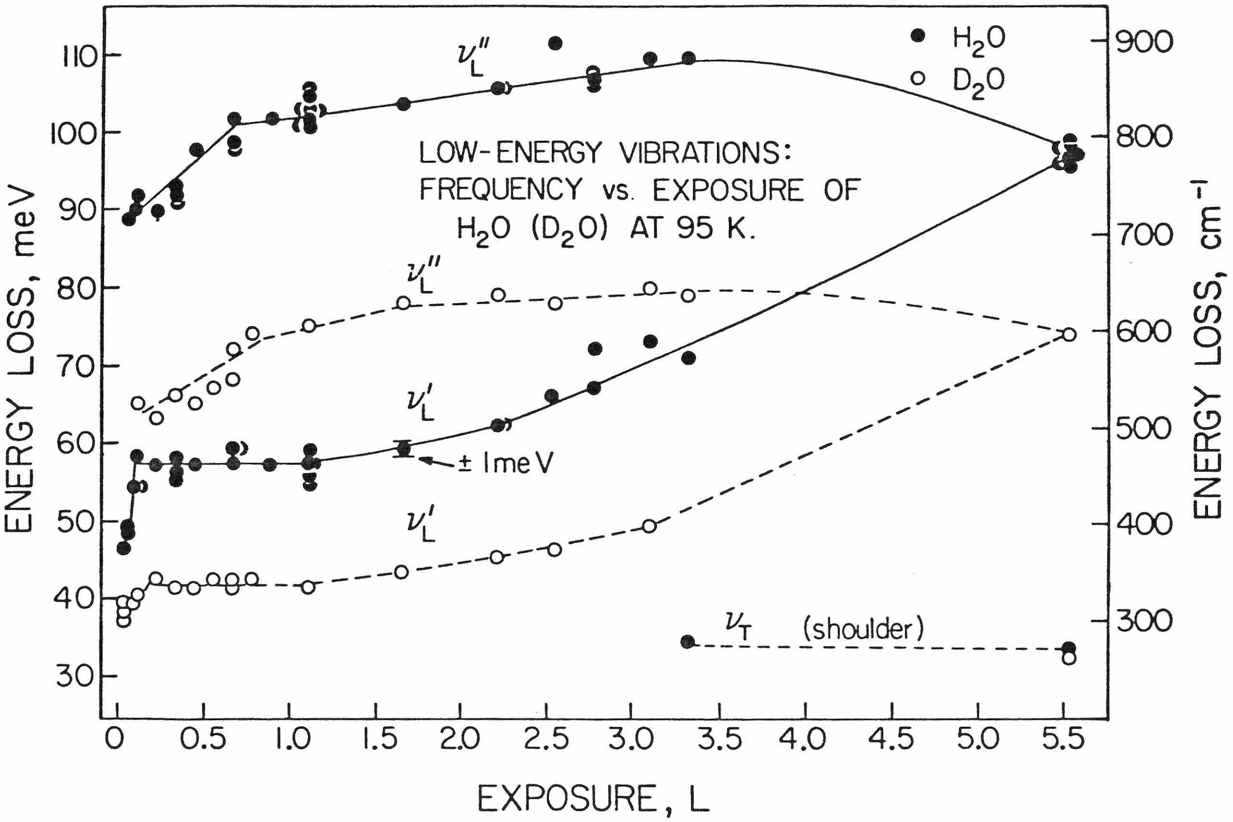

LOW-ENERGY VIBRATIONS:
FREQUENCY vs. EXPOSURE OF
H_2O (D_2O) AT 95 K.
● H_2O
○ D_2O
ν_L''
ν_L''
ν_L'
ν_L'
± 1meV
ν_T (shoulder)
ENERGY LOSS, meV
110
100
90
80
70
60
50
40
30
ENERGY LOSS, cm^{-1}
900
800
700
600
500
400
300
EXPOSURE, L
0
0.5
1.0
1.5
2.0
2.5
3.0
3.5
4.0
4.5
5.0
5.5

Figure 7

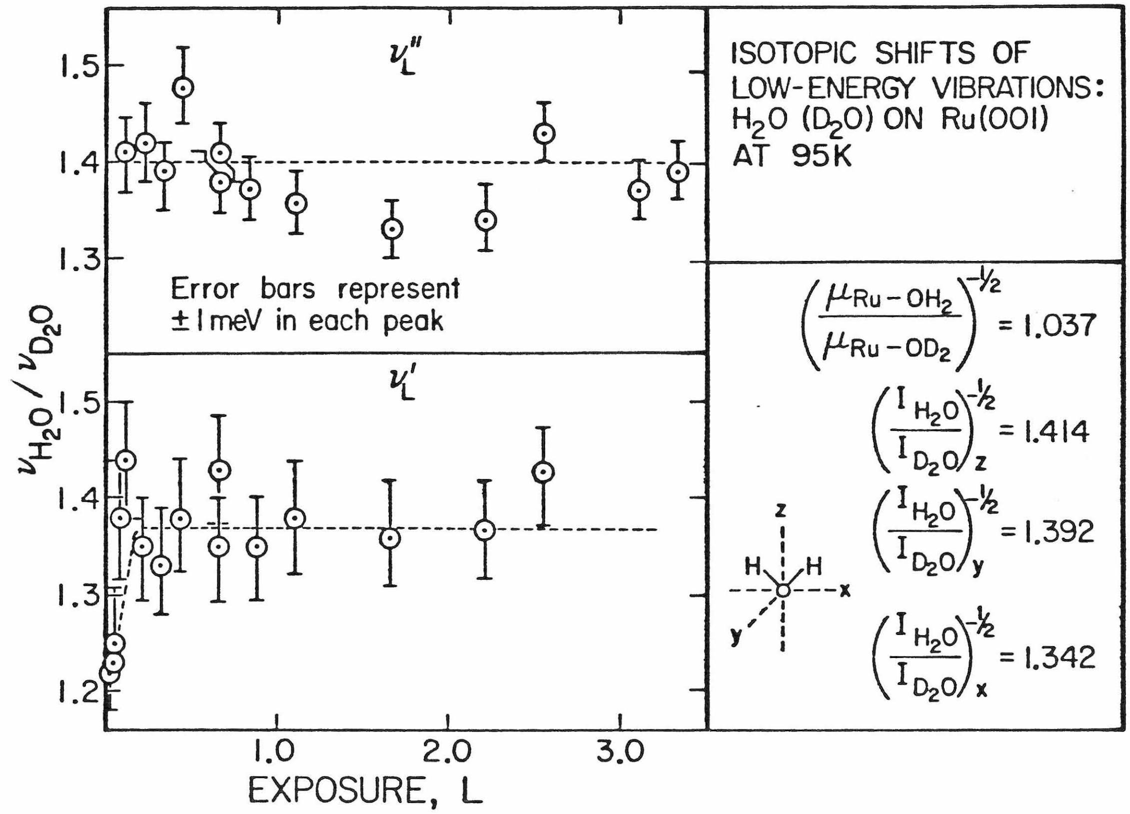
ISOTOPIC SHIFTS OF LOW-ENERGY VIBRATIONS: H_2O (D_2O) ON Ru(001) AT 95K
ν_L''
ν_L'
Error bars represent ±1meV in each peak
ν_{H_2O} / ν_{D_2O}
1.5
1.4
1.3
1.2
1.0
2.0
3.0
EXPOSURE, L
$\left(\frac{\mu_{Ru-OH_2}}{\mu_{Ru-OD_2}}\right)^{-1/2} = 1.037$
$\left(\frac{I_{H_2O}}{I_{D_2O}}\right)_z^{-1/2} = 1.414$
$\left(\frac{I_{H_2O}}{I_{D_2O}}\right)_y^{-1/2} = 1.392$
$\left(\frac{I_{H_2O}}{I_{D_2O}}\right)_x^{-1/2} = 1.342$
z
H
H
x
y

Figure 8

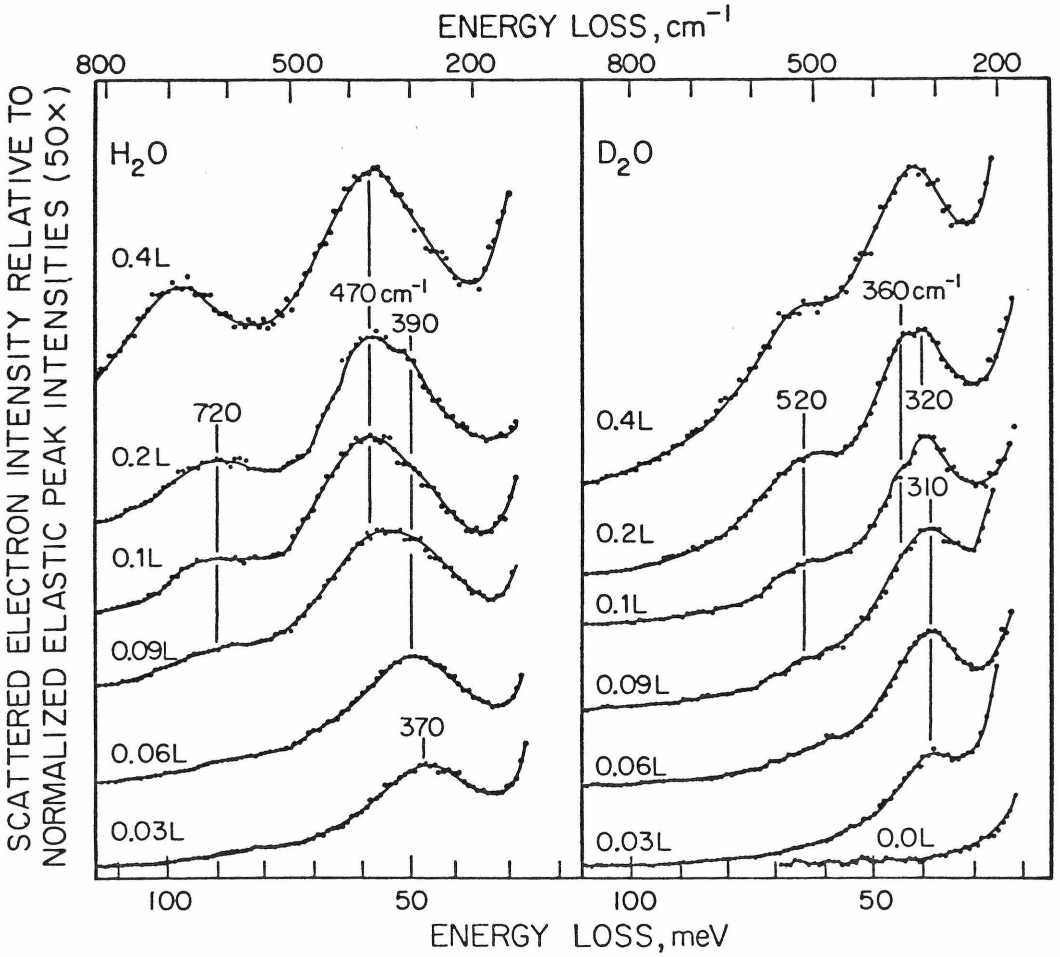
ENERGY LOSS, cm^{-1}
800
500
200
800
500
200
SCATTERED ELECTRON INTENSITY RELATIVE TO NORMALIZED ELASTIC PEAK INTENSITIES (50×)
H_2O
0.4L
470 cm^{-1}
390
720
0.2L
0.1L
0.09L
0.06L
370
0.03L
D_2O
360 cm^{-1}
0.4L
520
320
310
0.2L
0.1L
0.09L
0.06L
0.03L
0.0L
100
50
100
50
ENERGY LOSS, meV

Figure 9

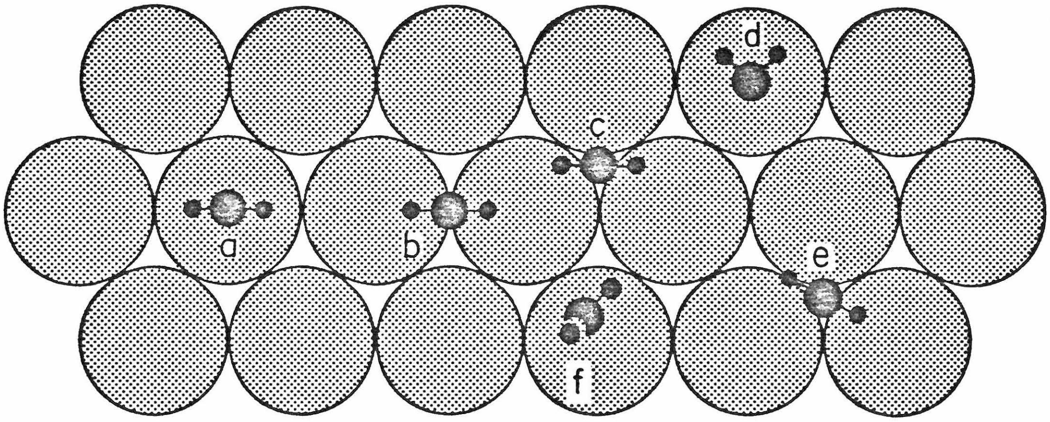

Figure 10

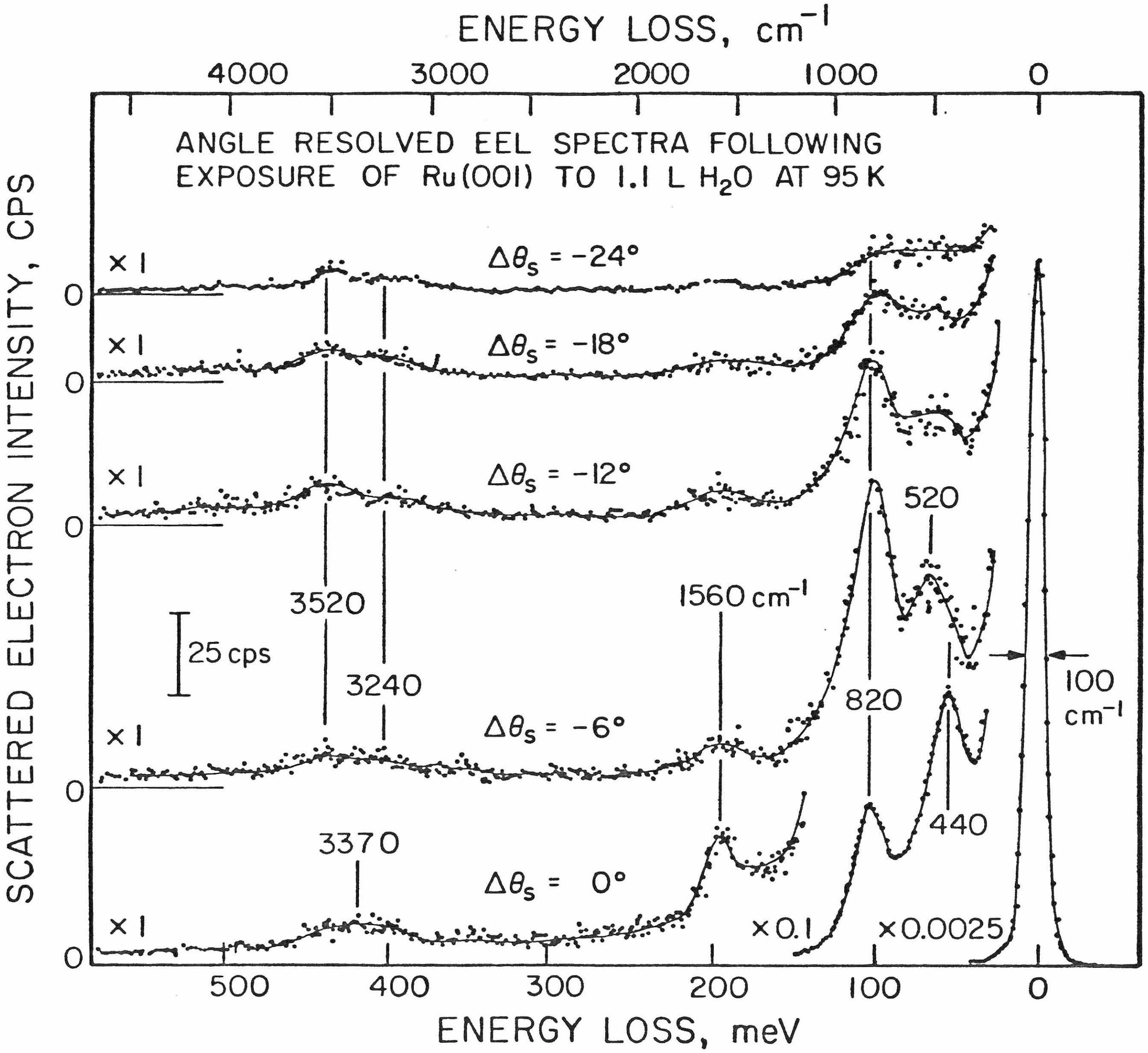
ENERGY LOSS, cm^{-1}
4000
3000
2000
1000
0
ANGLE RESOLVED EEL SPECTRA FOLLOWING
EXPOSURE OF Ru(001) TO 1.1 L H_2O AT 95 K
×1
$\Delta\theta_s$ = −24°
×1
$\Delta\theta_s$ = −18°
×1
$\Delta\theta_s$ = −12°
520
3520
1560 cm^{-1}
25 cps
3240
820
100 cm^{-1}
×1
$\Delta\theta_s$ = −6°
440
3370
$\Delta\theta_s$ = 0°
×1
×0.1
×0.0025
SCATTERED ELECTRON INTENSITY, CPS
0
0
0
0
0
500
400
300
200
100
0
ENERGY LOSS, meV

Figure 11

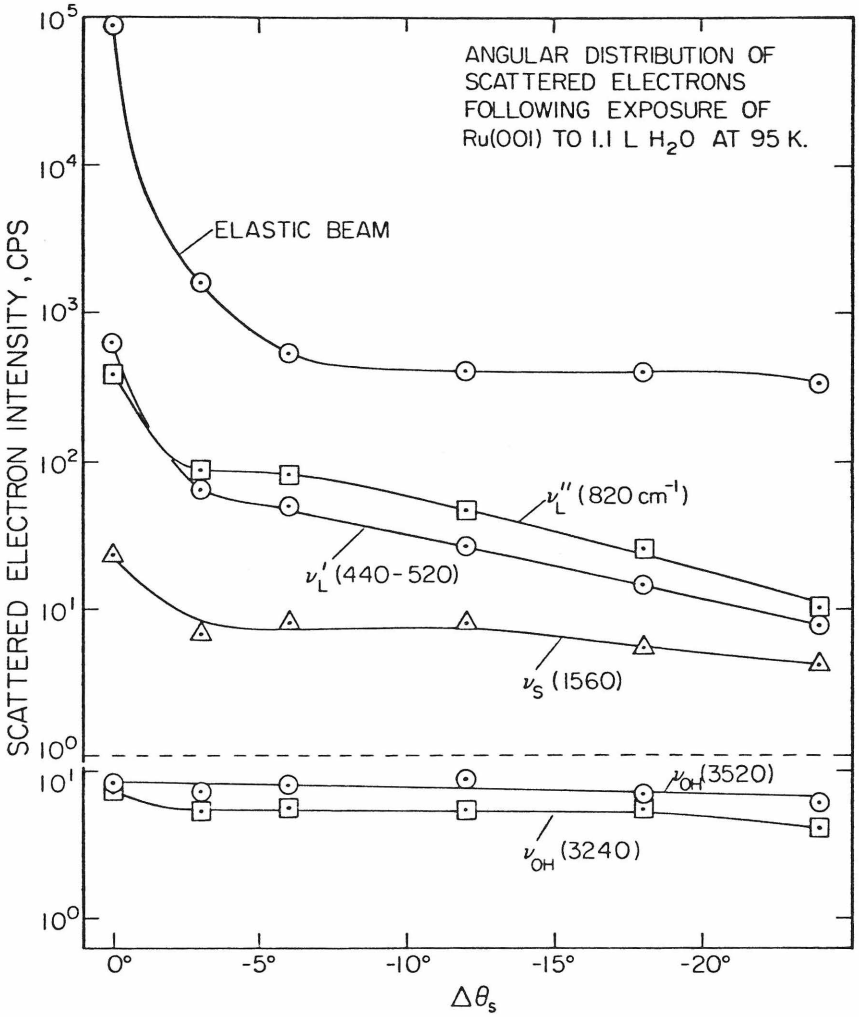
ANGULAR DISTRIBUTION OF
SCATTERED ELECTRONS
FOLLOWING EXPOSURE OF
Ru(001) TO 1.1 L H$_2$O AT 95 K.
ELASTIC BEAM
ν_L'' (820 cm^{-1})
ν_L' (440-520)
ν_S (1560)
ν_{OH} (3520)
ν_{OH} (3240)
SCATTERED ELECTRON INTENSITY, CPS
10^5
10^4
10^3
10^2
10^1
10^0
10^1
10^0
0°
-5°
-10°
-15°
-20°
$\Delta\theta_s$

Figure 12

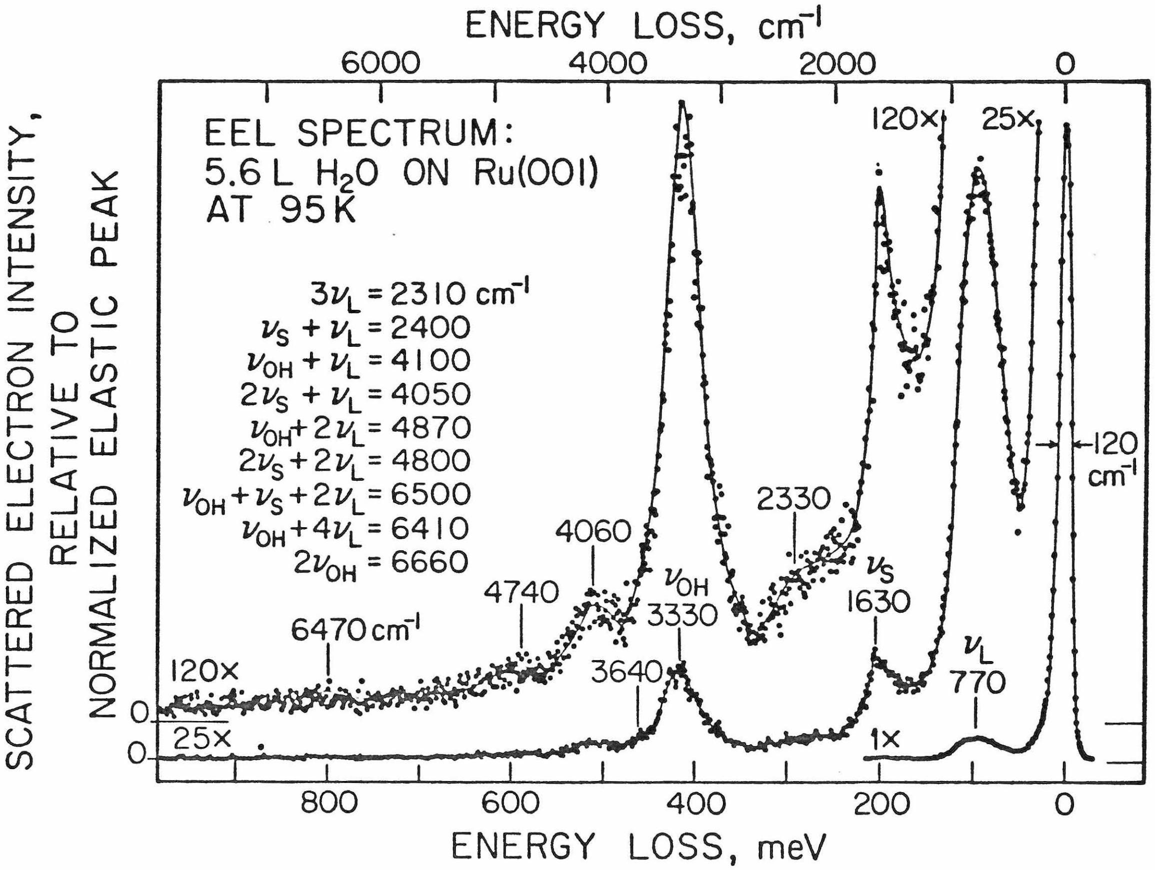
ENERGY LOSS, cm⁻¹
6000
4000
2000
0
EEL SPECTRUM:
5.6 L H₂O ON Ru(001)
AT 95 K
3νL = 2310 cm⁻¹
νS + νL = 2400
νOH + νL = 4100
2νS + νL = 4050
νOH + 2νL = 4870
2νS + 2νL = 4800
νOH + νS + 2νL = 6500
νOH + 4νL = 6410
2νOH = 6660
120×
25×
4060
2330
4740
6470 cm⁻¹
νOH
3330
νS
1630
3640
νL
770
120×
25×
1×
120 cm⁻¹
0
0
SCATTERED ELECTRON INTENSITY, RELATIVE TO NORMALIZED ELASTIC PEAK
800
600
400
200
0
ENERGY LOSS, meV

Figure 13

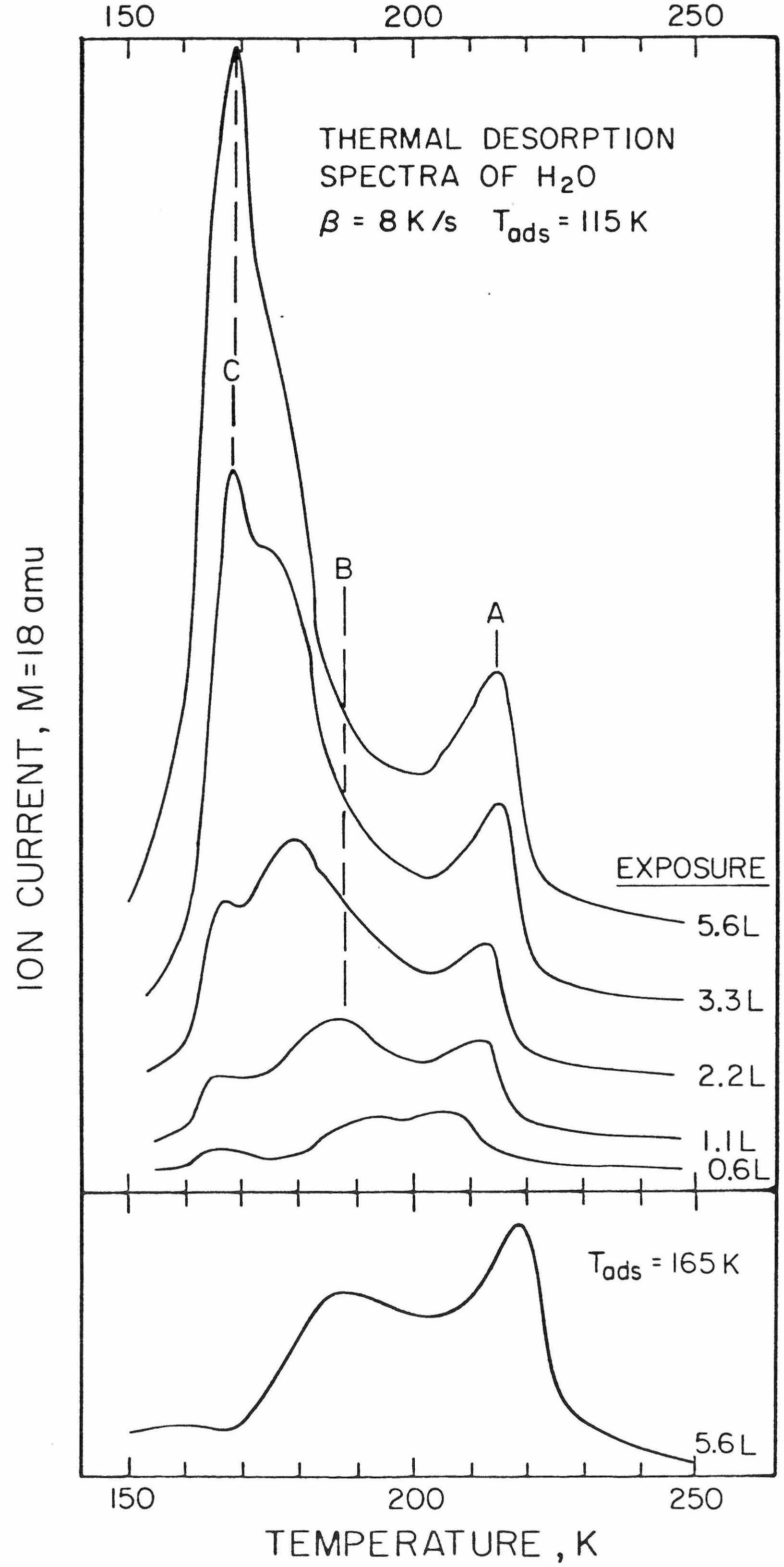
150
200
250
THERMAL DESORPTION
SPECTRA OF H_2O
β = 8 K/s T_{ads} = 115 K
C
B
A
EXPOSURE
5.6L
3.3L
2.2L
1.1L
0.6L
T_{ads} = 165 K
5.6L
ION CURRENT, M=18 amu
TEMPERATURE, K

Figure 14

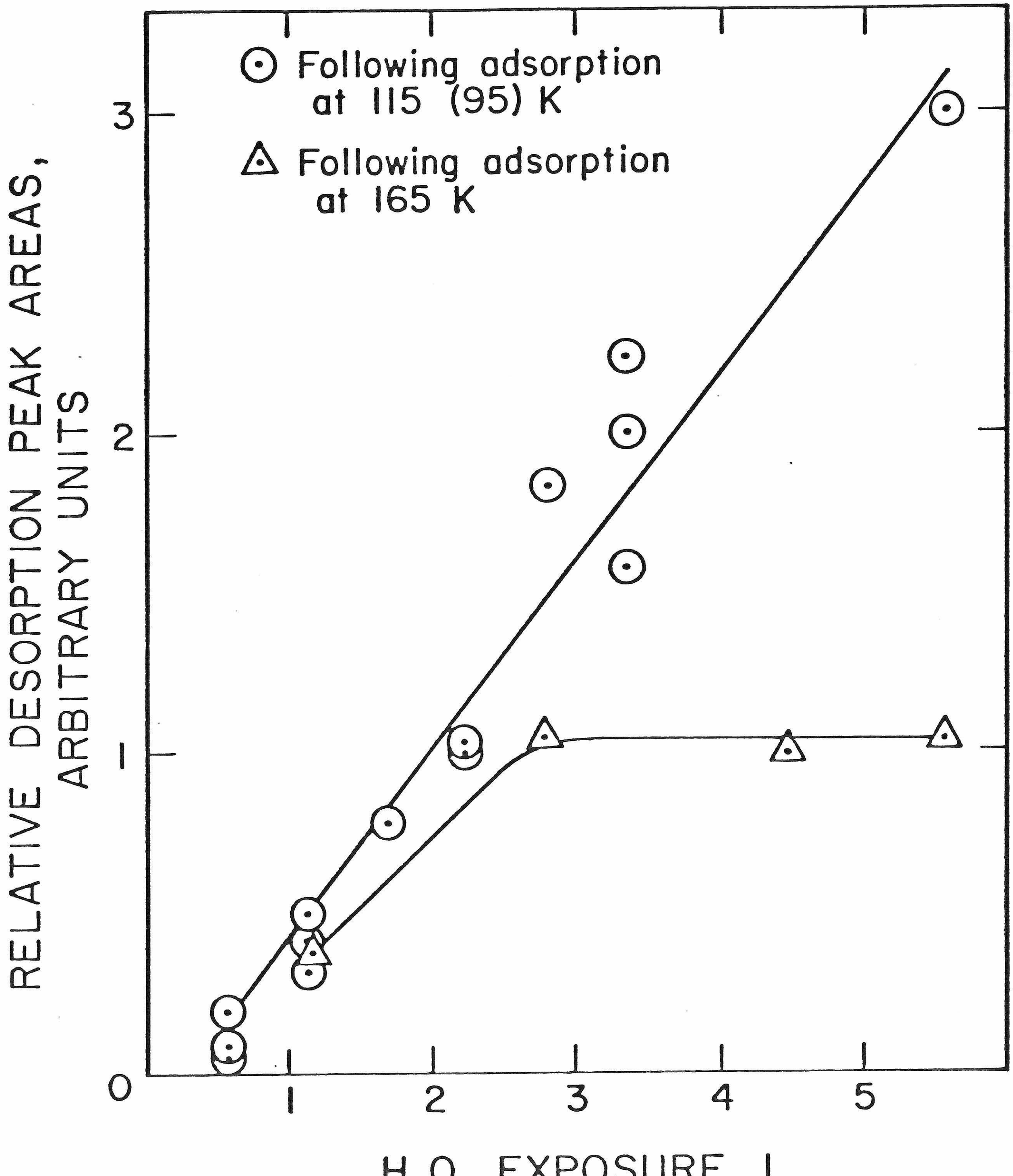
⊙ Following adsorption at 115 (95) K
△ Following adsorption at 165 K
RELATIVE DESORPTION PEAK AREAS, ARBITRARY UNITS
0
1
2
3
1
2
3
4
5
H_2O EXPOSURE, L

Figure 15

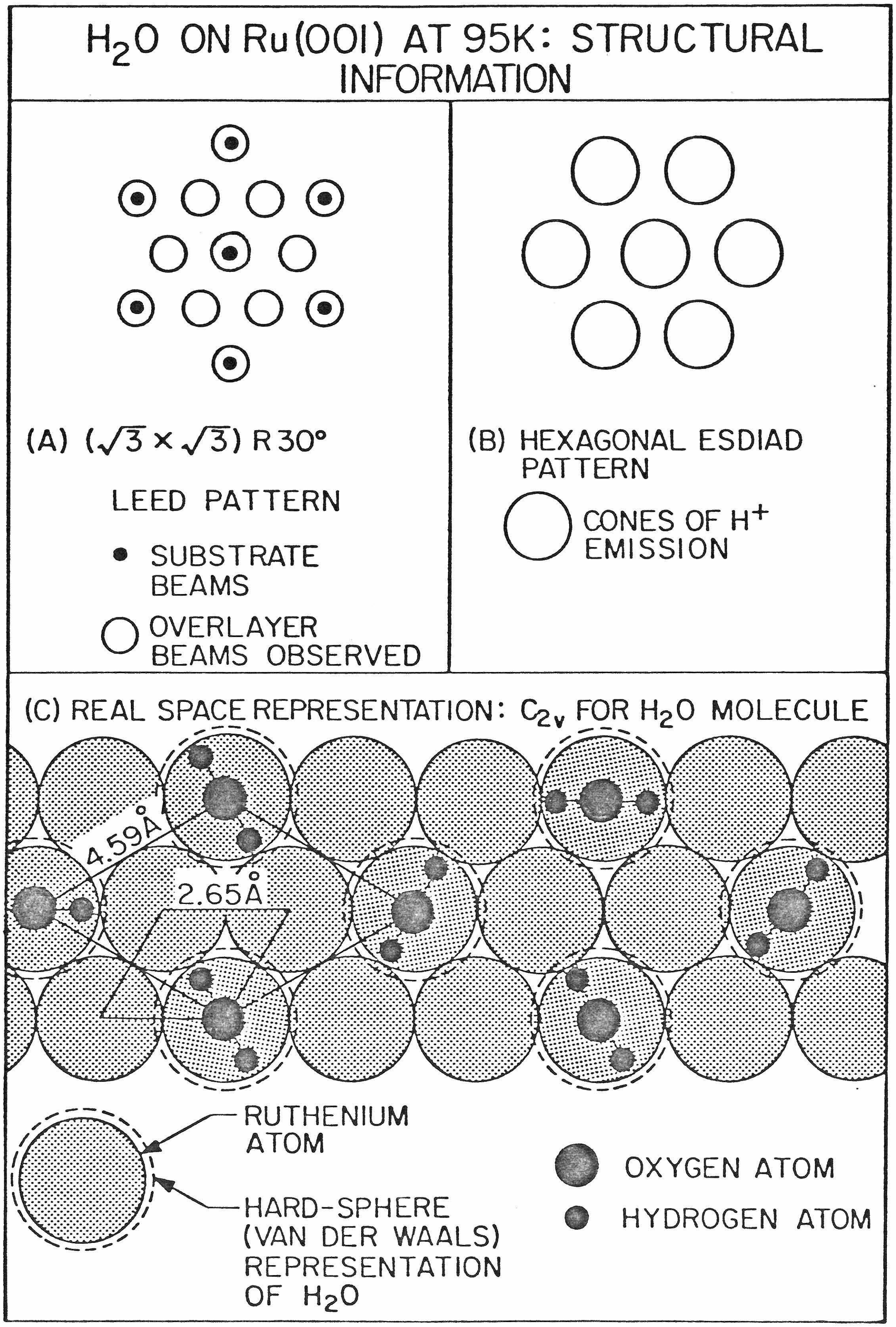
H_2O ON Ru(001) AT 95K: STRUCTURAL INFORMATION
(A) $(\sqrt{3} \times \sqrt{3})$ R30°
LEED PATTERN
● SUBSTRATE BEAMS
○ OVERLAYER BEAMS OBSERVED
(B) HEXAGONAL ESDIAD PATTERN
○ CONES OF H^+ EMISSION
(C) REAL SPACE REPRESENTATION: C_{2v} FOR H_2O MOLECULE
4.59Å
2.65Å
RUTHENIUM ATOM
HARD-SPHERE (VAN DER WAALS) REPRESENTATION OF H_2O
OXYGEN ATOM
HYDROGEN ATOM

Figure 16

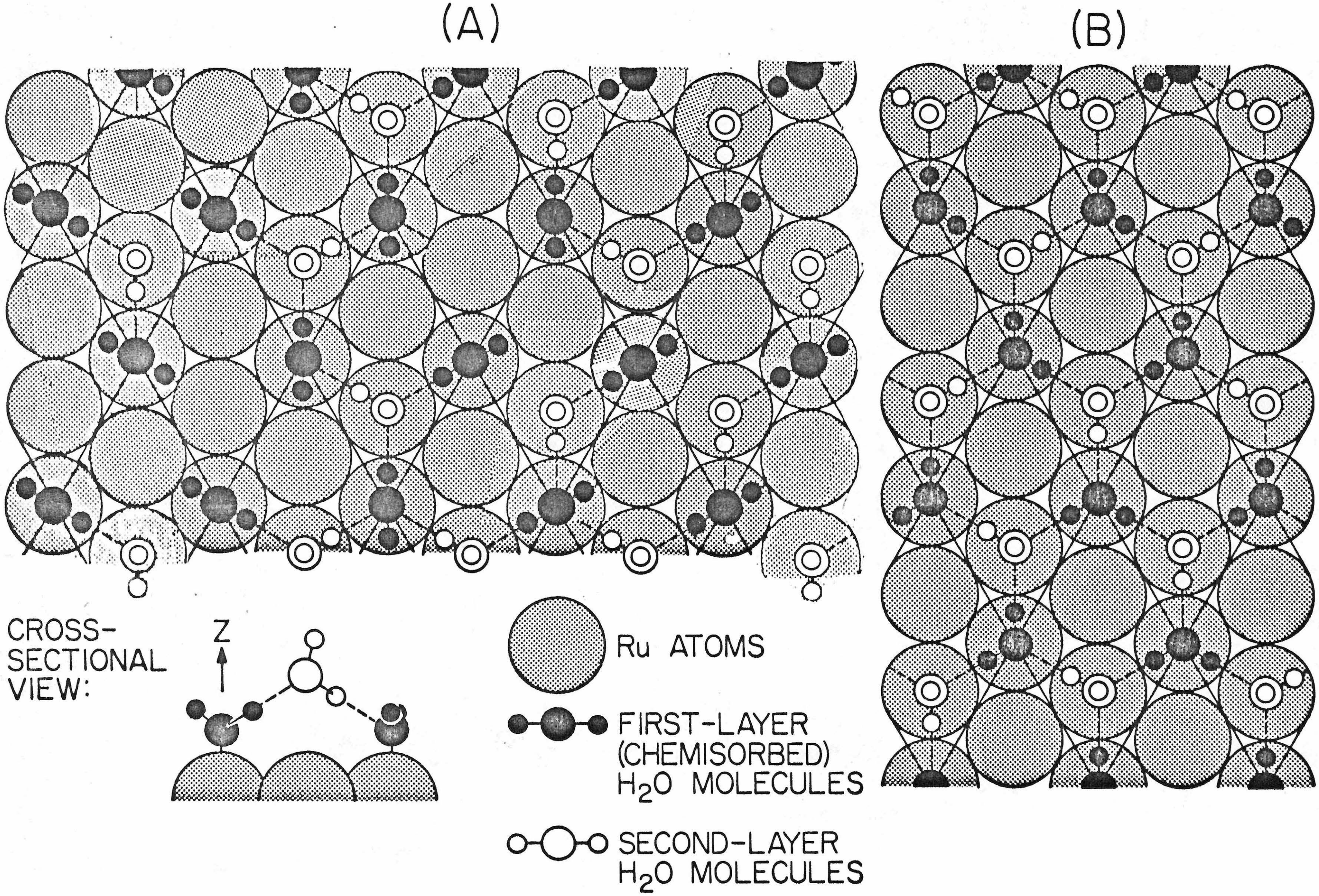
(A)
(B)
CROSS-SECTIONAL VIEW:
Z
Ru ATOMS
FIRST-LAYER (CHEMISORBED) H_2O MOLECULES
SECOND-LAYER H_2O MOLECULES

Figure 17

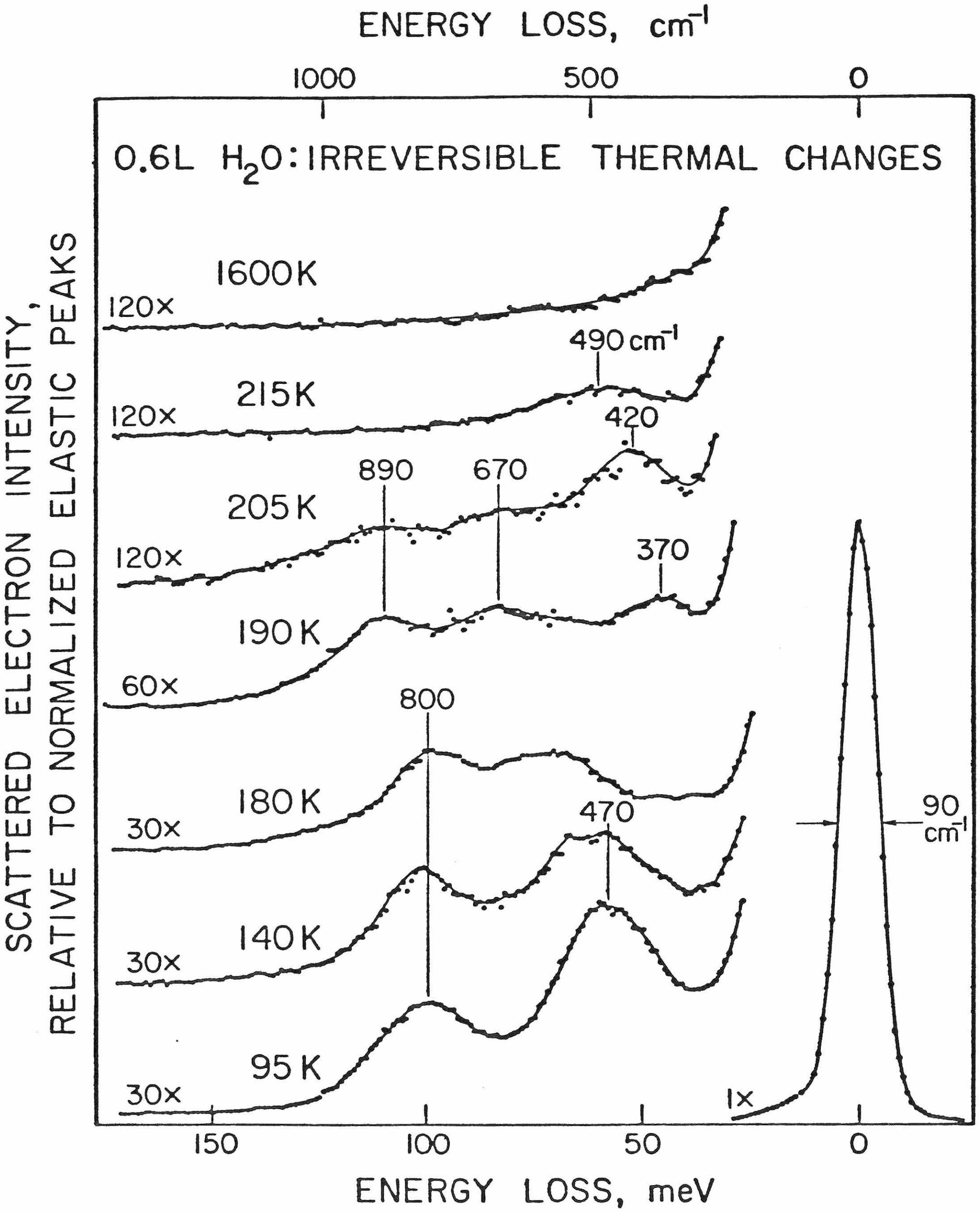
ENERGY LOSS, cm^{-1}
1000
500
0
0.6L H_2O: IRREVERSIBLE THERMAL CHANGES
SCATTERED ELECTRON INTENSITY, RELATIVE TO NORMALIZED ELASTIC PEAKS
1600K
120x
490 cm^{-1}
215K
120x
420
890
670
205K
120x
370
190K
60x
800
180K
30x
470
140K
30x
95K
30x
1x
90 cm^{-1}
150
100
50
0
ENERGY LOSS, meV

Figure 18

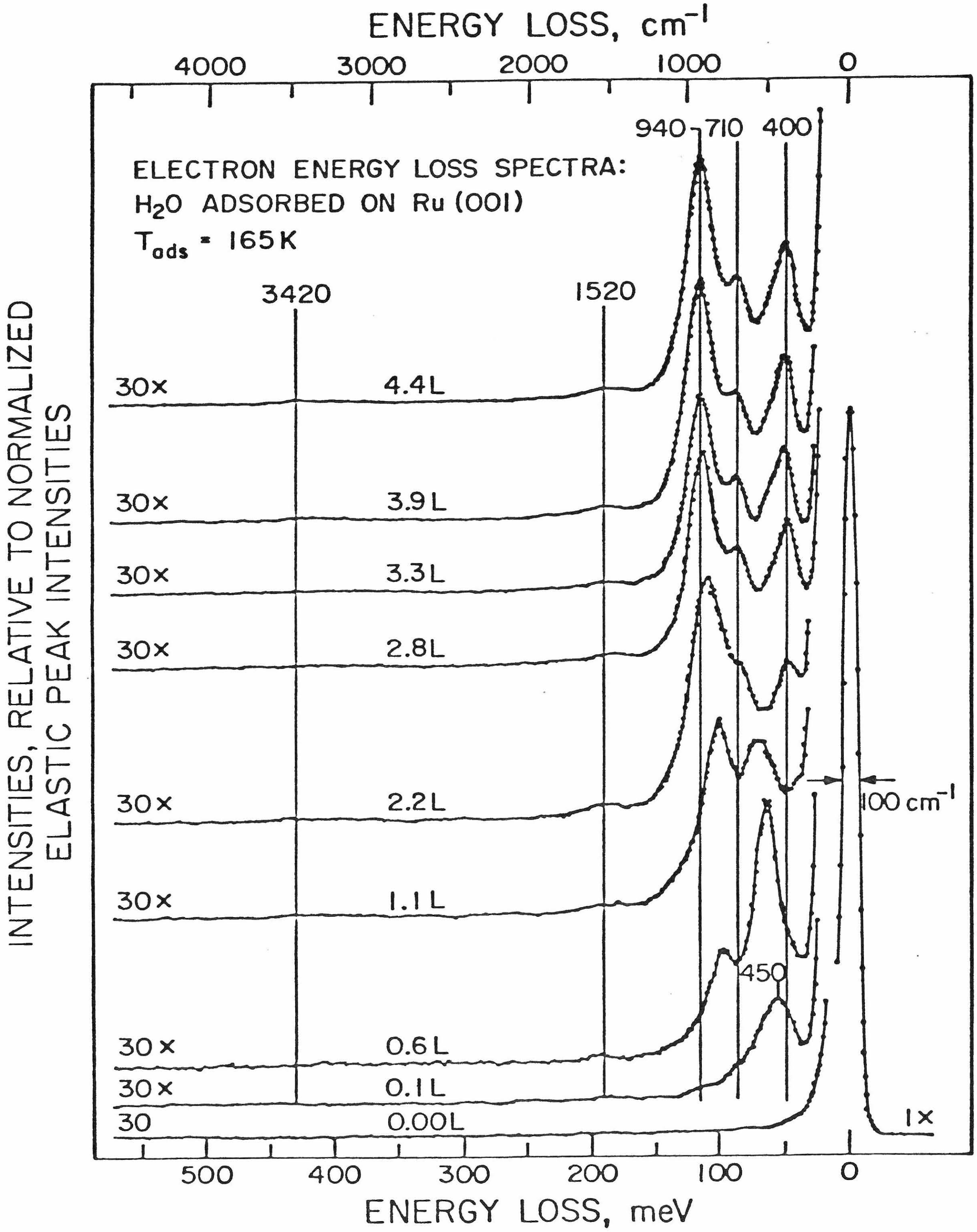
ENERGY LOSS, cm^{-1}
4000
3000
2000
1000
0
940
710
400
ELECTRON ENERGY LOSS SPECTRA:
H_2O ADSORBED ON Ru (001)
T_{ads} = 165K
3420
1520
30×
4.4L
30×
3.9L
30×
3.3L
30×
2.8L
30×
2.2L
100 cm^{-1}
30×
1.1L
450
30×
0.6L
30×
0.1L
30
0.00L
1×
500
400
300
200
100
0
ENERGY LOSS, meV
INTENSITIES, RELATIVE TO NORMALIZED ELASTIC PEAK INTENSITIES

Figure 19

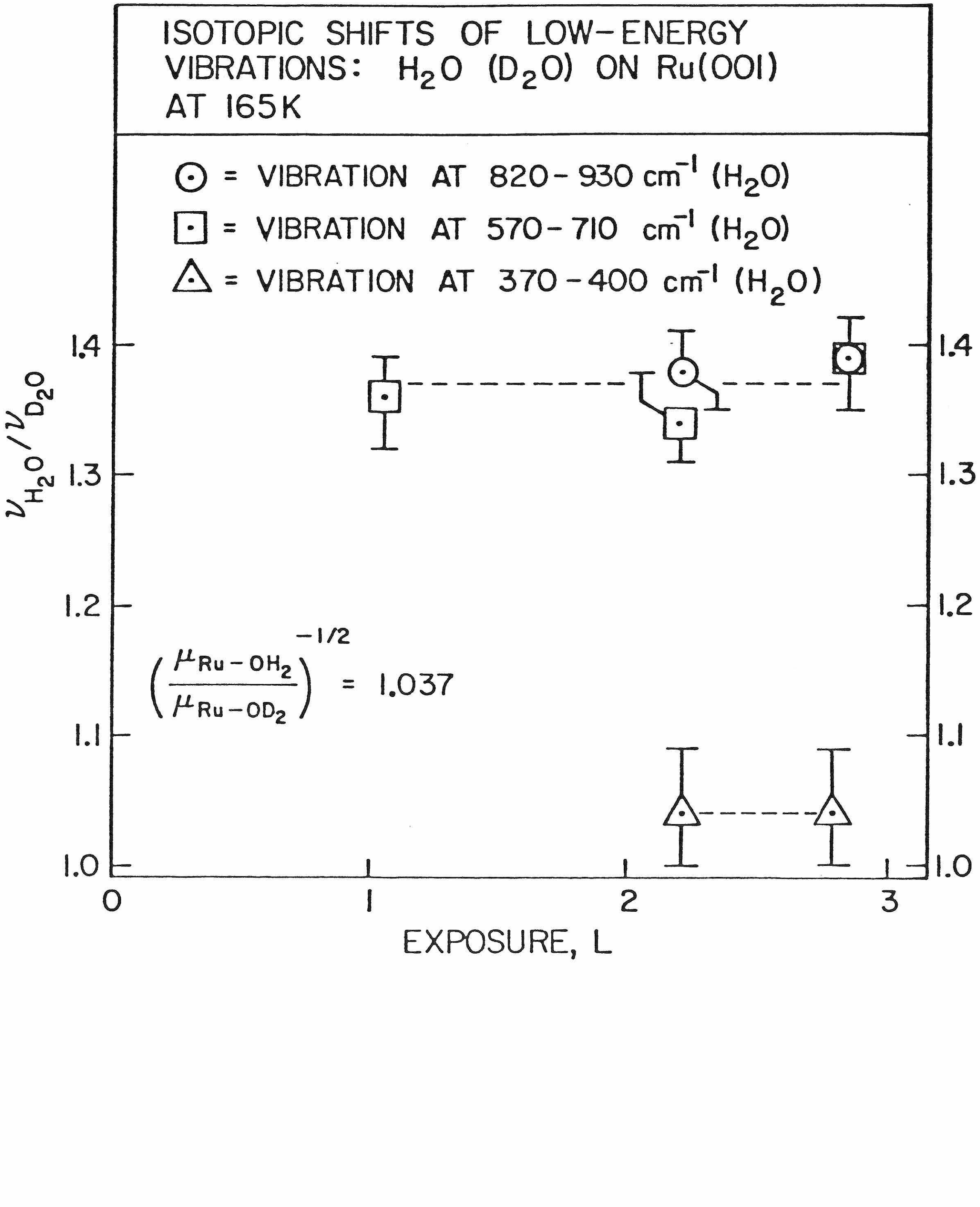
ISOTOPIC SHIFTS OF LOW-ENERGY VIBRATIONS: H_2O (D_2O) ON Ru(001) AT 165K
⊙ = VIBRATION AT 820-930 cm^{-1} (H_2O)
⊡ = VIBRATION AT 570-710 cm^{-1} (H_2O)
△ = VIBRATION AT 370-400 cm^{-1} (H_2O)
ν_{H_2O}/ν_{D_2O}
1.0
1.1
1.2
1.3
1.4
$\left(\frac{\mu_{Ru-OH_2}}{\mu_{Ru-OD_2}}\right)^{-1/2} = 1.037$
0
1
2
3
EXPOSURE, L

Figure 20

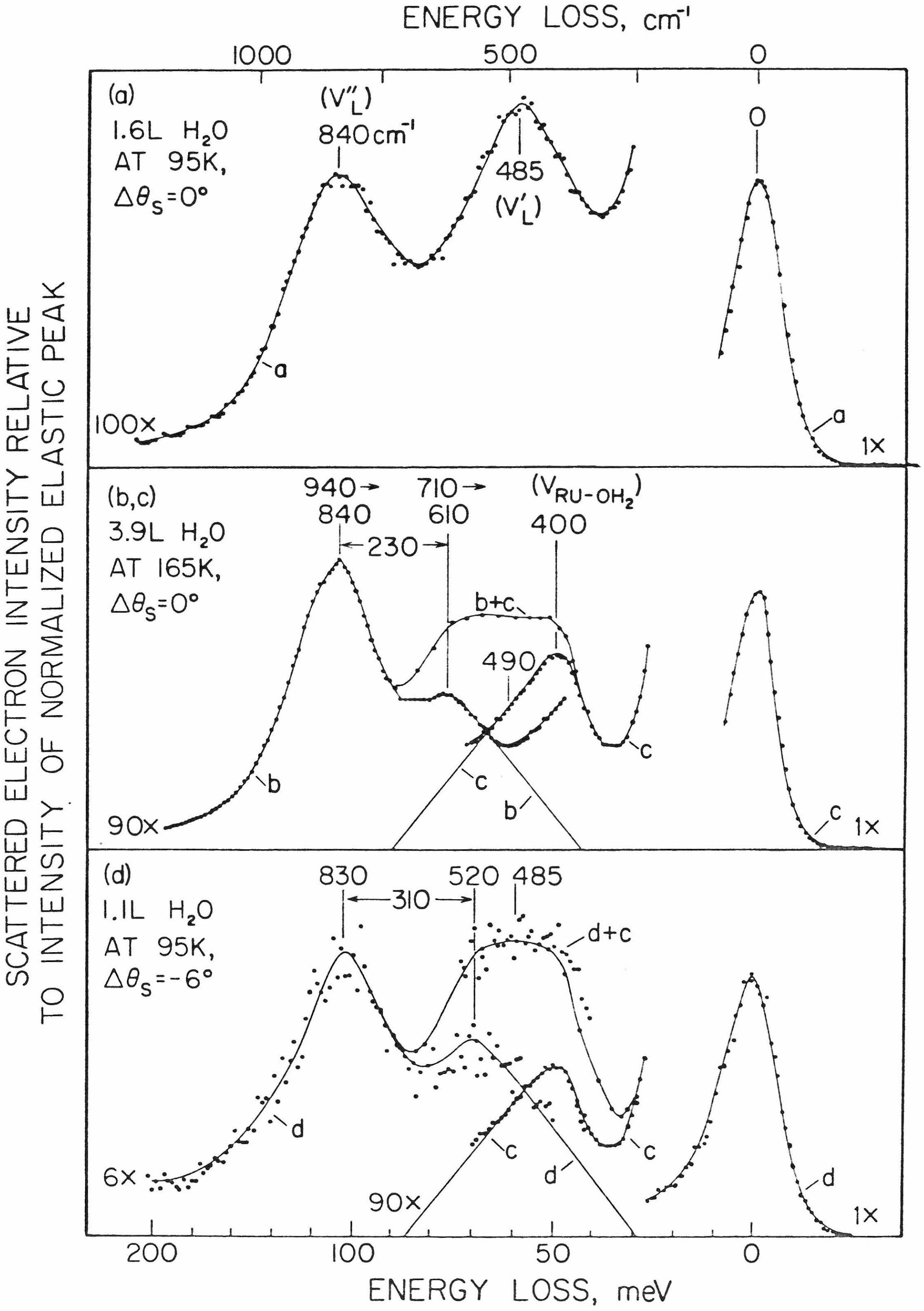
ENERGY LOSS, cm⁻¹
1000
500
0
(a)
1.6L H_2O
AT 95K,
$\Delta\theta_S$=0°
(V''_L)
840cm⁻¹
485
(V'_L)
0
a
100×
a
1×
(b,c)
3.9L H_2O
AT 165K,
$\Delta\theta_S$=0°
940→
840
710→
610
←230→
(V_{RU-OH_2})
400
b+c
490
b
c
b
c
c
90×
1×
(d)
1.1L H_2O
AT 95K,
$\Delta\theta_S$=-6°
830
←310→
520
485
d+c
d
c
c
d
d
6×
90×
1×
SCATTERED ELECTRON INTENSITY RELATIVE
TO INTENSITY OF NORMALIZED ELASTIC PEAK
200
100
50
0
ENERGY LOSS, meV

Figure 21

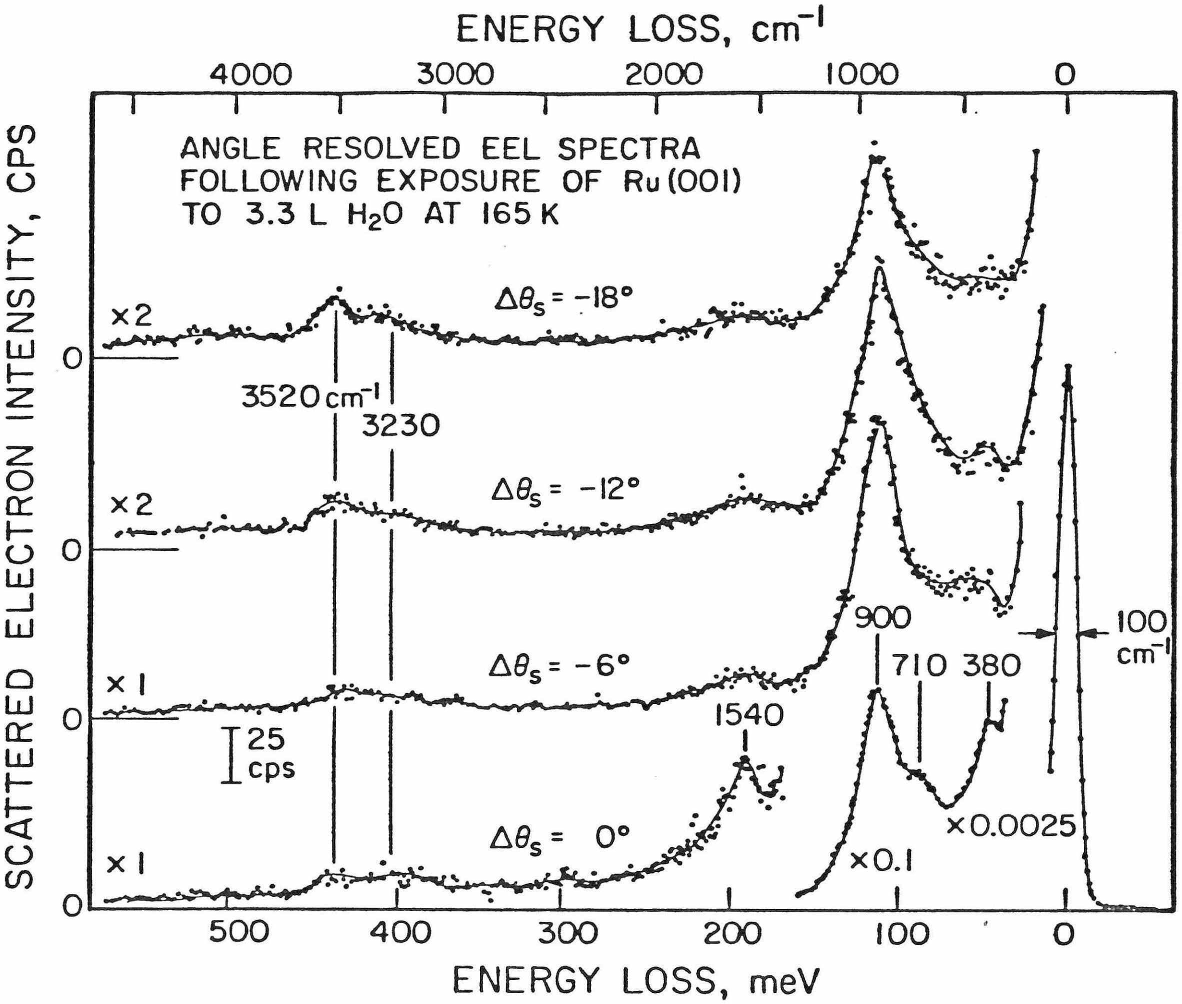
ENERGY LOSS, cm^{-1}
4000
3000
2000
1000
0
ANGLE RESOLVED EEL SPECTRA
FOLLOWING EXPOSURE OF Ru(001)
TO 3.3 L H_2O AT 165 K
×2
$\Delta\theta_s = -18°$
3520 cm^{-1}
3230
×2
$\Delta\theta_s = -12°$
900
710 380
100 cm^{-1}
×1
$\Delta\theta_s = -6°$
1540
25 cps
×0.0025
$\Delta\theta_s = 0°$
×0.1
×1
0
0
0
0
500
400
300
200
100
0
ENERGY LOSS, meV
SCATTERED ELECTRON INTENSITY, CPS

Figure 22

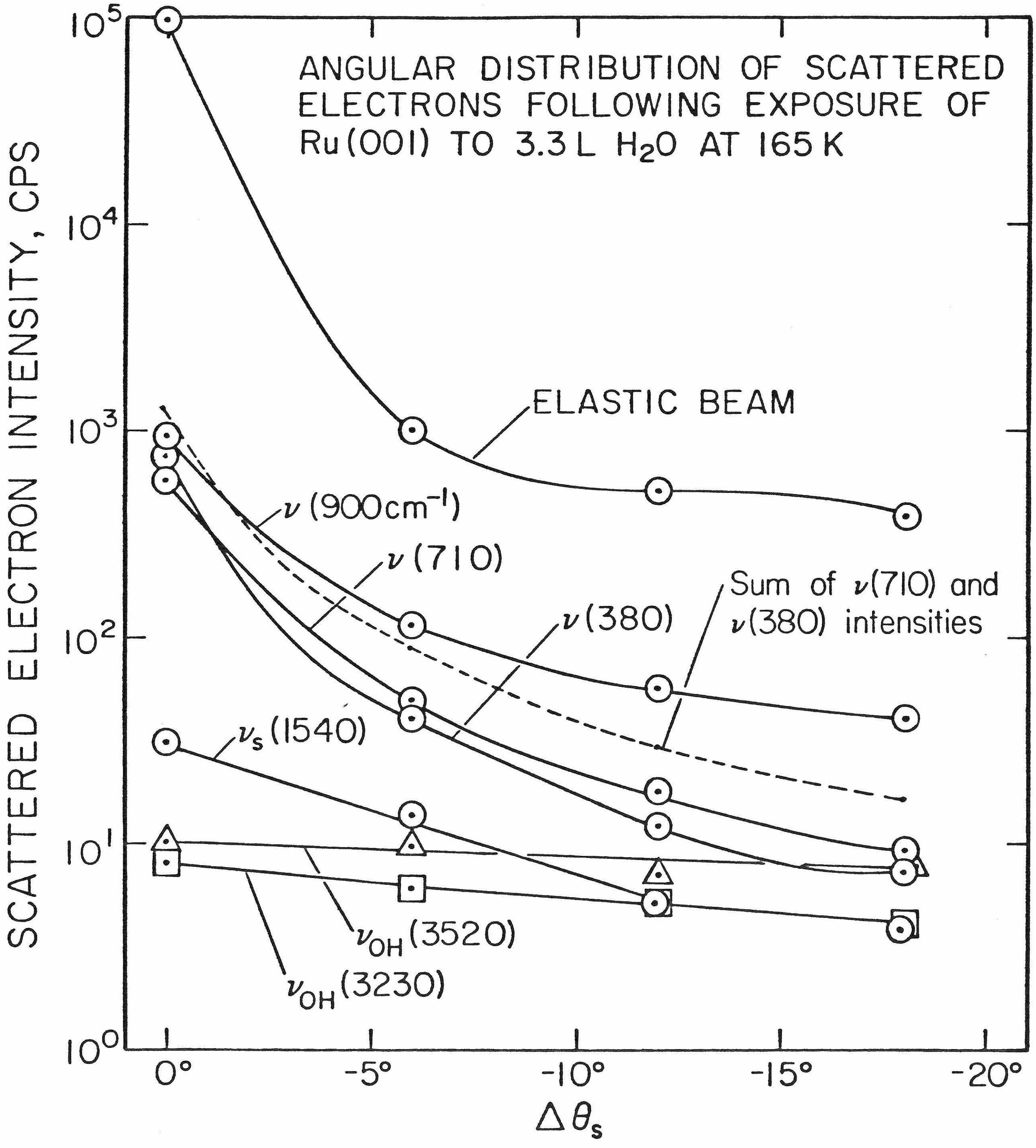
ANGULAR DISTRIBUTION OF SCATTERED ELECTRONS FOLLOWING EXPOSURE OF Ru(001) TO 3.3 L H_2O AT 165 K
SCATTERED ELECTRON INTENSITY, CPS
10^5
10^4
10^3
10^2
10^1
10^0
ELASTIC BEAM
ν (900 cm^{-1})
ν (710)
ν (380)
Sum of ν(710) and ν(380) intensities
ν_s (1540)
ν_{OH} (3520)
ν_{OH} (3230)
0°
-5°
-10°
-15°
-20°
$\Delta\theta_s$

Figure 23

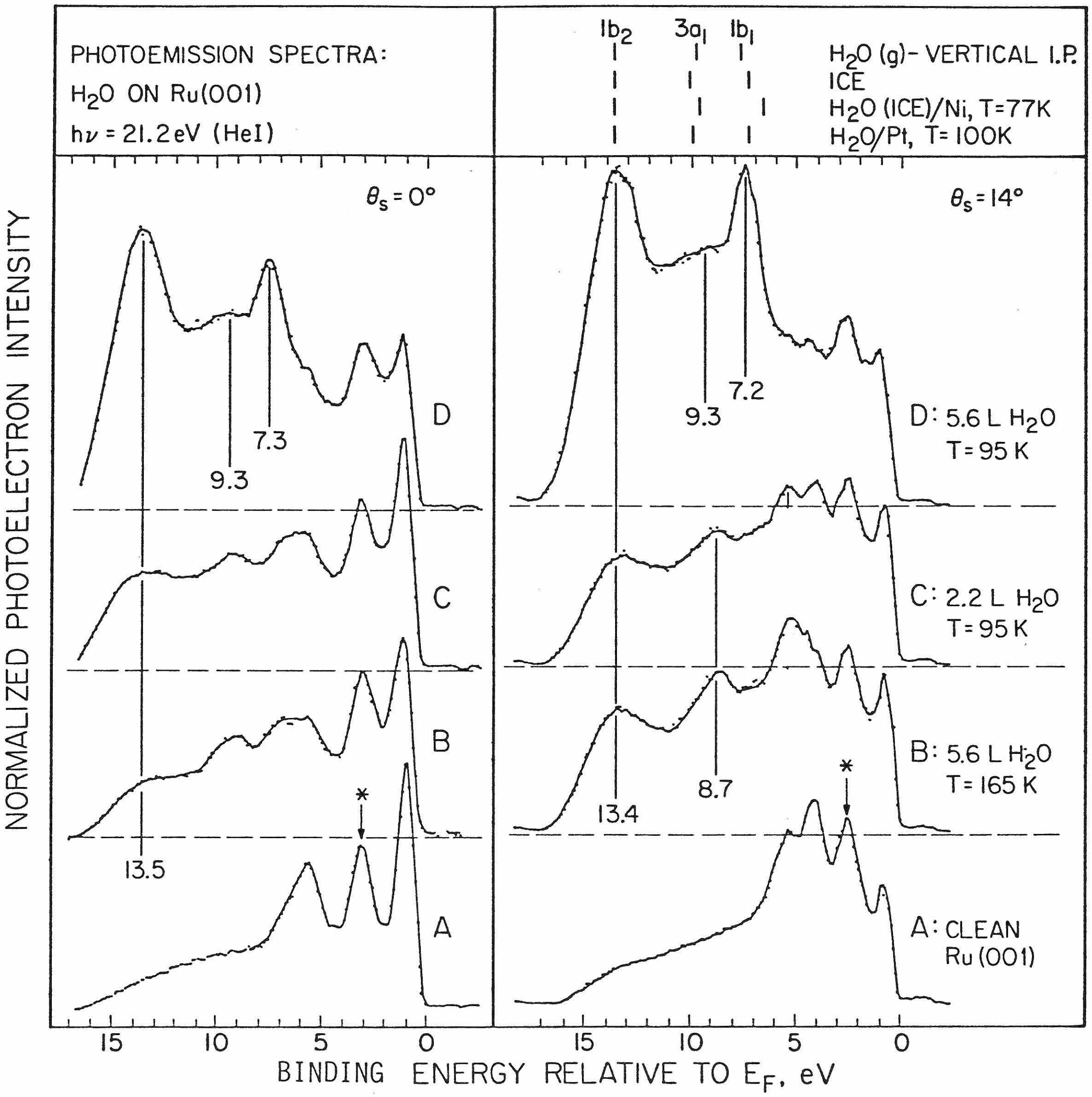
PHOTOEMISSION SPECTRA:
H2O ON Ru(001)
hν = 21.2 eV (HeI)
1b2
3a1
1b1
H2O (g)- VERTICAL I.P.
ICE
H2O (ICE)/Ni, T=77K
H2O/Pt, T= 100K
θs = 0°
θs = 14°
NORMALIZED PHOTOELECTRON INTENSITY
D
C
B
A
9.3
7.3
13.5
*
7.2
9.3
8.7
13.4
D: 5.6 L H2O T=95 K
C: 2.2 L H2O T=95 K
B: 5.6 L H2O T= 165 K
A: CLEAN Ru (001)
15
10
5
0
15
10
5
0
BINDING ENERGY RELATIVE TO EF, eV

Figure 24

Conclusions

The adsorption of oxygen, hydrogen, carbon monoxide, nitric oxide and water on Rh(111) and Ru(001) surfaces has been studied using the techniques of high resolution electron energy loss spectroscopy (EELS), low-energy electron diffraction (LEED), Auger electron spectroscopy (AES), ultraviolet photoelectron spectroscopy and thermal desorption mass spectrometry. In many cases, co-adsorption measurements have provided insight into the nature of the interactions between different adsorbates, with potential implications for heterogeneous catalytic reaction mechanisms. Both Rh and Ru are active catalysts commonly used in dispersed form to catalyze such heterogeneous reactions as Fischer-Tropsch methanation and reduction of nitric oxide.

Oxygen adsorbs on Rh(111) via a mobile precursor at 100 K, and orders irreversibly above 150 K to yield a (2 x 2) pattern in LEED experiments. The activation energy for ordering is 13.5 ± 0.5 kcal/mole. At temperatures above 280 K the oxygen disorders irreversibly, and above 400 K dissolution occurs into the subsurface region of the metal. Desorption of oxygen occurs above 800 K with an activation energy of 56 ± 2 kcal/mole, if the coverage of oxygen is sufficiently high. At low coverages, dissolution into the metal is the primary means of removal of oxygen from the Rh surface, with an activation energy of 8.2 ± 0.3 kcal/mole. Hydrogen adsorbs dissociatively on clean Rh(111) following second-order Langmuir adsorption kinetics, and the barrier to desorption is 18.6 kcal/mole.

The kinetics of the reaction of $H_2(g)$ with oxygen adsorbed on Rh(111) are different for ordered adsorbed oxygen than for the high-temperature disordered state, as determined by LEED and AES, which implies that the ordered oxygen overlayer has a higher probability of adsorbing and dissociating H_2 than does a region of disordered oxygen. This is supported by thermal desorption studies of the co-adsorbed overlayer, which confirm that the rate of adsorption of hydrogen is sensitive to the structure of the adsorbed oxygen lattice.

The interaction of carbon monoxide with Rh(111) was studied with LEED and thermal desorption mass spectrometry. The activation energy for first-order desorption of CO is 31.6 ± 1 kcal/mole. At saturation a (2 x 2) LEED pattern is observed which suggests, in conjunction with the desorption data, that two types of CO binding sites are populated.

The vibrational (EEL) spectra of NO on Ru(001) show that the dissociation of NO can prevent adsorption of molecular NO at the three-fold hollow sites. The activation energy for dissociation is coverage-dependent, which is related to the competitive interaction between the reactant (multiply coordinated NO) and products (N and O adatoms) in the dissociation reaction. A second type of molecular NO adsorbs linearly via coordination with a single metal atom. Carbon monoxide competes most directly with this linear NO for adsorption sites and can actually induce conversion of the molecular NO from linear to bridge sites. Competitive co-adsorption between hydrogen and the bridged NO is interpreted in terms of preferential occupation of the three-fold symmetric sites by hydrogen, in agreement with experimental results and theretical calculations for other surfaces also.

Water forms layered, hydrogen bonded clusters on a Ru(001) substrate at 95 K. The vibrational, electronic and thermodynamic properties of the first two layers are distinct from the properties of ice multilayers. A specific model for the structural arrangement of H_2O molecules in the first two layers has been developed. At an adsorption temperature of 165 K, only the first two layers are adsorbed, and the H_2O lattice is more well ordered than at 95 K, which is an effect analogous to the irreversible ordering which occurs in the vitreous-to-cubic phase transition in bulk ice at approximately this same temperature.

APPENDICES

Appendix 1

THE GEOMETRICAL AND VIBRATIONAL PROPERTIES OF THE Rh(111) SURFACE

1. Introduction.
2. Experimental Details.
   2.1. Apparatus.
   2.2. Crystal Preparation.
   2.3. Measurement of Debye-Waller Factor.
   2.4. Measurement of LEED Intensities as a Function of Electron Energy.
3. Debye-Waller Measurement.
4. Convolution-Transform Method.
5. Multiple-Scattering Analysis.
6. Conclusions.

Surface Science 76 (1978) 296–310
© North-Holland Publishing Company

THE GEOMETRICAL AND VIBRATIONAL PROPERTIES OF THE Rh(111) SURFACE [†]

Chi-Ming CHAN [*], Patricia A. THIEL [+], John T. YATES, Jr. [‡] and
W. Henry WEINBERG [§]
Division of Chemistry and Chemical Engineering, California Institute of Technology, Pasadena, California 91125, USA

Received 6 February 1978; manuscript received in final form 11 April 1978

Low-energy electron diffraction (LEED) data have been used to characterize the clean Rh(111) surface. The surface geometry, the degree of surface relaxation, and the Debye temperature have been determined. In the Debye temperature measurement, specular LEED beam intensities were monitored as a function of temperature over a range of electron energies from approximately 30 to 1000 eV. It was found that the bulk Debye temperature is 380 ± 23 K, and the normal component of the Debye temperature at the lowest electron energy used is 197 ± 12 K. The Rh(111) surface relaxation has been determined both by a convolution-transform analysis and by dynamical calculations. Within experimental error, neither expansion nor contraction of the topmost layer has been detected. The results of the convolution-transform analysis of specular beams at two angles of incidence and of a nonspecular beam at normal incidence suggest an expansion of the topmost layer of 3 ± 5% of the bulk layer spacing. In agreement with this, comparisons between the results of the dynamical calculation and experimental data for five nonspecular beams at normal incidence suggest that the surface layer relaxes by 0 ± 5%. In addition, the dynamical calculations indicate that the topmost layer maintains an fcc structure.

1. Introduction

Because of their importance as industrial catalysts, the Group VIII transition metals have been the object of extensive studies. Rhodium, one of the members of this group, is an important catalyst for a number of important types of catalytic

---

[†] Supported by the Army Research Office–Durham under Grant No. DAHCO4-75-0170.

[*] American Vacuum Society Predoctoral Scholar.

[+] National Science Foundation Predoctoral Fellow.

[‡] Sherman Fairchild Distinguished Scholar. Permanent address: National Bureau of Standards, Washington, DC 20234, USA.

[§] Camille and Henry Dreyfus Foundation Teacher-Scholar, and Alfred P. Sloan Foundation Fellow.

reactions. In this paper, we report the results of a study of the surface vibrational and surface structural properties of the close-packed Rh(111) plane.

Castner et al. [1] have studied small molecules chemisorbed on the Rh(111) and (100) surfaces by low-energy electron diffraction (LEED) and thermal desorption mass spectrometry. Mitchell et al. [2] have found from LEED data that the topmost layers of Rh(111) and (110) surface are relaxed outward by 0 ± 5% and by 3 ± 5%, respectively. There are no reports in the literature concerning measurements of the Debye temperature, θ_D, on the clean Rh(111) surface from LEED data.

We have studied the Debye temperatures for Rh(111) as a function of incident electron energies ranging approximately from 30 to 1000 eV. We also report new measurements of LEED intensity–voltage (*I–V*) beam profiles. These have been used to determine the surface relaxation of clean Rh(111) by both the convolution-transform method and dynamical calculations.

In section 2, the experimental procedures and apparatus are described. In section 3, a brief formalism and a discussion of the results of the Debye temperature measurement are presented. In sections 4 and 5, the results of the convolution-transform analysis and the dynamical calculations are presented. The conclusions of our work are summarized in section 6.

2. Experimental details

2.1. Apparatus

The experiments were done in an ion-pumped stainless steel ultra high vacuum system equipped with Ti sublimation pumping. The base pressure following bakeout was $<1 \times 10^{-10}$ Torr. The system was equipped with a four grid LEED display apparatus containing a movable Faraday cup for beam intensity measurements. The Faraday cup aperture subtended an angle of 4.6×10^{-3} steradians. The system also contained a quadrupole mass spectrometer, a cylindrical mirror single pass Auger spectrometer, and an ion gun for Ar^+ bombardment of the crystal for cleaning. Two pairs of Helmholtz coils were used to compensate the magnetic field of the earth inside the chamber during LEED measurements.

2.2. Crystal preparation

The Rh(111) single crystal disk was cut by means of an abrasive loaded stainless steel string saw from a Marz grade Rh single crystal rod (Materials Research Corporation, nominally 99.99% pure). The disk was ground and polished on both faces to within 0.3° of the Rh(111) plane using one micron diamond paste as the final polishing compound. At this point Laue back-reflection X-ray photographs indicated the presence of some surface disorder; this was removed by electropolishing the crystal surface in 50% aqueous HCl solution for 30 min at a dc current density of approximately 2×10^{-2} A/cm^2. The average diameter of the crystal was 0.6 cm and its final thickness was 0.05 cm. The polished crystal was welded to two parallel 0.025 cm diameter Ta heating wires which were clamped in a Cu holder which was part of a rotary manipulator assembly. A thermocouple consisting of 5%Re/95%W and 26%Re/74%W wires (0.0075 cm dia.) was welded to short sections of 0.25 cm dia. thermocouple leads which were welded together on the crystal face to make the junction. The Rh(111) crystal could be cooled to 85 K using liquid N_2 refrigeration, and it could be electrically heated to above 1400 K. The thermocouple calibration of Sandstrom and Withrow [3] was used below 273 K.

Cleaning of the Rh(111) crystal was accomplished by a combination of Ar^+ bombardment (~10 μA, 1 kV, 60 min, 5×10^{-5} Torr Ar, gettered with freshly deposited Ti) and high temperature O_2 treatment at 5×10^{-7} Torr, followed by flashing in vacuum to 1250 K. The Auger spectrum shown in fig. 1 is typical of our Rh(111) surface following this cleaning procedure. The seven Rh Auger features indicated in the figure are the same as those reported by Grant and Haas [4]. Small features at ~160 eV (S) and at ~130 eV (P?) may be removed to the levels shown in fig. 1 by heating in O_2 or by ion bombardment. As reported by others [1,2,5], a major surface contaminant is boron (185 eV) which diffuses from the bulk to the surface upon heating. To alleviate this problem, the bulk was partially depleted of B by heating and ion bombardment; a final condition was reached where diffusion to the surface was not detectable by Auger spectroscopy on heating the Rh(111) to 1250 K. Low levels of B and C contamination were easily removed by heating in O_2. The impurities in our Rh(111) crystal and the cleaning procedures used were similar to those of other workers [1,2,5].

It should be noted that O_2 treatment leaves behind a small broad O-Auger fea-

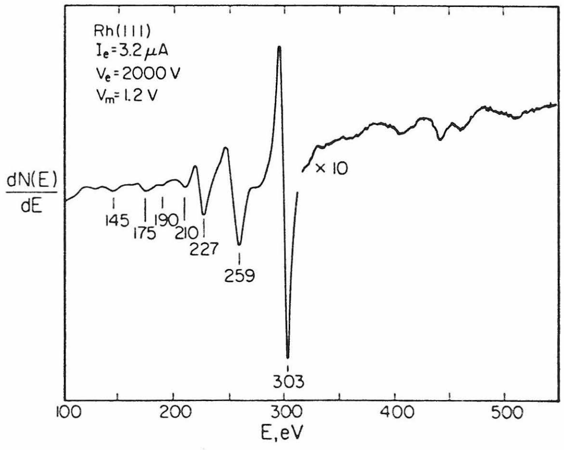

Fig. 1. A typical Auger spectrum of the Rh(111) surface following the cleaning procedure described in the text.

ture near 515 eV. The intensity of this feature could be reduced to 0.3–0.5% of the peak-to-peak intensity of the strong Rh Auger feature at 303 eV by heating the O_2 treated crystal in vacuum to 1250 K. Other small features at 406, 441 and 458 eV were essentially invariant with O_2 or Ar^+ cleaning procedures following annealing and may be characteristic of clean Rh surfaces. Similar low level Auger features have been seen on Ru(001) surfaces [6,7]. Examination of the Auger spectrum up to 2000 eV at highest sensitivity failed to reveal additional features.

2.3. Measurement of Debye–Waller factor

The crystal was tilted such that the specular beam was reflected at angles as high as 24° from the normal. To measure this angle the procedure of Cunningham and Weinberg [8] was employed. Essentially, this procedure involves photographing the diffraction pattern at an unknown angle of incidence. Measurement of the angle between the line joining the (00) spot and the center of the LEED screen and the lines joining other diffraction spots permits an accurate calculation of the angle of incidence with respect to the surface normal and the azimuthal angle. Since a number of diffracted beams are employed, the crystal angle and the azimuthal angle may be determined rather accurately. The estimated errors in the determination of the angle of incidence and the azimuthal angle using on the order of ten beams for each of the three orientations are approximately 0.3° and 1°, respectively.

Measurements of the dependence of the specular beam intensity on crystal temperature were made using the Faraday cup to monitor beam intensity as the crystal cooled slowly from an initial temperature of ~1100 to ~300 K, as monitored with the thermocouple. The specular beam intensity was continuously plotted against thermocouple potential during cooling.

2.4. Measurement of LEED intensities as a function of electron energy

In fig. 2 is shown a schematic diagram of the first order diffraction pattern from Rh(111) with the scheme for indexing beams and for definition of the azimuthal angle indicated.

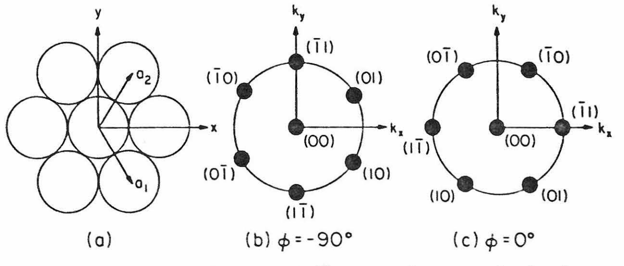

(a) (b) $\phi = -90°$ (c) $\phi = 0°$

Fig. 2. (a) The (111) crystal surface for $\phi = -90°$. a_1 and a_2 are the lattice vectors. (b) The reciprocal space of (a). (c) The reciprocal space for a (111) surface for $\phi = 0°$.

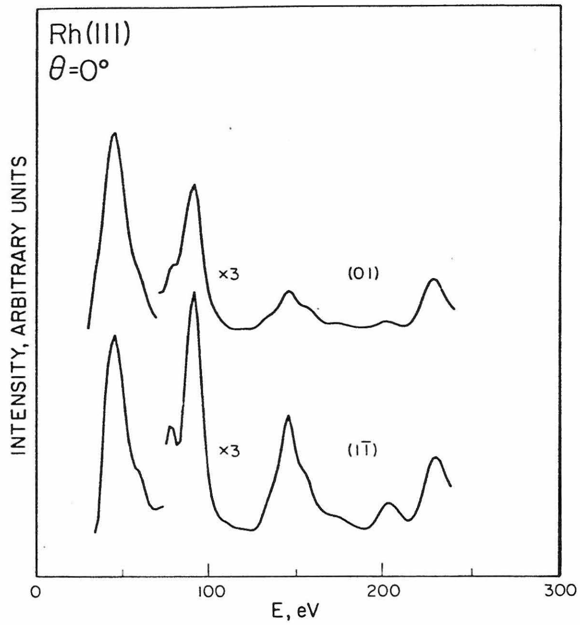

Fig. 3. Experimental I–V curves for two beams which should be equivalent at normal incidence.

Intensity–voltage curves for five non-equivalent diffracted beams were measured at 2 eV intervals, and these are shown in figs. 7–11. The measured intensity has been corrected for variation in the primary electron beam current (collected by the crystal) as the voltage was changed. In fig. 3 is shown the comparison of the I–V curves obtained for two equivalent first order beams. The satisfactory agreement obtained is indicative of small systematic errors which may exist due to inaccuracy of crystal positioning, residual magnetic fields, etc.

3. Debye–Waller factor measurement

The Debye temperature is related to the root-mean-square displacements of atoms from their equilibrium positions in the lattice and may be measured by studying the variation of the LEED beam intensity as a function of temperature. In the kinematic approximation, the intensity of the back scattered electrons, I, may be written as

$$I = I_0 \, e^{-2M} , \tag{1}$$

where $2M$ is the Debye–Waller factor. For the specular beam, the Debye–Waller factor is given as

$$2M = |\Delta k_\perp|^2 \langle u_\perp^2 \rangle \,, \tag{2}$$

where $\Delta k_\perp$ is the normal momentum transfer of the electron and $\langle u_\perp \rangle$ is the root-mean-square displacement of the surface atom perpendicular to the crystal surface. In the case of the specular beam, the perpendicular momentum transfer of the electron is determined by the energy of the electron and the angle of incidence of the electron beam with respect to the surface normal. It is given by

$$|\Delta k_\perp|^2 = (8m_e/\hbar^2)(E\cos^2\theta + V_0) \,, \tag{3}$$

where m_e is the mass of the electron, $2\pi\hbar$ is Planck's constant, E is the energy of the electron, θ is the angle of incidence with respect to the surface normal, and V_0 is the inner potential. In the high temperature limit, the perpendicular mean-square displacement of an atom in a solid is given by

$$\langle u_\perp^2 \rangle = 3\hbar^2 T/m_a k(\theta_{D\perp}^{\mathrm{EFF}})^2 \,, \tag{4}$$

where m_a is the mass of the atom, k is the Boltzmann constant, and $\theta_{\mathrm{D}\perp}^{\mathrm{EFF}}$ is the perpendicular component of the effective Debye temperature.

Combining eqs. (2), (3) and (4) gives

$$2M = 24 m_e(E\cos^2\theta + V_0)T/m_a k(\theta_{D\perp}^{\mathrm{EFF}})^2 \,. \tag{5}$$

Thus, from the slope of a plot of $\ln(I/I_0)$ versus temperature, $\theta_{\mathrm{D}\perp}^{\mathrm{EFF}}$ can be evaluated. To obtain the correct effective Debye temperature from eq. (1), however, the background intensity of scattered electrons must be subtracted from the experimentally measured intensity. This background intensity results from thermal diffuse scattering. Hence, eq. (1) should be written as

$$I - I_{\mathrm{bk}} = I_0\,\mathrm{e}^{-2M} \,, \tag{6}$$

where I_{bk} is the background intensity. An accurate background intensity is very difficult to determine experimentally, especially at high electron beam energies ($E >$ 500 eV) where the diffraction spots are closely spaced. Therefore, rather than using an experimentally measured background intensity, we have treated the background intensity as a variable in a least squares fitting procedure for the plot of $\ln(I-I_{\mathrm{bk}})$ versus T. If I_{bk} is determined correctly, the plot of $\ln(I-I_{\mathrm{bk}})$ versus T should be a straight line; hence, we allow the value of I_{bk} to vary within physically reasonable limits until the best straight line for $\ln(I-I_{\mathrm{bk}})$ as a function of T is obtained. In the least squares fitting procedure, the values of $\ln(I-I_{\mathrm{bk}})$ are weighted according to the experimentally measured intensities, causing the values of $\ln(I-I_{\mathrm{bk}})$ at lower tem-

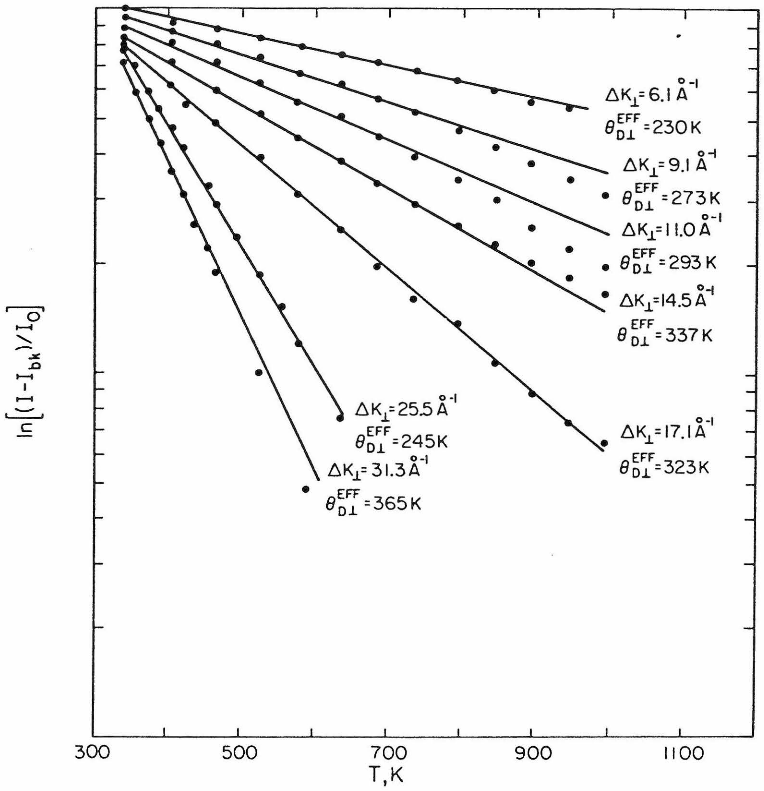

Fig. 4. Plots of representative experimental curves of $\ln(I{-}I_{\mathrm{bk}})$ versus T, using the best numerically determined I_{bk}. The curves are vertically displaced with respect with respect to each other for ease of presentation. $\theta = 10.5°$.

perature to be weighted more heavily than the values of $\ln(I{-}I_{\mathrm{bk}})$ at high temperatures. This is justified by the fact that the intensities at low temperatures can be measured more accurately and are less sensitive to the variation of the background intensity. The value of $\theta_{\mathrm{D}\perp}^{\mathrm{EFF}}$ is determined from the slope of the best straight line in the plot of $\ln(I{-}I_{\mathrm{bk}})$ versus T with appropriate weighting factors in the least squares fitting procedure. We have shown that use of different weighting schemes, such as weighting the values of $\ln(I{-}I_{\mathrm{bk}})$ according to the squares of the experimentally measured intensities, does not change the result by more than a few percent.

Fig. 4 shows several plots of our experimental curves of $\ln(I{-}I_{\mathrm{bk}})$ versus T, using the best numerically determined I_{bk}. In the calculation of the Debye temperature, a value of 10 eV was used for the inner potential, V_0. This value of V_0 was used also in the dynamical calculations discussed in section 5. Fig. 5 shows values of $\theta_{\mathrm{D}\perp}^{\mathrm{EFF}}$ as a function of $\Delta K_{\perp}$ for the (00) beam at three different angles of incidence: $\theta = 10.5°$, $\theta = 14.9°$, and $\theta = 23.9°$. The solid line in fig. 5 is a second degree least

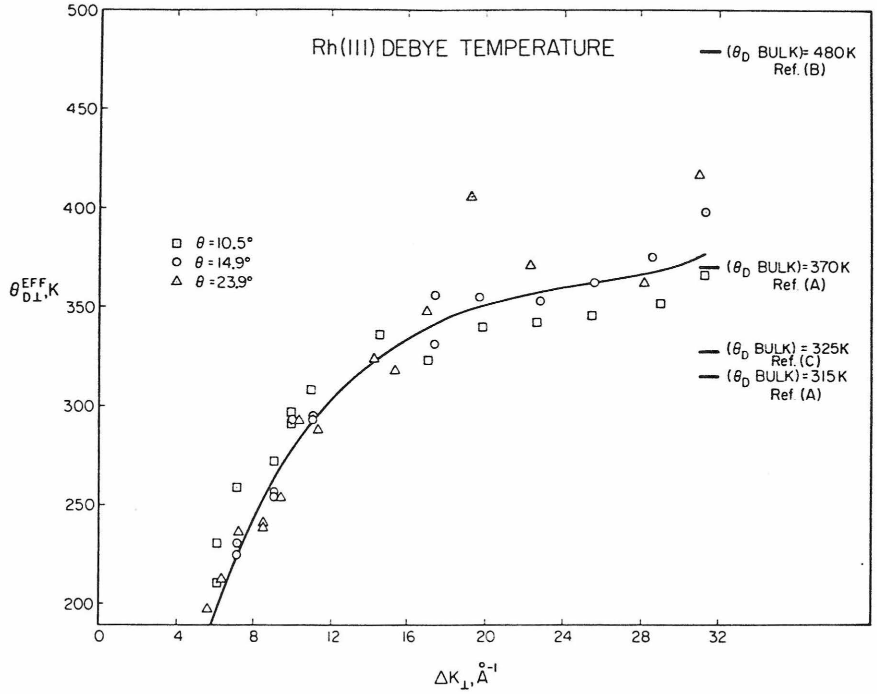

Fig. 5. Values of $\theta_{D\perp}^{EFF}$ as a function of $\Delta k_{\perp}$ for the (00) beam at three different angles of incidence: $\theta = 10.5°$, $\theta = 14.9°$ and $\theta = 23.9°$. The solid line in the figure is a second degree least squares polynomial fit to all the data points. Ref. A = ref. [9]; Ref. B = ref. [10]; Ref. C = ref. [11].

squares polynominal fit to all the data points. The value of $\theta_{D\perp}^{EFF}$ at the lowest value of $\Delta k_{\perp}$ is taken as the surface $\theta_{D\perp}$, although it is realized that even at this low value of $\Delta k_{\perp}$ we are sampling several atomic layers of the Rh crystal. From these data, this value is 197 ± 12 K. The high-energy asymptote of the curve of the polynominal fit to the data points gives a value for the bulk θ_D of 380 ± 23 K. The errors were estimated from the standard deviation of the measured data. The values for the bulk θ_D given in ref. [9] are 315 K, calculated from the melting point formula of Lindemann, and 370 K, deduced from the electrical conductivity. A value of 325 K has also been determined from heat capacity data [11]. Another value for the bulk θ_D given in ref. [10] is 480 K. Our bulk θ_D is in good agreement with the value of θ_D deduced from the electrical conductivity.

It would also be appropriate to use LEED to determine $\theta_{D\parallel}^{EFF}$ using non-specular LEED beams. Unfortunately, as pointed out by Farrell and Somorjai [12], one must work at high angles of incidence to obtain sufficient accuracy in $\theta_{D\parallel}^{EFF}$. The present geometry of our apparatus precluded this measurement.

4. Convolution-transform method

In earlier work, the convolution-transform method of LEED analysis has been described and used to determine the spacing of the outermost layer of several clean metal surfaces [13–17]. In the convolution-transform method, a least squares fit is made between the Patterson function of the data (the observed Patterson function) and the "calculated" Patterson function. The observed Patterson function $P_0(z)$ is the Fourier transform of the intensity from momentum space into real space. The "calculated" Patterson function $P_c(z)$ is constructed by convoluting the Fourier transform of a "window" function with a set of delta functions which represent the layer spacings of the crystal. The "window" function is chosen somewhat arbitrarily to define the energy range of the $I-V$ spectrum and is taken to be a smooth envelope of the data. The best fit between the observed and the "calculated" Patterson functions is found by searching for the minimum in a parameter termed the residual as a function of both V_0, the effective inner potential, and t, the percentage relaxation of the topmost layer. The inner potential is different from the one used in dynamical calculations. As discussed in detail elsewhere [15–17], it should be considered as an adjustable parameter in the convolution-transform method. The square of the residual is given by

$$R^2 = \int_0^\infty [P_0(z) - P_c(z)]^2 \, dz \, . \tag{13}$$

This minimum is characterized by a parameter Δ, defined as

$$\Delta = 100(R_{\text{ave}} - R_{\text{min}})/R_{\text{ave}} \, , \tag{14}$$

where R_{min} is the smallest value of the residual and R_{ave} is the average value of the residual. The position of the minimum gives the structure, and the value of Δ defines the goodness of fit.

Table 1
Summary of convolution-transform results

Beam	θ (deg)	ϕ (deg)	Energy range (eV)	V_0 (eV)	Δ (%)	t (%)
(00)	10.4	−76.5	46–220	3	30	+1
(00)	23.9	−76.5	60–234	9	15	+1
(11)	0		94–254	15	25	+7

V_0 = Effective inner potential.
Δ = Measure of quality of fit between observed and calculated Patterson functions.
t = % Expansion of the surface layer with respect to the bulk interlayer spacing of 2.196 Å for which a minimum occurs in the residual.

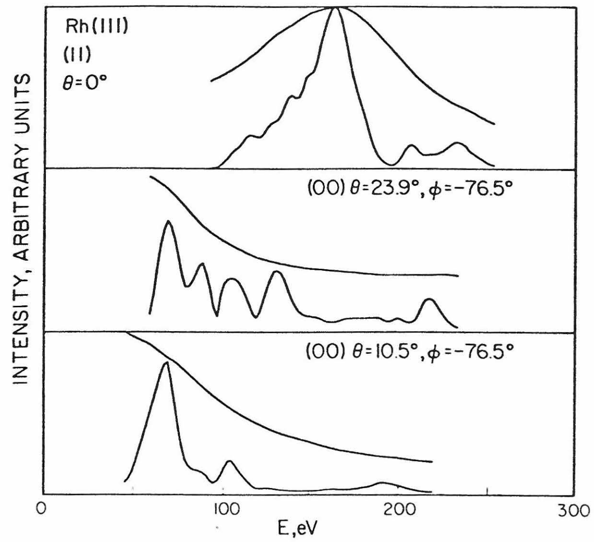

Fig. 6. $I-V$ spectra and drawn window for the Rh(111) surface. θ is the angle of incidence relative to the surface normal, and ϕ is the azimuthal angle with respect to the crystal x-axis.

Three Rh(111) $I-V$ spectra with their window functions are shown in fig. 6. The results of our calculations are summarized in table 1. The results vary from $t = +1\%$ to $t = +7\%$ and $V_0 = 3$ eV to $V_0 = 15$ eV. The weighted average of all beams, obtained by multiplying the relaxation t by the corresponding value of Δ and normalizing by the sum of Δ's, is $3 \pm 5\%$.

5. Multiple-scattering analysis

The computational method of analysis is very similar to that described previously [15]. Renormalized forward scattering [18] was used for rapid and good convergence. The LEED $I-V$ spectra for Rh(111) were calculated at a normal angle of incidence for five non-specular beams, namely, the (01), (10), (11), (02) and (20) beams.

The potential used for rhodium is a band structure potential which we obtained by scaling the relativistic Hartree–Fock–Slater potential of Rh with respect to Ir. This is possible since a band structure potential is available for Ir [19] as well as atomic potentials for Ir and Rh [20]. Eight phase shifts were used, properly modified for atomic vibrations. An assumed value of 15 eV was used for the real part of the inner potential (the muffin-tin zero). For the comparison between the theoretical and the experimental $I-V$ spectra, the inner potential was allowed to change by a rigid shift of the energy scale. An energy-independent imaginary part of the inner potential of 5 eV was used to represent all inelastic processes. The crystal temperature was 350 K, the nominal bulk Debye temperature used in the calculation was 300 K, and an enhancement factor of 1.43 was chosen for the surface mean-square vibrational amplitudes. At an energy of 210 eV, an equivalent of 36 beams were used in the calculations.

In the calculations, the outermost layer of the Rh(111) surface was allowed to relax from −15% (contraction) to +10% (expansion) in steps of 5%. It was found from the comparisons between the theoretical and experimental $I-V$ spectra for the five chosen beams, the unrelaxed surface agrees best with an inner potential of 10 eV. Figs. 7–11 show the comparison between the theoretical $I-V$ spectra modified with an inner potential of 10 eV and the experimental $I-V$ spectra.

The good agreement between experiment and theory indicates that a lateral shift of the top atomic layer to an hcp configuration is highly unlikely; hence, calcula-

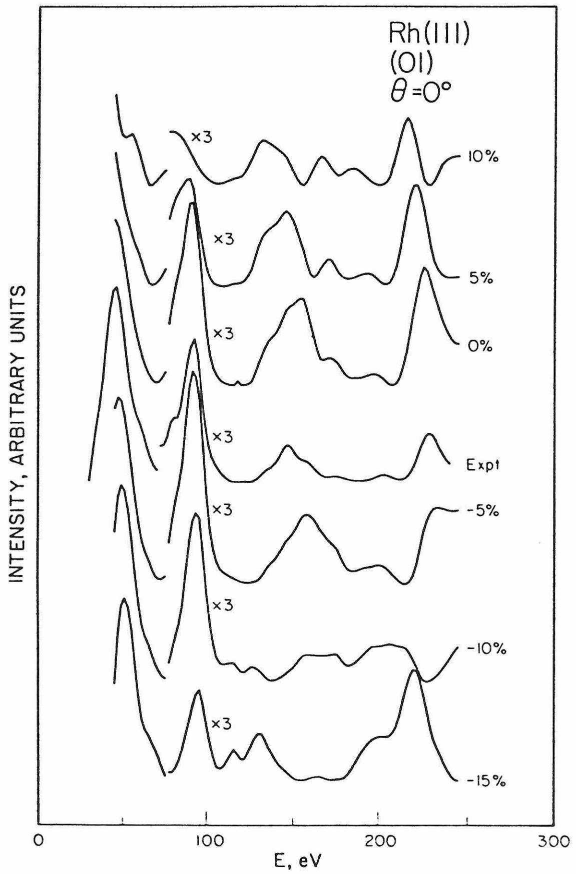

Fig. 7. Comparison between the theoretical $I-V$ spectra modified with an inner potential of 10 eV and the experimental $I-V$ spectrum of the (01) beam. The % parameter refers to expansion (+) or contraction (−) of the Rh interlayer spacing.

Fig. 8.

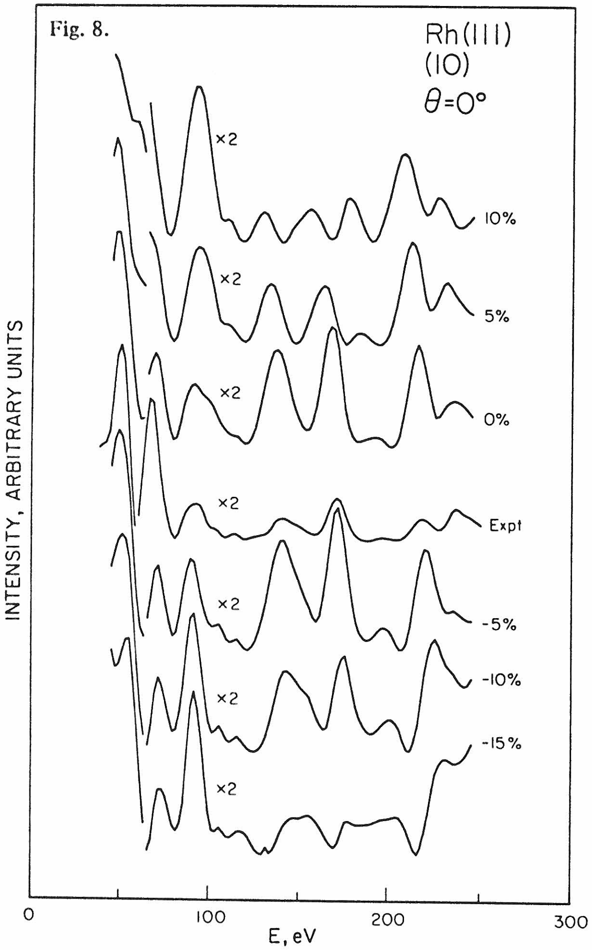

Fig. 9.

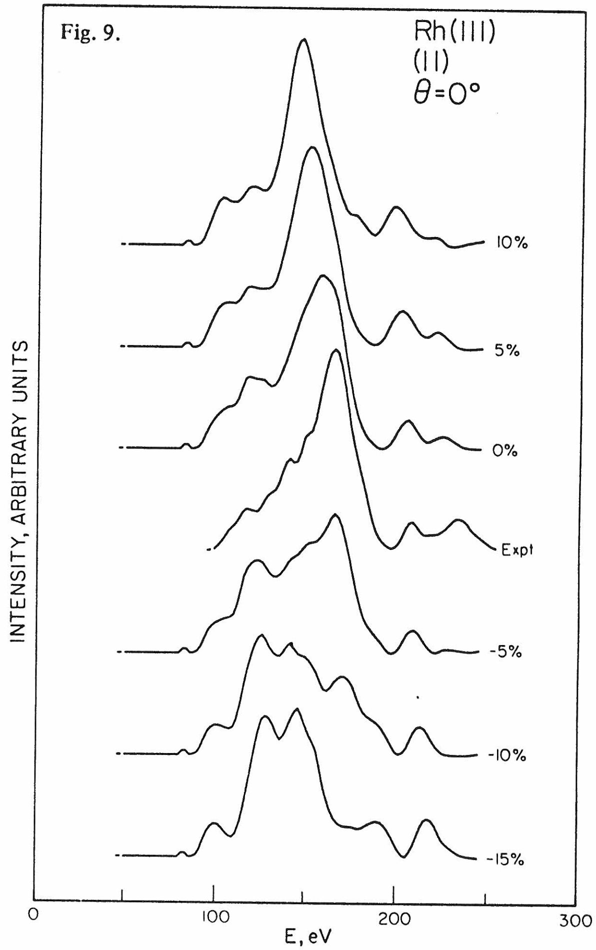

Fig. 8. Comparison between the theoretical $I-V$ spectra modified with an inner potential to 10 eV and the experimental $I-V$ spectrum for the (10) beam. The % parameter refers to expansion (+) or contraction (–) of the Rh interlayer spacing.

Fig. 9. Comparison between the theoretical $I-V$ spectra modified with an inner potential of 10 eV and the experimental $I-V$ spectrum for the (11) beam. The % parameter refers to expansion (+) or contraction (–) of the Rh interlayer spacing.

Fig. 10.

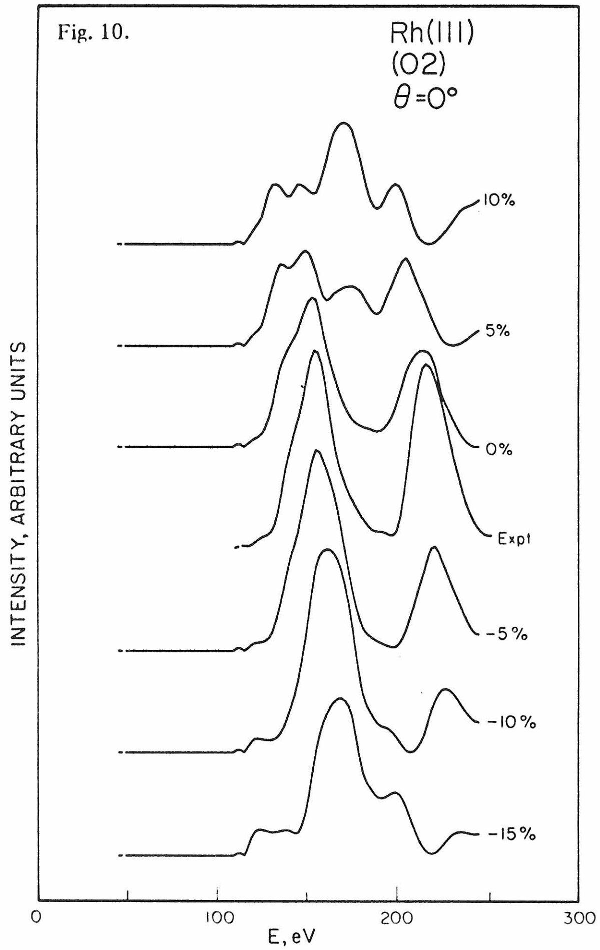

Fig. 11.

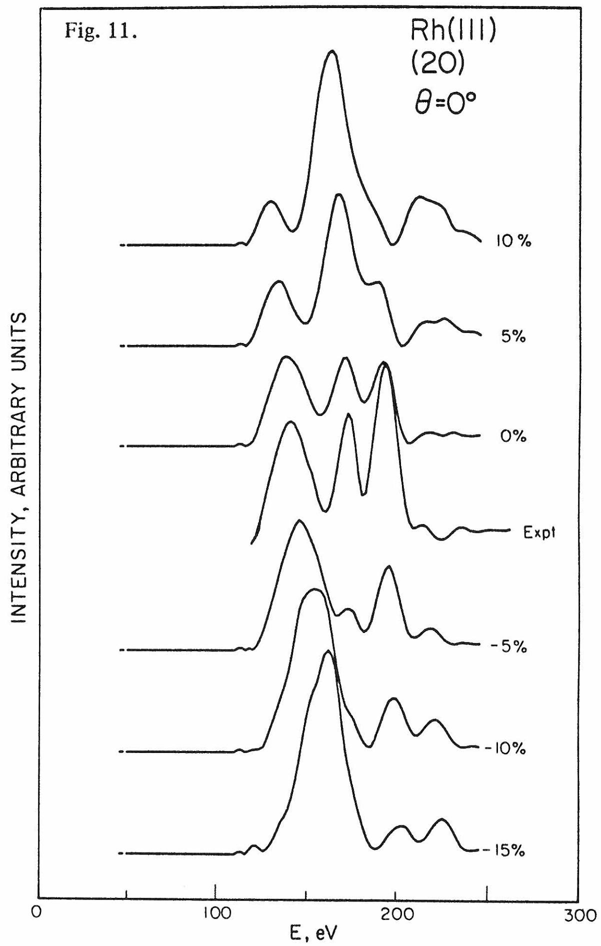

Fig. 10. Comparison between the theoretical *I–V* spectra modified with an inner potential of 10 eV and the experimental *I–V* spectrum for the (02) beam. The % parameter refers to expansion (+) or contraction (–) of the Rh interlayer spacing.

Fig. 11. Comparison between the theoretical *I–V* spectra modified with an inner potential of 10 eV and the experimental *I–V* spectrum for the (20) beam. The % parameter refers to expansion (+) or contraction (–) of the Rh interlayer spacing.

tions for such a shift were not undertaken. Based on the results of these comparisons between theory and experiment, we conclude that the topmost layer of Rh(111) exhibits a relaxation of 0 ± 5%.

6. Conclusions

Our major conclusions may be summarized as follows:
(1) The normal component of the Rh(111) surface Debye temperature is 197 ± 12 K, and the bulk Debye temperature of Rh is 380 ± 23 K. Our data indicate that $\theta_{D\perp}^{EFF}$ is a rather smooth function of $\Delta K_{\perp}$. For an accurate determination of $\theta_{D\parallel}^{EFF}$, the measurements of $I-V$ peak intensities as a function of temperature must be done at a very large angle of incidence.
(2) The results of a convolution-transform analysis indicate that the topmost layer of the Rh(111) surface is expanded outward by 3 ± 5%.
(3) The results of dynamical calculations indicate that the topmost layer of the Rh(111) surface is relaxed by 0 ± 5%.
(4) The dynamical calculations indicate that the first layer of the Rh(111) surface does not shift to an hcp configuration but maintains an fcc structure.

Acknowledgements

We gratefully acknowledge the nelp of Dr. S.L. Cunningham and Dr. M.A. Van Hove for setting up the programs for the dynamical calculations. One of us (J.T.Y.) acknowledges partial support of equipment facilities from the Division of Physical Research, Department of Energy.

References

[1] D.G. Castner, B.A. Sexton and G.A. Somorjai, Surface Sci. 71 (1978) 519.
[2] K.A.R. Mitchell, F.R. Shepherd, P.R. Watson and D.C. Frost, Surface Sci. 64 (1977) 737; D.C. Frost, K.A.R. Mitchell, F.R. Shepherd and P.R. Watson, in: Proc. 7th Intern. Vacuum Congr. and 3rd Intern. Conf. on Solid Surfaces, Vienna, 1977, p. A-2725.
[3] D.R. Sandstrom and S.P. Withrow, J. Vacuum Sci. Technol. 14 (1977) 748.
[4] J.T. Grant and T.W. Haas, Surface Sci. 21 (1970) 76.
[5] R.A. Marbrow and R.M. Lambert, Surface Sci. 67 (1977) 489.
[6] T.E. Madey, H.A. Engelhardt and D. Menzel, Surface Sci. 48 (1975) 304.
[7] D.W. Goodman, T.E. Madey, M. Ono and J.T. Yates, Jr., J. Catalysis 50 (1977) 279.
[8] S.L. Cunningham and W.H. Weinberg, Rev. Sci. Instr. 49 (1978) 7.
[9] N.F. Mott and H. Jones, The Theory of the Properties of Metals and Alloys (Oxford Univ. Press, London, 1936) p. 14.
[10] G.V. Samsonov, Handbook of Physicochemical Properties of the Elements (Plenum, New York, 1968) p. 284.

[11] G.T. Furukawa, M.L. Reilly and J.S. Gallagher, J. Phys. Chem. Ref. Data 3 (1974) 175.
[12] G.A. Somorjai and H.H. Farrell, Advan. Chem. Phys. 20 (1971) 215.
[13] S.L. Cunningham, C.-M. Chan and W.H. Weinberg, J. Vacuum Sci. Technol. 14 (1977) 312.
[14] C.-M. Chan, S.L. Cunningham and W.H. Weinberg, Bull. Am. Phys. Soc. 22 (1977) 357.
[15] C.-M. Chan, S.L. Cunningham, M.A. Van Hove, W.H. Weinberg and S.P. Withrow, Surface Sci. 66 (1977) 394.
[16] C.-M. Chan, S.L. Cunningham, M.A. Van Hove and W.H. Weinberg, Surface Sci. 67 (1977) 1.
[17] S.L. Cunningham, C.-M. Chan and W.H. Weinberg, Phys. Rev. B, in press.
[18] J.B. Pendry, Low-Energy Electron Diffraction (Academic Press, London, 1974).
[19] G.O. Arbman and S. Hörnfelt, J. Phys. F2 (1972) 1033.
[20] C.C. Lu, T.A. Carlson, F.B. Malik, T.C. Tucker and C.W. Nestor, Jr., Atomic Data 3 (1971) 50.

Appendix 2

THE STRUCTURE OF CO ADSORBED ON Pd(100: A LEED AND HREELS ANALYSIS

Surface Science 88 (1979) L59–L66
© North-Holland Publishing Company

SURFACE SCIENCE LETTERS

THE STRUCTURE OF CO ADSORBED ON Pd(100): A LEED AND HREELS ANALYSIS

R.J. BEHM, K. CHRISTMANN and G. ERTL
Institut für Physikalische Chemie, Universität München, München, West Germany

M.A. VAN HOVE *
Institut für Kristallographie und Mineralogie, Universität München, München, West Germany

and

P.A. THIEL ** and W.H. WEINBERG ***
Division of Chemistry and Chemical Engineering, California Institute of Technology, Pasadena, California 91125, USA

Received 16 May 1979; accepted for publication 31 July 1979

The voluminous literature concerning CO adsorption on transition metals testifies to the importance of determining the basic geometrical adsorption structure of CO on metals [1]. While in non-dissociative adsorption, experiments of various kinds indicate strongly that CO adsorbs by its carbon end to the metal substrate, further details such as binding site, tilt angle and bond lengths are more difficult to determine. Such information is particularly valuable as a calibration for studies showing binding-site changes as a function of coverage and/or temperature.

A Low-Energy Electron Diffraction (LEED) intensity analysis of Ni(100) + c(2 × 2)CO produced [2] a terminal-bonded geometry involving a tilt by about 34° of the molecular-axis with respect to the surface normal. However, the agreement between theory and experiment was unsatisfactory, in part because of CO dissociation. On the other hand, an Angle-Resolved Ultra-Violet Photoemission Spectroscopy (ARUPS) analysis [3] based on calculated emission patterns of oriented gas molecules [4] predicted an orientation near-perpendicular to the surface. The terminal site was confirmed by a more complete final-state multiple scattering ARUPS analysis [5] and supported by a High-Resolution Electron Energy Loss Spectroscopy (HREELS) analysis [6]. The controversy about the tilt angle of CO on

---

* Present address: Materials and Molecular Research Division, Lawrence Berkeley Laboratory, and Department of Chemistry, University of California, Berkeley, California 94720, USA.

** National Science Foundation Pre-doctoral Fellow.

*** Camille and Henry Dreyfus Foundation Teacher–Scholar.

Ni(100) appears at this moment however to be resolved in favor of the perpendicular orientation by three new sets of LEED measurements [7] associated with further LEED calculations [8].

We wish to report here on a parallel investigation of CO adsorbed on Pd(100) which presents unique features that provide more confidence in the structural results; almost no CO dissociation occurs under electron irradiation and the observed symmetries imply bridge site adsorption.

Previous work on the surface [9], using infrared reflectance spectroscopy, has shown that the observed vibrational losses are consistent with the bridge site at the coverage of interest to the present analysis, namely a half monolayer.

LEED measurements were performed with four-grid optics including an off-axis electron gun and a movable Faraday cup collector (aperture = 0.5 mm). Sample preparation and surface cleaning were performed with standard techniques [10,11]. The state of surface cleanliness was monitored by means of Auger spectroscopy, thermal desorption and work function ($\Delta\phi$) measurements. The maximum value for $\Delta\phi = 0.94$ eV at CO saturation was found to be the most sensitive probe for the absence of surface impurities.

LEED intensity/voltage (I/V) curves were recorded with a constant primary beam current of 0.6 μA at $T = 350$ K in an ambient CO pressure of 10^{-7} Torr. This procedure revealed itself to guarantee the stable formation of the superstructure at $\theta = 0.5$. The CO background atmosphere was introduced in order to compensate for the small rate of electron-beam induced desorption. It has to be emphasized that no noticeable dissociation of adsorbed CO due to electron impact could be discovered with the present system, quite in contrast to the Ni/CO system [12].

With the clean surface the (00), (10), $(0\bar{2})$, $(1\bar{2})$ and $(2\bar{2})$ beams were recorded between 38 and 250 eV, with the CO-covered surface [$(2\sqrt{2} \times \sqrt{2})R45°$ structure at $\theta = 0.5$] the I/V curves for the (00), (10), $(\frac{1}{2}\,\frac{1}{2})$, $(\frac{1}{4}\,\frac{3}{4})$ and $(\frac{1}{4}\,\frac{5}{4})$ beams were measured in the energy range between 38 and 150 eV. Except for the (00) beam (which was recorded at $\theta = 8.5°$ and $\phi = -12°$) all the measurements were performed at normal incidence of the primary beam. In order to check the normal incidence and the symmetry of the surface lattice, I/V curves for the (01) and (10) beams were recorded and found to be identical. The $(\frac{1}{4}\,\frac{1}{4})$ beam from the overlayer structure as reported by Tracy and Palmberg [11] had non-vanishing intensity only for off-normal incidence, which is in agreement with arguments based on the glide symmetry of the structure of the adsorbed layer.

The spectrometer used for the electron energy loss measurements has been fully described elsewhere [13]. The energy of the incident beam was 4 eV. The full-width at half-maximum of the elastic peak varied from 16 to 26 meV, with 3×10^4 cps of elastic electrons reflected specularly from the clean surface. The angle of incidence was 45° from the surface normal.

The Pd sample used in the loss experiments was cleaned in a separate UHV chamber equipped with facilities for Auger electron spectroscopy and LEED measurements. The cleaning procedure for this experiment will be fully described elsewhere. After cleaning, no evidence for impurities was detected with either Auger spectroscopy or energy loss spectroscopy.

Fig. 1 (right panel) shows the LEED pattern for one domain of a half monolayer of CO adsorbed on Pd(100) with structure $(2\sqrt{2} \times \sqrt{2})R45^\circ$ (the designation $c(4 \times 2)R45^\circ$ has been used in the past). As discussed by Tracy and Palmberg [11], the absence of certain beams at normal incidence indicates the presence of glide symmetry in the surface structure and implies the adsorption geometry shown in fig. 1 (left panel), cf. also refs. [14,15]. The two adsorbate molecules of each unit cell *must* therefore be bridgebonded to the substrate.

An unusual feature of this structure is that the surface lattice is a "coincidence lattice" [16] different from both the substrate lattice and the overlayer lattice. Therefore some of the observed diffraction beams are purely multiple-scattering beams not predicted by a kinematical theory. Only minor modifications to conventional LEED calculational methods [16] were required by the existence of a coincidence lattice. Details will be published elsewhere.

The Pd substrate was treated with an existing band structure potential [17]. Two sets of CO muffin-tin potentials were tested: a set of overlapping-atom potentials used by Jona et al. in several dissociated CO calculations, and a set calculated by Li and Tong for a NiCO linear cluster by the Xα method [8]. In this work, Jona's set of potentials gave the best agreement with experiment, followed closely

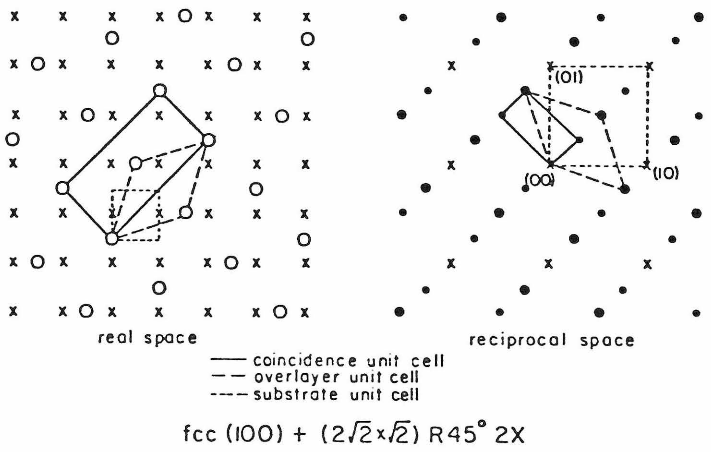

Fig. 1. Surface geometry for one domain of Pd(100) + $(2\sqrt{2} \times \sqrt{2})R45^\circ$ 2CO (left) and corresponding reciprocal lattice (right). A 90° rotation gives the second possible domain orientation. At left, crosses and circles indicate substrate atoms and adsorbates, respectively. At right, crosses correspond to clean surface diffraction spots, while large filled circles are kinematically predicted extra spots, and small filled circles are multiple-scattering spots. At normal incidence, the multiple-scattering spots emitted at azimuths $\phi = \pm 45^\circ$ vanish ($\phi = 0$ being the (10) spot azimuth).

by Li's. An imaginary part of the potential proportional to $E^{1/3}$ and of value −3.8 eV at 90 eV was used throughout. The muffin-tin constant was found to be at −10 eV for the clean surface, a value which was also found adequate for the CO layer. Thermal vibrations were based on a bulk Pd Debye temperature of 270 K; the vibration amplitudes were enhanced by about 20% for the Pd atoms and by variable amounts for the adsorbate.

A LEED intensity analysis of the clean Pd(100) surface produced good results with possibly a slight expansion by 0.05 ± 0.05 Å or 2.5 ± 2.5% of the top layer spacing relative to the bulk value.

For the CO covered surface, only the bridge sites as shown in fig. 1 (left panel) were considered for upright molecules, allowing variable top Pd–Pd, Pd–C and C–O interlayer spacings. The integral order beams were quite insensitive to the adsorption geometry. The best agreement between experiment and theory was obtained with a bulk Pd–Pd spacing, a Pd–C spacing of 1.36 ± 0.1 Å (corresponding to a Pd–C bond length of 1.93 ± 0.07 Å) and a C–O spacing of 1.15 ± 0.1 Å. Corresponding I/V curves are shown in fig. 2.

As discussed by Andersson and Pendry [2], the 1.15 Å C–O spacing can be taken to imply an untilted molecule, since it corresponds to typical values of C–O bond lengths found in metal–carbonyl complexes [18]: 1.07 to 1.17 Å for bridge sites. (To our knowledge no bond lengths for palladium carbonyl complexes are known.) The Pd–C bond length of 1.93 ± 0.07 Å is to be compared with values ranging from 1.82 Å (for Ni–C) to 2.09 Å (for Rh–C) for bridge-bonds in metal–carbonyl complexes. (Corresponding ranges for terminal- and hollow-bonded species are 1.70–1.91 Å and 2.00–2.23 Å, respectively.)

The best agreement between experiment and theory was obtained when the oxygen atoms were allowed to vibrate with an amplitude about double that of the palladium and carbon atoms. Thus, with increasing O vibration amplitude, the theoretical peak doublet at 60–70 eV in the $(\frac{1}{2}\ \frac{1}{2})$ beam coalesces, the peak at 55 eV in the $(\frac{1}{4}\ \frac{3}{4})$ beam decays, as does the peak at 70 eV in the $(\frac{1}{4}\ \frac{5}{4})$ beam.

It should be noted that a second structure with a top Pd–Pd spacing expanded by ~0.05 Å, a Pd–C spacing of 1.92 ± 0.1 Å (bond length 2.36 ± 0.07 Å) and a C–O spacing of 1.25 ± 0.1 Å gave only somewhat less good agreement between experiment and theory, but gives unlikely bond lengths. (It would also correspond to a C–O bond of order two, giving a stretching frequency [19] of about 1700 cm^{-1} which is not observed in our experiments.)

A vibrational spectrum of CO in the $(2\sqrt{2} \times \sqrt{2})R45^\circ$ structure at a temperature of 335 K is shown as an insert in fig. 3. The carbon–oxygen stretch is observed at 236 meV (1904 cm^{-1}), and the Pd–C stretch is observed at 42 meV (339 cm^{-1}). The frequency of both loss features is in keeping with that observed in the infrared spectra of palladium complexes containing bridge-bonded CO ligands [20]. In such complexes the C–O vibration occurs at 229–245 meV (1845–1979 cm^{-1}) and the Pd–C vibration occurs at 47–60 meV (378–483 cm^{-1}). For comparison, CO

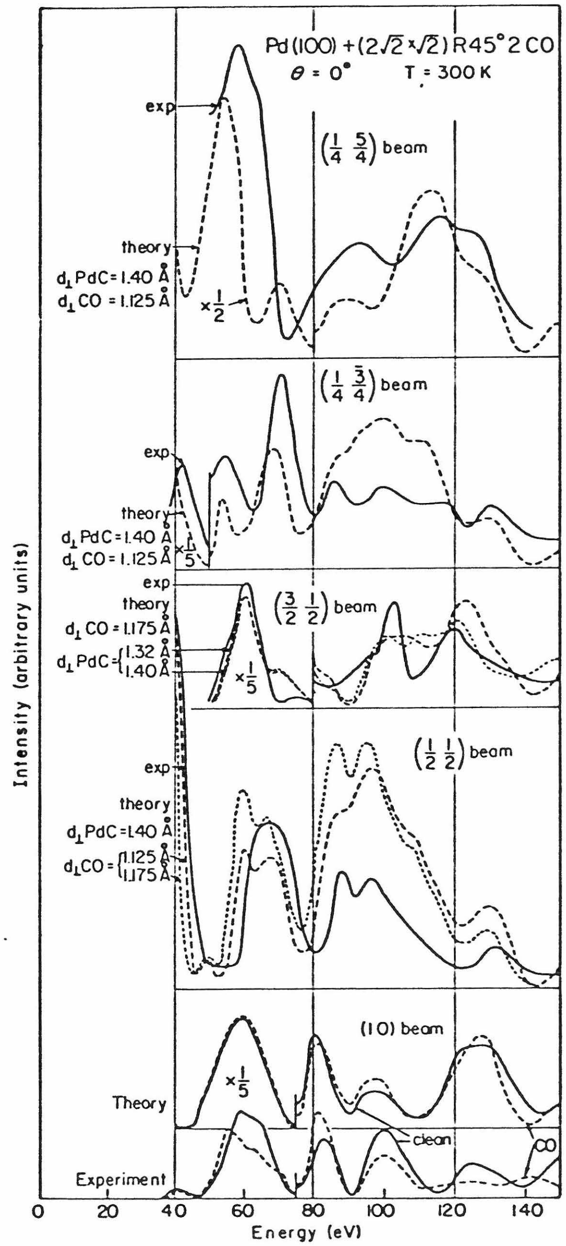

Fig. 2. *I*/*V* curves for Pd(100) + (2$\sqrt{2}$ X $\sqrt{2}$)R45° 2CO showing a comparison with clean-surface data and calculations, and showing variations with a few parameter changes.

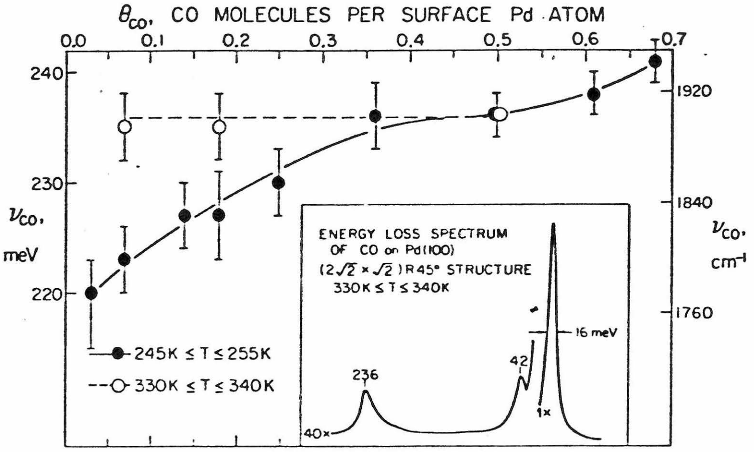

Fig. 3. Coverage and temperature dependence of the positions of EELS vibration loss peaks for CO adsorbed on Pd(100). Insert: EELS spectrum at a half-monolayer coverage (the right-hand peak is the elastic peak).

bridge-bonded on Pd(111) at a half-monolayer coverage has a C–O vibration frequency of 240.0 meV [9]. The frequencies reported here are comparable also to those observed by EELS for bridge-bonded CO on Ni(100) at low coverages, namely 239.5 and 44.5 meV [6], and on Ni(111) at one-third monolayer, namely 236.8 and 49.6 meV [21] (IR measurements also give 236.8 meV [22] for this C–O vibration). On Pt(111) the observed vibration frequencies for bridge-bonded CO at a half-monolayer coverage are 230 and 47 meV by EELS [23]. Equivalent values on Rh(111) are 231.8 and 52.1 meV [24] by EELS for coverages between $\frac{1}{3}$ and $\frac{3}{4}$ monolayer.

Also shown in fig. 3 is the shift in the carbon–oxygen stretching frequency as a function of CO coverage at two temperatures of exposure. The large shift observed at 250 K may reflect a lower degree of mobility of the CO molecules at this temperature, with partial occupation of highly coordinated sites (e.g., four-fold sites) at low coverage. The increase in frequency with increasing coverage would then be due to interaction effects as well as ordering into the two-fold bridged sites exclusively at one-half monolayer coverage. The nearly constant frequency at higher temperature would reflect a higher surface mobility of the CO molecules and population of only the two-fold sites at all coverages. There is evidence from ESDIAD measurements that CO is sufficiently more mobile at 380 K than at 250 K to cause a difference in the distribution of occupied sites on the Pd(210) surface [25]. The conclusion that CO molecules in the $(2\sqrt{2} \times \sqrt{2})R45°$ structure occupy two-fold sites on this surface was previously reached by Bradshaw and Hoffmann [9] on the basis of infrared reflectance measurements. The pattern of increasing frequency with increasing coverage shown in fig. 3 was observed also by these authors. However, the reason for the difference between the absolute magnitude of the frequency range observed by Bradshaw and Hoffmann (1895 to 1983 cm^{-1} at 300 K) and the frequency range observed in our measurement (1774 to 1944 cm^{-1} at 250 K) is not clear.

We conclude that CO molecules adsorbed in a $(2\sqrt{2} \times \sqrt{2})R45^\circ$ structure on Pd(100) stand perpendicularly to the surface in bridge sites with Pd–C and C–O bond lengths of 1.93 ± 0.07 Å and 1.15 ± 0.1 Å, respectively. We emphasize that the observed glide symmetry and restricted CO dissociation should make our result relatively reliable.

We are grateful for financial support by the Deutsche Forschungsgemeinschaft (SFB 128) and the National Science Foundation (Grant No. CHE 77-16314) and wish to thank Dr. W. Moritz and Dr. S.W. Wang for fruitful discussions. Also, we appreciate the assistance of J.J. Zinck in the cleaning and characterization of the Pd(100) surface prior to the energy loss measurements.

References

[1] A.M. Bradshaw, Surface Sci. 80 (1979) 215;
T. Engel and G. Ertl, Advan. Catalysis, in press.
[2] S. Andersson and J.B. Pendry, Surface Sci. 71 (1978) 75.
[3] C.L. Allyn, T. Gustafsson and E.W. Plummer, Solid State Commun. 28 (1978) 85.
[4] J.W. Davenport, Phys. Rev. Letters 36 (1976) 945.
[5] C.H. Li and S.Y. Tong, Phys. Rev. Letters 40 (1978) 46.
[6] S. Andersson, Solid State Commun. 21 (1977) 75.
[7] K. Müller, private communication;
A. Ignatiev, private communication;
S. Andersson, private communication.
[8] J.B. Pendry, private communication;
F. Jona, private communication;
S.Y. Tong, private communication;
M.A. Van Hove, unpublished.
[9] A.M. Bradshaw and F.M. Hoffmann, Surface Sci. 72 (1978) 513.
[10] R.L. Park and H.H. Madden, Surface Sci. 11 (1968) 158.
[11] J.C. Tracy and P.W. Palmberg, J. Chem. Phys. 51 (1969) 4852; Surface Sci. 14 (1969) 274.
[12] J.C. Tracy, J. Chem. Phys. 56 (1972) 2736;
H.H. Madden and G. Ertl, Surface Sci. 35 (1973) 211.
[13] G.E. Thomas and W.H. Weinberg, Rev. Sci. Instr. 50 (1979) 497.
[14] B.W. Holland and D.P. Woodruff, Surface Sci. 36 (1973) 488.
[15] E.D. Williams, C.M. Chan and W.H. Weinberg, Surface Sci. 81 (1979) L309.
[16] J.B. Pendry, Low Energy Electron Diffraction (Academic Press, London, 1974);
M.A. Van Hove and S.Y. Tong, Surface Crystallography by LEED (Springer, Heidelberg, 1979).
[17] V.L. Moruzzi, J.F. Janak and A.R. Williams, Calculated Electronic Properties of Metals (Pergamon, New York, 1978).

[18] P. Chini, G. Longoni and V.G. Albano, Advan. Organomet. Chem. 14 (1976) 285.
[19] G. Herzberg, Molecular Spectra and Molecular Structure (Van Nostrand–Reinhold, New York, 1945).
[20] S.C. Tripathi, S.C. Srivastava, R.P. Mani and A.K. Shrimal, Inorg. Chim. Acta 17 (1976) 257; and references therein.
[21] W. Erley, H. Wagner and H. Ibach, Surface Sci. 80 (1979) 612.
[22] J.C. Campuzano and R.G. Greenler, Surface Sci. 83 (1979) 301.
[23] H. Hopster and H. Ibach, Surface Sci. 77 (1979) 109.
[24] L.H. Dubois and G.A. Somorjai , Surface Sci. 91 (1980) 514.
[25] T.E. Madey, private communication.

Appendix 3

SEGREGATION OF CO-ADSORBED SPECIES: HYDROGEN AND CARBON MONOXIDE ON THE (111) SURFACE OF RHODIUM

[*This chapter was published as a paper by E. D. Williams, P. A. Thiel, W. H. Weinberg and J. T. Yates, Jr. in* The Journal of Chemical Physics *72 (1980) 3496.*]

Abstract

The co-adsorption of CO and H_2 on Rh(111) at low temperature (∿100 K) has been studied using thermal desorption mass spectrometry (TDMS) and Low-Energy Electron Diffraction (LEED). The probability of adsorption of CO on rhodium pretreated with hydrogen has been found to vary nonlinearly with the amount of hydrogen on the surface. In addition, the effect of surface hydrogen on the CO LEED patterns indicates segregation of hydrogen and CO. These results can be explained qualitatively in terms of a strong repulsive CO-hydrogen interaction and a mobile precursor model of CO adsorption.

1. Introduction

The mechanisms of the catalytic reaction of CO and hydrogen in the Fischer-Tropsch and methanation reaction has been a topic of continued interest and dispute (1,2). Of the two commonly posited reaction intermediates, one, an active form of surface carbon, has been discredited for some time in favor of the other, a hydrogen-CO surface complex. Recent work, however, has shown that surface carbon, formed by dissociation of CO under reaction conditions, is much more readily hydrogenated to methane than is molecular CO (3 - 9). At the same time, there is increasing evidence to suggest that surface complexes of CO and hydrogen do exist (10 - 12) and that direct hydrogenation of molecular CO is an alternate route to hydrocarbon formation (3). Apparently, both types of intermediates do occur, possibly with different effects on the product distribution. This duality may explain the diversity of activity and selectivity among the transition metals that catalyze the methanation and Fischer-Tropsch reactions. If there is a competition between the two sequences of elementary reactions, then the varying ability of different metals to promote CO dissociation as opposed to formation of hydrogen-CO complexes will give rise to a different extent of the reaction proceeding by each mechanism. The product distribution due to each mechanism individually, as well as that due to interactions among the different types of intermediates, then should give rise to an overall product distribution characteristics of the metal.

In order to understand better the fundamental processes governing the formation of hydrogen-CO complexes, the interaction of co-adsorbed hydrogen and CO on Rh(111) has been studied under conditions where reaction does not occur. The individual chemisorption of hydrogen and CO has been studied previously and is well characterized (13 - 15). Hydrogen adsorbs dissociatively and forms no ordered structures observable by LEED. Hydrogen desorbs with an activation energy of 19 kcal/mole at zero coverage. On the other hand, CO adsorbs molecularly and forms three ordered super-structures at 100 K. These are a weak primitive (2x2) at $\theta_{CO} = 1/4$ ($\theta_{CO} \equiv$ the number of CO molecules per surface rhodium atom), a $(\sqrt{3} \times \sqrt{3})R30^{0}$ at $\theta_{CO} = 1/3$, and a (2x2) with three CO molecules per unit cell at $\theta_{CO} = 3/4$ which is the saturation coverage. The activation energy for the desorption of CO is 32 kcal/mole in the limit of zero coverage.

The catalytic behavior of supported and polycrystalline rhodium has been studied also (8,16). Rhodium has somewhat lower activity for the methanation reaction than nickel, but similar selectivity. CO apparently dissociates on polycrystalline Rh under the reaction conditions (575 K and one atmosphere) and surface carbon is implicated as a reaction intermediate (8).

2. Experimental Details

The experiments were performed in a stainless steel ultra-high vacuum system equipped with ion pumps and titanium sublimation pumps. Following bakeout, the base pressure was below 1×10^{-10} torr. The system is equipped with four-grid LEED optics and a moveable Faraday cup in which the diameter of the aperture is 1.5 mm. The Faraday cup can be used to monitor the intensity of a diffracted LEED beam continuously as a function of exposure. The system also contains a quadrupole mass spectrometer and a single pass cylindrical mirror Auger electron spectrometer.

Experiments were performed with two different Rh crystals, cut from the same boule. The Rh surfaces were oriented, cut and polished to within 1^{o} of the (111) orientation using standard methods. The polished crystals were spotwelded to two parallel 0.025 cm diameter Ta heating wires that were clamped in a Cu holder. Thermocouple leads of 5%Re/95%W and 26%Re/74%W were spotwelded together on a small piece of Ta foil on the crystal surface to make a junction. The crystal could be cooled to 90 K using liquid nitrogen refrigeration, and heated to above 1600 K resistively. The thermocouple calibration of Sandstrom and Withrow (17) was used below 273 K.

Initial contaminants of P, B, S and C were depleted from the near surface region by a combination of ion bombardment and oxygen treatment as described previously (18). The continued cleanliness of the surface following numerous thermal desorption experiments involving both CO and H_2 was monitored using AES.

Hydrogen and CO pressures during adsorption were measured with a Bayard-Alpert guage. All exposures are expressed in Langmuirs (1 Langmuir $\equiv$ 1 L $\equiv$ 10^{-6} torr-s) and were calculated using the appropriate guage sensitivities for H_2 and CO. Following exposure to a gas, the sample chamber was again evacuated to the base pressure of approximately 10^{-10} torr.

Thermal desorption experiments were performed using a heating rate of approximately 20 K per second and with the crystal positioned in line of site of the mass spectrometer. Desorption of CO from the cold Cu support caused a gradually increasing background during CO desorption experiments. This background was estimated as linearly increasing below the desorption peaks in order to determine peak areas.

LEED experiments were performed using as low a beam flux as possible ($0.1 - 0.2\ \mu A/mm^2$) to minimize electron beam induced desorption and/or dissociation.

3. Results and Analysis

Thermal desorption mass spectrometry (TDS) and low-energy electron diffraction (LEED) were used to characterize the co-adsorption of hydrogen and CO. TDS of H_2 was used to determine the relative coverage ($\hat{\theta}_H \equiv$ the fraction of the saturation coverage of hydrogen) as a function of exposure and the activation energy of desorption for H_2 from clean and CO covered rhodium. TDS of CO provided coverage-exposure relationships for CO adsorption onto surfaces pre-exposed to varying amounts of hydrogen. In addition, the coverage-exposure behavior was analyzed to determine the adsorption mechanism of CO. LEED was used to correlate the realtive coverages of CO ($\hat{\theta}_{CO}$) determined by TDS with absolute coverages (θ_{CO}). The geometric structure of co-adsorbed layers of CO and hydrogen was studied by monitoring the intensity of the LEED patterns due to CO as a function of exposure to both hydrogen and CO.

3.1. Thermal Desorption of Hydrogen

The relative coverage of hydrogen as a function of exposure as determined from the areas under thermal desorption peaks, is shown in Fig. 1 for adsorption at 100 K. The upper curve (drawn empirically) represents adsorption onto the clean surface; the lower, adsorption onto a surface covered with 0.21 monolayer of CO. The presence of CO causes the probability of adsorption of hydrogen to decrease much more rapidly than for adsorption onto a clean surface. However, the approach to saturation is much slower on the CO covered surface, and saturation does not appear to be achieved even after an exposure to 20 L of H_2. At a higher initial coveage of CO ($\theta_{CO} = 0.42$), less than a tenth of a monolayer of hydrogen adsorbs during an exposure to 4 L of hydrogen. This indicates that even a moderate coverage of CO is highly efficient in blocking hydrogen adsorption.

The amount of CO desorbed from the co-adsorbed layer is constant within experimental uncertainty for constant initial coverages of CO and varying exposures to hydrogen. This indicates that hydrogen does not displace CO and that, to within a few percent, no reaction products due to CO + H are formed under these conditions, as expected (8).

Co-adsorption with CO decreases the desorption temperature of H_2 markedly. The results of an analysis of the desorption parameters for hydrogen on clean and CO covered Rh(111) by the method of Chan et al. (19) are shown in Fig. 2. The values calculated for the clean surface are in full agreement with previous results (13). The apparent energy of desorption from the CO covered surface is 1.5 to more than 3 kcal/mole lower than from the clean surface. The pre-exponential factor for the CO-covered surface will depend on the effective saturation density of hydrogen, n_s, in the presence of CO. For instance, if the saturation coverage of hydrogen on the surface precovered with 0.21 monolayer of CO were 0.6 hydrogen atoms per rhodium atom, then the limiting value of the pre-exponential factor would be of magnitude 10^{-1} cm^2/s. However, the values calculated for desorption from the co-adsorbed system can be treated only as "apparent" parameters. A correct treatment of the changing nature of the mixed overlayer structure as H_2 desorbs would require a much more complex analysis than performed here.

3.2. Thermal Desorption of CO

No change in the activation energy of desorption for CO was observed upon co-adsorption with hydrogen. This result is not surprising since hydrogen desorbs at a lower temperature than CO.

In Fig. 3, the coverage-exposure relationship is shown for CO adsorption onto a surface precovered with increasing amounts of hydrogen. The most striking aspect of these data is the decrease in the initial probability of adsorption of CO with increasing hydrogen coverage and the extended linear dependence of CO coverage on exposure indicated by the dashed lines for each set of data. The saturation coverage of CO($\hat{\theta}_s$) decreases linearly with increasing amounts of hydrogen on the surface, as might be expected. Surprisingly, the initial slope decreases nonlinearly with increasing hydrogen coverage. The values of the saturation coverage of CO and the initial slope for each initial coverage of hydrogen are listed in Table 1.

Measurements of the amount of hydrogen on the surface following exposure to CO shows that there is a gradual loss of hydrogen with increasing coverage of CO. This loss is most severe for high initial coverages of hydrogen, where as much as a quarter of a monolayer of hydrogen is displaced.

To understand the mechanism of adsorption of CO, the expected behavior according both to first-order Langmuir and to mobile precursor (20) adsorption kinetics has been compared. To do this, both models were modified to account for the presence of hydrogen on the surface. This modification is very simple in the case of Langmuir kinetics, which predicts that the probability of adsorption is directly proportional to the number of empty sites. In adsorption onto a clean surface,

$$\frac{d\hat{\theta}}{d\varepsilon} \propto (1 - \hat{\theta}) ,$$

where ε is the exposure. When hydrogen is present, the number of available sites is reduced according to

$$\frac{d\hat{\theta}}{d\varepsilon} \propto (\hat{\theta}_S - \hat{\theta})$$

where

$$\hat{\theta}_S = 1 - a\hat{\theta}_H$$

and a is a constant proportionality.

A description of the mobile precursor model and details of the derivation of the kinetics of adsorption for the clean and hydrogen covered surface using this model are given in Section 6. The result is

$$\frac{d\hat{\theta}}{d\varepsilon} \alpha\, c_1 \frac{(\hat{\theta}_s - \hat{\theta})}{(c_2 + \hat{\theta}_s - \hat{\theta})}$$

A comparison of the behavior of the two models in the limit of zero coverage of CO yields the following:

Langmuir $$\lim_{\hat{\theta} \to 0} \frac{d\hat{\theta}}{d\varepsilon} \alpha\, \hat{\theta}_s$$

Mobile Precursor $$\lim_{\hat{\theta} \to 0} \frac{d\theta}{d\varepsilon} \alpha \frac{\hat{\theta}_s}{(c_2 + \hat{\theta}_s)}$$

The nonlinear dependence of the limiting slope on the saturation coverage predicted by the mobile precursor model is a results of the possibility of the desorption of physically adsorbed CO from above sites occupied by hydrogen atoms.

The two models were fit to the data for adsorption of CO onto the clean surface. Using the parameters estimated from this fit, the coverage-exposure relationships are the following:

Langmuir $$\frac{d\hat{\theta}}{d\varepsilon} = 0.4(\hat{\theta}_s - \hat{\theta})$$

Mobile Precursor $$\frac{d\hat{\theta}}{d\varepsilon} = 0.525 \left(\frac{\hat{\theta}_s - \hat{\theta}}{0.5 + \hat{\theta}_s - \hat{\theta}} \right)$$

where $\hat{\theta}_s$ is the measured relative saturation coverage of CO for the given initial coverage of hydrogen. These equations were used without change to calculate the coverage-exposure behavior for adsorption onto a hydrogen precovered surface. The calculated behavior is shown with the full range of the data for initial hydrogen coverages of 0.0 and 0.58 in Fig. 4. For adsorption onto the clean surface, the Langmuir model fails to agree with the data in the coverage range 0.6 - 0.9. The mobile precursor model agrees somewhat better, except that it predicts a more rapid approach to saturation above $\hat{\theta}_{CO} = 0.9$ than is observed. This could be due to the close packing of the CO molecules at this coverage which might change the probability of adsorption into an "open" site. For an initial hydrogen coverage of 0.58, using the parameters determined for the clean surface, the mobile precursor model is clearly much more successful in fitting the data than the Langmuir model. The quality of agreement for the other initial coverages of hydrogen is similar.

A major factor in the poor agreement of the Langmuir model is that it predicts too rapid a decrease in the initial slope. A comparison of the apparent initial slopes (calculated in the low coverage region of the theoretical curves which would appear linear within experimental uncertainty) for both models with the data is shown in Fig. 5. While neither model agrees quantitatively with the data, the mobile precursor model is more successful qualitatively in predicting the gradual non-linear dependence of the initial slope on saturation coverage.

The mobile precursor model used here is obviously too simple to describe completely the complex co-adsorption system. To model this system correctly, the shifting geometric structure of the CO overlayer with coverage, the displacement of hydrogen, and the possibility of different desorption probabilities for CO physically adsorbed above sites occupied by hydrogen or by CO would have to be taken into account. However, the level of agreement with even this simple model strongly supports the basic assumption of a physically adsorbed mobile precursor to adsorption.

Gorte and Schmidt (21) have shown that desorption via a "mobile precusor" intermediate can lead to a strong decrease in desorption temperature with increasing coverage for first-order desorption under some conditions. Since, by the principle of microscopic reversibility, adsorption and desorption must occur by the same elementary steps, this could explain the apparent, strong dependence of desorption energy and pre-exponential factor on coverage previously observed for CO on Rh(111) (14).

3.3. LEED

Intensity-exposure measurements of the three LEED patterns [p(2x2), $(\sqrt{3} \times \sqrt{3})R30^{\circ}$ and high coverage (2x2), hereafter referred to as (2x2)] observed for CO adsorption on Rh(111) at 100 K have been reported previously (14). The p(2x2) was not discussed before. Further observation confirms that, though very weak, it is a reproducible feature of CO adsorption. It increases in intensity steadily from zero coverage, suggesting island formation. For a p(2x2) superstructure, island formation is the result of an attractive third neighbor CO-CO interaction. The decrease in intensity of the p(2x2) structure is concomitant with the development of the $(\sqrt{3} \times \sqrt{3})R30^{\circ}$ structure ($\sqrt{3}$ structure), and a superposition of the two patterns is briefly visible. The p(2x2) reaches maximum intensity at $\theta_{CO} = 0.23$, slightly less than the value of 0.25 expected for a p(2x2) structure. This is probably due to local development of the $\sqrt{3}$ structure before the surface is completely covered by the p(2x2) structure.

No new LEED patterns were observed for co-adsorbed hydrogen and CO. However, the clean surface CO structures do form, under some circumstances, with modified intensity during co-adsorption. The effect of exposing the different CO superstructures to hydrogen and the formation of the CO superstructures on hydrogen covered surfaces have been investigated by monitoring the intensity of the LEED beams as a function of exposure to either hydrogen or CO.

Addition of hydrogen to the fully ordered ($\theta_{CO} = 0.23$) p(2x2) structure causes a rapid decrease in intensity of the p(2x2) pattern. Similarly, addition of hydrogen to the fully ordered ($\theta_{CO} = 0.35$) $\sqrt{3}$ structure causes a loss in intensity of the $\sqrt{3}$ pattern. Clearly, hydrogen atoms cannot occupy a position within either the p(2x2) or the $\sqrt{3}$ unit cell without perturbing the neighboring CO molecules.

The effect of hydrogen on the $\sqrt{3}$ structure for coverages of CO less than one-third is illustrated in Fig. 6. The dashed line shows the intensity-exposure behavior for CO adsorption on the clean surface. If exposure to CO is terminated before maximum ordering occurs, and followed by exposure to hydrogen, the solid curves result. At $\theta_{CO} = 0.25$ and 0.30, hydrogen increases the amount of the ordered $\sqrt{3}$ structure. At $\theta_{CO} = 0.21$, where only the p(2x2) CO structure is present, addition of hydrogen causes a transformation from the p(2x2) to the $\sqrt{3}$ structure.

The maximum intensities obtained by addition of hydrogen are less than the maximum reached for CO adsorption above. The asymmetric decrease in intensity with hydrogen exposure beyond the maxima is due to the decreasing probability of adsorption of hydrogen (cf. Fig. 1).

Addition of hydrogen to the partially ordered ($\theta_{CO} < 0.23$) p(2x2) structure does not increase the order as for the $\sqrt{3}$ structure. Rather, there is a steady loss of intensity which is slower for lower coverages of CO.

Exposure to hydrogen caused no change in intensity of the partially ordered ($\theta_{CO} = 0.5$ and 0.7) (2x2) structure. This may be due to the small probability of adsorption of hydrogen when a high coverage of CO is present.

The adsorption of CO onto a hydrogen precovered surface mimics adsorption onto the clean surface, as shown in Figs. 7 and 8. In both figures, curve (a) represents the intensity-exposure behavior for adsorption onto the clean surface. Curves (b) - (e) are for CO adsorption onto a surface covered with increasing amounts of hydrogen. As on the clean surface, on a hydrogen-covered surface, CO first forms a p(2x2) structure which is quickly transformed to a $\sqrt{3}$ structure. Then the final (2x2) structure is formed by continuous compression of the $\sqrt{3}$ structure. However, on the hydrogen covered surface, the CO structures form at lower coverage and with lower intensity than on the clean surface.

4. Discussion

4.1 Physical Nature of the CO-Adsorbed Overlayers

The LEED results indicate that the structure of the mixed overlayer is considerably different depending on the order of adsorption of hydrogen and CO. The results of the thermal desorption experiments, together with the intensity-exposure behavior give a consistent picture of the co-adsorbed system.

In the case where CO is adsorbed first, followed by hydrogen, it has been seen that hydrogen disrupts both the p(2x2) and the $\sqrt{3}$ unit cells for CO. Yet, while hydrogen decreases the order of a partially ordered p(2x2) overlayer, it increases the order of the $\sqrt{3}$ structure for θ_{CO} less than one-third. The destruction of the p(2x2) CO structure occurs because of the hydrogen induced transformation to the $\sqrt{3}$ structure. This raises the question of how hydrogen causes the transformation. If a hydrogen atom scattered electrons identically to a CO molecule (which is highly unlikely), addition of hydrogen could cause the transformation in the same way as addition of CO. However, in this case, addition of hydrogen should cause a maximum intensity equal to that for CO only, which is not observed. A second possibility is that a hydrogen atom attracts nearby CO molecules into a $\sqrt{3}$ structure around it. This requires that a hydrogen atom can occupy a $\sqrt{3}$ unit cell of CO without disturbing it, which is not the case. The final possibility, which is consistent with the experimental evidence, is that a hydrogen atom added to a p(2x2) structure repels the nearby CO molecules. To reduce the repulsive interaction, the CO molecules move away, causing a local increase in density of CO and transformation to the higher density $\sqrt{3}$ structure. As more hydrogen is added to the overlayer, a significant surface area will be covered by the $\sqrt{3}$ structure. Some hydrogen undoubtedly will then adsorb within the $\sqrt{3}$ areas, although the sticking probability for hydrogen should be lower in regions of higher density of CO, disrupting the $\sqrt{3}$ structure. Thus, the maxima in the solid curves in Fig. 6 probably do not correspond to complete ordering of CO in the $\sqrt{3}$ structure.

The nature of the CO-hydrogen repulsive interaction is of some interest. If addition of hydrogen to the p(2x2) structure only disrupted the attractive third neighbor CO-CO interaction responsible for the p(2x2), disordering of the p(2x2) structure but not transformation to the $\sqrt{3}$ structure would occur. A true repulsion between hydrogen and CO is required to cause the transformation. The existence of a true repulsive interaction is confirmed by the decrease in activation energy of desorption for hydrogen added to a CO overlayer.

Geometrically, a hydrogen atom can be placed in the p(2x2) CO unit cell in a position 3.1 Å from each of three CO molecules or 2.7 Å from each of two CO molecules. The hard core radius of CO, determined from the distance of closest approach in the saturation structure is 1.55 Å (<u>14</u>). The radius of a chemisorbed hydrogen atom is probably less than 0.75 Å (<u>22</u>). Thus, the repulsive interaction between hydrogen and CO, at low coverages, must be a through-metal effect (<u>23</u>,<u>24</u>) rather than the result of orbital overlap.

When CO is added to a hydrogen precovered surface, initial formation of the p(2x2) structure occurs readily. The intensity of the p(2x2) pattern for CO added to a hydrogen covered surface is compared to that for CO on a clean surface in Fig. 9. The smooth curve is the clean surface behavior. The points represent the maximum intensity for CO added to a surface with different coverages of hydrogen as in curves (b) - (e) of Fig. 7. The decrease in intensity for the mixed overlayer corresponds to less than 0.03 monolayer more disordered CO than on the clean surface for each precoverage of hydrogen. The amount of hydrogen on the surface (0.26 to 0.92 monolayer) would be enough to prevent the formation of any p(2x2) CO structure, if it were distributed uniformly. The fact that p(2x2) CO structures do form with intensity comparable to that on the clean surface indicates that there is segregation of hydrogen and CO.

The transformation of the p(2x2) CO structures on the hydrogen covered surfaces to $\sqrt{3}$ and then (2x2) structures undoubtedly takes place via addition of CO to the already existing ordered p(2x2) regions. At the same time, it is reasonable to assume that some CO adsorbs in regions of high hydrogen density in a random configuration that does not contribute to the LEED intensity.

In Table 2, the coverages of CO at which the three structures reach maximum intensity are listed for different precoverages of hydrogen. In addition, the ratios of the coverages for the $\sqrt{3}$ to the p(2x2) and the (2x2) to the $\sqrt{3}$ structures are shown. On the clean surface, these ratios should ideally be 1.33 and 2.25, respectively. The experimental values for the clean surface are rather close to what is expected. Since both the number of disordered CO molecules and the excluded area they occupy are unknown for the mixed overlayers, the meaning of the ratios for the hydrogen covered surfaces cannot be determined quantitatively. However, the large values for the ratio when the p(2x2) is transformed to the $\sqrt{3}$ structure are significant. This indicates that the net CO coverage increases in the transformation far more than is needed to account for the structural change, even if the excluded area per disorded CO has decreased, i.e. more CO molecules are added than are needed to complete the transformation. The additional molecules either increase the size of the ordered CO region, or are added to the hydrogen region; in all likelihood, both processes occur.

The ratio of coverages for the $\sqrt{3}$ to (2x2) structural change is nearly invariant for all hydrogen coverages. This suggests that the excluded area for the disordered CO molecules has decreased during the transformation. Otherwise, the ratios for the hydrogen covered surfaces would have been lower. In addition (and possibly causing the smaller excluded area), additional CO may have been added as in the p(2x2) to $\sqrt{3}$ transformation.

The mechanism for formation and growth of CO islands on a hydrogen covered surface deduced from these measurements is illustrated schematically in Fig. 10. The nucleation of an island is shown in Fig. 10(a). There, the initial chemisorption of a mobile precursor CO molecule causes migration of the relatively mobile (22) hydrogen atoms away from its vicinity due to the repulsive hydrogen-CO interaction. Other mobile precursor CO molecules adsorb preferentially near a chemisorbed CO, minimizing the CO-hydrogen interaction and initiating island formation.

As more CO adsorbs, statistically some nucleation sites will fail to develop. Pockets of CO, either lone molecules or small clusters, will then be trapped in regions of high hydrogen density. Similarly, some hydrogen atoms may be trapped in the growing CO islands. These trapped species are not shown in Fig. 10. The p(2x2) island is shown at maximum size in Fig. 10(b). At this point, when a mobile precursor CO encounters the island, addition of the molecule at the edge of the island, which would cause either a decreased CO-H distance or a decreased H-H distance, becomes energetically less favorable than addition of a CO to the interior of the island causing a decreased CO-CO distance. Transformation of the island to the $\sqrt{3}$ structure begins and is possibly accompanied by additional adsorption of CO into the hydrogen region. The completion of the transformation is shown in Fig. 10(c). At this point, the energy balance changes in favor of island growth. The $\sqrt{3}$ island increases in size until, in Fig. 10(d), the increase in CO-H repulsive energy and the compression of the hydrogen layer become too unfavorable to allow further growth. Addition of CO into the island is still energetically feasible, and CO adsorption into the hydrogen region with displacement of hydrogen may take place also. Adsorption of CO continues until the island is completely transformed to the high coverage (2x2) structure, shown in Fig. 10(e).

4.2. Relationship to Catalytic Behavior

The segregation of CO and hydrogen observed at 100 K, of course would not persist at high temperatures where effects of entropy dominate.

Thus, there would not be an appreciable effect on the catalytic behavior of rhodium due to segregation. However, the repulsive interaction between hydrogen and CO is a microscopic, not a macroscopic, property and will occur regardless of the temperature or degree of segregation. This repulsion could decrease the probability of direct reaction of hydrogen and CO on Rh as compared to other metals for which the interaction is not repulsive.

Few studies resulting in direct information on the nature of the CO-hydrogen interaction have been reported. There is apparently a weak attractive interaction between hydrogen and CO on Pd(110) (25). On Ir(110), there appears to be little or no direct interaction (26). Correlation of such studies with those concerning the formation of complexes of CO and hydrogen (10 - 12,27) may be useful in determining the details of the reaction mechanisms for the hydrogenation of CO over transition metals.

5. Synopsis

(1) Adsorption of CO on Rh(111) proceeds via a physically adsorbed intermediate, a mobile precursor to adsorption.

(2) There is a strong repulsive interaction between co-adsorbed CO molecules and hydrogen atoms on rhodium. This results in partial segregation of hydrogen and CO following adsorption of CO onto an adlayer of hydrogen at 100 K. The interaction is apparent at distances up to 2.7 - 3.1 Å, indicating that it is a through-metal effect. At smaller distances, of course, orbital overlap may be important.

6. Derivation of Adsorption Kinetics Using the First-Order Mobile Precursor Model (20)

Each molecule impinging upon the surface has a probability of entering a physically adsorbed state either above a filled or an empty site. Its subsequent beahvior is governed by a set of probabilities:

P_a ≡ The probability that a molecule, physically adsorbed above an empty site, chemisorbs in that site.

P_b ≡ The probability that a molecule above an empty site desorbs.

P'_b ≡ The probability that a molecule above a filled site desorbs.

P_c ≡ The probability that the physically adsorbed molecule diffuses to a position above another site.

On the clean surface, the frequency of encounter of empty sites is $1 - \hat{\theta}$; the frequency of encounter of filled sites is $\hat{\theta}$. Thus, a newly physically adsorbed molecule has a probability $P_{a1} = P_a(1 - \hat{\theta})$ of chemisorbing, $P_{b1} = P_b(1 - \hat{\theta}) + P'_b\hat{\theta}$ of desorbing, and $P_{c1} = 1 - P_{a1} - P_{b1}$ of diffusing to another site. If it diffuses, it then has probability, $P_{a2} = P_{c1}P_{a1}$ of chemisorbing, etc. Summation of the probabilities of chemisorption, P_{a1}, P_{a2}, ..., then leads to

$$\frac{d\hat{\theta}}{d\varepsilon} \quad \frac{P_a}{P_a + P_b} \frac{1 - \hat{\theta}}{1 - c\hat{\theta}}$$

where
$$c \equiv \left(1 - \frac{P'_b}{P_1 + P_b}\right)$$

and ε is the exposure.

On a hydrogen covered surface, the frequency of encounter of empty sites is $\hat{\theta}_s - \hat{\theta}$, where $\hat{\theta}_s = 1 - a\hat{\theta}_H$ and a is a constant of proportionality. The frequency of encounter of filled sites is $1 - \hat{\theta}_s + \hat{\theta}$. Therefore, on a hydrogen covered surface, the newly physically adsorbed molecule has probability $P_{a1} = P_a(\hat{\theta}_s - \hat{\theta})$ of chemisorbing, $P_{b1} = P_b(\hat{\theta}_s - \hat{\theta}) + P_b'(1 - \hat{\theta}_s + \hat{\theta})$ of desorbing, and $P_{c1} = 1 - P_{a1} - P_{b1}$ of diffusing to another site. In this case, summation of the probabilities of chemisorption leads to

$$\frac{d\hat{\theta}}{d\varepsilon} \alpha \frac{P_a}{P_a + P_b - P_b'} \frac{\hat{\theta}_s - \hat{\theta}}{c_2 + \hat{\theta}_s - \hat{\theta}}$$

where $$c_2 \equiv \frac{P_b'}{P_a + P_b - P_b'}$$

This reduces to the clean surface equation in the limit of zero coverage of hydrogen.

References

1. M. A. Vannice, Catal. Rev. 14, 153 (1976).
2. G. C. Bond, Catalysis by Metals, Academic Press, New York, 1962.
3. J. A. Rabo, A. P. Risch and M. L. Pontsma, J. Catal. 53, 295 (1978).
4. M. Araki and V. Ponec, J. Catal. 44, 439 (1976).
5. R. D. Kelley, T. E. Madey and J. T. Yates, Jr., J. Catal. 50, 301 (1977).
6. T. E. Madey, D. W. Goodman and R. D. Kelley, J. Vacuum Sci. Technol. 16, 433 (1979).
7. R. D. Kelley, T. E. Madey, K. Revesz, J. T. Yates, Jr., Appl. Surface Sci. 1, 266 (1978).
8. B. A. Sexton and G. A. Somorjai, J. Catal. 46, 167 (1977).
9. D. J. Dwyer and G. A. Somorjai, J. Catal. 52, 291 (1978).
10. K. Kraemer and D. Menzel, Ber. Buns. Ges. 79, 649 (1975).
11. V. H. Baldwin and J. B. Hudson, J. Vacuum Sci. 8, 49 (1971).
12. J. C. Bertolini and B. Imelik, Surface Sci. 80, 586 (1979).
13. J. T. Yates, Jr., P. A. Thiel and W. H. Weinberg, Surface Sci. 84, 427 (1979).
14. P. A. Thiel, E. D. Williams, J. T. Yates, Jr. and W. H. Weinberg, Surface Sci. 84, 54 (1979).
15. D. G. Castner, B. A. Sexton and G. A. Somorjai, Surface Sci. 71, 519 (1978).
16. M. A. Vannice, J. Catal. 37, 449 (1975).
17. D. R. Sandstrom and S. P. Withrow, J. Vacuum Sci. Technol. 14, 748 (1977).

18. C.-M. Chan, P. A. Thiel, J. T. Yates, Jr. and W. H. Weinberg, Surface Sci. 76, 296 (1978).

19. C.-M. Chan, R. Aris and W. H. Weinberg, Appl. Surface Sci. 1, 360 (1978).

20. P. Kisliuk, J. Phys. Chem. Solids 3, 95 (1957).

21. R. Gorte and L. D. Schmidt, Surface Sci. 76, 559 (1978).

22. K. Christmann, R. J. Behm, G. Ertl, M. A. Van Hove and W. H. Weinberg, J. Chem. Phys. 70, 4168 (1979).

23. T. B. Grimley and M. Torrini, J. Phys. C 6, 868 (1973).

24. T. Einstein and J. R. Schrieffer, Phys. Rev. B 7, 3629 (1973).

25. H. Conrad, G. Ertl and E. E. Latta, J. Catal. 35, 363 (1974).

26. D. E. Ibbotson, T. S. Wittrig and W. H. Weinberg, Surface Sci. 97, 297 (1980).

27. J. T. Yates, Jr., S. D. Worley, T. M. Duncan and R. W. Vaughan, J. Chem. Phys. 70, 1225 (1979).

Table Captions

Table 1: Parameters for adsorption of CO onto hydrogen covered surface. $\hat{\theta}_H$ is the initial coverage of hydrogen. $\hat{\theta}_s$ is the saturation coverage of CO. $d\hat{\theta}/d\varepsilon$ is the slope of the linear region of the $\hat{\theta}_{CO} - \varepsilon$ curve.

Table 2: Absolute coverages of CO at the points of maximum intensity for the three CO structures at different initial coverages of hydrogen.

(a) Ratio of the coverage in the $\sqrt{3}$ structure to that in the p(2x2).

(b) Ratio of the coverage in the (2x2) structure to that in the $\sqrt{3}$.

Table 1

$\hat{\theta}_H$	$\hat{\theta}_s$	$\frac{d\hat{\theta}}{d\varepsilon}$, L^{-1}
0.0	1.0	0.30
0.42	0.71	0.25
0.58	0.57	0.23
0.75	0.40	0.20
0.92	0.28	0.16
0.99	0.22	—

Table 2

$\hat{\theta}_H$	$\theta_{CO}^{p(2x2)}$	$\theta_{CO}^{\sqrt{3}}$	$\theta_{CO}^{(2x2)}$	(a) $R\left[\frac{\sqrt{3}}{p(2x2)}\right]$	(b) $R\left[\frac{(2x2)}{\sqrt{3}}\right]$
0.0	$.23^1$	$.34^6$	$.75^0$	1.52	2.13
0.26	$.14^7$	-	$.60^0$	-	-
0.42	$.11^4$	$.24^7$	$.53^6$	2.17	2.17
0.58	$.09^2$	$.20^4$	$.43^0$	2.22	2.11
0.75	$.06^9$	$.14^3$	$.30^2$	2.07	2.11
0.92	$.04^0$	$.07^5$	$.20^7$	1.88	2.76

Figure Captions

Fig. 1: Coverage-exposure behavior for adsorption of hydrogen at approximately 100 K. Circles correspond to adsorption onto the clean surface. (Open and closed circles represent data taken on two different crystals.) Triangles correspond to adsorption onto a surface with 0.21 monolayer of CO present.

Fig. 2: Desorption parameters for hydrogen. E_d is the activation energy for desorption. $\nu_0^{(2)}$ is the pre-exponential factor of the desorption rate coefficient. n_s is the number of density of hydrogen at saturation. Circles represent desorption from the clean surface. Triangles represent desorption from the surface with 0.21 monolayer of CO present. Straight lines are drawn according to a linear least squares fit to the data.

Fig. 3: Coverage-exposure behavior for adsorption of CO onto the surface with varying amounts of hydrogen present. Adsorption temperature is approximately 100 K. Data points at $\hat{\theta}_{CO} < 0.5$ for adsorption on the clean surface have been omitted for clarity (see Fig. 4). Open and closed circles represent data from two different crystals.

Fig. 4: Comparison of coverage-exposure data with curves predicted by first-order Langmuir and mobile precursor adsorption kinetics. Open and closed circles are data points for adsorption onto a clean surface as in Fig. 3. Stars are data points for adsorption onto a surface precovered with 0.58 of the saturation coverage of hydrogen.

Fig. 5: Comparison of the apparent initial slope (see text) of the coverage-exposure curve for two models of adsorption with the experimental values.

Fig. 6: LEED intensity as a function of exposure for the $\sqrt{3}$ structure. Dashed line shows the result of exposing the clean surface to CO. Solid lines show the results of terminating CO exposure at various coverages and initiating exposure to hydrogen. T_{Rh} is approximately 100 K. Intensities are normalized to unity at the maximum intensity of the $\sqrt{3}$ structure on the clean surface.

Fig. 7: LEED intensity as a function of exposure to CO for the two (2x2) structures on a surface covered with varying amounts of hydrogen.

(a) $\hat{\theta}_H = 0$
(b) $\hat{\theta}_H = 0.26$
(c) $\hat{\theta}_H = 0.42$
(d) $\hat{\theta}_H = 0.58$
(e) $\hat{\theta}_H = 0.75$

Intensities are normalized to unity at the maximum intensity of the $\sqrt{3}$ structure on the clean surface.

Fig. 8: LEED intensity as a function of exposure to CO for the $\sqrt{3}$ structure on a surface covered with varying amounts of hydrogen.

(a) $\hat{\theta}_H = 0$
(b) $\hat{\theta}_H = 0.42$
(c) $\hat{\theta}_H = 0.58$
(d) $\hat{\theta}_H = 0.75$
(e) $\hat{\theta}_H = 0.92$

Fig. 10: Schematic illustration of adsorption of CO onto a surface covered with hydrogen. Open circles are rhodium atoms with d = 2.7 Å. Shaded circles are CO molecules with d = 3.1 Å. Shaded circles with arrow are physically adsorbed, mobile precursor CO molecules. Solid circles are H atoms with d = 1.5 Å (estimated). Adsorption sites shown have been chosen arbitrarily. Hydrogen and CO trapped in the "wrong" regions are not shown for clarity. See text for discussion.

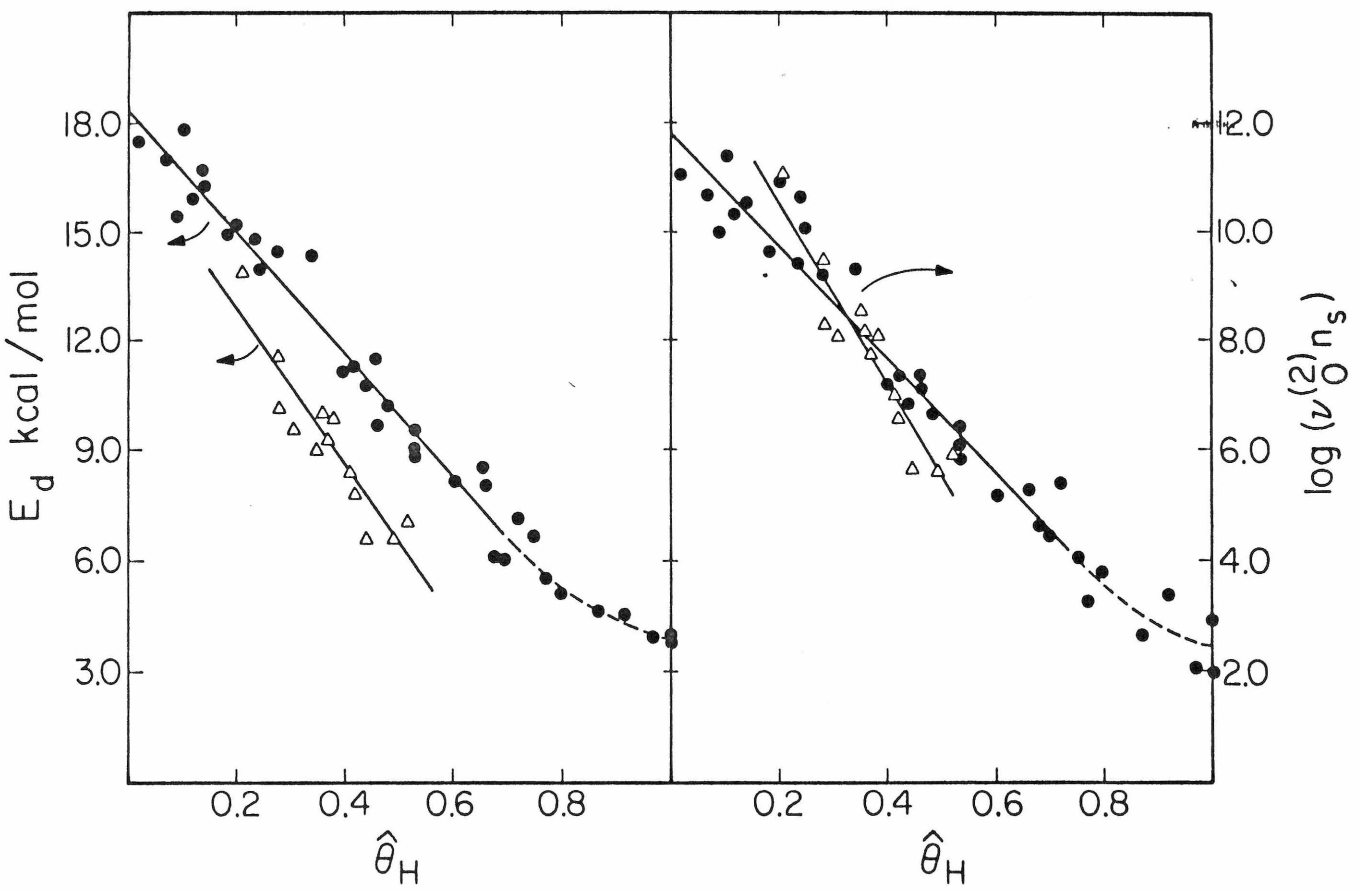
E_d kcal/mol
18.0
15.0
12.0
9.0
6.0
3.0
0.2
0.4
0.6
0.8
$\hat{\theta}_H$
0.2
0.4
0.6
0.8
$\hat{\theta}_H$
12.0
10.0
8.0
6.0
4.0
2.0
log $(\nu_0^{(2)} n_s)$

Figure 1.

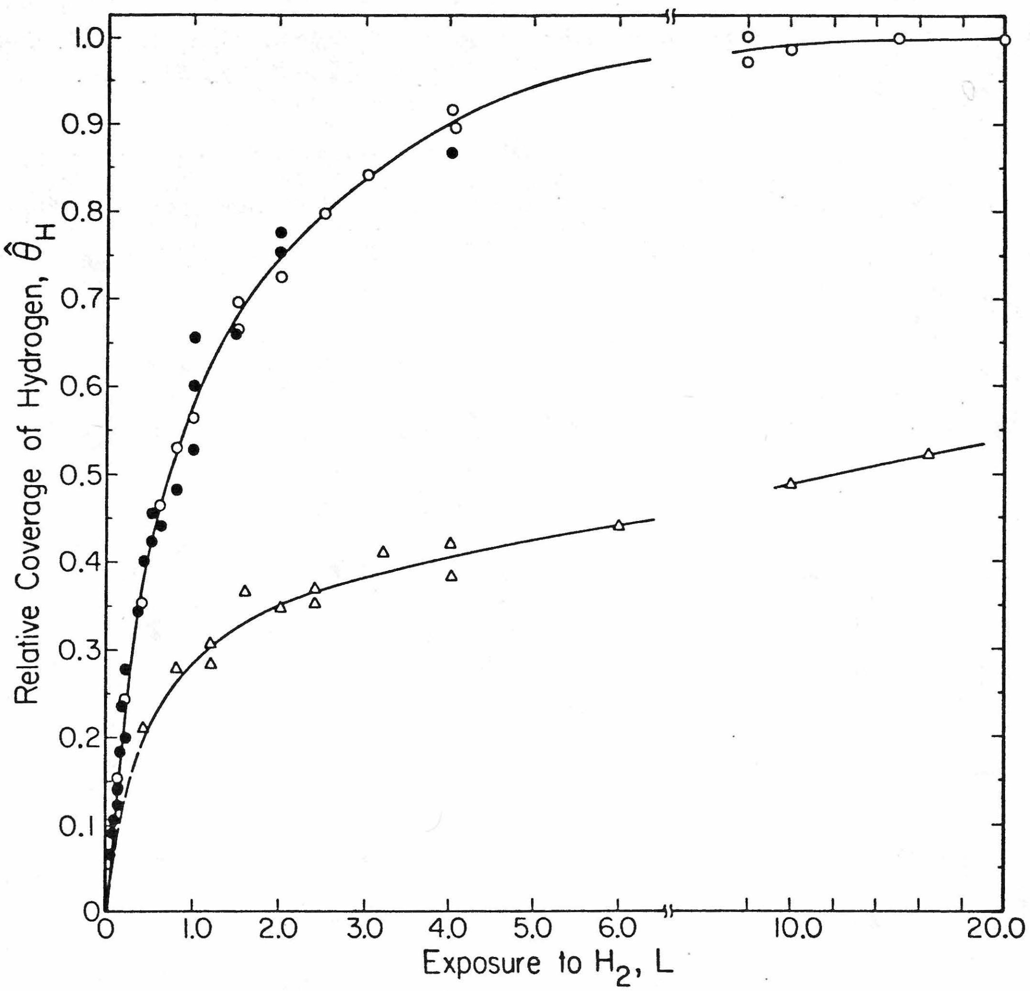

Relative Coverage of Hydrogen, $\hat{\theta}_H$
1.0
0.9
0.8
0.7
0.6
0.5
0.4
0.3
0.2
0.1
0
0
1.0
2.0
3.0
4.0
5.0
6.0
10.0
20.0
Exposure to H_2, L

Figure 2.

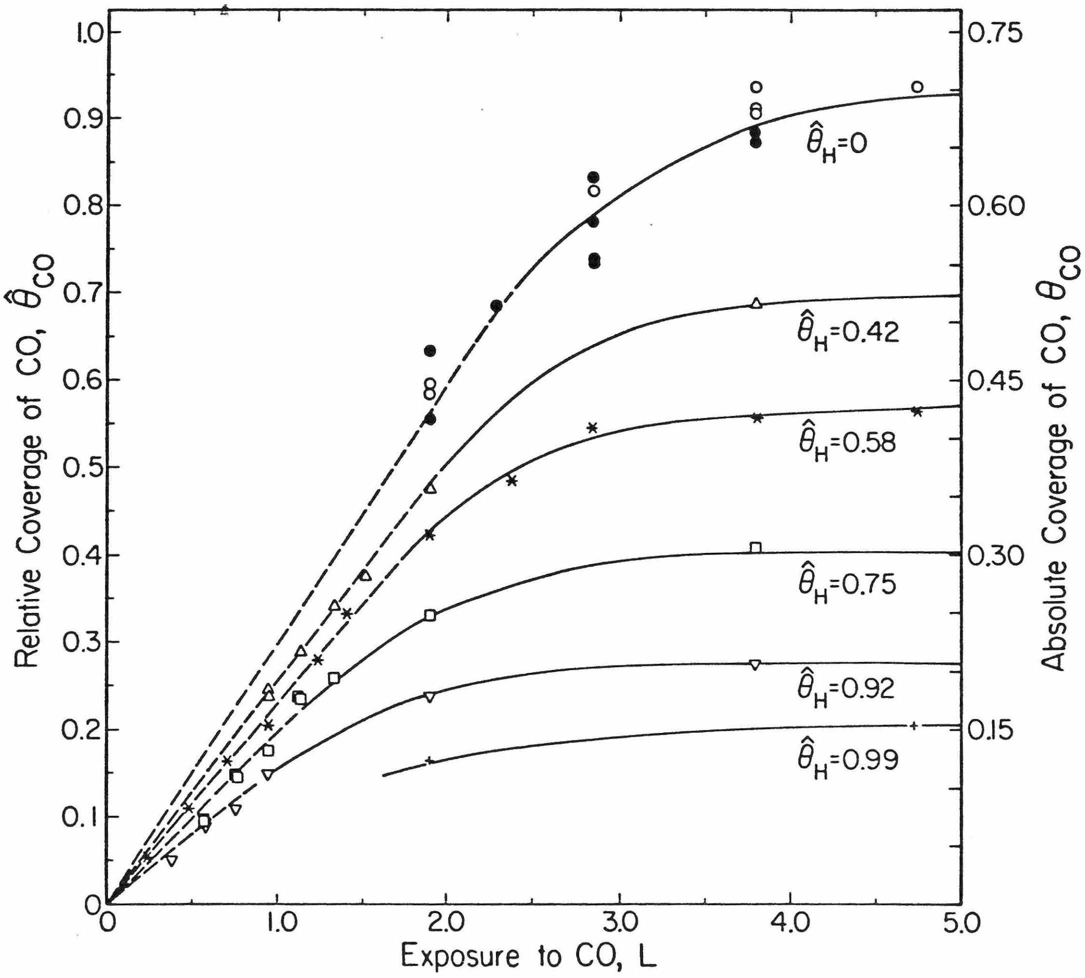
Relative Coverage of CO, $\hat{\theta}_{CO}$
Absolute Coverage of CO, θ_{CO}
Exposure to CO, L
0
1.0
2.0
3.0
4.0
5.0
0.1
0.2
0.3
0.4
0.5
0.6
0.7
0.8
0.9
1.0
0.15
0.30
0.45
0.60
0.75
$\hat{\theta}_H$=0
$\hat{\theta}_H$=0.42
$\hat{\theta}_H$=0.58
$\hat{\theta}_H$=0.75
$\hat{\theta}_H$=0.92
$\hat{\theta}_H$=0.99

Figure 3.

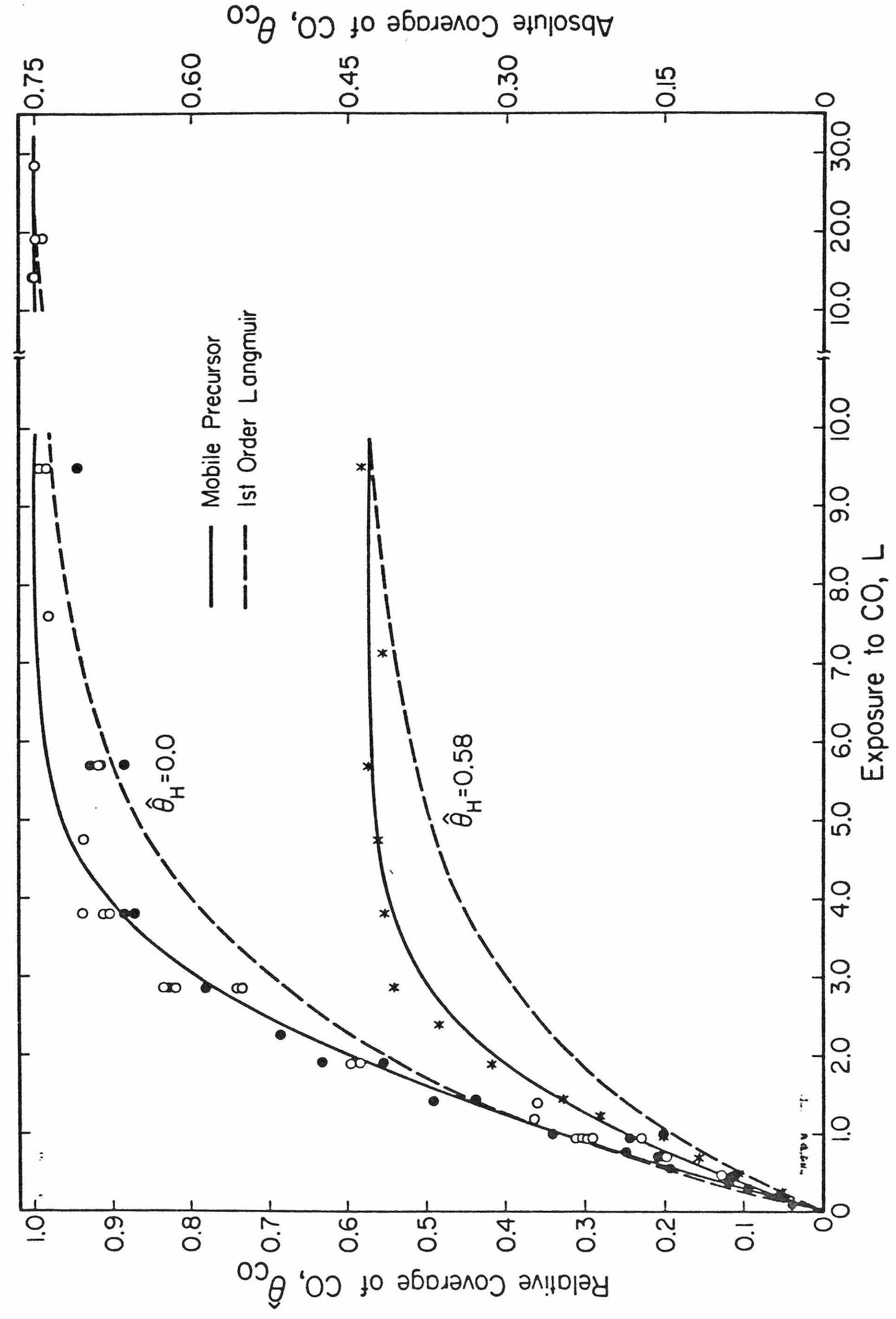
Absolute Coverage of CO, θ_{CO}
0.75
0.60
0.45
0.30
0.15
0
Relative Coverage of CO, $\hat{\theta}_{CO}$
1.0
0.9
0.8
0.7
0.6
0.5
0.4
0.3
0.2
0.1
0
Exposure to CO, L
1.0
2.0
3.0
4.0
5.0
6.0
7.0
8.0
9.0
10.0
20.0
30.0
Mobile Precursor
1st Order Langmuir
$\hat{\theta}_H$=0.0
$\hat{\theta}_H$=0.58

Figure 4.

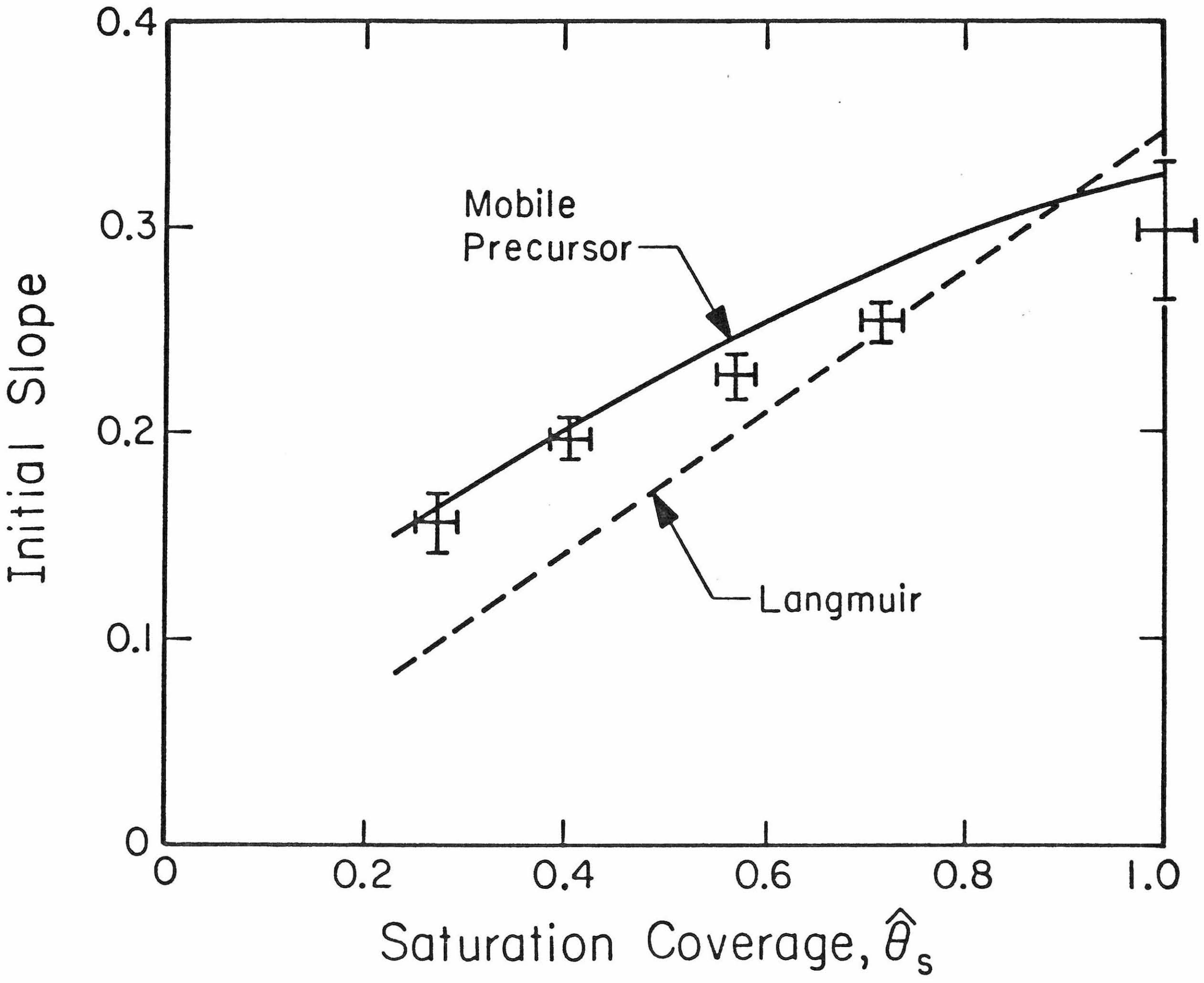
0.4
0.3
0.2
0.1
0
Initial Slope
0
0.2
0.4
0.6
0.8
1.0
Saturation Coverage, $\hat{\theta}_s$
Mobile Precursor
Langmuir

Figure 5.

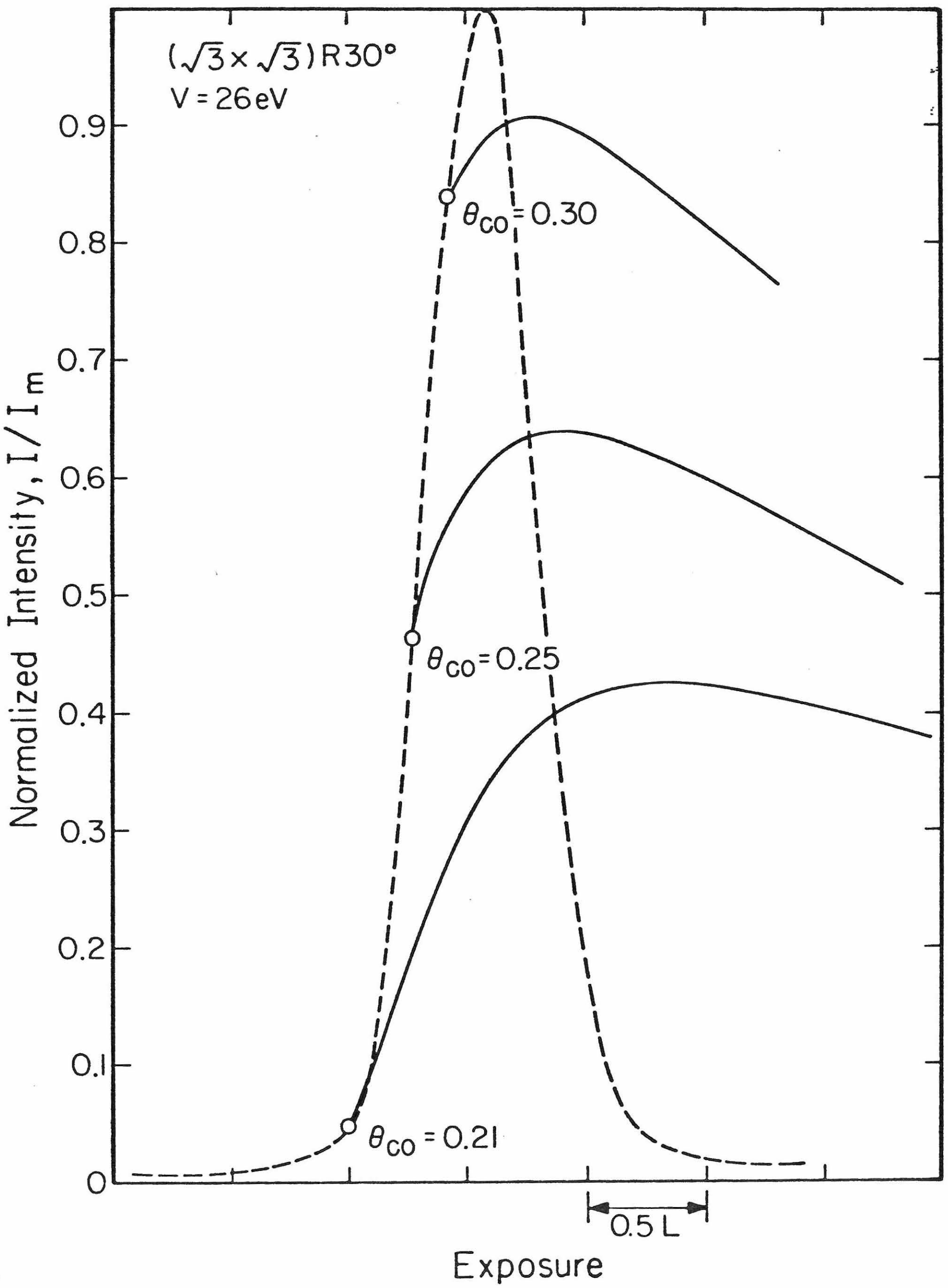

$(\sqrt{3}\times\sqrt{3})R30°$
V = 26 eV
θ_{CO} = 0.30
θ_{CO} = 0.25
θ_{CO} = 0.21
Normalized Intensity, I/I_m
0
0.1
0.2
0.3
0.4
0.5
0.6
0.7
0.8
0.9
0.5 L
Exposure

Figure 6.

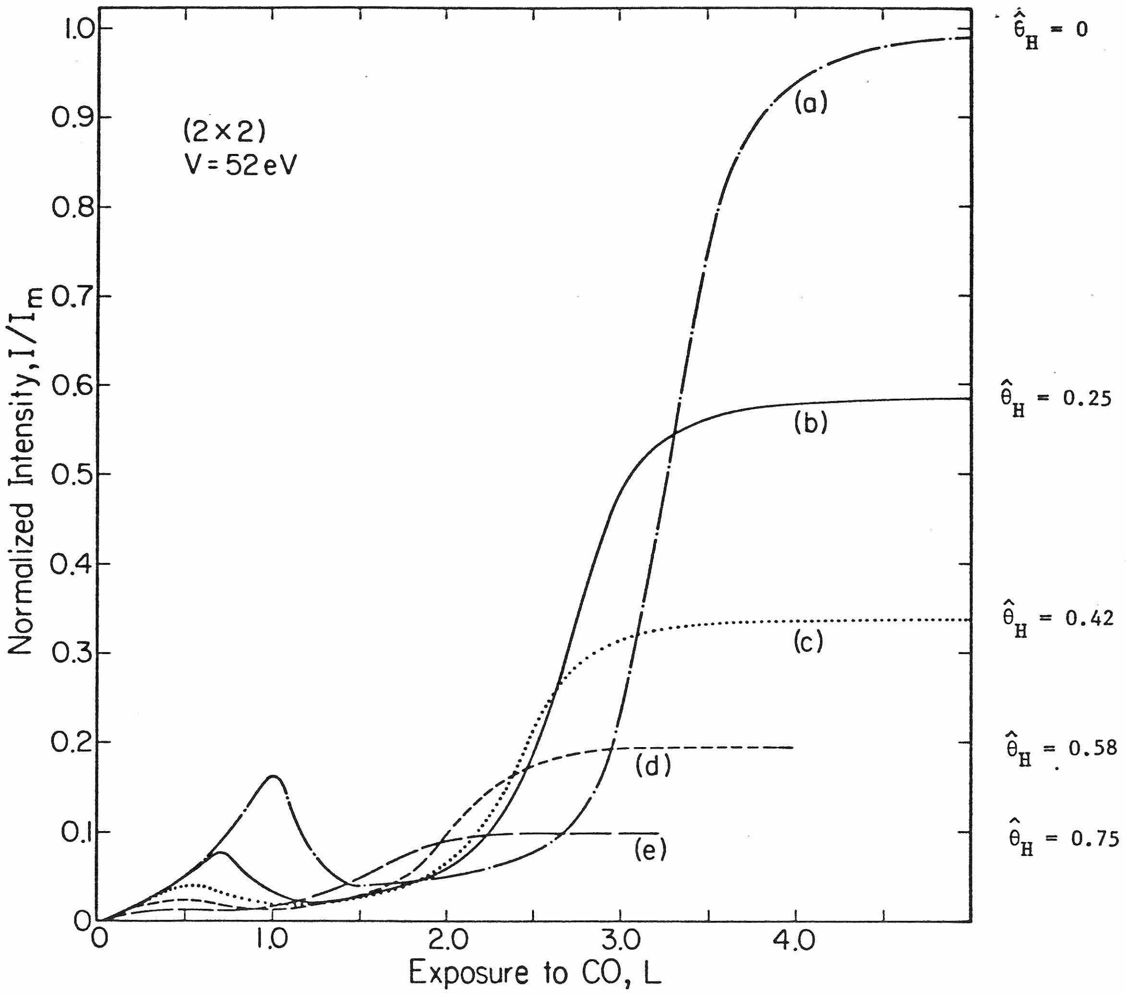
(2×2)
V = 52 eV
Normalized Intensity, I/I_m
Exposure to CO, L
0
0.1
0.2
0.3
0.4
0.5
0.6
0.7
0.8
0.9
1.0
0
1.0
2.0
3.0
4.0
(a)
(b)
(c)
(d)
(e)
$\hat{\theta}_H$ = 0
$\hat{\theta}_H$ = 0.25
$\hat{\theta}_H$ = 0.42
$\hat{\theta}_H$ = 0.58
$\hat{\theta}_H$ = 0.75

Figure 7.

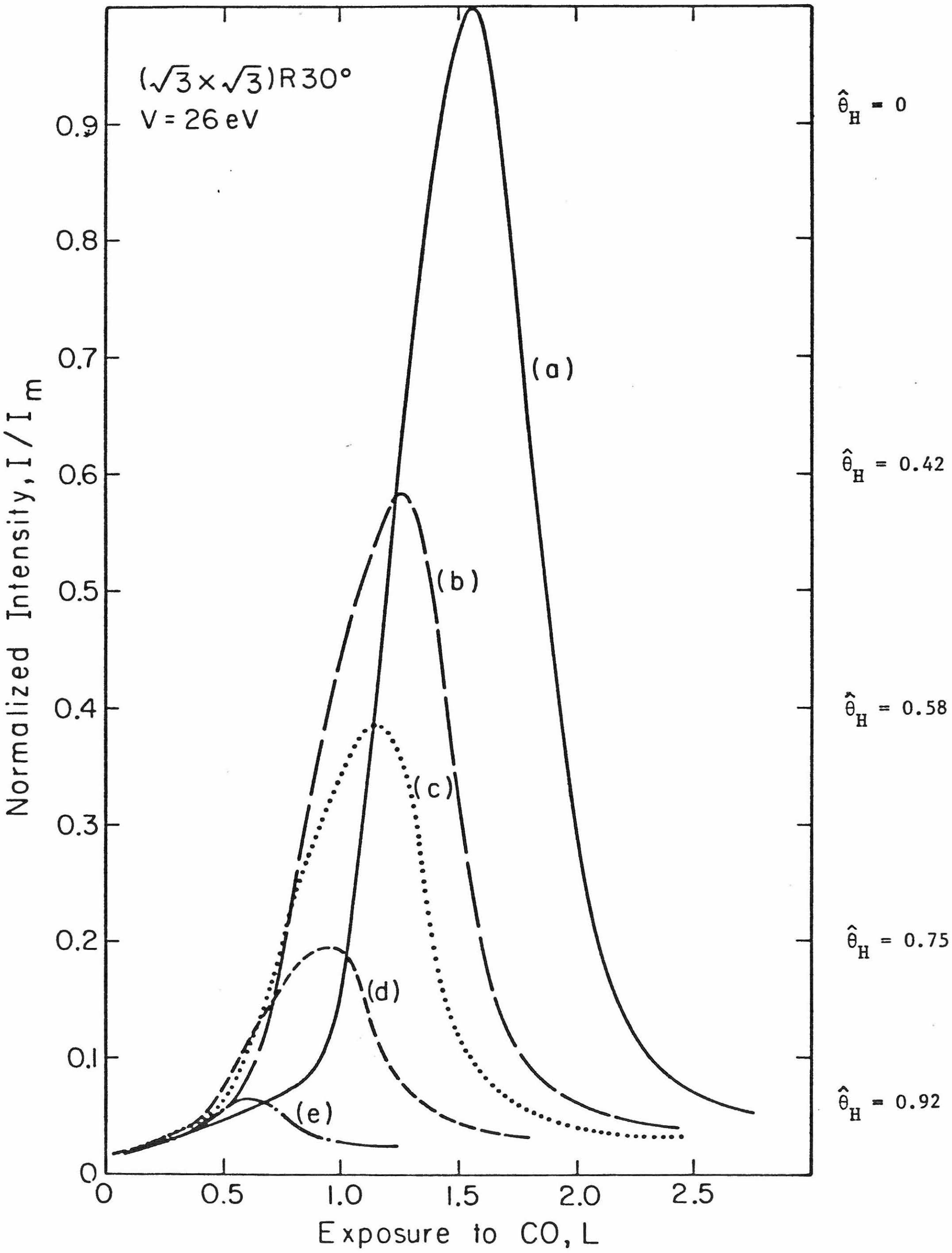
(√3 × √3)R30°
V = 26 eV
Normalized Intensity, I / I m
Exposure to CO, L
0
0.1
0.2
0.3
0.4
0.5
0.6
0.7
0.8
0.9
0
0.5
1.0
1.5
2.0
2.5
(a)
(b)
(c)
(d)
(e)
$\hat{\theta}_H = 0$
$\hat{\theta}_H = 0.42$
$\hat{\theta}_H = 0.58$
$\hat{\theta}_H = 0.75$
$\hat{\theta}_H = 0.92$

Figure 8.

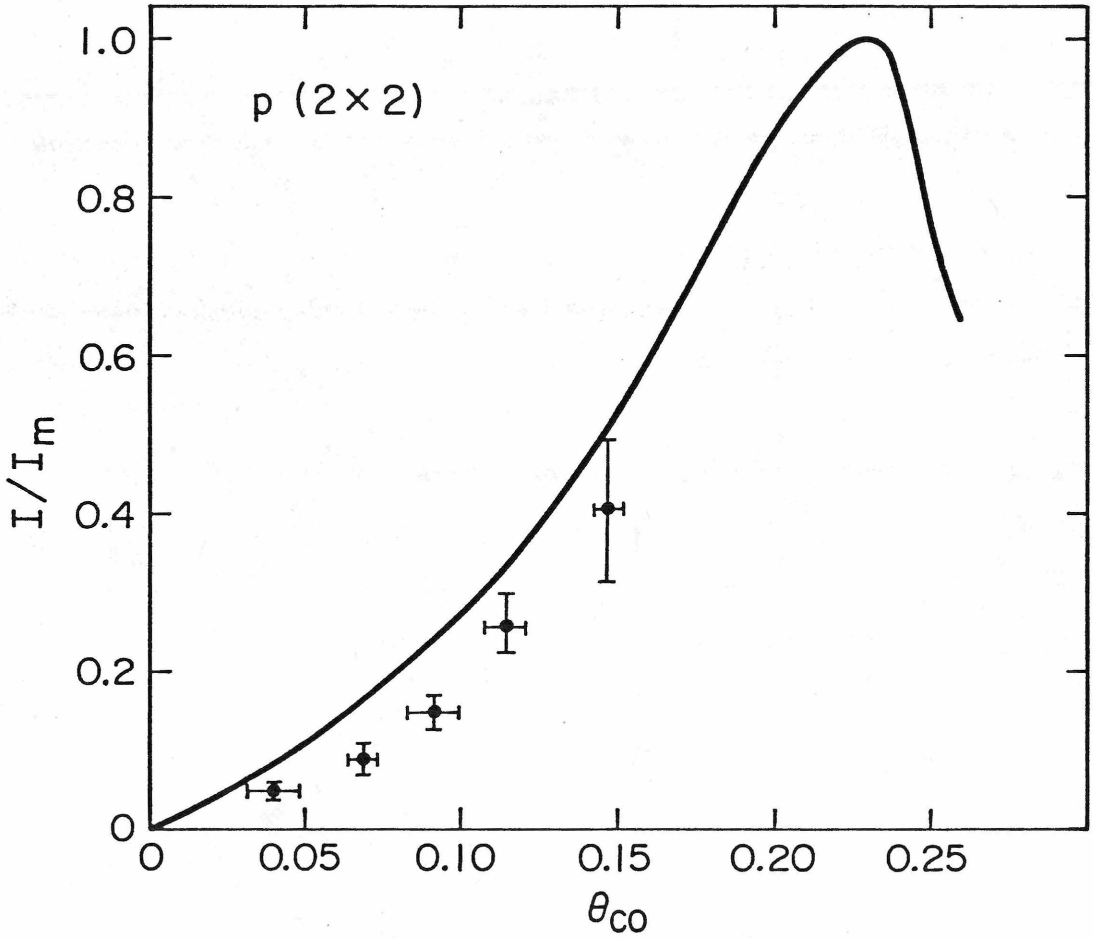

Figure 9.

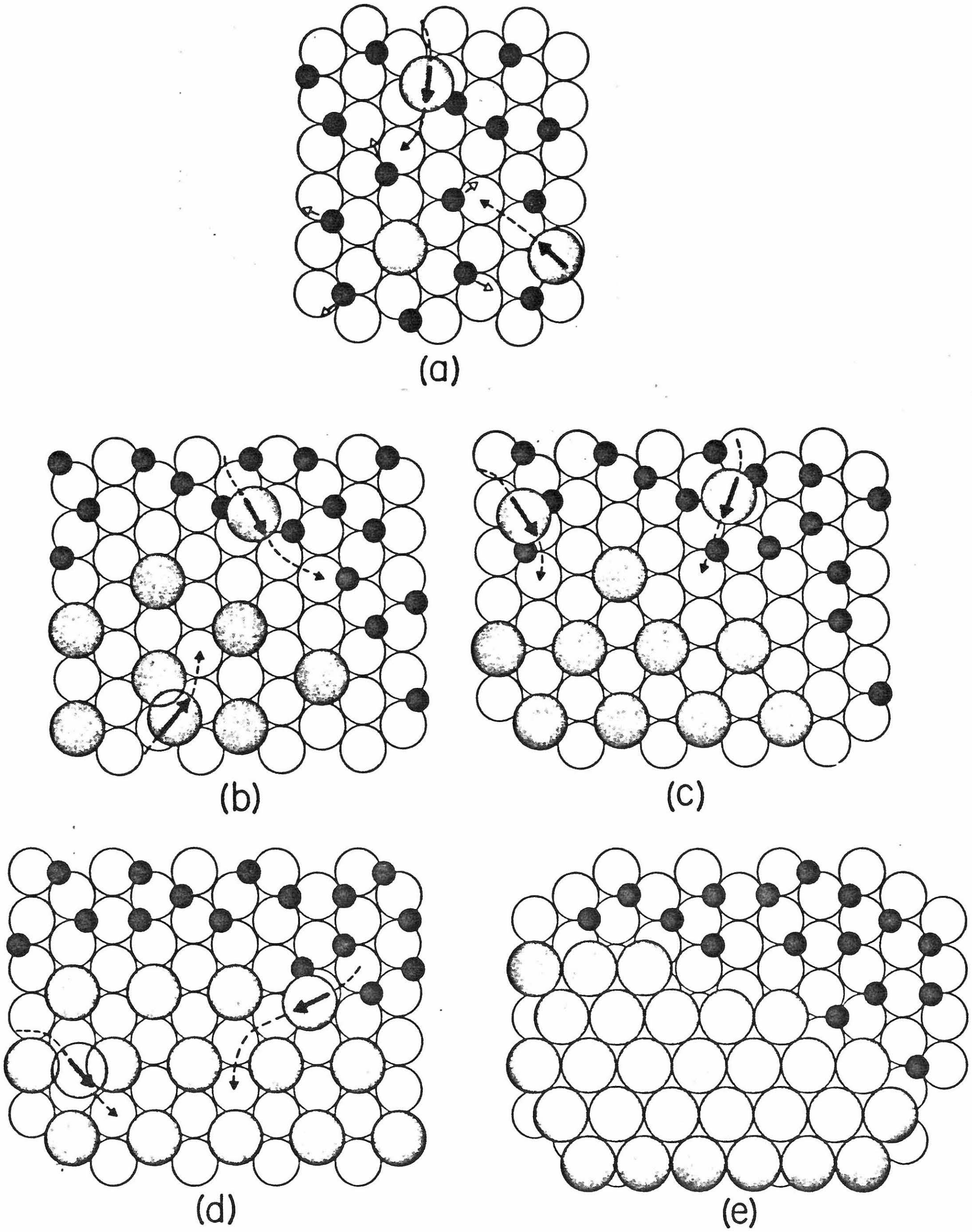

(a)

(b)

(c)

(d)

(e)

Figure 10.

Appendix 4

CONSTRUCTION AND OPERATION OF AN ULTRAVIOLET RADIATION SOURCE FOR USE IN ANGLE-RESOLVED PHOTOEMISSION STUDIES

1. Introduction

The design and construction of an ultraviolet radiation source for use in ultraviolet photoelectron spectroscopy (UPS) experiments from metal surfaces has been completed. As a result, it is possible to analyze the kinetic energies of electrons emitted from valence orbitals of adsorbates, as well as the angular distributions of these photoemitted electrons. This in turn can yield information regarding the chemical state of the adsorbed gas, the relaxation energy of the orbitals due to the final state screening effects, the chemical shfits of the bonding orbitals, and the orientations of the molecular orbitals of the adsorbate (1). The radiation source has been attached to an experimental system equipped with a spectrometer for high resolution low-energy electron energy loss (EEL) spectroscopy (2). (Particularly difficult spatial constraints have been imposed upon the lamp design, however, because of the geometry of this scattering apparatus and the decision to affix the lamp to a vacuum port in a nonhorizontal plane.) The rotatable energy analyzer of the EEL spectrometer can now be used also to dedetermine the angular- and energy-distributions of the photoelectrons. As a result, this system has the unique capability of performing both angle-resolved EEL and UPS experiments in situ, and applying the selection rules associated with both experiments independently to determine adsorbate orientations (3).

2. Lamp Construction

2.1 Description

An ultraviolet lamp has been designed and used. This lamp is similar in design to lamps which are presently in use at Cornell University (4) and at T. J. Watson IBM Research Center, Yorktown Heights (5). The lamp provides HeI radiation (21.2 eV) from a d.c. discharge in 1 - 10 torr helium. The major design criteria which were considered in building this lamp were as follow:

(1) Since no known window material will pass 21.2 eV radiation, there must be line of sight between the He discharge and the scattering center.

(2) Samson (6) reports that the HeI line reaches its maximum intensity in a discharge of about 1 torr He pressure. The pressure in the ultrahigh vacuum chamber which contains the crystal must be kept as low as possible to prevent surface contamination, and also to minimize exposure of the ion pumps to He, which is detrimental to their overall performance. In the present design, the discharge has been interfaced with the ultrahigh vacuum chamber by a series of narrow capillaries, with differential pumping at the gaps between the capillaries. This design feature is commonly used in UV lamps for UHV photoemission studies (7 - 9).

(3) One wishes to maximize photon flux at the crystal surface, which requires short capillaries and inter-capillary gaps to minimize self-absorption by He atoms after the discharge.

(4) Most of the materials must be vacuum-tight (no gases except

He are admissible in the lamp).

(5) Because the sample must be positioned at the scattering center, and because the electron energy analyzer rotates about the scattering center and has a small acceptance angle (4.5°), it is desirable that the spot of UV radiation incident upon the crystal be as large as possible. This facilitates positioning the lamp with respect to the sample, which can be relatively difficult.

(6) Although Starbuck (4) and others (10) indicate that overall capillary alignment is not so important as alignment at the ends of the capillary segments, due to radiative losses by multiple internal reflections, great care has been taken in glassblowing and machining the lamp components to achieve the best capillary alignment possible.

Consideration of points (5) and (6) above leads to the conclusion that the capillary diameters should be as large as possible. However, the related pressure and conductance limitations discussed in Section 2.2 favor very narrow capillaries. The design of the lamp thus required optimization of several related parameters: capillary diameter, pumping speed and pump throughput, expense and size of pumps, and ultimate pressure of He in the experimental chamber. These factors were eventually balanced with a lamp, a schematic of which is shown in Fig. 1. Its arrangement relative to the UHV system is shown in Fig. 2, and a detailed drawing of the components is presented in Fig. 3. Figures 4-7 are photographs of the completed pieces.

A schematic of the lamp is shown in Fig. 1. Its arrangement relative to the UHV system is shown in Fig. 2, and a detailed drawing of the components is presented in Fig. 3. Figures 4 - 7 are photographs of the completed pieces.

The lamp is pumped at two stages, labelled (1) and (2) in Fig. 1. There is an 4" diffusion pump at the first stage, between the anode and the middle capillary, and a 2" diffusion pump at the straight-through valve, between the middle capillary and the final capillary. The lamp can be closed off at the straight-through valve, a commercial Varian 5/8" valve, when not in use so that the diffusion pumps need not be operated continuously. Butterfly valves between the diffusion pumps and the lamp prevent backstreaming of pump oil into the lamp when the pumps are off. Both diffusion pumps are backed by a single large mechanical pump. Cryotraps between the diffusion pumps and the lamp prevent backstreaming of the pump oil, a special polyether known as "Santovac 5", when the lamp is in operation.

The discharge occurs in a water-cooled quartz capillary. The pressure at the discharge is measured roughly with a thermistor gauge. The helium enters through an air-cooled aluminum orifice and passes through an aluminum cathode at 1000 volts d.c. This assembly is shown in Fig.4. A copper anode at ground potential, held in place with an o-ring, is the first conductance-limiting capillary in the helium flow path after the discharge. This is electrically isolated from the cathode by the quartz discharge tube and by six phenolic support rods. The stainless steel block which contains the anode and first pumping port is shown in Fig. 6. The inlet tube, discharge tube, cathode, pressure gauge, and pumping port assembly are shown in Fig. 4.

The middle capillary (Pyrex) is attached to a stainless steel insert, held in place in the straight-through valve by o-rings. The final capillary is held in place by a fitting welded to the main body of the straight-through valve flange. The final capillary is coated with gold to prevent problems with electrical charging on an insulative surface so close to the scattering center. A tungsten spring wrapped around the coated capillary is spot-welded to the valve flange face to provide an electrical path to ground. The final capillary is physically protected by a removable stainless steel sheath, mounted on a collar welded to the straight-through valve flange face. This is shown in Fig. 7.

The discharge tube is protected by a large phenolic cyclinder which provides safety from electrical and mechanical mishaps. A small squirrel fan is attached to the cage to cool the cathode. The cage is hinged so that it can be opened conveniently without removing it from the lamp.

The lamp position is adjustable with respect to the scattering center to compensate for a possible misorientation of the bell jar port on which the lamp is mounted. Varian specifications indicate that the port is aligned to within ±2° with respect to the scattering center. A simple calculation showed that a misalignment of 2° could cause the UV radiation to miss the crystal entirely, so the lamp was designed to be adjustable by ±5° in any direction. This was achieved by placing a gimbles between the bell jar port and the straight-through valve, and supporting the lamp with an adjustable mounting bracket which fixes its final position. The gimbles, consisting mainly of three concentric rotatable rings and a welded metal bellows, is shown in Fig. 5.

The photoemitted electrons from the sample are analyzed by the computer-interfaced, rotatable energy analyzer used in the electron energy loss experiments. It subtends an acceptance angle of 4.5° and has a calculated resolution of 70 meV, i.e. 0.4% or better, for the energy range of the photoemission experiment. The angles of photon incidence and electron emission can be changed independently, within limits. These limits are imposed by the orientation of the sample and the range of analyzer angles. The sample is mounted at present on a rotatable cold finger, with the sample's surface normal at an angle of 34 ± 1° to the axis of rotation. As one rotates the cold finger, the polar and azimuthal emission angles from the sample (for a fixed analyzer angle) are both changing. The limitations imposed by this particular sample configuration can be changed by mounting the sample differently, but not without changing the conditions used in the EEL experiments also.

The angular range of the analyzer is determined by three factors:

(1) The flexible Ceramaseal cables, which are sheathed with stainless steel braid and which connect the monochromator and analyzer, are greatly strained if the angle separating the two halves of the spectrometer exceeds 180°.

(2) The analyzer cannot approach the lamp port closer than 45° without blocking the incident UV radiation (<u>11</u>); and

(3) The monochromator intersects the same horizontal plane as the exit capillary of the lamp. Because the monochromator and analyzer are both mounted on the top 14" Wheeler flange, the position of the monochromator in the scattering plane affects the range of angles available to the analyzer. As shown in Fig. 8, the monochromator cannot come closer than 40° to the UV exit capillary without blocking the radiation and without risking contact with the capillary sheath. The latter is true even though $\alpha_B = 30^0$ in Fig. 8, since the physical act of rotating the top Wheeler flange is usually a clumsy operation.

With these considerations in mind, the ranges of angles which are presently available for the UPS experiment are shown in Fig. 9 for two azimuthal sample angles, separated by 180°. Figure 9(A) shows the arrangement which is presently used for the high-resolution, low-energy EEL experiments. In this arrangement the angle of incidence, θ_i, of the UV radiation is 32° from the surface normal; in Fig. 9(B) $\theta_i = 81°$. This arrangement thus allows reasonable flexibility in both incidence and emission angles, with the sample situated perpendicular to the scattering plane. This configuration of sample, spectrometer and lamp has been used successfully in angle-resolved photoemission studies of cyclopropane on Ru(001) in determining adsorbate orientation (3).

2.2 Pressure Calculations

The critical dimensions and calculated operating parameters of this lamp are summarized in Table I. The operating parameters were calculated from the formulas described below.

The type of flow through any orifice is determined by the ratio of D/λ, where D is the diameter in centimeters and λ is the mean free path of the gas molecules. Values of $D/\lambda < 1$ indicate molecular flow, while $D/\lambda > 110$ indicate viscous flow. λ is given by (12):

$$\lambda(\mathrm{cm}) = 2.33 \times 10^{-20}\ T/(\xi\bar{P}) , \tag{1}$$

where T is the temperature (K), ξ is the atomic radius of the gas molecule (2.61×10^{-8} cm for He), and $\bar{P}$ is the average pressure in torr. For gas flow through the anode and through the first pumping port, labelled (1) in Fig. 1, the value of D/λ fell in the intermediate category. Gas flow through all other orifices was molecular.

For molecular flow through a cylindrical orifice, the conductance is given by (12):

$$C^{mol}(1/s) = \frac{30.48}{8}(T/M)^{\frac{1}{2}}\left\{\frac{D^3}{L + 1.33D}\right\} \tag{2}$$

where M is the molecular weight of the gas and L is the length of the tube. For intermediate flow, the conductance through a cylinder is given by (13):

$$C^{int}(1/s) = C^{mol}\left(0.1472\frac{D}{2\lambda} + Z\right) , \tag{3}$$

where Z is an empirical parameter given by:

$$Z = \frac{1 + 2.057(D/2\lambda)}{1 + 3.095(D/2\lambda)} \tag{4}$$

Table I. Critical Dimensions and Calculated Operating Parameters for Ultraviolet Lamp (see Figure 1).

Discharge pressure, nominal	3 torr
Capillary diameter	2 mm (0.079")
Anode length	2 cm (0.79")
Mid-capillary length	6.65 cm (2.62")
Final capillary length	26.16 cm (10.32")
Pressure at first stage	2.4×10^{-2} torr
Pressure at second stage	1.8×10^{-5} torr
Pressure at bell jar (for discharge at 3 torr He)	3.7×10^{-9} torr
Pressure at bell jar (for discharge at 1 torr He)	1.3×10^{-9} torr
Pumping speed at first port (4" diffusion pump)	39.8 l/s
Pumping speed at second port (2" diffusion pump)	51.5 l/s
Pumping speed at bell jar	48 l/s
Conductance of anode	0.32 l/s
Conductance of middle capillary	0.038 l/s
Conductance of final capillary	0.0010 l/s
Throughput at first stage	0.9 torr-l/s
Throughput at second stage	9.0×10^{-4} torr-l/s
Distance from end of capillary to crystal (scattering center)	6.43 cm (2.53")
Vertical distance from end of capillary to crystal	2.67 cm (1.05")

For gas flowing through the anode:

$D = 0.20$ cm

$\lambda = 0.0114$ cm ($T = 500K$, $\bar{P} = 1.5$ torr)

$Z = 0.817$

$D/\lambda = 17.54$

$C^{mol}_{anode} = 0.15$ 1/s

$C^{int}_{anode} = 0.316$ 1/s

The pressure at any stage, i, is given by

$$P_i = P_{i-1}(C_i/S_i) \tag{5}$$

where S_i is the pumping speed at stage i and C_i is the conductance of the capillary connection to the preceding stage. In these calculations, it was assumed that the discharge pressure was 3 torr. The throughput is the product of the pumping speed and the pressure.

The conductance of the pumping port at stage (1) was calculated to be 43.5 1/s by treating the port outlet and the bellows as two straight cylinders in series with D = 2.54 cm (1"), L = 6.35 cm (2.5"), and D = 3.81 cm (1.5"), L = 2.54 cm (1"), respectively. It is reasonable to assume that these conductances are the limiting conductances in the connections between the pump and stage 1, i.e. that other conductances are negligibly large. The pumping speed of the 4" diffusion pump, with cryotrap, is 487 1/s. Thus, we have

$$P_1 = (3 \text{ torr}) \frac{(0.316 \text{ 1/s})}{{\frac{1}{487} + \frac{1}{43.5}}^{-1} \text{ 1/s}} = 2.37 \times 10^{-2} \text{ torr}$$

For the second stage, which is pumped by the 2" pump at the straight-through valve, the geometry of the connection at the bellows was approximated with a right-angle bend as shown below for purposes of calculating the conductance.

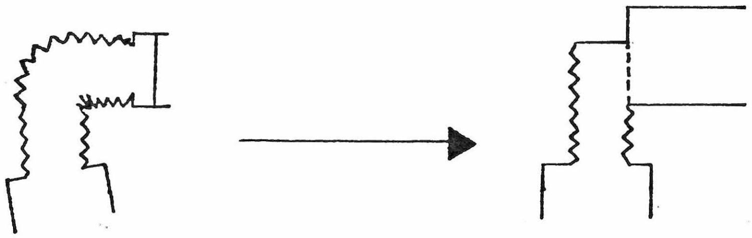

For this geometry, the effective value for L to be used in equation (2) is (12):

$$L = L_{ax} + 1.33 \frac{\Theta}{180°} D \tag{6}$$

where L_{ax} is the axial length and $\Theta = 90°$ in this case. Thus, for $D = 3.81$ cm and $L = 15.88$ cm, the conductance of the pump connection at stage (2) is 87 l/s. The conductance of the middle capillary (molecular flow, since $D/\lambda = 0.4$ for $\bar{P} = 0.02$ torr) with $D = 0.20$ cm and $L = 6.65$ cm was found from equation (2) to be 0.038 l/s. The pumping speed of the 2" diffusion pump and cryotrap is 127 l/s, so we find that

$$P_2 = (2.37 \times 10^{-2} \text{ torr} \left\{ \frac{0.038 \text{ l/s}}{\frac{1}{87} + \frac{1}{127}^{-1} \text{ l/s}} \right\} = 1.75 \times 10^{-5} \text{torr}$$

Similarly, the conductance of the last capillary section ($L = 26.16$ cm and $D = 0.20$ cm) is 1.0×10^{-2} l/s. The ion pumps in the bell jar have a nominal pumping speed of 200 l/s for N_2. The pumping efficiency at 2×10^{-9} torr is 80%, and the efficiency when pumping helium is only 30% of the rated value for N_2. Therefore, as far as the UV lamp is concerned, the pumping speed of the bell jar is ∿40 l/s. This yields the result that the base pressure of the bell jar during lamp operation is, from equation (5),

$$P_{\text{chamber}} = (1.75 \times 10^{-5} \text{ torr}) \frac{(1.0 \times 10^{-2} \text{ l/s}}{(48 \text{ l/s})} + 1 \times 10^{-10} \text{ torr}$$

$$= 3.7 \times 10^{-9} \text{ torr} .$$

If the lamp is operated at a discharge pressure of 1 torr, P_{chamber} decreases to 1.3×10^{-9} torr.

3. Operation

The following section discusses the basic procedures which are important in using and maintaining the UV lamp, and also summarizes typical operating parameters.

It is usually helpful to prepare an incident beam of electrons from the monochromator with 20 eV kinetic energy, and tune the analyzer for resolution and/or sensitivity by reflection from the crystal. This is not absolutely necessary, however, as tuning is not so critical in achieving the energy resolution necessary for UPS as for EELS, and settings which were satisfactory in previous experiments can probably be returned to easily.

In initially locating and positioning the incident spot of UV radiation, no reflection has ever been observed from the face of the crystal because of its smoothness, but one can locate the spot by observing diffuse scattering of blue-purple light from the crystal edges and support wires, if the room is darkened.

A discharge is established by flowing He through the water-cooled capillary such that the thermistor gauge at the anode reads 10 to 100 Torr (14) and applying a voltage of 2 to 4 kV to the cathode. After the plasma is obtained, the discharge current is adjusted to approximately 150 mA and the cathode voltage to about 800 V. Under steady-state operating conditions, the total pressure measured by the ion gauge in the UHV chamber is 1 to 3 x 10^{-9} Torr. If the pressure at the discharge is about 10 Torr, then the calculation presented in Section 2.2 predicts a total pressure of He in the scattering chamber of 1.3 x 10^{-8} Torr. This is in reasonable agreement with the value which is observed during lamp operation, since the ionization efficiency of helium relative to nitrogen is 0.161. Applying this correction factor, the true observed pressure of He in the UHV chamber then is 0.6 to 1.9 x 10^{-8} Torr. The total photocurrent at the crystal is surprisingly insensitive to variations in discharge pressure, cathode potential or discharge current. For the grazing angle of incident radiation shown in Fig. 9(B), the photocurrent at the crystal (positive current to ground) is 6 x 10^{-10} A, and about 2 x 10^{-9} A for the situation of Fig. 9(A). The maximum count rates at the Fermi edge under these two conditions are about 1 to 3 x 10^{4} cps and 5 x 10^{3} cps, respectively.

It is important to use the spanner wrench to counteract the torque which must be applied to open or close the straight-through valve. This avoids straining the valve and warping the body. It is also important to protect the lamp from heat during bakeout of the system, unless it is disassembled and all parts are removed which contain Viton (15) items.

Typical spectra which have been obtained with this lamp are shown in Fig. 24 of Chapter 9 for the adsorption of H_2O on Ru(001).

References

1. For a more thorough discussion, the reader is referred to the review article by B. Feuerbacher and B. Fitton, "Photoemission Spectroscopy", Ch. 5 in Electron Spectroscopy for Surface Analysis H. Ibach, Ed., Springer-Verlag, Berlin (1977) pp. 151-203.
2. G. E. Thomas and W. H. Weinberg, Rev. Sci. Instrum 50, 497 (1979).
3. F. M. Hoffmann, T. E. Felter and W. H. Weinberg, in preparation.
4. J. E. Starbuck, MS Thesis, Cornell University, Ithaca, New York (1974).
5. J. E. Demuth, private communication.
6. J. A. R. Samson, Techniques of Vacuum Ultraviolet Spectroscopy, John Wiley and Sons, New York (1967).
7. J. E. Rowe, S. B. Christman, E. E. Chaban, J. A. Simpson and C. E. Kuyatt, Rev. Sci. Instrum. 44, 1675 (1973).
8. J. K. Cashion, J. L. Mees and D. E. Eastman, Rev. Sci. Instrum. 42, 1670 (1971).
9. R. T. Poole, J. Liesegang, R. C. G. Leckey and J. G. Jenkin, J. Electron Spectroscopy and Related Phenom. 5, 773 (1974).
10. C. Brucker, private communication.
11. The energy analyzer is in no danger of ever actually hitting the beam doser or lamp sheath, however, since the latter two items were designed specifically to clear the horizontal plane of rotation of the bottom edge of the analyzer. This is, in fact, the reason why the distance between these probes and the scattering center is so long, 2.5".

12. A. Roth, *Vacuum Technology*, North-Holland, Amsterdam (1976).
13. S. Dushmann, *Scientific Foundations of Vacuum Technique*, second edition, John Wiley and Sons, Inc., New York (1962).
14. The thermistor gauges are simply thermal conductivity gauges using a bead thermistor as the sensing element. Unfortunately, the sensitivity of thermistor (and thermocouple) gauges to helium is nonlinear and almost meaningless in the pressure range of interest, 1 - 10 torr. Therefore, the gauge reading at the anode is not to be taken literally, but rather as a mere qualitative operating parameter.
15. Viton is bakeable to 200°C if it is not under pressure in contact with a metal surface during bakeout, e.g. in the case of the butterfly valves, if they are open. Otherwise the Viton partially adheres to the metal at bakeout temperatures greater than 120°C.

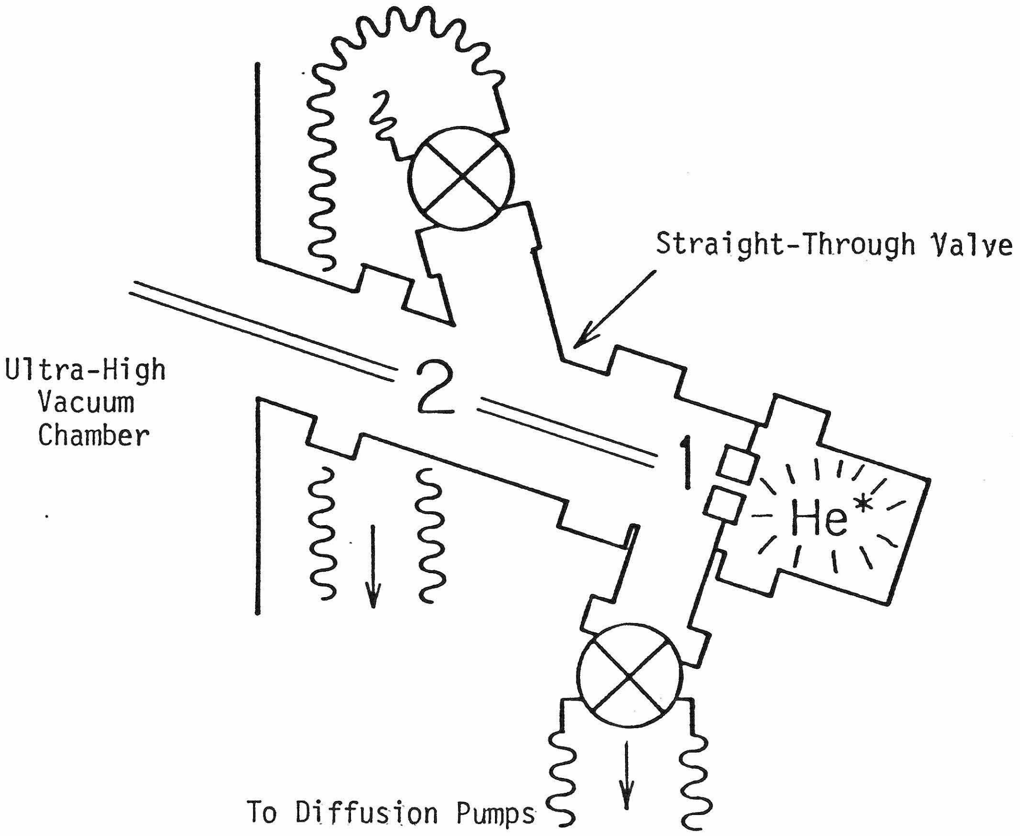

Figure 1. Schematic drawing of lamp assembly, side view.

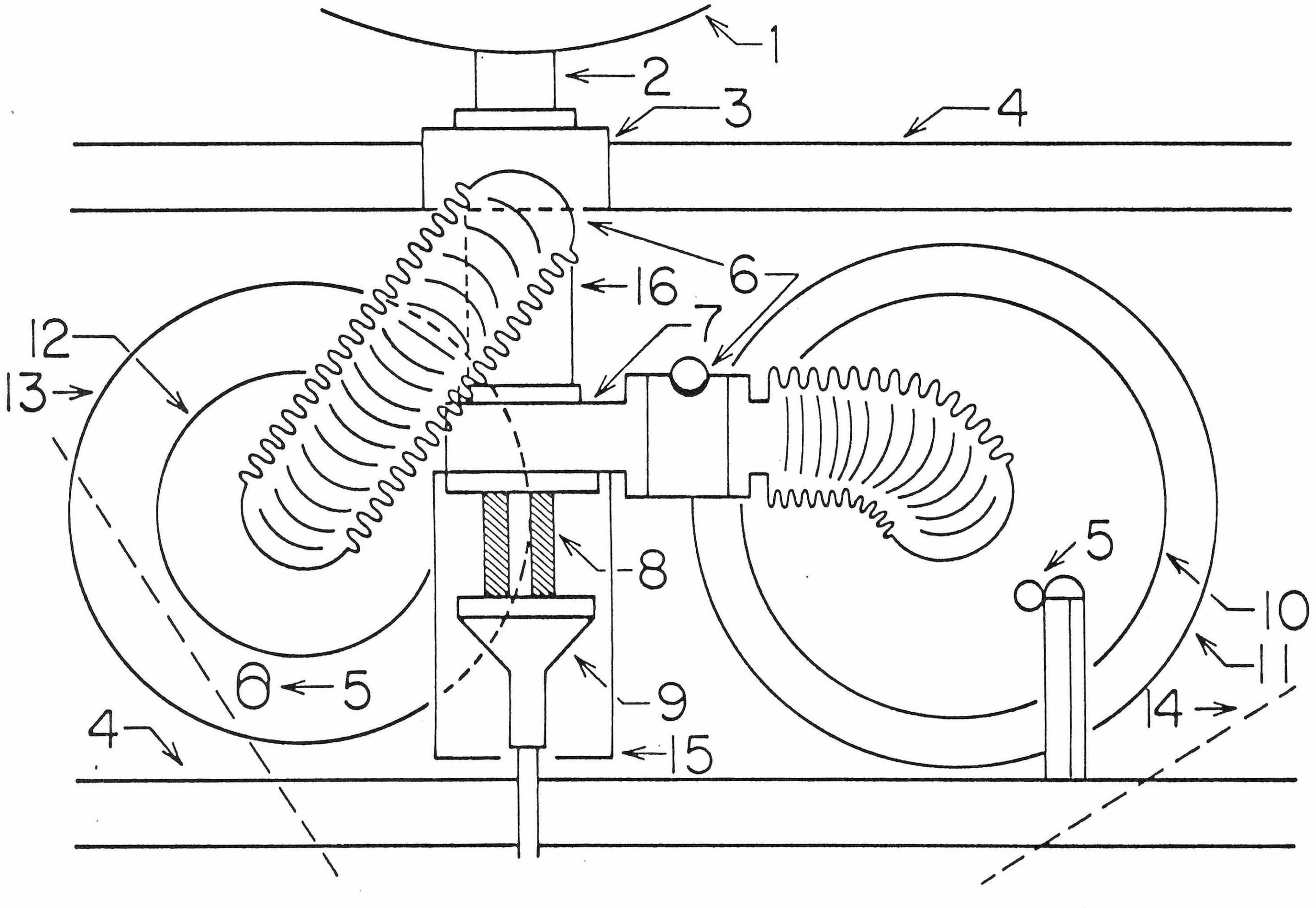

Figure 2. Top view of ultraviolet lamp and pumps (see next page for Key).

Figure 2 Key:

1. Ultrahigh vacuum chamber (bell jar).
2. Bell jar port.
3. Gimbles.
4. Unistrut framework for tabletop.
5. Fill and vent tube for cryotrap.
6. Butterfly valve.
7. "T-piece" containing anode.
8. Phenolic support rods surrounding discharge tube.
9. Air-cooled aluminum piece containing cathode.
10. Flange, 9" o.d.
11. Cryotrap for 4" diffusion pump, 925 ml capacity, 2.5 hr. lifetime.
12. Flange, 6" o.d.
13. Cryotrap for 2" diffusion pump, 1500 ml capacity, 7.5 hr. lifetime.
14. Lines indicate position of bakeout ovens during bakeout.
15. Protective, hinged phenolic cage with cooling fan attached underneath.
16. Straight-through valve.

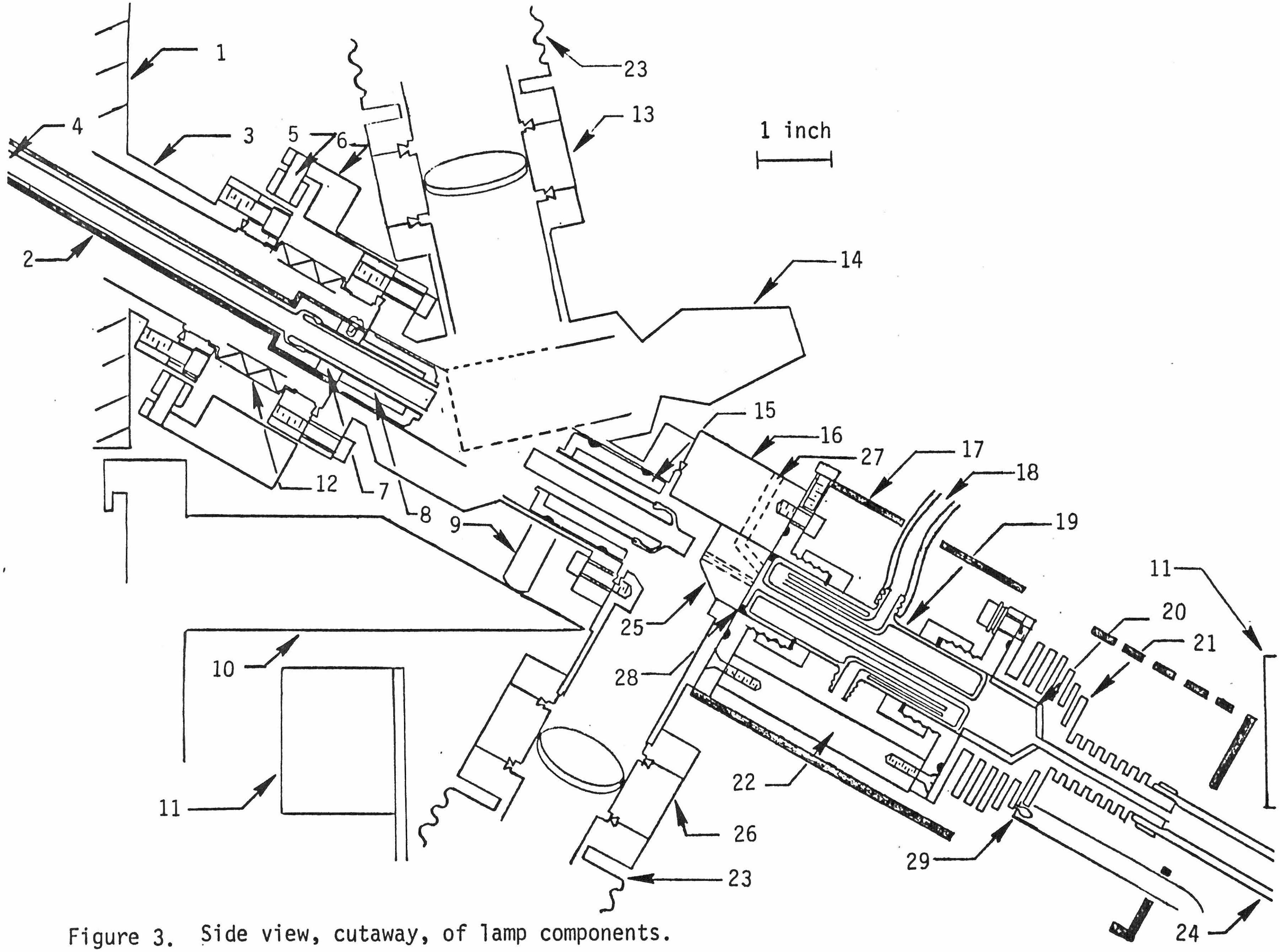

Figure 3. Side view, cutaway, of lamp components.

Figure 3 Key:

1. Bell jar wall.
2. Protective stainless steel sheath.
3. Bell jar port.
4. Pyrex capillary, 7.5 mm o.d. and 2.0 mm i.d.
5. Gimbles pin, about which the outer two gimbles rings rotate. Two pins at 90° to these are not shown.
6. Gimbles.
7. Support ring to which protective sheath (2) is attached.
8. Kovar sleeve, welded to stainless steel insert which is welded in place in valve.
9. Adjustable support arm (not completely drawn) which attaches to straight-through valve with set screws.
10. Fixed support arm, which attaches to base of bell jar and supports weight of lamp.
11. Tabletop unistrut.
12. Welded metal bellows.
13. Butterfly valve to 2" diffusion pump.
14. Straight-through valve.
15. Removable stainless steel insert welded to Kovar sleeve which attaches to middle capillary section.
16. Stainless steel block which contains anode and first pumping port, known as the "T-piece".
17. Protective phenolic safety cage.
18. Water inlet.

Figure 3 Key (continued)

19. Quartz discharge tube.
20. Aluminum cathode.
21. Air-cooled helium inlet.
22. Phenolic support rods (one of six is shown).
23. Preformed metal bellows.
24. Tygon tubing to helium tank (zeolite purification trap in between).
25. Copper anode.
26. Butterfly valve to 4" diffusion pump.
27. Duct for measuring pressure at discharge.
28. O-ring spacer to prevent contact between quartz discharge tube and copper anode, and prevent possible breakage.
29. Banana plug and receptacle for connection with CVC high voltage SDC-100 power supply.

Note: All dimensions are accurately drawn to scale. However, some artistic liberties were taken for the sake of clarity. For example, only one phenolic rod (22) is drawn, but there are actually two in the plane of the paper. The first pumping port points out to the side, as drawn in Figure 2, but in this figure it is presented as pointing downward. The adjustable support arm (9) is only sketched, since to have drawn this piece entirely would have obscured more important lamp components.

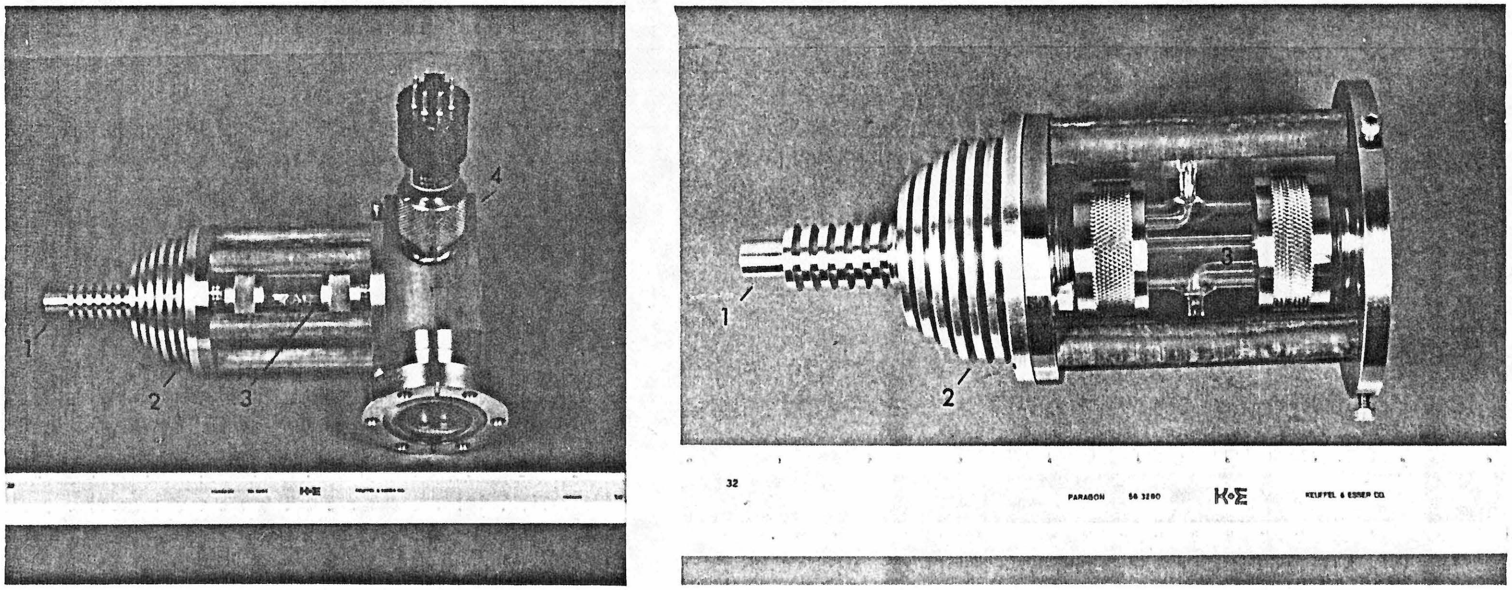

Figure 4. Discharge assembly, with He inlet (1), Al cathode (2), water-cooled quartz capillary (3), and the T-piece of Fig. 6 (4).

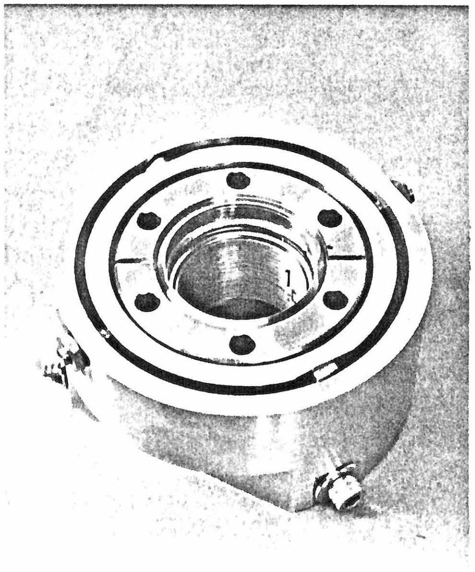

Figure 5. Gimbles assembly, with welded metal bellows (1) attached to three rotatable concentric rings, one of which is the 2.75" flange. The overall length of the gimbles is fixed by the length of the outer concentric ring, which connects the two 2.75" flanges.

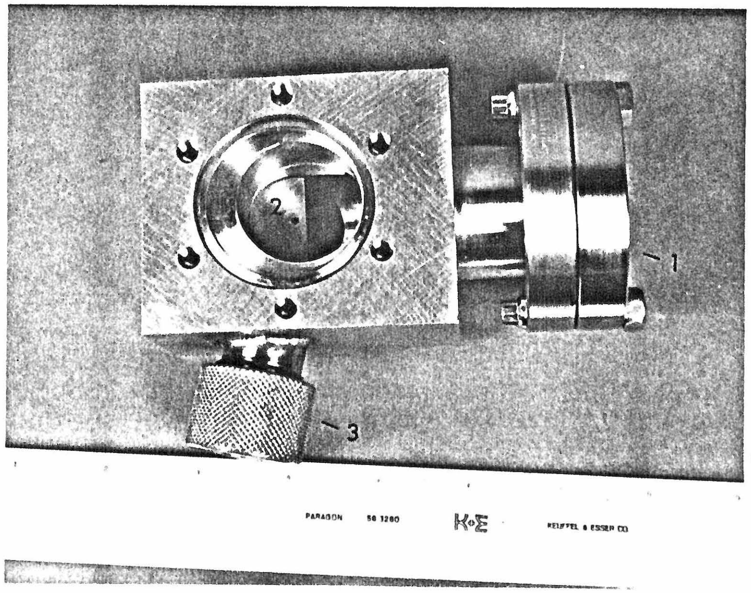

Figure 6. "T-piece" assembly, with first pumping port (1), copper anode (2), and thermistor gauge cap (3) in place.

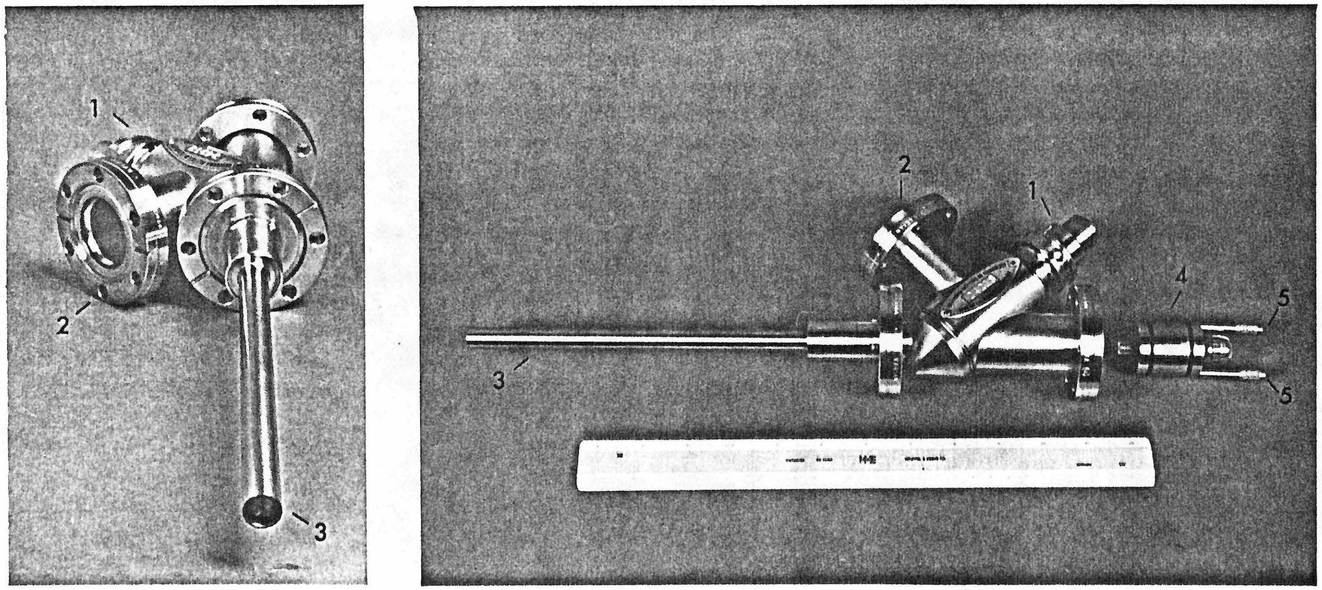

(A)

(B)

Figure 7. Straight-through valve (1), pumping port for 2" diffusion pump between middle and final capillaries (2), exit capillary with stainless steel sheath in place (3), and middle capillary removed from valve body (4). The middle capillary assembly is also shown with two "pullers" in place (5) for use in removing the middle capillary from the valve.

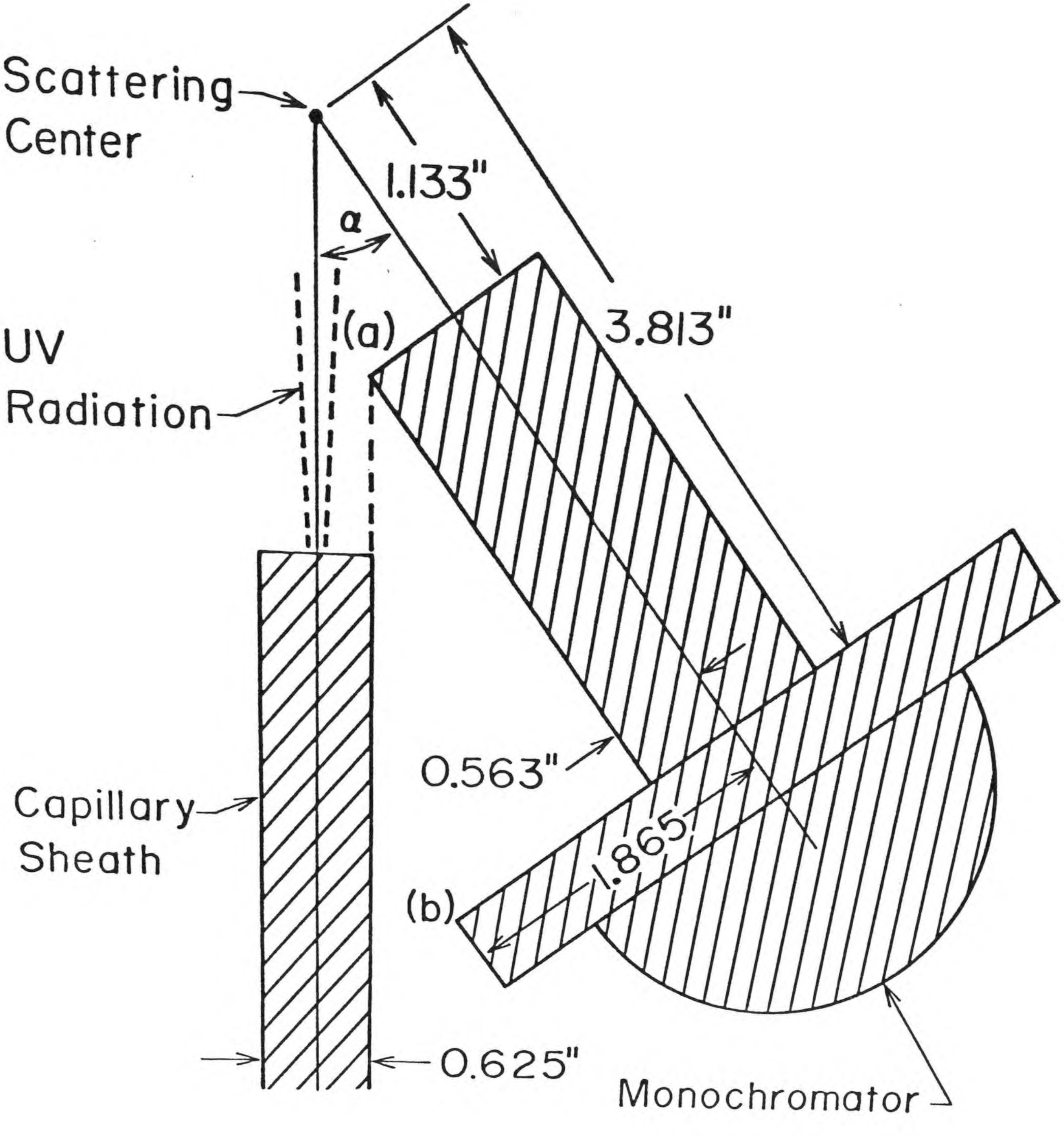

Figure 8. The dimensions which limit the angle of approach of the electron monochromater to the UV lamp exit capillary, α, are shown above, which is a schematic drawing of the view if one looks perpendicular to the horizontal scattering plane. If possible interference between the UV radiation and the gun edge at point (a) is considered, $\alpha_a = 40^o$. If physical contact between the capillary sheath and the gun edge at point (b) is considered, then $\alpha_b = 30^o$. The larger angle, 40^o, is the actual limiting value. Only the dimensions which are critical to the calculation of α have been labelled and drawn to scale.

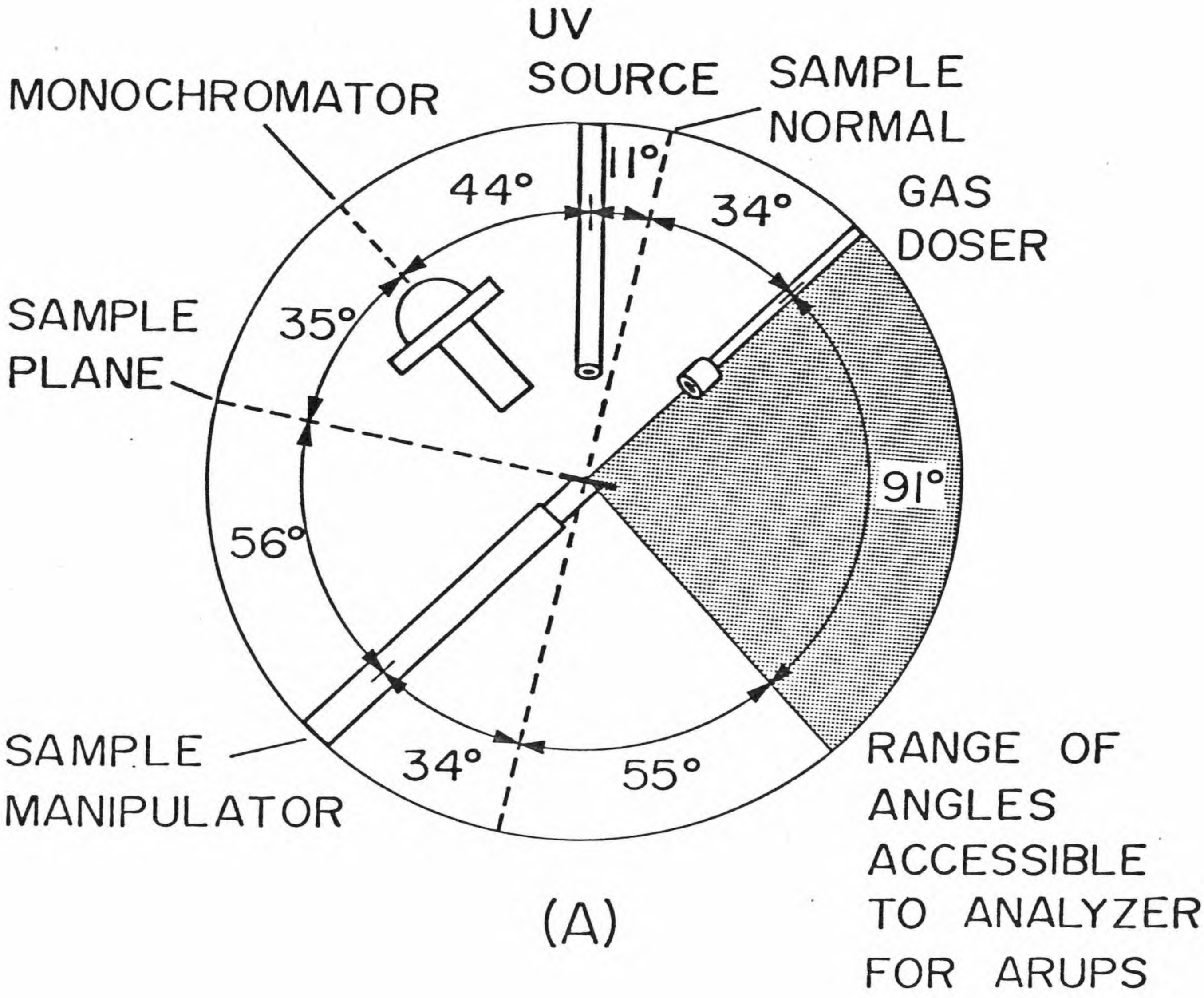

Figure 9(A). Cross sectional view of the EEL spectrometer and probes, within the scattering plane. This configuration is compatible with the vibrational EEL experiment. The angle of incidence of the UV radiation is 32° from the sample normal, and the analyzer can move within +34° and +90° from the sample normal for angle-resolved UPS.

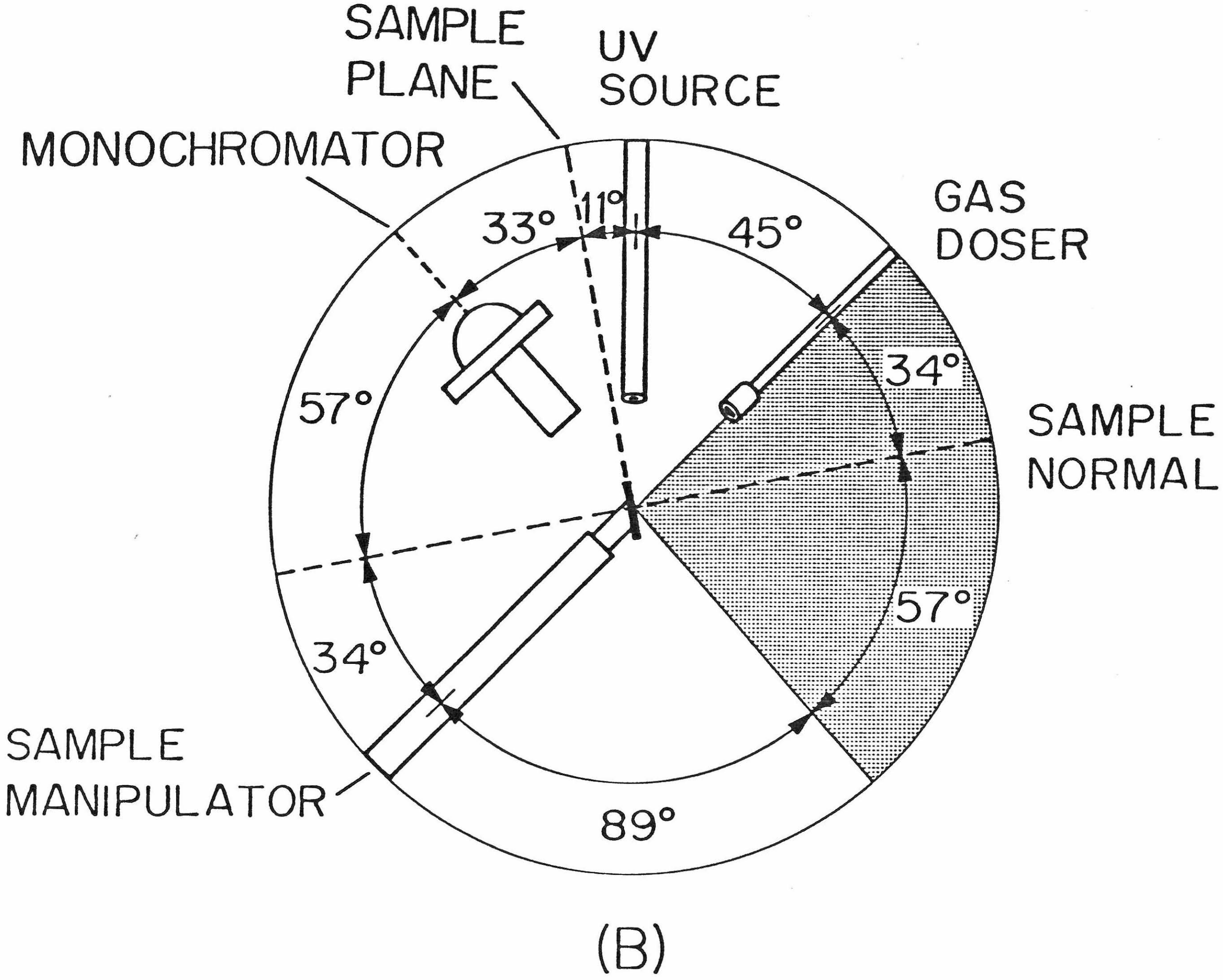

Figure 9(B). Configuration of spectrometer and probes with the sample rotated 180° from Fig. 9(A). The angle of incidence of the UV radiation here is 81°, and the analyzer can move between -34° and +57° from the sample normal. Note that the analyzer should be moved away from the gas doser to dose the crystal, to avoid blocking the gas beam. With the analyzer positioned 180° from the monochromator, the top gear reads "212°".